UNIVERSITÀ DI PARMA

UNIVERSITÀ DEGLI STUDI DI PARMA

DOTTORATO DI RICERCA IN

"FISICA"

CICLO XXXI

Spin Spectroscopy of Materials for Quantum Information Processing, Data Storage and Energy Conversion

Coordinatore:
Chiar.mo Prof. Cristiano Viappiani

Tutore:
Chiar.mo Prof. Giuseppe Allodi

Co-Tutore:
Chiar.mo Prof. Stefano Carretta

Dottorando: Riaz Hussain

Anni 2015/2018

Spin Spectroscopy of Materials for

Quantum Information Processing, Data Storage and Energy Conversion

by

Riaz Hussain

Supervisor: Prof. Giuseppe Allodi

Co-Supervisor: Prof. Stefano Carretta

Department of Mathematical, Physical and Computer Sciences

University of Parma
Parma, PR, Italy

January 2019

Commission of the final examination

External Members:
Prof. Stephen J. Blundell
Prof. Alessandro Lascialfari

Internal Member:
Prof. Paolo Santini

Final examination:

February 2019

Department of Mathematical, Physical and Computer Sciences, University of Parma, Parma, Italy

Abstract

Magnetic materials are of fundamental importance not only as a playground for a wide class of physical phenomena but also for future technological advances. Lanthanide-based molecular nanomagnets are particularly promising for quantum computing and magnetic data storage applications, while Fe_2P based MnFePSi alloys are being regarded as the top candidates to replace conventional refrigerators based on gas compression technology.

The diverse applications of these materials require a deep understanding of their underlying physics. This involves, for instance, a detailed modeling of the intra-molecular interactions and the spin relaxation dynamics for molecular nanomagnets, and a precise characterization of the magnetic phase transition in MnFePSi compounds. Only after an insight into the material physics has been achieved, the free parameters left to the material synthesis can be tuned in order to meet the requirements of real-case applications.

However, there is a dearth of experimental methods capable of handling the entangled electron-nuclear mixed states in lanthanide molecular nanomagnets of interest for quantum information processing, while a sound model spin Hamiltonian for the coupled lanthanide ion and nucleus is also lacking in the literature. In addition, the spin relaxation dynamics of the newly synthesized dysprosocenium single ion magnet demands for urgent investigation, in view of its possible application to high-density data storage at the highest temperatures ever attained in this class of magnets. Finally, the nature of the first order magneto-structural transitions and the so-called mixed magnetism in MnFePSi compounds are not completely understood as well.

In order to tackle all these issues, in this thesis work we employed two different spectroscopies suitable to investigate magnetic systems. On one hand we used nuclear magnetic resonance (NMR), which is a probe of electronic spins in direct space, capable to detect low-energy spin excitations of the system and magnetic order on a local scale, as well as possible inhomogeneities in the latter. On the other hand, we applied inelastic neutron scattering (INS) as a versatile technique sensitive to a higher energy scale than NMR, which can access directly the excited levels and the internal exchange couplings of molecular nanomagnets.

By means of NMR we succeeded to completely characterize the lowest-energy levels of the coupled nuclear and electronic spins and study their coherent dynamics in a [Yb(trensal)] molecular nanomagnet. We detected nuclear transitions of ^{173}Yb, studied their decoherence processes, drove several cycles of Rabi oscillations and demonstrated the possibility to implement a quantum error-protected qubit by its multi-level pattern of nuclear transitions, exploiting its electron-nuclear coupling. We studied the proton spin-lattice relaxations in dysprosocenium, which probe the spin-flip dynamics of the electronic moments through their dipolar coupling to ^{1}H nuclei, thus providing valuable knowledge about the relaxation pathways of the out-of-equilibrium magnetization. Moreover, a family of MnFePS alloys was investigated by both zero- and applied-field NMR. Through our experiments we demonstrated the first order nature of the magnetic transitions even in cases where the transition was believed second order from macroscopic measurements, and we helped elucidating the nature of the so-called mixed magnetism in these compounds. The power of the inelastic neutron scattering spectroscopy, on the

other hand, provided a unique insight into the crystal field (CF) splitting and exchange interactions of a family of Kramers lanthanide dimers, enabling us to determine a sound model for the CF interactions and exchange couplings.

Table of Contents

List of Figures

List of Tables

Abbreviations

MNM	Molecular Nanomagnet
SMM	Single Molecule Magnet
SIM	Single Ion Magnet
QIP	Quantum Information Processing
EPR	Electron Paramagnetic Resonance
CF	Crystal Field
QEC	Quantum Error Correction
MCE	Magnetocaloric Effect
GMCE	Giant Magnetocaloric Effect
FOMT	First Order Magnetic Transition
SOMT	Second Order Magnetic Transition
NMR	Nuclear Magnetic Resonance
INS	Inelastic Neutron Scattering
ZFNMR	Zero Field Nuclear Magnetic Resonance
FID	Free Induction Decay
CPMG	Carr Purcell Meiboom Gill
TOF	Time of Flight
FWHM	Full Width Half Maximum
S/N	Signal to Noise
CFP	Crystal Field Parameters
CASSCF-SO	Complete Active Space Self-consistent Field-Spin Orbit
PCM	Point Charge Modeling
PM	Paramagnetic
FM	Ferromagnetic
XRD	X-ray Diffraction
SQUID	Superconducting Quantum Interference Device

Chapter 0

Introduction

Driven by the advances in quantum mechanics during early 20th century, magnetism has become a research field, which apart from contributing in the basic understanding of matter, underpins some of the most advanced technologies current human society thrives upon. Magnetism and magnetic materials are now an annual multi-billion dollar industry, including simple applications like compasses to the advanced applications like computer hard drives, debit/credit cards, MRI scanners, and synchrotrons. However, even more ambitious high tech advances require the complete knowledge of the fundamental aspects of spin and magnetism phenomena. Revolutionary technologies envisaged by the scientific community from the magnetic materials research include dense memory storage at atomic/molecular level, computers employing quantum mechanical laws to perform computation, and the refrigerators harnessing magnetism driven cooling effects.

In this thesis, we aim to contribute towards the scientific knowledge for the advancement of all of these research fields. We address quantum computing and compact data storage applications by studying the systems that aim to achieve both of these objectives by magnetism and spin interactions at a molecular level, while the research related to magnetic refrigeration is contributed-for by investigating a family of ferromagnetic materials. The thesis is principally based on exploiting two experimental spectroscopies for the advancement of the fundamental understanding and possible applications of cutting-edge materials in next generation magnetic devices mentioned above. In the following sections, we introduce the two classes materials studied in this thesis with a brief overview of their properties and how they can be used from the applications point of view, starting with molecular nanomagnets.

0.1 Molecular Nanomagnets

Molecular magnetism, a field branched out from magnetochemistry, can be considered a research area at the interface of physics and chemistry, where the ideas about the new molecular materials are conceived and realized, their electronic, magnetic and physical properties are investigated for fundamental and applied aspects, and the feedback is looped back to synthesize novel and

improved molecular architectures, with a bottom-up approach, to go through the same cycle again [1]. The close collaboration among physicists, either theoretical or experimental, and synthetic chemists have ensured the advancement of this field towards realization of practical applications.

Molecular nanomagnets (MNMs) are one of the main class of materials in this field. They are 'nano-sized' and contain at least one magnetic atom at their core surrounded by the organic ligands [2]. Due to the effective shielding of organic ligands, each MNM unit is magnetically isolated from other identical units in a crystal. This essentially means that the crystal behaves as a collection of identical entities, where the single molecule properties can be probed by the bulk measurement. Further, every molecule can be described with an effective Hamiltonian.

0.1.1 The evolution of MNMs

Modern interest in molecular magnetism research can be traced back to the early 90's with the report of unique magnetic properties of Mn_{12}-Ac with four Mn(IV) and eight Mn(III) ions, by Caneschi et al. [3]. They employed magnetization and AC-susceptibility measurements with EPR to reveal that the magnetization of this compound relaxes slowly at low temperatures. They further discovered that at scales much smaller than the *superparamagnets*, these clusters resemble their magnetic behavior [3]. Further investigations below liquid-He temperature revealed that the relaxation times of magnetization in this molecule was very long, resulting in a magnetic hysteresis in the M vs H curve (magnetization versus magnetic field) at a single molecule levels [4]. The Mn_{12}-Ac molecule has a high spin ground state (S = 10), resulting from the coupling of individual Mn ionic spins.

The discovery of quantum tunneling of magnetization (QTM) at extremely low temperatures for specific values of the field, where QTM is competing against thermal relaxations, causing the steps in the M vs H plot, was another milestone in the field of molecular nanomagnetism [5]. The name *single molecule magnets* (SMMs), for the zero dimensional molecular magnets exhibiting slow relaxation of magnetization soon became popular [6], although the field itself has much wider scope.

The next family of MNMs with similar behavior were Fe_8 based SMMs [7, 8], which also have been extensively studied ever since. The field of MNMs quickly broadened to include other 3d SMMs containing vanadium [9], cobalt [10], and nickel [11]. Further expansion of the field resulted in the inclusion of pure 4d, 5d, 4f, and 5f [12–15], as well as mixed 3d - 4d [16], 3d - 5d [12], and 3d-4f [17] SMMs in the MNM family. Considering the scope of this thesis, we will just return to the lanthanide (4f) systems in next section.

SMMs retain their magnetization once they are magnetized, even when the magnetizing field is removed, if temperature stays below a certain value called the blocking temperature (T_B). The origin of T_B is the so-called magnetic bistability arising from the effective energy barrier (U_{eff}) to the reversal of the large ground-state spin S due to a large uni-axial magnetic anisotropy term $D*S_z^2$, which must be overcome. The larger U_{eff}, the more time is needed for the magnetization reversal.

The first generation of SMMs focused on increasing the net magnitude of the total ground-state spin S, hoping to maximize the energy barrier due to the relation $U_{eff} = |D|\ S^2$, and consequently achieve higher blocking temperatures. However, it soon became clear that higher

spin may not lead to a grater energy barrier, because of the associated decrease in $|D|$ as S increases [18–20], and the scientific community turned its attention towards the '*rational design* of the SMMs', for the desired applications by 'chemical tailoring'.

0.2 Lanthanide MNMs

The next paradigm shift in the molecular magnetism field arrived with the introduction of MNMs containing f-elements. Indeed, because of the large angular momenta and anisotropies per ion of lanthanide (Ln), 4f-based SMMs seemed a natural choice. However, the weak exchange interactions and large unquenched orbital angular moments common in Ln-ions made them problematic systems hindering further interest in designing and studying the Ln-based SMMs for some time. The report of first Ln-SMM appeared in 2003, 10 years after the slow relaxation of magnetization was reported in Mn_{12}-Ac, when Ishikawa et al. found slow relaxation of magnetization in the compound family $[Ln(Pc)_2]^m$·[TBA], where TBA = tetrabutylammonium, Ln = Tb, Dy, Ho, Tm, or Yb; Pc = dianion phthalocyanine; and m = 1, 0, and +1. In particular, only the $Dy(Pc)_2$ and $Tb(Pc)_2$ showed the properties of SMMs, also exhibiting energy barriers almost four times greater than the record at that time [14].

The advent of slow relaxation of the magnetization in MNMs with single ions at the core, initiated a new class of materials called single ion magnets (SIMs). SIMs possess much simpler structures, as compared to the molecular architectures of a number of poly-metallic 3d ion complexes [19]. The crystal field (CF) felt by the Ln-ion causes the splitting of the 4f ground state given by the total magnetic moment J, into $\pm M_j$ doublets. If the splitting results in the high $|M|_j$ being the ground doublet, a thermal (energy) barrier to the magnetization reversal may appear, often with a magnitude of more than a few hundred wave numbers [21], resulting in the SMM behavior in Ln-SIMs. This energy splitting depends upon the particular Ln-ion, the CF symmetry and molecular structure distortion. The Ln-SIMs have advanced a long way since then and the now they possess the record for the highest magnetization blocking temperature up to 80 K reported this year [22]. This report follows two simultaneous independent reports published last year, which pushed the blocking temperature from 14 K up to 60 K using dysprosocenium SIM [23, 24]. The latter is also one of the samples studied in this thesis, see chapter 5.

So far, we have hinted upon the time line of SMMs or SIMs, exclusively for their ability to block (or store) magnetization, which merely covers one aspect of MNMs applications as classical data storage units (or bits). Still another significant area of research in MNMs is their envisaged applications as quantum bits (qubits). A qubit is a basic unit in quantum computing and quantum information processing (QIP). Often the same MNM maybe regarded as an SMM/SIM or a molecular spin quantum-bit, depending upon the type of experiment carried out. However, there exist some differences between the type of MNM desired for each application. Whilst the magnetization orientation of an SMM/SIM can be simply described by a classical bit, the arbitrary superposition of quantum states needs to be addressed for qubits.
We now turn towards MNMs and their promise in QIP, limiting ourselves to just Ln-based MNMs.

0.2.1 Ln-MNMs for QIP

Leuenberger and Loss were the first to propose that distinct energy levels in SMMs can be harnessed to implement Grovers' database search algorithm [25]. Following this, the first scheme for the encoding of single- and two-qubit gates was put forward by Troiani et al. in 2005 [26], by using the example of antiferromagnetic molecular rings. They followed this by experimentally and theoretically characterizing the Cr_7Ni molecular ring, by studying its energy structure and simulating the time evolution induced by pulsed magnetic fields [26]. Furthermore, they were able to estimate the spin decoherence time and by comparing it with the gating time. In this paper, they clearly stated the possibility for the application of the Cr_7Ni rings as qubits. Two year later, Ardavan and co workers practically measured the decoherence times for the Cr_7Mn and Cr_7Ni SMMs at cryogenic temperatures using electron paramagnetic resonance (EPR), and definitively showed that the coherence time is long enough to implement the quantum gate operations [27].

Following these early proposals and experiments, the molecular transition-metal spin based systems emerged as truly promising systems for the QIP applications, with remarkably long coherence times, thus enabling their coherent manipulation by employing EPR pulses [28–35] and the demonstration of single-qubit gates [36–39]. Coordination chemistry was exploited for these systems to link molecular qubits in pairs [40], generating entangled two-qubit states[41]. Moreover, the tailoring of their reciprocal interaction enabled the synthesis of molecular qubits with switchable couplings [42–44] and the experimental demonstration of two-qubit gates [45, 46]. Ln complexes are a rather unexplored but very interesting class of MNMs qubits [47–50]. They can present advantages such as narrow lines in spectroscopic measurements including EPR or optical spectroscopy, optical addressing and detection by luminescence [51].

In order to use a Ln-MNM as a spin qubit, there are some special considerations which should be accounted for, including the surrounding of the magnetic molecule, the tunneling gap in the Ln ground state and the nuclear spins. The environmental decoherence in MNMs may arise from the interactions with surrounding spins and phonons [52, 53]. The *decoherence* is a process through which a quantum system loses its quantum properties (or superposition state) due to the interactions with the environment. One major source of decoherence in Ln-MNMs, i.e. the interactions with neighboring spins, can be reduced by dilution of magnetic molecules in diamagnetic hosts. The nuclear spins on the ligand ions may cause decoherence as well, however the Ln-ion's own nuclear spin cannot cause the same as it is strongly coupled with the electronic spin. Therefore decoherence can also be reduced by using nuclear-spin-free ligands. MNMs systems are generally robust against the phonon-induced decoherence. The CF surrounding the Ln-ion can be used to achieve the controlled and well defined wave-function mixing of a subset of energy levels and keep this subset isolated from the remaining spectrum. Ln-MNMs can offer a large ground state tunneling gap (Δ) and atomic clock transitions at the level crossings, making them less sensitive to sources of decoherence. Therefore Ln-MNMs could present a clear advantage over cluster-type SMMs in terms of longer coherence times [54]. Although the large tunneling gap is good for qubit applications, it diminishes the SMM magnetic behavior in Ln-MNMs.

0.3 Quantum Information Processing

A quantum computer is a device which exploits quantum phenomena like superposition and entanglement, to perform calculations. It consists of many quantum gates acting on an array of qubits. The qubits are the fundamental units in the of a quantum processor having two distinct (orthogonal) states, usually denoted as $|0\rangle$ and $|1\rangle$. Indeed a qubit encodes a single bit of information just like its classical analog, since it can be prepared in either of the two states. However, a qubit drastically differs from its classical counterpart as it can be prepared and exist in any superposition of two quantum states $|\psi\rangle = \alpha|0\rangle + \beta|1\rangle$. The quantum gates are represented by unitary operators acting on the qubit wave-functions. Any two (orthogonal) state quantum system can physically implement a qubit (for example the horizontal and vertical polarization states of a photon, a spin-1/2 particle's spin orientation, an atom's pair of electronic energy levels, a trapped ion, or the spin of a quantum dot or a nucleus).

Often it is convenient to describe a qubit as a S=1/2 particle and exploit the Pauli matrices corresponding to the three components of the angular momentum in units of $\hbar/2$ as

$$\sigma_x = \begin{pmatrix} 0 & 1 \\ 1 & 0 \end{pmatrix}, \sigma_y = \begin{pmatrix} 0 & -i \\ i & 0 \end{pmatrix}, \sigma_z = \begin{pmatrix} 1 & 0 \\ 0 & -1 \end{pmatrix},$$

and the identity operator

$$\hat{I} = \begin{pmatrix} 1 & 0 \\ 0 & 1 \end{pmatrix}. \tag{1}$$

A qubit is usually described by a 2-dimensional Hilbert space, and graphically any point on a so-called *Bloch sphere* represents an arbitrary state of the qubit. The Bloch sphere is a sphere of unit radius, with each point on its surface corresponding to a different pure state. Opposite points on this sphere represent a pair of mutually orthogonal states. For instance, the north and south poles correspond to the states $|0\rangle$ and $|1\rangle$. The most general spin-1/2 state is

$$|\psi\rangle = \cos\left(\frac{\theta}{2}\right)|0\rangle + e^{i\varphi}\sin\left(\frac{\theta}{2}\right)|1\rangle \tag{2}$$

It can be shown that any unitary operator acting on a single qubit can be written in the form

$$\hat{U} = e^{i\alpha}\left(\cos\beta\hat{I} + i\sin\beta\vec{a}\cdot\vec{\sigma}\right) \tag{3}$$

where α and β are real constants and $\vec{a}$ is unit vector. The α simply change the overall phase of the state vector (and has no physical consequences), while **a** describes an axis in the Bloch sphere and 2β is the rotation of the Bloch vector about that axis.

The unitary transformation above can be realized if we can produce a Hamiltonian proportional to $\vec{a}\cdot\vec{\sigma}$ and control the interaction time. In MNM systems, the basic process that implements these manipulations of the qubits is called *Rabi oscillation*. Rabi oscillations in MNMs are obtained by applying periodic electric or magnetic fields to the spins, at suitable

time intervals. We will apply radio frequency fields to demonstrate our capability to coherently manipulate nuclear spins for sufficiently long times, see chapter 3.

It is not possible to read the quantum state while the computation process is ongoing because it will collapse it and we will not be able to recover the computation back. Considering the fragility of quantum states, errors can always occur during the computation process. A real life quantum computer will certainly require error correction. Quantum error correction (QEC) and the fault-tolerant quantum computation is one of the most critical tasks for the experimental realization of QIP.

Quantum error correction

Noise is always present in physical systems, whether classical or quantum. Classical errors typically result from anomalous flips of the initially stored information in the form of bits. The task of classical error correction is then to detect the erroneous bits and correct them. This is usually achieved by encoding information in multiple bits by making several additional copies of the bit, then using the probability theory and taking a majority vote at the end of a measurement to ensure that the probability of error is minimal. Quantum mechanical computations on the other hand are significantly more susceptible to errors than their classical counterparts, considering that quantum systems are extremely fragile and complex. Quantum errors, in addition to bit flip errors, can also be the result of phase-flip-errors. Thus, the process of error correction in quantum computing is not so simple because of several reasons, for instance [55]:

- It is not possible to make copies of an unknown qubit or quantum data, the so-named *no-cloning theorem*. This is in contrast to the classical error correction where the data-copying is universally used. Forthermore, the *superposition of qubits* has no classical analog.
- In quantum computation the errors are continuous i.e. the complete bit/phase flip is not necessary in an error, as opposed to the discrete classical errors.
- The measurement of all encoded quantum states is not possible, as the quantum superposition state is lost once a measurement is performed.

In spite of problems we mentioned above, several quantum error correction schemes have been developed. Considering the scope of this thesis, we will not indulge into the detailed introduction of QEC; for that there are excellent tutorial reviews available, e.g. see references [56, 57].

Novertheless, at the very basic level, QEC employs the redundant (or additional) encoding method. In this method, the total dimension of the Hilbert space is enlarged further than what is strictly required to store an information (or a qubit), resulting in the error mapping onto a greater orthogonal subspace than the individual qubits. The dimension of the subspace required is determined by the number of qubits utilized in a particular scheme. In physical systems, there are two general strategies to acquire additional subspace. The so-called *block encoding* employs several physical qubits to encode a single logical qubit. On the other hand, in the *Qudit encoding* schemes, a single d (d$>$2) level system is used to encode the single logical qubit. Evidently, more physical resources are required for block encoding. As we will discuss in chapter (3), we have

proposed to exploit multiple energy levels available in a lanthanide MNM to protect against the errors.

0.4 Magnetocaloric Materials

Refrigeration technologies can be found all around us including but not limited to homes, offices, hospitals, schools, data centers, and storage houses. The conventional vapor compression refrigeration mostly contains coolants that cause environmental and health damages. But as a result of population growth, climate change and rising expectations regarding the quality of life, the global energy requirements for the cooling processes are growing even faster. An alternative clean and environment-friendly route to meet this worldwide demand would be the magnetic refrigeration based on the magnetocaloric effect (MCE). The MCE is the release or absorption of heat occurring under the effect of a variable magnetic field in a suitable *magnetocaloric material*. The MCE promises an end to the harmful refrigerants affecting the environment. Furthermore, the cooling efficiency of the magnetic refrigerators can reach up to 60% of the theoretical limit in contrast to the best gas compression refrigeration units with efficiency of about 45% [58, 59].

Scientists have known about the MCE for a long time. It was first reported in 1881 by German physicist Emil Warburg, who observed the change in temperature of an iron sample by placing it into a magnetic field [60]. The advancement of the field was not very rapid, however, and the next significant proposals for a magnetic refrigeration based on MCE appeared about five decades later [61, 62]. Successful demonstration of the effect came further down the line in 1933 when Giauque and MacDougall achieved ultra low temperature using paramagnetic salt as refrigerant [63]. Using the Gd as refrigerant, in 1976, Brown demonstrated the possibility of designing a magnetic refrigerator operating close to room temperature [64]. However, it was not until 1997 when V. K. Pecharsky and K. A. Gschneidner discovered a huge magnetocaloric effect in the ternary intermetallic $Gd_5(Si, Ge)_2$ compound [65], that interest in the magnetic refrigeration was revived. MCE in this compound was about 50% larger than the Gd metal because of first order magnetic transition (FOMT) below the ambient temperature which was accompanied by a magneto-structural transition. This phenomenon was named *giant magnetocaloric effect* (GMCE).

Years immediately following this landmark discovery, many other families of materials exhibiting GMCE were reported. Although, the FeRh compound with GMCE was discovered before $Gd_5(Si, Ge)_2$ [66], it did not receive much attention due to the high cost and rare availability of Rhenium metal. Other major families exhibiting GMCE include the $La(Fe,Si)_{13}$ family [67, 68], MnCoGeBx alloys [69], the MnAs and $MnAs_{1-x}Sb_x$ materials [70, 71]. The Heusler alloys (Ni Mn)-X; X = Ga, Mn, etc; such as the $Ni_{0.50}$ $Mn_{0.50-x}$ Sn_x [72] showing inverse MCE, with other examples [73–75], and the Fe_2P-based $(Mn,Fe)_2(P, X)$ (X =Si, As, Ge, B) compounds [76–80] are other promising classes of materials. For a detailed survey of GMCE materials readers are referred to the reviews [81–83].

There are some important considerations one has to make while choosing the magnetocaloric material from the applications point of view. Some of the sought-after traits are cheap raw material and low cost of production, environmentally benign, large tunable magnetic anisotropy and critical temperature, stable and corrosion free material etc. Fe_2P based $(Mn,Fe)_2(P, Si,$

$B)_1$, compounds are among the best candidates for energy conversion and magnetic refrigeration applications owing to the high tunability of their giant magnetocaloric effect and working temperature, stability of composition, low hysteresis, and non-toxicity and relatively low cost materials. The GMCE and FOMT in these compounds stems from an interplay of magnetic, structural and electronic properties. The complex mechanisms driving these effects are still far from understood, and there is a lot of research going on with different approaches and materials.

0.5 Thesis Outline

In this thesis, we have employed spin spectroscopies to understand the fundamental physics of a few state-of-the-art materials for quantum information processing, data storage, and magnetic refrigeration applications In the preceding introductory part, we covered some motivations for this research and the historical evolution of both the molecular nanomagnets and magnetocaloric materials. We also introduced some relevant basic concepts of QIP and quantum error correction. The rest of this thesis is arranged as follows:

- **Chapter 1** collects the basic theoretical concepts useful for the later studies on the molecular nanomagnets. This includes the effective Hamiltonian approach targeted to the lanthanide molecular nanomagnets. The magnetocaloric effect relevant for the emerging materials in magnetic energy conversion applications is introduced in the later part of this chapter, followed by few comments on the first and second order magnetic transitions.

- **Chapter 2** details the experimental methods we have used for our studies, namely nuclear magnetic resonance and inelastic neutron scattering. We start by introducing the necessary physics behind these techniques and then outline the various technical aspects and practical parameters of the instruments used during this study.

- **Chapter 3** is devoted to the study of Yb(trensal) MNM, characterized using the NMR spectroscopy. The nuclear-electronic interactions, spin-spin and spin-lattice relaxations were probed with ^{173}Yb NMR. A complex pulse sequence (CPMG) was implemented to demonstrate the enhancement of phase memory time using multiple refocusing pulses. Rabi Oscillations were driven between various nuclear energy levels, thus demonstrating the coherent manipulations of the nuclear qudit. Finally, using this electronic-nuclear coupled multi-level system, an error protected qubit was proposed.

- **Chapter 4** deals with a lanthanide (Ln=Er, Yb, Dy, Lu) based dimer family of MNMs, explored using the INS spectroscopy. Starting with the common introduction of the molecules, their structure, and the specific instrument settings, the rest of the chapter is arranged in three broad categories dedicated to the results of each individual magnetic dimer. Each section so arranged includes the INS results for both the crystal field and exchange splitting in these dimers, comparison of experimental results with the calculations, and few electron paramagnetic resonance spectroscopy results (the latter for Er_2 and Yb_2 MNMs). In case of Dy dimer, we also briefly outline the preliminary results from a point charge modeling approach, which is still underway.

- **Chapter 5** outlines the NMR experiments carried out on the dysprosocenium single ion magnet. Protons (^{1}H) are used as a probe for the SIMs relaxation dynamics. We will briefly introduce the basic theoretical concepts which are later going to be used for modeling. The detailed analysis of these results is still ongoing and here we have presented only the preliminary results.

- **Chapter 6** presents the results from the NMR experiments on Fe_2P based MnFePSi alloys for magnetic refrigeration applications. ^{55}Mn NMR measurements in both zero and applied field is carried out to understand the nature of magnetic transitions in these compounds. The magnetic moment evolution and the spin-spin relaxation dynamics are also reported. The results are discussed and the conclusion are drawn at the end of chapter.

Chapter 1

Theoretical Background

In this chapter we will narrate the theoretical aspects that forms the basis of the experimental data interpretation, explored in the later part of this thesis, both for the Ln-based molecular nanomagnets and the Fe_2P based magnetocaloric materials. We will be touching upon the introductory concepts broadly categorized in two themes: i) a summary of the underlying energy structure in the lanthanide molecular magnetism and ii) the relevant introduction of the magnetocaloric effect.

1.1 Lanthanide molecular magnetism

All the interesting magnetism phenomena in lanthanide MNMs (Ln-MNMs) stem from the magnetic moment of the incomplete 4f orbital of the magnetic ion. The general electronic configuration of the atomic ground state of the lanthanide elements, starting from lanthanum (n = 0, Z = 57) and ending at lutetium (n = 14, Z = 71), is [Xe]$4f^n$ $6s^2$. [1] However, La, Ce, Lu, and Gd have the [Xe]$4f^{n-1}$ $5d^1$ $6s^2$ electronic configuration. The most stable oxidation state of lanthanide ions is Ln^{3+}, with few exceptions. [2] The Ln-ions tend to donate the 6s (and 5d) electrons before 4f. Within the Ln-atoms, 4f orbitals are contracted inside the inner space and are efficiently screened by the outer, completely occupied, 5s and 5p shells. The Ln magnetic moment is not actively involved in the interactions with neighboring atoms, which is in contrast to the highly spread out d orbital in transition metals. Therefore, as a first approximation, the magnetic properties of Ln-MNMs in a tripositive state can be considered as the ones from a free Ln^{3+} ion with an essentially unquenched orbital angular momentum, even in the presence of a ligand field [84].

The interactions in the Ln-MNMs are rationalized as follows: Coulomb repulsion between electrons and correlations effects cause the splitting of electronic 4f configuration, with total orbital and spin angular momenta (**L** and **S**, respectively) being the good quantum numbers. The energy splitting due to electrostatic Coulomb interaction is of the order of $\sim 10^4$ cm^{-1}, with

[1] [Xe]=$1s^2$ $2s^2$ $2p^6$ $3s^2$ $3p^6$ $3d^{10}$ $4s^2$ $4p^6$ $4d^{10}$ $5s^2$ $5p^6$.

[2] Examples of stable exceptions to tripositive electron configurations are Eu^{2+}, Ce^{4+}, and Tb^{4+}.

Hund′s first two rules and Pauli exclusion principle stating the $^{2S+1}$L energy levels ordering scheme (2S+1 is the spin multiplicity). Spin-orbit coupling then splits the $^{2S+1}$L levels into $^{2S+1}$L$_J$ levels, with **J=L + S** as the total angular momentum whose value ranges from $|$ L $-$ S$|$ to L + S. According to Hund′s third rule the ground state is described by J = L + S, if the outermost sub-shell is more than half filled (i.e. $n > 7$), whereas for $n \leq 7$ the J = $|$ L $-$ S$|$. The

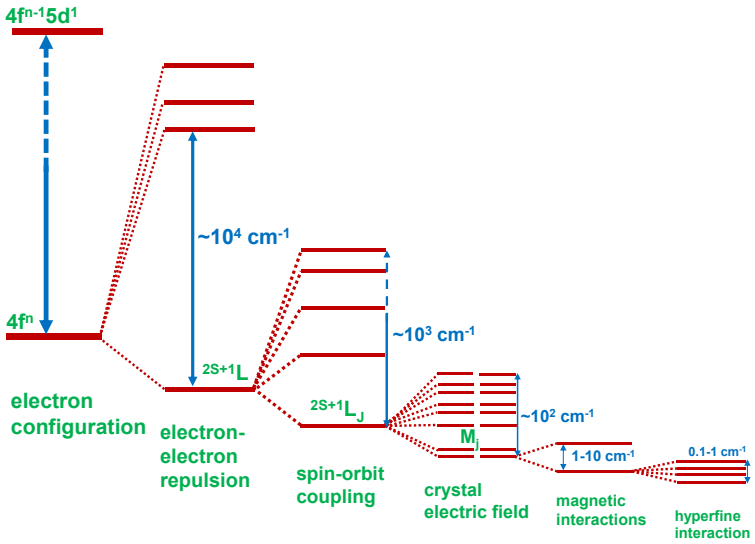

Figure 1.1: Energy structure illustration of the typical energy levels of a Kramers lanthanide ion due to the electron configuration, Coulomb repulsion, spin-orbit, ligand-field, magnetic, and hyperfine interactions. The estimate of magnetic interactions is assumed with an external field of the order of 1 T.

energy gap between ground and the excited $^{2S+1}$L$_J$ terms is so large that the excited levels are not populated even at ambient temperatures. Therefore, Ln-MNMs magnetism is determined by the ground $^{2S+1}$L$_J$ term only as well as the fact that in the J ground state the spins are parallel to the orbital angular momentum for ions with $n > 7$ and anti-parallel for the $n \leq 7$ ions. The figure 1.1 summarize a typical Ln-ion's energy levels splittings and their relative magnitudes due to inter-electron repulsion, spin-orbit, ligand-field, magnetic, and hyperfine interactions.The magnetic interaction is assumed to represent the exchange, dipole and Zeeman terms for Ln-MNMs, the later in the external field of $\sim$ 1 T.

In order to realize the applications of Ln-MNM systems, one needs to study their properties in both the stable magnetic state and the systems' recovery mechanism once any perturbation is applied. In this thesis, only the nuclear relaxation mechanisms will be discussed, and they are outlined in the next chapter.

1.1.1 The effective Hamiltonian approach

The intra-molecular magnetic interactions in MNMs are fundamental to the understanding of their low temperature magnetism. In the transition metal MNMs, spin Hamiltonian approach is

frequently utilized to interpret, model, and classify the magnetic and spectroscopic experimental data without invoking the fundamental theories. In transition metal spin Hamiltonian formalism, all the orbital degrees of freedom are replaced with their spin counterparts by invoking the systems' symmetry properties. However, a key assumption in spin Hamiltonian approach is the quenching of orbital angular momentum, which − as we stated above − is not true for Ln-based MNMs. The total angular momentum J (=L+S) with unquenched orbital moment in Ln-MNMs, is good quantum number, so we must replace the spin quantum number (S) by the J, within the spin-Hamiltonian formalism. The Hamiltonian for Ln-MNM systems, which can adequately account for the most of observed magnetic phenomena can be written as:

$$\mathcal{H}_{eff} = \mathcal{H}_{CF} + \mathcal{H}_{Zee} + \mathcal{H}_{ex} \tag{1.1}$$

where the $\mathcal{H}_{CF}$ represents the crystal-field Hamiltonian (single ion term), the $\mathcal{H}_{Zee}$ is the Zeeman Hamiltonian, while the $\mathcal{H}_{ex}$ represents the exchange interaction between two magnetic centers. Here, we have taken only the ground term in spin-orbit multiplets. Yet another term we did not include in the Hamiltonian above (1.1) is the electron-nucleus hyperfine interaction ($\mathcal{H}_{hf}$), which is usually tiny in comparison (figure 1.1) and can be easily omitted. However, for the low-energy spectroscopies (e.g. NMR) and the complete understanding of magnetic relaxations, the hyperfine term must be included.

The crystal electric field

If a Ln-ion is placed in a molecular or crystalline environment of lower-than-spherical symmetry, the ligands surrounding the ion creates a field, called the ligand or crystal electric field (CEF). Due to the localized nature of 4f orbital and electronic screening the CEF effect is much smaller than the electron correlations and spin-orbit interactions, so it can be taken as a perturbation. The CEF however, perturbs the partially occupied 4f shell and lifts the $^{2S+1}\mathrm{L}_J$ term degeneracy, splitting it into M_J states. The splitting strongly depends on the local environment/symmetry around the Ln-ion.

The electronic states in the systems with odd number of electrons in the presence of a crystal field of any symmetry, are at least two-fold degenerate in the absence of a magnetic field. This theorem is called *Kramers theorem* and the ions with an odd number of electrons (or equivalently, half-integer J value) are called the *Kramers ions*. The M_J splitting for Kramers ions will have two-fold degeneracy, with a maximum of (2J+1)/2 levels. For the non Kramer ions, the crystal field degeneracy results in a maximum of 2J+1 levels for each $^{2S+1}\mathrm{L}_J$ term. Since all the systems studied in this project were Kramers ions, we will mostly limit our discussion to these systems.

The crystal field theory (CFT), first developed by Bethe in 1929 [85], is used to analyze and simulate the f-element energy level schemes. In CFT, the CF Hamiltonian is written under the *weak-field approximation* which assumes that the typical energy of CF splitting is much smaller than the spin-orbit (and electronic correlation) level splitting, rendering the total angular momentum (J) as good quantum number. For rare-earth ions this approximation works well as the CEF interaction energies are typically an order of magnitude (or more) smaller than the spin-orbit interactions, figure 1.1. The CFT starts with assuming that the potential energy for a

magnetic ion in a crystal, with n electrons in the unfilled shell is given by a one body potential as $\mathcal{H}_{CF} = -e\sum_{i=1}^{n} V(r_i, \theta_i, \varphi_i)$ where the sum is over all the electrons of central ion and

$$V(\mathbf{r}_i) \;=\; \sum_{k=1}^{N} \frac{-e\, Z_k}{|\mathbf{R}_k - \mathbf{r}_i|}, \tag{1.2}$$

where N is the total number of ions contributing to the crystal potential, Z_k is the effective charge of k-th ligand ($Z_k > 0$ for negative ion), and r_i and R_k are the vector positions of the i-th and k-th electron and ligand, respectively. The term $1/|\mathbf{R}_k - \mathbf{r}_i|$ can be expanded in terms of spherical harmonics $Y_l^m(\theta_i, \varphi_i)$ reducing the terms involved inside the summation as well as making the calculation of the Hamiltonian matrix elements much easier as the $|LSJM_J\rangle$ states are the linear combinations of spherical harmonics. The CF Hamiltonian can be written as

$$\mathcal{H}_{CF} = \sum_{i=1}^{n}\sum_{l=0}^{\infty}\sum_{m=-l}^{l} \tilde{A}_l^m r_i^l Y_l^m(\theta_i, \varphi_i) \tag{1.3}$$

where

$$\tilde{A}_l^m = e^2 \frac{4\pi}{2l+1} \sum_{K=1}^{N} \frac{Z_k Y_l^{m*}(\theta_k, \varphi_k)}{R_k^{l+1}}.$$

The coefficients $\tilde{A}_l^m$ in equation (1.3) can be calculated if the geometry of the system is known [84]. Taking electrons of same type and some geometry considerations, one can simplify the Hamiltonian 1.3, however for many electrons systems its calculation is complicated and the parameterization of CF potential proposed by Stevens [86], is universally used in molecular magnetism.

Stevens argued that any electrostatic potential, meeting the symmetry requirements around any Ln-ion and within one J multiplet by neglecting the J-mixing, can be computed by summing the equivalent angular momentum operators which replace the spatial coordinates. These operators are called the *Stevens equivalent operators*. The effective crystal field Hamiltonian for Ln-ions in Stevens′ formalism, can be written as [84]

$$\mathcal{H}_{CF} \;=\; \sum_{l=2,4,6}\sum_{m=-l}^{l} A_l^m \langle r^l \rangle\, \alpha_l\, \hat{O}_l^m = \sum_{l=2,4,6}\sum_{m=-l}^{l} B_l^m \hat{O}_l^m, \tag{1.4}$$

where α_l are the Stevens′ factors different for each f^n configurations and distinct l values, the $\langle r^l \rangle$ is the expectation value of r^l (the radius of the 4f orbital) which has been tabulated. $B_l^m = A_l^m \langle r^l \rangle \alpha_l$ are the Stevens′ crystal field parameters and $\hat{O}_l^m$ are the Stevens′ operator equivalent of CF potential. The Stevens′ CF parameters B_k^q are always real. The Stevens' operator equivalent method is widely used for obtaining the energy estimates of the CF splittings and the crystal field parameters (CFPs) of the ground-state multiplets, directly from the experimental measurements like the inelastic neutron scattering (INS) transitions, EPR, and magnetic measurements. The l and m can take a maximum of 27 parameters B_l^m, because of their relation with operators related to spherical harmonics Y_l^m.

The equivalent operators are immensely useful for CF splitting within a single $^{2S+1}L_J$ level without multiplet mixing contribution. For the heavy Ln′s, multiplet mixing approximation is reasonable for the magnetic behavior description below room temperature, because the ground and excited spin-orbit state splitting is more than 2000 cm^{-1}. If the Ln ion environment is of high-symmetry, then some terms in the CF Hamiltonian vanish and the CF parameters calculation complexity can be reduced greatly. However, often the Ln-MNMs crystallize in a very low Ln-site point-symmetry making the CF Hamiltonian calculations rather cumbersome [87]. We now extend the discussion to include magnetic interactions of Ln-MNMs between multiple magnetic centers and external magnetic field.

Exchange interactions

Exchange interactions between two Ln-ions are an important contribution to cooperative effects in the Ln-MNMs. The effective Hamiltonian for exchange interaction is given as [88]:

$$\mathcal{H}_{ex} \;=\; -2\sum_{i>j}\mathbf{J}_i\cdot\mathcal{J}_{ij}\cdot\mathbf{J}_j, \tag{1.5}$$

where the $\mathcal{J}_{ij}$ are the generalized exchange tensors and J are the total angular momenta. Exchange interactions in 4f MNMs are generally small and can be of the same order of the dipolar interactions. The latter can be described by the same Hamiltonian (1.5) with coefficients calculated in the point-dipole approximation.

In transition metal MNMs however, generally superexchange is sizable and for most situations, the direct dipolar coupling is one or two orders of magnitude weaker than the leading indirect exchange between nearest neighbors and only the Heisenberg term can provide a reasonable approximation, which is not the case for Ln-MNMs.

Zeeman interaction

In the presence of an external magnetic field, the lanthanide J multiplet degeneracy is removed by the so-called *Zeeman effect*. The populations of the 2J+1 energy levels of Kramers ions, depend on the temperature. The magnitude of this splitting, typically around 1 cm^{-1}, is much smaller than the inter-electron, spin-orbit, and the CF interactions. The Zeeman Hamiltonian reads [84]:

$$\mathcal{H}_{Zee} \;=\; -\mu_B\boldsymbol{\mu}\cdot\mathbf{H}_0, \tag{1.6}$$

with $\mathbf{H}_0$ the external magnetic field, μ_B the Bohr magneton, and μ is the operator for magnetic moment given as $\boldsymbol{\mu} = \sum_i (g_s\, s_i + l_i)$. Here g_s is the gyromagnetic factor equal to 2.0023, s_i and l_i are the spin and angular momenta in the $\hbar$ units. The magnetic moment $\boldsymbol{\mu}$ can be conveniently written in the *Russell−Saunders* (RS) or *intermediate* coupling regimes (respectively for the very weak or intermediate spin-orbit coupling as compared to the electron repulsion), as: $\boldsymbol{\mu} = \mathbf{L} + g_s\,\mathbf{S}$. The matrix element of the magnetic moment operator ($\boldsymbol{\mu}$) between the states $|JM\rangle$ can be shown as proportional to the **J** operator, using the Wigner - Eckart theorem as

$$\langle JM|\mathbf{L}+2\mathbf{S}|JM'\rangle \;=\; g\,\langle JM|\mathbf{J}|JM'\rangle, \tag{1.7}$$

with the Landé factor $g = g_J$ for the RS coupling limit, given as

$$g = 1 + \frac{J(J+1) - L(L+1) + S(S+1)}{2J(J+1)}.$$

Therefore, the $\boldsymbol{\mu}$ in equation (1.6) for the Zeeman interaction in the J-multiplet, can be written as $\boldsymbol{\mu} = g\,\mathbf{J}$.

Once the CF−ion is placed inside an external magnetic field, one has to add the Zeeman term to the CF Hamiltonian. The Kramers ions are in general good candidates for the observation of transitions between Zeeman split levels using EPR. The spin-Hamiltonian approach is used to model/interpret the spectra obtained from the EPR. The basic assumption in this case, is that the transitions are induced in a multiplet which can be represented by a pseudo (or effective) spin (S′) in a way that the degeneracy of the multiplet without the external magnetic field is equal to 2S′+1. Using this assumption for the Kramers ground doublet, the pseudo-spin will be S′= 1/2, while the spin Hamiltonian given as

$$\mathcal{H}_{spin} = \mu_B \mathbf{S}' \cdot \overline{\mathbf{g}} \cdot \mathbf{H}_0 \tag{1.8}$$

where $\overline{\mathbf{g}}$ is the *spectroscopic splitting tensor*.

Hyperfine interactions

The nuclei in atoms/ions often possess a magnetic moment, which results from intrinsic angular momentum of their components (nucleons) coupling to a non-zero spin. The hyperfine coupling between 4f rare-earth ion spin-orbit coupled electronic cloud and the nuclear spins usually has negligible effect upon the magnetic moment properties of the electrons. However, it can influence the relaxation mechanism by so-called quantum tunneling of magnetization, and the coherence properties of the lanthanide single ion MNMs. The interaction between the Ln-electronic moment and the nuclear spin $\mathbf{I}$ is given as:

$$\mathcal{H}_{hf} = \sum_i \mathbf{I} \cdot \mathbf{A}_i \cdot \mathbf{J}_i \tag{1.9}$$

where $\mathbf{A}_i$ is the electron-nuclear magnetic interaction tensor and usually have values around a few μeV. Two main contributions to the hyperfine interaction are the *contact* and *dipolar* terms. The contact hyperfine coupling is only relevant for the s-orbitals, while the dipolar part is expressed as in the equation (1.9), with $\mathbf{A}_i$ replaced by A_{dip}. The electric quadrupole interaction (NQI) for the nucleus also adds a term in the energy proportional to $p_Q\, I_z^2$ as the first order approximation. NQI results in an unevenly spaced 2I+1 levels in the nuclear multiplet.

Somewhat more detailed and generalized treatment of the electron-nuclear interactions will be presented in the chapter 2, section 2.1.3.

1.2 The magnetocaloric effect

The emission or absorption of heat by magnetic materials due to the influence of an external magnetic field is termed the *magnetocaloric effect* (MCE). The MCE is essentially a temperature

or entropy change due to the variation of an applied magnetic field under adiabatic or isothermal conditions. Under isothermal conditions, the thermal (lattice plus electronic) entropy is constant, while the application of a magnetic field reduces the magnetic entropy. On the other hand, under adiabatic conditions, the thermal entropy rises to compensate for the decrease of magnetic entropy in order to keep the total entropy constant.

Let us take an example of the entropy of a paramagnetic or ferromagnetic spin system close to its ordering temperature (T_C). The entropy here consists of two contributions, the system temperature entropy and the magnetic ordering entropy. If an external magnetic field is applied under the adiabatic conditions (i.e. there is no heat exchange with the surrounding), the thermal or lattice entropy (neglecting the electronic contribution) must increase to preserve the constant total entropy of the system. This results in the system heating up and its temperature rises. Conversely, the demagnetization should manifest in the cooling down of the magnetic system using the same arguments. The temperature variation effect we just summarized for a spin system, due to spin coupling with the applied magnetic field, is termed the MCE. The magnetic materials can roughly be considered as consisting of magnetic, lattice, and conduction electrons subsystems, all of which contribute to the total system entropy for 3d-transition metal systems (S_{tot} = S_l + S_m + S_e), by not taking electron–phonon interaction into account.

1.2.1 First and second order transitions

Phase transitions are often associated with the ordering and they may occur in the thermodynamic systems. There are two basic types of phase transitions, the first order and the second order, depending on which of the corresponding first or second derivatives of the thermodynamic potentials with respect to the thermodynamic variables are discontinuous (have a jump). The magnitude of change in entropy (ΔS) is large near the magnetic phase transition, therefore a significant MCE is expected at temperatures close to magnetic phase transitions. The generalized coordinates like entropy, volume, and magnetization of a system are the first-order derivatives of the Gibbs free energy.

There are no jumps in the first derivative of Gibbs free energy (i.e. entropy, thermal expansion, or magnetization) in the second-order phase transition. Furthermore, there is no latent heat and the specific heat changes discontinuously at the second-order transition. These phase transitions are also named the continuous phase transitions. The continuous change in the magnetization and finite value of specific heat gives rise to to a low entropy situation, therefore at a second order phase transition, only a weak magnetocaloric effect is expected.

Conversely for a magnetic transition of the first-order, the first derivative of Gibbs free energy (i.e. the magnetization, entropy, and the lattice parameters) change discontinuously while the latent heat approaches infinity at the transition temperature (T_C). The resulting MCE is much larger and these transitions are often associated with sudden volume changes. However, first order magnetic transition materials also exhibit a sizable thermal hysteresis making them unsuitable for the thermo-magnetic cycles.
The best magnetocaloric materials to date are the ones that have a magnetic transition somewhere in-between the first and the second order. Consequently, they have a contribution from the latent heat (i.e. a significant magnetocaloric effect) as well as a small thermal hysteresis.

Chapter 2

Experimental Techniques

In science, and particularly physics, the experiment is the ultimate test of knowledge and a tool for the advancement of the understanding of natural phenomenon. In order to tackle the study of magnetism and the magnetic excitations in condensed matter, a variety of techniques have been developed and applied. The choice of the most appropriate technique depends on the specific material under investigation and on the relevant time and space scales involved. Figure

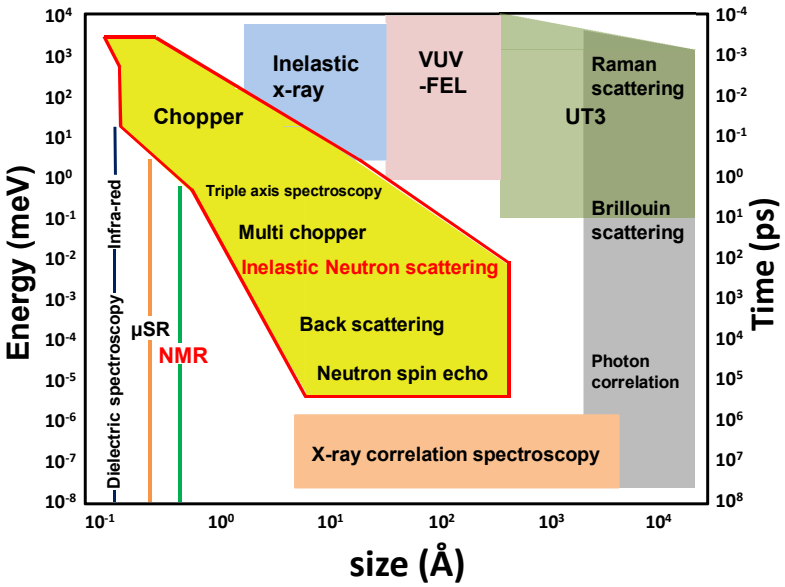

Figure 2.1: The size, time and energy scales accessibility ranges for various condensed matter probes. INS can access the higher energies and longer correlation lengths whereas the NMR is specialized for the slower dynamics in condensed matter.

2.1, shows a schematic diagram comparing various experimental techniques for magnetism in condensed matter. Evidently, neutron scattering is one of the most versatile probes, thanks to

its characteristic time and space scales spanning several decades, which in principle, makes it access any magnetic excitation. NMR on the other hand, is more sensitive to slower (i.e. lower energy) spin excitations, beyond the range accessible to neutrons. Moreover, NMR is a probe in direct space and can detect short range magnetic order or disordered magnetism, where a probe in reciprocal space like neutron scattering is poorly sensitive. Therefore, the two techniques effectively complement each other.

This chapter is devoted to a brief review of the experimental techniques employed during this PhD project: Nuclear Magnetic Resonance and Inelastic Neutron Scattering, focusing mainly on the aspects most relevant to the experiments later described in the thesis.

2.1 Nuclear Magnetic Resonance

Nuclear magnetic resonance (NMR) spectroscopy is an accomplished technique which has found its application in several branches of both fundamental and applied science. While the most widespread applications of NMR are encountered nowadays in medicine and analytical chemistry, in the form of magnetic resonance imaging (MRI) and high-resolution NMR, this technique is still a valuable investigation tool for condensed matter physics, where it was originally developed and applied. In comparison with the electron magnetic moment, the nuclear moment is smaller by a few orders of magnitudes, which means it cannot be detected using the conventional static methods. The method of magnetic resonance was developed around the mid-nineteenth century to study nuclear magnetism. The magnetic resonance phenomenon can take place, in principle, in any ensemble of angular moments (referred to as "spins" for short, regardless of their spin or orbital origin), endowed with a magnetic moment proportional to their spin (in view of the Wigner-Eckart theorem). The resonance consists of the coherent oscillation (or precession) of the moments, driven by an alternating magnetic field whose frequency matches to that of the spins. For most nuclei with non-zero spin, their typical resonance frequencies fall into the radio-frequency (rf) region of the electromagnetic spectrum. In a typical NMR experiment, the atomic nuclei in an external magnetic field (H_0) are excited by a resonant rf pulse and the response of atomic nuclei is recorded, retrieving information on the localized spin-charge surrounding of the nucleus being probed by the hyperfine coupling. Moreover, NMR is sensitive to the spin fluctuations traced by the nuclear magnetization relaxations.

In the following few paragraphs we will briefly introduce the concept of magnetic resonance in a semi classical approach and how it naturally leads to the concepts of nuclear spin relaxation phenomena. We will be focusing on the aspects of the NMR spectroscopy which will be used later in this thesis. The NMR theory and concepts presented in this section, are mainly based on the Slichter, Abragam, and Fukushima−Roeder textbooks [89–91], and the theses [92, 93].

2.1.1 Simple resonance picture

A nucleus is made up of one or more nucleons coupled together, so that in the ground state the nucleus carries a total magnetic moment $\boldsymbol{\mu}_n$ and a total angular momentum $\mathbf{I}$, such that

$$\mu_n = \gamma \mathbf{I} \tag{2.1}$$

where the scalar γ is termed the nuclear gyromagnetic ratio [1]. In the quantum mechanical theory, the vector quantities $\boldsymbol{\mu}_n$ and $\mathbf{I}$ are taken as the operators. We can define a dimensionless angular momentum operator $\hat{\mathbf{I}}$ in the following manner:

$$\mathbf{I} = \hbar\hat{\mathbf{I}}$$

$\hat{\mathbf{I}}^2$ then has eigenvalues of $I(I+1)$, where I can take either integer or half-integer values. The components I_z commute with $\hat{\mathbf{I}}^2$, so its eigenvalues 'm' may take any of the $2I+1$ values $-I$, $-I+1$, ...,$I-1$, I. The expression (2.1) can then be rewritten as

$$\langle Im|\mu_{x'}|Im'\rangle = \gamma\hbar\langle Im|I_{x'}|Im'\rangle$$

here $\mu_{x'}$ and $I_{x'}$ are the components of the operators μ and $\mathbf{I}$ along any arbitrary direction x'. If we apply an external magnetic field $\mathbf{H}$ along the z direction, the energy levels are split by the Zeeman interaction, and the nuclear Zeeman Hamiltonian is given as:

$$\mathcal{H}_{Zee} \;=\; -\mu_n \cdot \mathbf{H} = \gamma\hbar\mathbf{I} \cdot H_0, \tag{2.2}$$

where H_0 is the magnetic field component along z. The eigenvalues of $\mathcal{H}_{Zee}$ are:

$$E_m = -\gamma\hbar H_0 m \tag{2.3}$$

Each level pair E_m, E'_m in equation (2.3) may give rise to transitions between these levels due to electromagnetic absorption, provided that the interaction Hamiltonian has a non-vanishing matrix element between the two levels. To satisfy the law of conservation of energy, the said interaction must be time dependent and with an angular frequency ω of

$$\hbar\omega = \Delta E$$

where ΔE is the difference of energy between the initial and final nuclear Zeeman energies. In order to produce the magnetic resonances phenomenon, an alternating magnetic field is applied perpendicular to the static field, adding a perturbing term to the Hamiltonian:

$$\mathcal{H}_{pert} = -2\gamma\hbar H_1 I_x cos(\omega t), \tag{2.4}$$

with H_1 being the amplitude of the rotating and counter-rotating field components. The operator I_x has non-vanishing matrix elements $\langle m|I_x|m'\rangle$ only for the transitions $m' = m \pm 1$ (i.e. the selection rule for the transition is $\Delta m = \pm 1$). Thereupon, only the transitions between adjacent energy levels ($m \rightarrow m \pm 1$) are allowed, giving

$$\begin{aligned} \hbar\omega = \Delta E = \gamma\hbar H_0 \qquad & \text{or} \\ \omega = \gamma H_0 \qquad & \end{aligned} \tag{2.5}$$

In the case of pure Zeeman Hamiltonian, the quantum system evolution following a rf pulse corresponds to classical Larmor precession (2.5) with Larmor frequency $\omega_L = \gamma\ H_0$, therefore we can resort to the classical description of the time evolution of the nuclear spin ensemble, which we handle in the next section.

[1] Nuclear gyromagnetic ratio is given as $\gamma = g\ \mu_N/\hbar$, with μ_N = e $\hbar$ / 2 m_p = 5.05 $\times$ 10^{-27} A m^2 is the nuclear magneton, m_p is the proton rest mass and g is the Landé's g-factor for the nucleus

2.1.2 Bloch equations

We outline a treatment capable of describing the transient response of the nuclear magnetization under the effect of the static field, a driving rf field and irreversible "friction" processes (the relaxation effects), and not just the average rf absorption. Such a description closely corresponds to the modern pulsed NMR technique. The simplest approach is describing nuclei as classical spins, subject to Larmor precession and ad-hoc relaxation terms, leading to so-named *Bloch equations* [94]. If quadrupolar and spin-spin interaction terms can be neglected, Bloch equations turn out to be also validated by a fully quantum treatment. In any typical NMR experiment the alternating rf field (H_1) applied in the $x, y-$plane, say in the x-direction, flips the position of nuclear spins from their initial polarization produced by the static magnetic field (H_0) along z-axis. After switching-off H_1, the nuclear magnetization will return to the equilibrium position with a time constant of T_1 due to the interaction with the environment (lattice), so we can write

$$\frac{dM_z}{dt} = \frac{M_0 - M_z}{T_1}, \tag{2.6}$$

where $M_z = \gamma\hbar n/2$ for I = 1/2 in general, and the thermal equilibrium magnetization value is M_0, with $M_0 = \chi_n H_0$ in terms of nuclear magnetic susceptibility (χ_n).
The torque due to the magnetic field H_0 drives the magnetization M to precess around the magnetic field as:

$$\frac{dM_z}{dt} = \frac{1}{T_1} + \gamma(\mathbf{M} \times \mathbf{H})_z. \tag{2.7}$$

Combining the precession (2.7) and relaxation (2.6) equations, we get

$$\frac{dM_z}{dt} = \frac{M_0 - M_z}{T_1} + \gamma(\mathbf{M} \times \mathbf{H})_z. \tag{2.8}$$

Moreover, in a static field H_0 the transverse components of the nuclear magnetization vanish at the thermal equilibrium. Thus

$$\begin{aligned} \frac{dM_x}{dt} &= \gamma(\mathbf{M} \times \mathbf{H})_x - \frac{M_x}{T_2} \\ \frac{dM_y}{dt} &= \gamma(\mathbf{M} \times \mathbf{H})_y - \frac{M_y}{T_2} \end{aligned} \tag{2.9}$$

Here we have introduced relaxation time T_2, the decay time for the transverse $x-$ and $y-$ directions, different from the T_1, the longitudinal relaxation/decay time. T_2 is called the *spin-spin relaxation time*, which leads to a simple exponential decay (2.9). A simple mechanism for T_2 is the perturbations in the spin precession rates of a nuclei due to interactions with surrounding nuclear spins, whence its definition. The inhomogeneities of the applied magnetic field H_0 can also cause the T_2 decay, as well as any mechanism leading to coherence loss in the precessing spin ensemble.

We can transform the equations (2.8) and (2.9) into a more manageable form by a coordinate transformation which eliminates the time dependence of $\mathbf{H}$. To this end, an oscillating field (2.4), may be viewed as the superposition of a rotating and a counter-rotating field, and since the

counter-rotating component is ineffective we can consider just one rotating field component. We account for the rotation of the applied rf field H_1 by moving into a coordinate frame rotating at the same angular frequency of ω around $z-$axis. This means the rotating frame equations (2.9), can be written as:

$$\frac{dM_z}{dt} = -\gamma M_y H_1 + \frac{M_0 - M_z}{T_1} \tag{2.10a}$$

$$\frac{dM_x}{dt} = -\gamma M_y H' - \frac{M_x}{T_2} \tag{2.10b}$$

$$\frac{dM_y}{dt} = \gamma(M_z H_1 - M_x H') - \frac{M_y}{T_2} \tag{2.10c}$$

where we have taken $H' = \mathbf{H}_0 + \frac{\omega}{\gamma}$. The equations (2.10) are named the *Bloch equations*− proposed by Felix Bloch in his classic 1946 paper [94].
From equation (2.10), the free evolution (H_1) of the transverse magnetization (M_{xy}) in the rotating frame at resonance (H' = 0) is an exponential decay:

$$M_{xy}(t) = M_{xy}(0)e^{-\frac{t}{T_2}} \tag{2.11}$$

The time constant T_2 in the equation (2.11), has contributions from both the distribution of static fields as well as dynamic ones. The longitudinal component of magnetization from Bloch equations (2.10) approaches towards equilibrium following an exponential law with a time constant T_1:

$$M_z(t) = M_0 + (M_z(0) - M_0)e^{-\frac{t}{T_1}} \tag{2.12}$$

In the simpler case of a spin $I = 1/2$ system, $1/T_1$ decay (or recovery) rate of the off-equilibrium longitudinal nuclear magnetization, as of equation (2.12), coincides with the transition rate $2W$ between two adjacent nuclear levels m_I, m_{I+1}. A microscopic treatment of the Bloch equations will be presented in the section 2.1.4.

2.1.3 The nuclear Hamiltonian

So far we have neglected all the possible interactions a nuclei can have (except the Zeeman one), while describing the behavior of nuclear spin systems. However, this is not the situation in the physical systems. Indeed, the nuclear interactions can shift and/or broaden the nuclear energy levels as well as induce spontaneous nuclear transitions (i.e. nuclear spin relaxations). A general nuclear Hamiltonian containing all interactions among the nuclear spins and with their surrounding electronic cloud, in the presence of an external magnetic field, can be written as:

$$\mathcal{H}_{nuclear} = \mathcal{H}_{Zee} + \mathcal{H}_{n-e} + \mathcal{H}_Q + \mathcal{H}_{n-n} \tag{2.13}$$

We will individually discuss all the terms in equation (2.13) concisely, and comment on their effects upon the shape/shift of the NMR spectra.

The first term was already introduced in (2.2), as the Zeeman interaction between the nucleus and the applied magnetic field. From the Zeeman and the electron-nucleus term in equation (2.13), one gets an effective Zeeman Hamiltonian as equation (2.2) when averaged over the

electronic degrees of freedom. There, the field H that matters is the field at the nucleus, which differs from the bare external field due to Knight and chemical shifts. In magnetic materials it also includes a term independent of the external field (hyperfine or dipolar in origin) properly referred to as the *internal field*.

Hyperfine interactions

The second term in the Hamiltonian (2.13) is the *hyperfine interaction*, i.e. the electron-nucleus magnetic moment coupling. The electronic moment has contributions both from spin and orbital angular momenta, but in solids, orbital moment is often quenched by the crystal field and usually does not participate in the magnetism to the leading order, although there are exceptions. However, orbital coupling does not vanish in the second order perturbation theory, and gives rise to temperature-independent shifts of the resonance line, referred to as the *chemical shift*. The hyperfine interactions $\mathcal{H}_{n-e}$ are the source of additional magnetic fields at the nuclei and therefore result in the shift of NMR lines, as compared to the resonance frequencies of bare nuclei. The electron-nuclear hyperfine Hamiltonian is given as [90]:

$$\mathcal{H}_{n-e} \;=\; \gamma\,\gamma_e\hbar^2\mathbf{I}\cdot\left[\overbrace{\left(3\,\frac{(\mathbf{S}\cdot\mathbf{r})\mathbf{r}}{r^5}\;-\;\frac{\mathbf{S}}{r^3}\right)}^{dipolar}+\overbrace{\frac{8\pi}{3}\mathbf{S}\delta(\mathbf{r})}^{contact}+\overbrace{\frac{\mathbf{L}}{r^3}}^{orbital}\right] \tag{2.14}$$

where $\mathbf{S}$ is the spin and $\mathbf{L}$ is the orbital angular momentum of the electron, $\mathbf{r}$ is the distance between electron and nucleus whereas γ_e is the electronic gyromagnetic ratio. Equation (2.14) accounts only for a single electron coupling with a nucleus. In order to derive an effective hyperfine Hamiltonian of the nucleus summed over all electrons, one needs to average over the orbital degrees of freedom.

There are three parts of equation (2.14): the first represents the point-dipolar interactions between the nuclear spins and the electron spins, based further on the assumption that the electrons and nucleus are far apart. This holds true for p- d- and f-orbital systems but not for s-electron systems. In the latter, however, the dipolar interaction vanishes due to the spherical symmetry. The s-orbital is then described by the second entry in the equation (2.14), named as the *Fermi contact term*. The probability of finding the $(s-)$ electron at the nuclear site is proportional to the NMR line shift resulting from this interaction. The Fermi contact contributions are isotropic while the dipolar-term is anisotropic because it depends on the crystal orientation relative to the applied magnetic field. The last term in the hyperfine Hamiltonian is the 'orbital interaction' due to the nuclear spin interaction with the orbital momentum of the electron, hinted at above. For ions with a net spin S, an effective form of the hyperfine interaction of equation (2.14), may be written as a coupling term between S and the nuclear spin I as:

$$\mathcal{H}_{spin} \;=\; -\,\mathbf{I_i}\tilde{\mathbf{A}}^{\mathbf{j}}_{\mathbf{i}}\langle\mathbf{S}^{\mathbf{j}}_{\mathbf{i}}\rangle \tag{2.15}$$

where $\tilde{A}^j_i$ is called the *hyperfine coupling tensor*, representing the strength of the transferred hyperfine interaction between nuclear spin and the j^{th} electronic moment along the i^{th}-path. The term $\langle S^j\rangle$ is the thermal average of the i-component ($i = x, y, z$) of the j^{th} electronic spin.

The effective Hamiltonian (2.15), may also be written as $\mathcal{H} = -I \cdot H_{hf}$, where the quantity $H_{hf} = \tilde{A}\langle S\rangle$ is defined as the hyperfine field.

If the hyperfine coupling $\tilde{A}$ is known, the $\langle S\rangle$ can be directly estimated from the spontaneous resonance frequencies in the internal field (see below), or from the shift in the frequency $\omega = \omega_0(1 + \Delta K)$, where ΔK is the amount by which the resonance frequency has shifted. Conversely, an unknown hyperfine coupling can be estimated from the NMR frequency if $\langle S\rangle$ is known by some other technique (e.g. magnetization). An effective negative contribution in the hyperfine coupling $\tilde{A}$ is the core polarization interaction resulting from the (negative) electronic spin of a many-electron ion, induced by outer spin polarized d-orbital in the deeper s-shells.

In the ordered-phase of magnetic materials, the spontaneous hyperfine field arising from the ordered moment $\langle S\rangle$, can be used to perform zero-field NMR (ZFNMR) studies. ZFNMR can elucidate the ground state (e.g. the valence) of the magnetic ion and the temperature dependence of the magnetic order parameter. Although indirectly, ZFNMR can also provide information on the micromagnetic properties such as the magnetic anisotropies and the domain texture, through their effect on the rf enhancement at the nucleus. The hyperfine contributions described above contribute to the huge enhancement of local rf magnetic field on the nucleus; because the electronic moments are three orders of magnitude larger than the nuclear moments. They have a much larger susceptibility and are more strongly coupled to the rf field in the sample coil compared to their nuclear counterparts. These electronic moments are paired to the nuclei by a large hyperfine coupling.

Electric quadrupole interactions

The next term in (2.13) are the interactions arising from the $I > 1/2$ nuclei due to their non-spherical charge distribution. Their electric quadrupole moment, which can have a non-zero value even if their electric dipole moment is zero, interacts with the gradient of the electric field due to the electron charge distribution around the nucleus. It can lift the degeneracy of nuclear Zeeman levels without any applied magnetic field hence making the nuclear quadrupole resonance (NQR) spectroscopy possible. The quadrupolar Hamiltonian is [90]:

$$\mathcal{H}_Q = \frac{e^2qQ}{4I(2I-1)}\left[3I_z^2 - I(I+1) + \frac{\eta}{2}(I_+^2 - I_-^2)\right] \tag{2.16}$$

where e is electric charge, Q is the nucleus quadrupolar moment, I_+^2 and I_-^2 are the raising and lowering operators ($I_\pm = I_X \pm iI_Y$), $eq = V_{zz}$ is the largest element of the electric field gradient (EFG) tensor in the reference of its principal axes (X, Y, Z), and η is the asymmetry parameter of the EFG tensor given as:

$$\eta = \frac{V_{xx} - V_{yy}}{V_{zz}},\ 0 \leq \eta \leq 1 \tag{2.17}$$

with $|V_{zz}| \geq |V_{yy}| \geq |V_{xx}|$. For a spherical or cubical symmetry site of the nucleus, $V_{zz} = V_{yy} = V_{xx} = 0$ and the quadrupole coupling is zero. The eigenvalues of the Hamiltonian (2.16) along with the selection rule $\Delta m = \pm 1$, give rise to one (for I $\leq$ 2/3) or more (I>3/2) non-degenerate transitions, observable in the zero-field NQR experiments.

In the presence of an external magnetic field, if the Zeeman and quadrupolar interaction are both present, depending on the relative size of the two interactions, EFG-perturbed Zeeman transitions (quadrupole-perturbed NMR) or magnetic-field-perturbed quadrupolar transitions (Zeeman-perturbed NQR) are observed. In either case, the degenerate unperturbed transitions are split by the perturbing interaction, and satellite lines appear, whose positions depend on the relative orientations of the magnetic field and the EFG. In the case (of frequent interest)

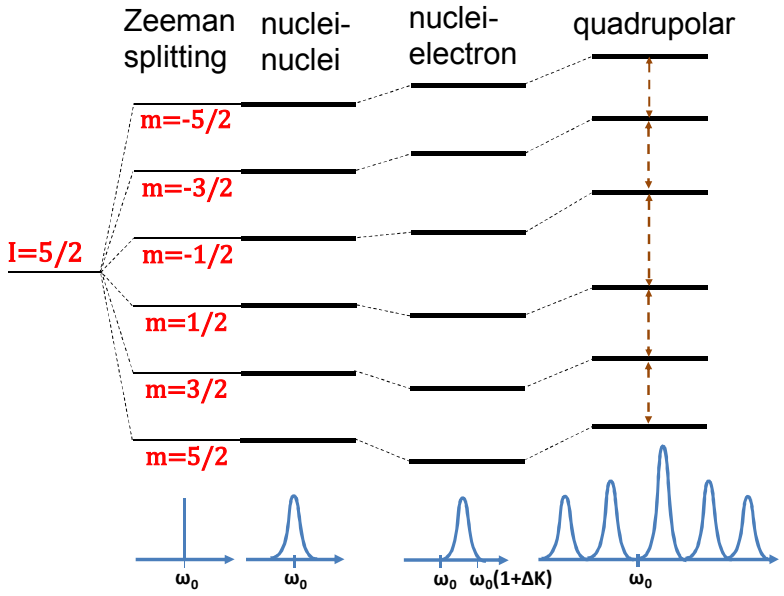

Figure 2.2: The nuclear energy levels (above) and NMR spectra (below) splitting and shifts scheme for an $I = 5/2$ nuclei. The Zeeman interaction causes level splitting and single line NMR signal, nuclei-nuclei dipole interaction results in the spectra broadening, the nuclei-electron interaction shifts the spectra by an amount mentioned in the text, while the quadrupolar interactions split the spectra.

of an odd spin I and a small EFG behaving as a perturbation of the leading Zeeman interaction, for instance, the central transition ($1/2 \leftrightarrow -1/2$) is unshifted to leading order in ν_Q/ν_{Zeeman}, while the (2I -1) angle-dependent satellite lines appear on either side of the central transition.

In the polycrystalline samples, the angular average of the satellite lines gives rise to the broad spectra with peculiar features (powder singularities), while the central transition of an odd spin I is only affected to second order by the EFG and yields a relatively sharp line. Power singularities may not be distinguished however in the case of a very inhomogeneous EFG, and a featureless broad spectrum is detected in place.

Nuclear dipole interaction

The last term in the Hamiltonian (2.13) is the classical interaction between nuclear spins, given as [90]:

$$\mathcal{H}_{n-n} = \sum_{j<k} \frac{\hbar^2\gamma^2}{r_{jk}^3} \left\{ \mathbf{I}_j \cdot \mathbf{I}_k \; - 3 \, \frac{(\mathbf{I}_j \cdot \mathbf{r}_{jk})(\mathbf{I}_k \cdot \mathbf{r}_{jk})}{r_{jk}^2} \right\} \tag{2.18}$$

where $\mathbf{r}_{jk}$ is a vector from nuclear spin $\mathbf{I}_j$ to $\mathbf{I}_k$. The nuclear dipole-dipole interaction is anisotropic in solids, and it gives rise to the so-called homonuclear linewidth, in the order of a few Gauss. Usually n-n interaction is the weakest term in nuclear Hamiltonian and is not expected to be important in magnetism.

In MNMs however, the coupling to electronic spins is reduced by dilution and, in strongly anisotropic systems like Dy-cene (chapter 5, thermally activated electronic spin flips are inhibited by a large energy barrier. On the other hand, nuclear spins are not diluted at all (there are proton nuclei everywhere in the hosting matrix), and may become an important spin relaxation channel. In nuclei with a strong hyperfine coupling to their ion, like e.g. ytterbium in Yb(trensal) (chapter 3) and Mn in MnFePSi alloys (chapter 6), on the other hand the n-n interaction can be safely neglected.
Figure (2.2) summarizes an illustration of the nuclear interactions, their effects on the nuclear energy levels and the corresponding nuclear magnetic resonance spectra evolution for an I = 5/2 system. The electric quadrupole interaction is assumed in a uni-axial symmetry (η=0) with electric field principal axis parallel to the external magnetic field.

2.1.4 The Redfield theory

In the paragraph (2.1.2), we presented the Bloch equations as a simple phenomenological theory, with no microscopic interpretation for the T_1 and T_2 relaxation times. In case of quadrupole-resolved Zeeman transitions in solids, for instance, one needs to resort to a microscopic theory called - 'the Redfield theory' [95], which is closely related to the relaxation theory approach of *Wangsness and Bloch* [96, 97]. We will just briefly touch upon it here in this thesis.

In order to state the Redfield theory results, we will include the relaxation of nuclear spins in the presence of electron-nuclear interactions under an applied magnetic field, following the formalism developed in section (2.1.1). The thermal fluctuations in the electronic spin cause random variations in the hyperfine and dipolar fields whence the nuclear spin-lattice relaxations. The members of spin ensemble are not coupled to each other, but to a fluctuating field produced by electron spins, having components along x- y- and z- axis, which is different for each individual nuclear spin. The whole system is under a static magnetic field H_0 (possibly including the time average of the hyperfine field) along z-direction. We can write the Hamiltonian for each site as:

$$\mathcal{H}_{nuc} = \mathcal{H}_0 + \mathcal{H}_{hyp} = -\gamma_N \hbar H_0 I_z - \gamma\hbar \mathbf{H}_{hf}(t)\mathbf{I}$$

where the Larmor frequency is $\omega_L = \gamma \, H_0$ and $\mathbf{H}_{hf}(t)$ is the fluctuating hyperfine field:

$$\mathbf{H}_{hf}(t) \; = \; -\hbar\gamma_e \sum_{i=1}^{N} \delta(r_i)\mathbf{s}_i \cdot \mathbf{I} + \left(\frac{\delta\mathbf{s_i}(t)}{r_i^3} \; - \; 3\frac{\mathbf{r_i}(\delta\mathbf{s_i}(t) \cdot \mathbf{r_i})}{r_i^5} \right) \tag{2.19}$$

where N is the total number of magnetic ions with i labeling their index, r_i is their distance from the proton, $\mathbf{s_i}$ is the spin operator, with $\delta\mathbf{s_i}(t) = \mathbf{s_i}(t) - \langle\mathbf{s_i}\rangle$. The first term outside the brackets in equation (2.19) is the contact hyperfine while the terms inside the brackets are (pseudo−) dipolar interactions.

Skipping the complete mathematical steps to derive the T_1 and T_2, the longitudinal and transverse magnetization decays respectively, and write the results as [89]:

$$\begin{aligned} \frac{1}{T_1} &= \gamma^2[k_{xx}(\omega_L) + k_{yy}(\omega_L)] \\ \frac{1}{T_2} &= \frac{1}{2T_1} + \gamma^2 k_{zz}(0) \end{aligned} \tag{2.20}$$

where $q = x, y, z$; and k_{qq} is the Fourier transform of the correlation function of $\mathbf{H}_{hf}$ defined as the spectral density of interactions:

$$k_{qq}(\omega) = \frac{1}{2}\int_{-\infty}^{+\infty} \overline{H_{hf,q}(t)H_{hf,q}(t+\tau)}\, e^{-i\omega t} d\tau$$

From equation (2.20), $1/T_1$ relaxations are due to the transverse fluctuations at the Larmor frequency, whereas $1/T_2$ is made of a T_1-like term and a so-called secular term (the longitudinal fluctuations at vanishing frequency).

With larger nuclear spin I (I $>$ 1/2) and non-degenerate Zeeman transitions however, the quantity accessed experimentally is the population difference of the level pair involved in the observed nuclear resonance, rather than the entire nuclear magnetization. The rate equations for the nuclear populations then lead to multi-exponential recovery laws for each resonance even in the case of a single transition probability W [98], with up to 2I exponential components exhibiting enhanced rates $2W$, $6W$, $12W$, $20W$, $30W$, ... Their weights depend on the preparation (i.e. saturation) method for the nuclear ensemble, namely, whether just the populations of the observed transition are altered, or the preparation pulse sequence is long enough to allow for a recovery to thermal equilibrium for the other nuclear levels, or any intermediate case between the previous ones.

2.1.5 Free Induction Decay and Hahn Spin Echo

Modern pulsed NMR techniques allow the alteration of a nuclear magnetization vector from its equilibrium values by using intense rf pulse ($H_1 \neq 0$), followed by the free evolution of the spin system (H_1 = 0). If the rf-field is resonant with the Larmor frequency (ω_L = γ H_0), the system will start precessing around the static effective field (in the rotating frame) $H_1\hat{x}$ by a nutation angle $\theta = \gamma H_1 \tau_p$, where τ_p is the pulse duration, in response to the applied rf pulse. By suitably tuning the pulse intensity H_1 and duration τ_p one may obtain a so-called 90° (θ=π/2) pulse which rotates the magnetization into the transverse xy-plane; or a 180° (θ=π) pulse inverting the nuclear magnetization and so on. To achieve a correct 90° pulse, one can use the fact that NMR signal induction into the coil is maximum, if the nuclear magnetization is precessing in the xy-plane. Therefore, by systematically varying the τ_p (or equivalently transmitter power) and plotting the integrated echo intensity, one can calibrate the correct 90° pulse.

As mentioned before, on evolving freely after the pulse, the system damps exponentially its collective precession, and the corresponding damped signal, detected by the pickup coil wound around the sample, is called "free induction decay" (FID). The NMR absorption spectrum is then obtained in principle, as the real part of the FID signal (after a suitable phase correction). However, in the solid state materials, especially in the magnetic ones, the excitation of FID signal by means of a single pulse is rarely applicable. In these systems, the inhomogeneous line widths are typically so large that the decay time of the FID signal, inversely proportional to the line width, is shorter than the unavoidable dead time of the receiver following the transmission of a pulse, and the signal is completely decayed before it can be detected.

To overcome the shortcomings of the FID, the *Hahn spin echo* (named after the inventor [99]) is a universally used pulse sequence. Hahn sequence works as follows: a 90° pulse rotates the nuclear magnetization into the xy-plane. The FID is induced as a result, then after time τ another 180° (or 90° sometimes) pulse flips the magnetization still in the xy-plane. If the line broadening is dominantly inhomogeneous (i.e. essentially due to a spatially inhomogeneous distribution of the static fields), then the dephasing of the spins responsible for the decay of the free-induction signal is reversible and the spins refocus (the signal reappears, and reaches a maximum) at the time τ past the last pulse. By choosing the τ larger than the dead time, an echo signal can be detected even when the FID signal cannot. The so-generated echo intensity is related to the magnitude of magnetization component in the xy-plane (M_{xy}). The echo is essentially a replica of the free-induction signal excited by a single pulse and therefore the NMR absorption spectrum can be obtained similarly, namely, by Fourier-transforming the echo signal from its maximum. However, in solids, especially in magnetic materials, often the resonance lines are very broad (up to tens or even hundreds MHz). In these cases it is not possible to excite the entire NMR spectrum by a single echo and the spectra is therefore constructed point-by-point at discrete frequency steps.

2.1.6 Spin-spin relaxation time T_2

The spin-spin relaxation time T_2 (more precisely, T_2^*) introduced in the Bloch equations is the decay time of transverse nuclear magnetization in the xy-plane, coincident with the reciprocal half width at half maximum (HWHM) $1/\Delta_\omega$. The finite linewidth is caused by the contributions from the the time-dependent random fields at the nucleus (fluctuations) and the static inhomogeneities (the spatial distribution of the static field H_0 at the nucleus). These fluctuations produce an irreversible spin dephasing and affect the decay of spin-echo vs. τ also, while the spin-dephasing by the static inhomogeneities is reversible and is refocused by the spin echo whose decay is not affected (unlike FIDs). To measure the intrinsic T_2, rather than T_2^*, the Hahn-echo sequence is applied repeatedly while gradually increasing the time τ between the first and the second pulse. The recorded integrated echo intensity plotted against τ gives the spin-spin decay profile of nuclear spin (T_2), which can be fitted with a single exponential decay, as reported in equation (2.11). An illustrative diagram of a T_2 measurement sequence, will be presented in the next section when we will discuss the experimental setup. An alternative, more efficient way of measuring the spin-spin relaxation time is the CPMG pulse sequence, presented in next paragraph.

2.1.7 Carr-Purcell-Meiboom-Gill Sequence

The Hahn spin echo technique, in spite of excellent applicability, has an important limitation e.g. in liquids in the presence of a magnetic field gradient, since in that case spin diffusion gives rise to a random modulation of the local field at the nucleus. The latter produces an irreversible spin dephasing since the precise refocusing of the nuclear magnetization is only possible if each individual nucleus remains firmly in a constant magnetic field for all the measurement duration (2τ). The spin depolarization due to spin diffusion, which is not regarded as a true T_2 process, depends on the diffusion coefficient D and the field gradient according to a non-exponential law:

$$M(2\tau) \;=\; M(0)\, e^{-2\tau/T_2}\, e^{-\left[\left(\frac{\gamma\partial \mathbf{H}}{\partial z}\right)^2 \frac{2}{3} D\tau^3\right]} \tag{2.21}$$

In the equation (2.21), we notice that the initial depolarization due to spin-diffusion is slower than an exponential. This means that its effect can be singled out from the proper T_2 relaxation by repeatedly refocusing spins, as follows.

The sequence starts with the application of a well-calibrated $\pi/2$ pulse at t=0, bringing the magnetization into the xy-plane and along the +y-axis, if the H_1 was along +x-axis. A π pulse at time t=τ_{cp} follows the first pulse producing the echo at t=2 τ_{cp} with magnetization being along $-y$. Another π pulse at $3\tau_{cp}$ will result in another echo at $4\tau_{cp}$ along +x-axis. Therefore, following the same arguments, continuous pulses at times $(2n + 1)\tau_{cp}$ (n= 0, 1, 2, ...) would result in the echoes at $(2n+2)\tau_{cp}$, with echoes along -y-axis for odd n and +y-axis for even n. As all the magnetization components in the xy-plane are exponentially decaying with T_2 time constant, the echo pattern will similarly follow the exponential decay. This clever scheme was invented by Carr and Purcell (CP) in order to mitigate the τ^3 term effect. Their method measures the complete envelope of echo amplitudes as a function of 2τ, giving the value of T_2 in one go, using a train of rf pulses, as described above.

The spin diffusion may also be encountered in solids, in the form of spectral diffusion, consisting in the polarization transfer between spatially close spins coupled by the dipolar or indirect dipolar interactions, but resonating in different portions of the spectrum. It has also been shown in such cases that the effect of spin diffusion can be mitigated by applying the CPMG sequence [100, 101]. The CP-sequence is particularly advantageous for measuring the weaker NMR signals with low signal-to-noise (S/N) ratio. This diffusion effect can also be almost entirely removed if τ_{cp} is short enough, to not let the diffusion process take place.

If the CP pulse sequence deviates even slightly from the π pulse, the resulting effects add up quickly and become substantial enough to make the measurements unreliable. Since the H_1 field is never uniform in the entire sample, these cumulative effects, in practice, always become significant. Meiboom and Gill recognized this problem and modified the CP pulse sequence (hence the name CPMG). In CPMG pulse sequence, after the initial $\pi/2$ pulse with H_1 along +y-axis, the H_1 for π pulse would be applied along +x-axis. As a result, all the echoes are formed along +x-axis and the errors in the pulse calibration does not accumulate. Another way of mitigating the same effect is to apply the π pulse by alternating them along $\pm x$-axis.

2.1.8 Spin-lattice relaxation time T_1

The spin-lattice relaxation time is the mean recovery time of the longitudinal nuclear magnetization (M_z). The T_1 relaxation process arises due to either the magnetic or the EFG fluctuations (later only for the quadrupolar nuclei), or a combination of both. The magnetic part of the fluctuations is contributed for by the nuclear spin-spin interactions, fluctuations in the electron spin and conduction electron interactions. The EFG fluctuations on the other hand, depend on the charge fluctuations and dynamic lattice distortions (e.g. phonons). Therefore an experimental measure of T_1 provides a useful insight regarding all these dynamics.

In order to to measure the spin-lattice relaxations, the saturation recovery method was always used in this thesis. In this method, a series of pulses are used to saturate the spin system to virtually no net polarization, which also corresponds to an infinite spin temperature. The spins are then allowed to freely evolve and re-polarize due to energy exchange with the thermal bath of magnetic and/or charge excitations. A usual spin echo detection sequence (e.g. the Hahn echo), is then used to measure the process of re-polarization. The sequence is repeated with different delays between the last saturating pulse and the beginning of detection sequence, giving an experimental curve for saturation recovery law, which can then be fitted to the single-exponential recovery law of the equation (2.12). In the case of a $I > 1/2$ spin and non-degenerate Zeeman transitions (because of e.g. the quadrupolar interaction), a multiexponential recovery is observed experimentally. Such behavior can be accounted for in detail by rate equations for the nuclear populations in the framework of the Redfield theory, as discussed earlier in the last part of section 2.1.4.

2.1.9 Rabi Oscillations

The periodic nutation of the net nuclear magnetization driven by a resonant field, whence the periodic absorption and release of the Zeeman energy by the nuclear spin is called *Rabi oscillation* and the frequency of this oscillation is called the Rabi frequency. Driving several Rabi oscillation cycles demonstrates the ability to coherently manipulate spins over sufficiently long times, which is required by QIP. In order to observe the Rabi oscillations in spin-echo sequence, one needs to fix the properly calibrated detection pulse (180° or π), and change the first pulse (t_{Rabi}) duration systematically, while recording the echo amplitude. Fourier transformed and phase corrected echo amplitude as a function of t_{Rabi} yields the Rabi oscillations. Rabi oscillations are damped in practice by T_2 relaxations or the inhomogeneities of the driving rf field H_1, whichever of the two is stronger. The Rabi oscillations show linear dependence of Rabi frequency on the applied rf field strength, which is also a way to ascertain that the particular spin nutations are indeed the Rabi oscillations.

2.1.10 Practical considerations

In this thesis we are dealing with the NMR measurements of the single crystals of MNMs and the powder samples of MnFePSi compounds. In principle, all the NMR−active nuclei (the ones with $I \neq 0$) in these systems can be measured with NMR, however there are some bad nuclei, such as the ^{57}Fe and ^{29}Si in the MnFePSi alloys, which cannot be measured in practice. The signal

in magnetic ion species can be greatly enhanced by the hyperfine coupling between electronic cloud and nuclei, which we can detect with resonant rf excitations, although its magnitude is still much smaller ($\sim 10^3$ times) than its electronic counterpart. Furthermore, thanks to the the resonant character of the NMR, the off-resonance spin excitation (like electronic moment and/or other nuclear species) signals are not detected in the measurements.

The on-site hyperfine coupling strength ranges from tens of Tesla in transition metals to the hundreds of Tesla in the rare-earth systems, making their detection rather difficult due to either over relaxed NMR signals or resonance frequencies in microwave range (up to a few GHz for rare earths), which is not within the accessible frequency range of our spectrometer. However, we are able to measure ^{173}Yb NMR in Yb(trensal) MNM (chapter 3 of this thesis) because of the relatively small gyromagnetic ratio of ^{173}Yb, which brings the resonance frequency of this system back into the rf passband of our spectrometer. On the other hand, in the case of ^{161}Dy and ^{163}Dy in dysprosocenium molecule (chapter 5 of this thesis), the resonance frequency was outside of our experimental frequency band and the measurements were carried out on the ligand protons (^1H).

The ^1H, with 100% natural abundance and high gyromagnetic ratio γ, is one of the best nuclei as far as sensitivity is concerned and its weaker dipole-dipole coupling interaction to its neighboring ions falls beautifully into the time-frequency window of our experimental setup. However, the inhomogeneous coupling of ^1H due to inequivalent sites in the crystal with varying distances from the magnetic ions, gives rise to a non-exponential decay or recovery law for the nuclear magnetization due to the distributions in the T_1 and T_2 time constants, making the subsequent data analysis rather complicated. Another difficulty, from the experimenters point of view, is the ubiquitous presence of ^1H signal, practically from everywhere (from air to the experimental equipment and so on). In fact, one needs to be extra-careful about cleaning the sample holder, coil, and the surrounding areas of the probe head while measuring the proton NMR.

2.1.11 The instrument: HyResSpect

In pulsed NMR experiments on magnetic materials, inhomogeneous line widths are so large that spectra must be recorded point by point by detecting spin echoes as a function of frequency in discrete steps. T_2 and T_1 relaxation times are usually short in these materials. Therefore, the most important requirements in an NMR spectrometer designed for the study of magnetism are: wide frequency span, a uniform frequency response, the smallest instrument dead time, and a large receiver bandwidth. All of the NMR experiments were performed by using an entirely home-built broadband NMR spectrometer, named 'HyReSpect' [102], after the *Hyperfine Resonance Spectrometer*. The HyReSpect spectrometer is particularly optimized for magnetism studies. In the following subsections, we summarize some of the main electronics and software controls of the HyResSpect, the magnets and cryogenics, and the probehead used during the experiments. We end this section by mentioning the pulse sequences in lieu of the HyReSpect software commands.

Main electronics

The HyReSpect features a flat frequency response over the 8−800 MHz frequency span, a pass-band of ±3MHz around its working frequency, a fast-repeating digitizer with a maximum sampling rate of 25Msample/s, and timing provided by a microcontroller clocked at 84MHz, capable of triggering variable pulses from a minimum length of 95ns (8 clock cycles) in steps of 1 clock cycle. It has a dead time of less than 2 μs and it is equipped with an external rf power amplifier. The rectangular rf pulses of different selectable lengths are cut out from a continuous-wave signal source by a fast switch (rise time $<$ 10 ns), which is gated by the microcontroller, while their level is controlled by a programmable attenuator in steps of 1 dB. The low-level pulses (peak power $\leq$ 1 mW) are boosted by a power rf pulse amplifier in the range of 10-100 W and transmitted to the tuned LC resonator circuit in the probe head containing the sample inside the coil. The coil in the resonator circuit both generates the rf field which excites the resonance and acts as a receiver pickup to detect the induced e.m.f. from the precessing nuclei. The received NMR signal passes through a fast-recovery low-noise broadband preamplifier and into the receiver (RX) stage of the spectrometer.

The transmitter (TX) and the RX circuits are both coupled to the probe-head resonator and decoupled from each other by the duplexer, which is a passive circuit made up of a resonant $\lambda/4$ transmission line and two pairs of cross-polarized silicon diodes. The $\lambda/4$ line is a coaxial

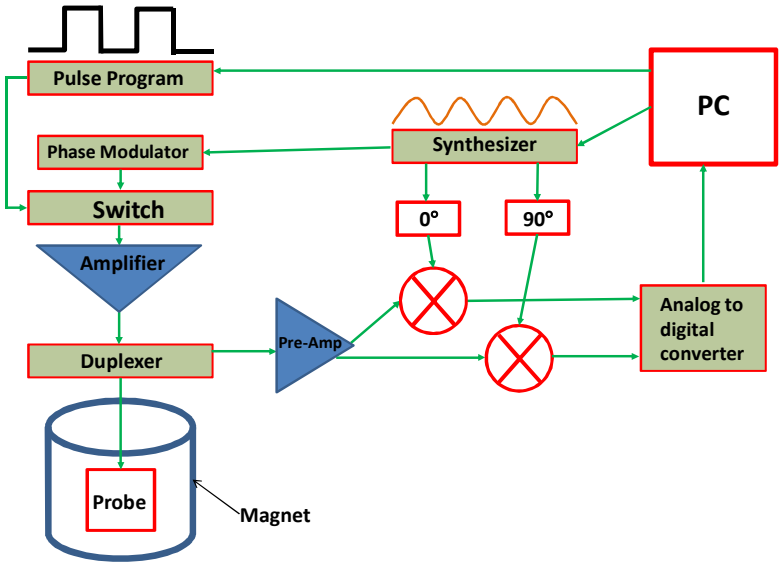

Figure 2.3: An illustrative block diagram indicating some of the important components of a typical NMR spectrometer

cable whose electrical length is equal to a quarter of the working frequency wavelength. It acts as an impedance transformer, transforming a shorted end into a high impedance on the opposite side, and vice versa. An oversimplified block diagram of a typical NMR spectrometer is shown is figure 2.3. The diode pairs are open circuits for the NMR signal, in the sub-mV range and hence below the conduction threshold of a silicon junction diode, while they are open

circuits for the high power rf pulses. It can be easily verified that the RX and TX lines are seen as high-impedance loads from the other side during, respectively, pulse transmission and signal reception, so that these two ports are effectively isolated. The diode pair in front of the preamplifier also serves as a protection from over-voltages which otherwise could damage it.

Magnets and cryogenics

Superconducting magnets are common with NMR setups as they provide large magnetic field without the requirements of a huge external power supply, they are stable and provide uniform magnetic fields. Our experimental setup includes a Maglab EXA (Oxford Instruments) 0-9T variable field superconducting cold-bore cryomagnet equipped with a helium flow variable temperature insert (VTI) as a sample environment. The EXA superconducting coil windings are made of niobium-titanium alloys immersed inside the liquid helium (He) bath which has a cylindrical liquid nitrogen reservoir surrounding it for the insulation. Both the reservoirs are separated from each other, and from the outside environment by vacuum chambers.

The EXA magnet is versatile with fully software controlled fast (1 T/min) field variation, which comes at a price of reduced field homogeneity as compared to the normal NMR spectrometers. But for our studies on magnetic materials with broad resonance lines, this is not a critical requirement as compared to the capability of swift field variation. The VTI cryostat takes the He flow from the liquid He bath in which the superconducting solenoid is also immersed, providing a stable temperature control from 250 K to 1.4 K, and a hold time of several days. The sample is placed inside a coil of a resonant probe circuit (the probe head) hosted by the VTI. The heater and temperature sensor of VTI are controlled by an Oxford ITC 503 temperature controller. For the ZFNMR measurements, a separate VTI cryostat is used, which is placed in a special holder away from the magnet.

The second magnet in our setup is a Cryomagnetics warm 89 mm bore 7.96 T fixed-field superconducting magnet with a VTI cryostat. The heater and temperature sensor of VTI in this case are controlled by an Oxford ITC 4 temperature controller. This set up is usually used for fixed- or zero-field studies at liquid nitrogen temperatures.

GUI and Software controls

The operations of the HyResSpect are controlled through a graphical user interface (GUI) based program, called *gtknmr*. The scripting language used is the bash shell of the Linux/Unix with some additional specialized commands e.g. for starting the experiment, taking and saving the data input, and terminating the program. The temperature and magnet controls are also embedded in the gtknmr setup. For the setting up and optimization of an NMR experiment, one needs to adjust a number of *gtknmr* parameters.
Here we list some of the important *gtknmr* parameter names and their functions:

- The optimization of the pulse level is controlled by the transmitter attenuation (TxAtt) in steps of 1 dB and the pulse duration (P1, P2, ... for the first, second, ... pulse, respectively) commands, which should be optimized to get the maximum signal (π/2 or π pulse as required). The larger the Txatt, the lower the power transmitted to the sample. The entries

in the P1, P2 fields are written for example as 0.5u, 0.5u (for equal pulses) or 0.5u, 1u (for 90°-180° type sequence), and 0 to end the sequence.

- The pulse phases (ph1, ph2, ...) are specified in Phase Cycle field in the 'Sequence Tab'. The values phase can be given as 0, 1, 2, 3; with 0 means no flip and 2 to flip the signal, whereas 1 and 3 results in $\pm 90^\circ$ phase shift of the rf carrier.

- D1 represents the delay between two pulses for spin-echo sequence. The D1 must be kept much shorter than the T_2 time and at least slightly longer than the receiver dead time.

- The signal acquisition delay must always be kept shorter than D1. It is the sum of (Rinh) and (Acqd): the former is the time the rf RX stage is switched off, while the latter is the delay between the RX enabling, and the actual trigger of the acquisition.

- The receiver gain is actually controlled by a programmable attenuator between two amplifying stages. Its attenuation ratio (RxAtt), must be high enough to avoid the receiver saturation.

- The relaxation delay (RlxD) is the repetition time between two NMR scans. The term 'scan' here signifies a complete cycle starting with an initial pulse sequence, and ending with the detection of the transient NMR signal. In order to get a good S/N ratio, the digitized NMR signals are typically acquired and averaged over several hundred/thousand scans. RlxD therefore must allow a full re-polarization of the nuclei before the next scan, and for that its value should be at least a few spin-lattice relaxation times (T_1). Furthermore, at very low temperatures RlxD must must be long enough to avoid significant sample heating by the rf power transmitted onto the sample. On the other hand, unnecessarily long RlxD results in a waste of measurement time, especially in the cases when a large number of scans are required for improving S/N ratio.

- The maximum number of scans (MxScan) is the number of repetitions the whole sequence will be repeated for and signal summed (averaged) for improving S/N ratio. Values are typically chosen based on the trade off between sensitivity and the time consumption.

- There are also optional fields in the 'Sequence Tab', for applying pulse trains in e.g. T_1 measurements, or selecting the specialized CPMG mode.

The Probe-head

The NMR probe is nothing more than a custom made RLC resonant circuit; with R being the parasitic resistance of the coil (made of a few turns of copper), L its inductance, and C is the variable capacitor. The resonant circuit must be tunable to the required frequency range. The sample is inserted inside the inductor. The coil should be designed in a way that the sample fills the whole space available. A good strategy to build up the coil is to wind it tightly around a dummy sample of similar shape and size as the original sample and then replace the dummy with the actual sample. The number of turns in the coil, in reality, are determined by the frequency range one wants to explore, but it should be designed in a way to maximize the quality factor

Q, ($Q = \omega L/R$), to which sensitivity is proportional. However, if the Q factor is too high, it could lead to an excessive increase in the receiver dead time, which in turn is detrimental for measuring the samples with short T_2 (which is the case with many MNM samples). Therefore in these situations, one needs to decrease the Q-factor by inserting another resistor R' in parallel to the variable capacitor C.

The variable capacitor makes it possible to tune the circuit to the desired resonance frequency by changing the capacitance ($\omega_0 \approx \frac{1}{\sqrt{LC}}$) and hence covering a wide frequency region. In tuning the capacitor, it is ensured that $\omega_0 = \omega_L$, where ω_L is the Larmor frequency of the targeted nuclei. A schematic diagram of the probe-head circuit is presented in the figure 2.4. Maximum

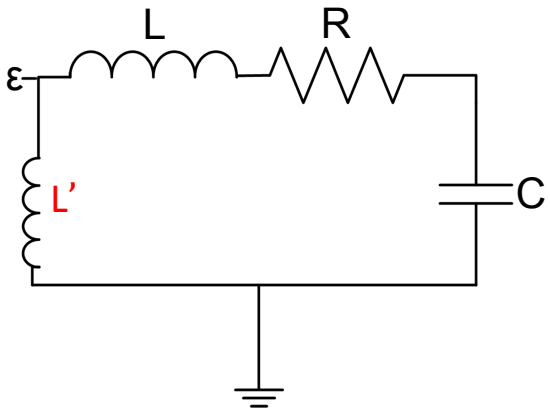

Figure 2.4: Circuit diagram of a tunable probe head employing a variable capacitor (C), the characteristic impedance is matched using secondary induction (L′). The sample is placed inside the inductor (L), an optional resistor parallel to C can be used as mentioned in the text.

power is transmitted to the sample when the impedance of the transmission circuit (50Ω) is matched with the series RLC circuit impedance [91]. This is achieved by an additional properly chosen inductance L' parallel to the RLC series circuit. On the other hand for the ZFNMR measurements in ferromagnets, usually one does not require a tuning resonant circuit thanks to the large rf enhancement at the nucleus in the order of hundreds or thousands, as a results the circuit in this case is simply an RL-circuit.

The pulse sequences

Before concluding the NMR theory, measurement and instrumentation part, a summary of the pulse sequences including the *gtknmr* notation, which is used throughout the current thesis, is presented in this paragraph. NMR spectra were measured using the Hahn echo pulse sequence, as described before (2.1.5): a first pulse (P1) is applied followed by a delay (D1) in which the spin system undergoes FID (not recorded). After D1 the second pulse (P2) is applied, following which the echo appears and is recorded. For NMR spectra, the process is repeated point-by-point at each frequency step. We have opted for a $\pi/2 - \pi/2$ (i.e. equal pulse sequence) instead of the standard $\pi/2 - \pi$ echo sequence: the former is advantageous in our case of magnetic systems with very broad lines where only a portion of the spectrum, proportional to the Fourier

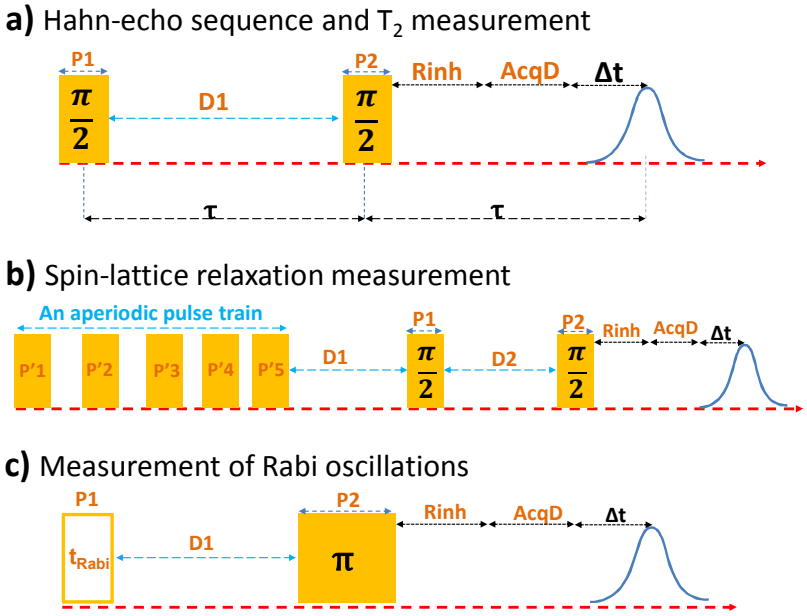

Figure 2.5: Sketch of pulse sequences for the measurement of a) Hahn echo and spin-spin decay, b) Spin lattice relaxations using saturation recovery method, and c) Rabi oscillations measurement, with t_{Rabi} being the variable pulse duration.

transform of the longer pulse, is excited by the echo, rendering the efficiency gain of the latter unimportant. On the other hand, an equal-pulse sequence is favorable in the cases where T_2 is very short because of an overall shorter duration, and is tolerant to an excessive rf power level due to any imperfect pulse calibration.

The same pulse sequence was used to measure spin-spin relaxation, by sitting at the resonance and changing the delay D1 between P1 and P2 (and correspondingly Rinh+AcqD as well). Plotting the echo amplitude against the time 2τ yields the T_2 decay law, as shown in figure (2.5-a). Spin-lattice relaxation was always measured using the saturation recovery method. An aperiodic train of pulses $P'1, P'2, ...P'n$ was applied to saturate the system. The system was allowed to evolve freely after the pulse train, for a variable duration D1. A usual Hahn-echo sequence was then used to measure the magnetization recovery. The plot of echo amplitude against different D1 gave the longitudinal magnetization component. Finally, Rabi oscillations were driven using the similar Hahn echoes, with the only difference being that this time the pulse P1 was of variable duration (t_{Rabi}) and P2 was a 180° pulse applied after D1. A plot of the amplitude of the phase corrected echo vs. the t_{Rabi} yields the Rabi spin nutation oscillations.

2.2 Neutron Scattering

Neutrons are charge-less particles with 1/2 spin and non zero magnetic moment which weakly interacts with the matter (i.e. they are non destructive) while penetrating deeply. Furthermore, with the thermal neutron De Broglie wavelength of ≈1.8 angstrom and the energy of both thermal and cold neutrons ranging from less than 1 meV to 100 meV, they are ideally suited to the study of inter-atomic spacing and magnetic/spin excitations in condensed matter [103, 104]. In any simple neutron scattering experiment, neutrons generated from a source (e.g. a reactor or spallation source) are directed onto a sample from which they get scattered via some interaction. The scattered neutrons are then recorded using detectors as a function of the scattering angle and analyzed to get the required (structural, vibrational or magnetic) information about the sample. Neutron-matter interactions can be divided into three broad categories:

Table 2.1: An overview of the basic neutron properties

Property	**Value**
Mass	1.674928 (1)$\times$ 10^{24} g
Charge	0
$\beta-$decay life time	885.8 $\pm$ 0.9 s
Spin	1/2
Magnetic moment	-1.9130427 (5) μ_N

- Nuclear scattering, in which the neutrons are scattered by the atomic nuclei (so-called elastic and phonon scattering)
- Magnetic scattering; the scattering from an interaction between neutrons and the magnetic moment of an atomic cloud (inelastic magnetic scattering), because the neutrons have a spin and a magnetic moment, as mentioned above, thus they interact with the unpaired electrons in atoms.
- Absorption; a neutron gets absorbed inside the nuclei forming a compound nucleus (an unwanted process)

In the current study we have measured spin dynamics of MNMs with inelastic magnetic scattering, therefore we will limit our discussion to a brief introduction of concepts later used in this thesis. We will follow the standard textbooks [103–105], and PhD theses [92, 106]. INS is a well established technique for the study of magnetic and vibrational excitations in the condensed matter in general, and MNMs in particular. It provides direct information on the eigenvalues and eigenvectors of these molecular systems. Furthermore, all the spin-Hamiltonian parameters can be directly extracted from the INS data analysis, without requiring application of an external magnetic field.

2.2.1 Neutron Scattering Theory

We start by considering an incident neutron beam with wave vector (k_i) and energy E_i, which is scattered after interacting with the sample, with final wave vector k_f and energy E_f. The angle between the incident and final neutrons is labeled as 2θ. The momentum transfer during this process in terms of the scattered neutrons is

$$\hbar\mathbf{Q} = \hbar(\mathbf{k_i} - \mathbf{k_f}), \tag{2.22}$$

with **Q** being the *scattering vector*. Here we have invoked the law of conservation of momentum for this scattering process comprising both the neutrons and the sample. The **Q** forms the

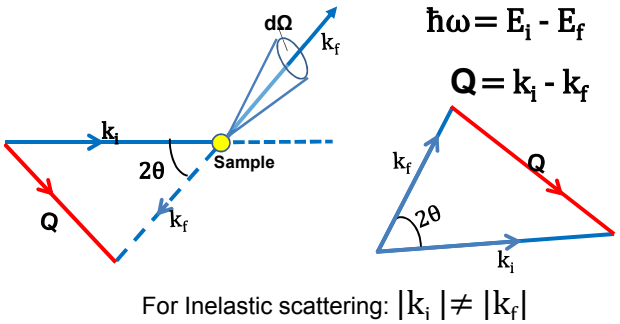

Figure 2.6: A geometry diagram of a neutron scattering experimental vectors. The incident wave vector k_i denotes the incoming neutrons from the moderator, which are then scattered by the sample into a final wave vector k_f. dΩ is a small solid-angle subtended by the detector. The scattering triangle is defined by the scattering wave vector **Q** = k_i - k_f.

scattering triangle along with k_i, and k_f, as shown in figure 2.6. For inelastic interactions, the energy transfer (Δ E = $\hbar\,\omega$) can be given by the law of conservation of energy:

$$\Delta E = \hbar\omega = E_i - E_f = \frac{\hbar^2}{2m_n}(\mathbf{k_i}^2 - \mathbf{k_f}^2), \tag{2.23}$$

where E_i and E_f are the incident and final energies of neutrons, and m_n is the mass of neutron. Of course, ΔE is zero for elastic neutron scattering whereas the experimental information about the energy change reveals the coherent sample dynamics in the inelastic scattering experiments.

Neutron scattering cross-section

The basic quantity measured during a neutron scattering experiment is the *partial (or double) differential cross-section*, which is defined as the number of neutrons scattered per second into a small solid-angle dΩ in the direction specified by the angles θ and ϕ.

$$\frac{d^2\sigma}{d\Omega dE} = \frac{\left(\begin{array}{c}\text{number of neutrons scattered per second into} \\ d\Omega(\theta,\phi) \text{ with } E_f \text{ between E and E + dE}\end{array}\right)}{\Phi\; d\Omega\; dE} \tag{2.24}$$

where Φ is the flux of incident neutrons in the direction measured perpendicular to the incoming neutron beam. The scattering cross section is a rather weak interaction process (measured in the units of barn; where 1 barn = 10^{-28} m^2). We can therefore make use of a fundamental result in quantum mechanics, namely the *Fermi's Golden Rule* for first order perturbation to derive the transition probability of neutrons from an initial quantum wave-vector k_i to a final wave-vector k_f. In scattering theory this is also equivalent to the Born approximation, if both the incoming and scattered neutron beams are plane waves. Double differential cross section is can be written as

$$\frac{d^2\sigma}{d\Omega d\omega} = \frac{k_f}{k_i}\left(\frac{m_n}{2\pi\hbar^2}\right)^2 |\langle \mathbf{k_f}\lambda'|V(\mathbf{Q})|\mathbf{k_i}\lambda\rangle|^2 \delta(\mathbf{E_i} - \mathbf{E_f} + \mathbf{E}_{\lambda_i} - \mathbf{E}_{\lambda_f}) \tag{2.25}$$

where $E_i - E_f = \hbar\omega$, λ and λ' are the initial and final states of the sample, and V(**Q**) is the Fourier transform of the interaction potential function between the neutron and the sample V(**r**):

$$V(\mathbf{Q}) = \int V(\mathbf{r}) e^{i\mathbf{Q}.\mathbf{r}} d^3\mathbf{r}. \tag{2.26}$$

The scattering cross section, equation (2.25), depends on the type of neutron-sample interaction, and hence on the V(**r**) in equation (2.26). At this point we introduce the *scattering function* S(**Q**, ω), related to the scattering cross section as

$$S(\mathbf{Q},\omega) = \left(\frac{2\pi\hbar^2}{m_n}\right)^2 \frac{k_i}{k_f}\frac{d^2\sigma}{d\Omega dE}, \tag{2.27}$$

There are two types of contributions to the scattering function, the nuclear and the magnetic one:

$$S(\mathbf{Q},\omega) = S_{nuclear}(\mathbf{Q},\omega) + S_{magnetic}(\mathbf{Q},\omega) \tag{2.28}$$

We will skip the details of the nuclear scattering contributions into the scattering profile (both coherent and incoherent), and jump directly onto the concepts of (inelastic) magnetic scattering which is going to be used later in this thesis. For the for detailed derivations and theory, readers are suggested to refer to the books by Squires, Lovesey, and Furrer, [103–105].

The Magnetic Scattering

The magnetic scattering of neutrons is due to the interaction of the magnetic moment of the neutron ($\hat{\boldsymbol{\mu}}_n$) with the magnetic field **H** generated by the spins and orbital angular momenta of the unpaired electrons of magnetic ions in the sample. The neutron magnetic moment is given as

$$\hat{\boldsymbol{\mu}}_n = -\gamma_n \mu_n \hat{\boldsymbol{\sigma}}, \tag{2.29}$$

where $\gamma_n \approx 1.913$ is the gyromagnetic ratio, μ_N = e $\hbar$ / ($2m_p$) is nuclear magneton, and $\hat{\sigma}$ is the Pauli spin operator having eigenvalues $\pm$ 1. Similarly, the electron magnetic dipole moment is $\hat{\mu}_e$ = - γ_e μ_B $\hat{\mathbf{s}}$; with γ_e = 2 is electron gyromagnetic factor and μ_B is Bohr magneton. [2]

[2] Here $\hat{\mathbf{s}} = \hat{\boldsymbol{\sigma}}/2$ and $\mu_n = \frac{m_e}{m_n}\mu_B$; m_n and m_e are respectively the neutron and electron masses.

The Hamiltonian for a neutron magnetic moment ($\hat{\boldsymbol{\mu}}_n$), moving under the magnetic field (**H**) generated by the electron's spin and orbital motion is given as

$$\hat{H} = -\hat{\boldsymbol{\mu}}_n \cdot \mathbf{H}. \tag{2.30}$$

An electron moving at velocity $\mathbf{v}_e$ generates a magnetic field

$$\mathbf{H} = \nabla \times \left(\frac{\boldsymbol{\mu}_e \times \mathbf{R}}{|\mathbf{R}|^3} \right) + \frac{(-e)}{c} \frac{\mathbf{v}_e \times \mathbf{R}}{|\mathbf{R}|^3}, \tag{2.31}$$

where **R** is the distance between the electron and the point of measurement. Incorporating electron magnetic moment and equation (2.31) with equation (2.30), while considering only the magnetic contribution, we get

$$-\gamma_n \mu_n \hat{\boldsymbol{\sigma}} \cdot \mathbf{H} = \gamma_n \mu_n \left[2\mu_B \hat{\boldsymbol{\sigma}} \cdot \nabla \times \left(\frac{\hat{\mathbf{s}} \times \mathbf{R}}{|\mathbf{R}|^3} \right) - \frac{e}{2m_e c} \left(\hat{\mathbf{p}}_e \cdot \frac{\hat{\boldsymbol{\sigma}} \times \mathbf{R}}{|\mathbf{R}|^3} + \frac{\hat{\boldsymbol{\sigma}} \times \mathbf{R}}{|\mathbf{R}|^3} \cdot \hat{\mathbf{p}}_e \right) \right],$$

the first part of this equation represents a dipole-dipole interaction term whereas the second term is the interaction of the electron and neutron arising from the electron's translational motion. $\hat{\mathbf{p}}_e$ is the electron's linear momentum. Considering the magnetic interaction of the sample's (magnetic) ions with the incoming neutron beam in any inelastic neutron scattering experiment, the differential cross section from equation (2.25) becomes

$$\begin{aligned} \frac{d^2\sigma}{d\Omega dE} = (2\gamma_n \mu_n \mu_B)^2 \frac{k_f}{k_i} \sum_{\lambda\lambda'} \sum_{\sigma\sigma'} \Bigg[& p_\lambda p_\sigma \\ & |\langle \mathbf{k}_f \lambda' \sigma' | \sum_i \boldsymbol{\sigma} \cdot \nabla \times \frac{\hat{\mathbf{s}}_i \times \mathbf{R}}{|\mathbf{R}|^3} - \frac{1}{2\hbar} \left(\hat{\mathbf{p}}_i \cdot \frac{\hat{\boldsymbol{\sigma}} \times \mathbf{R}}{|\mathbf{R}|^3} + \frac{\hat{\boldsymbol{\sigma}} \times \mathbf{R}}{|\mathbf{R}|^3} \cdot \hat{\mathbf{p}}_i \right) |\mathbf{k}_i \lambda \sigma\rangle|^2 \\ & \delta\left(\hbar\omega + E_\lambda - E_{\lambda'}\right) \Bigg], \end{aligned} \tag{2.32}$$

here $|\lambda\rangle$ and $|\lambda'\rangle$ represent the initial and final state of the target (sample) with corresponding energies E_λ and $E_{\lambda'}$. The $|\sigma\rangle$ and $|\sigma'\rangle$ are the initial and final polarization states of the neutron respectively, while the initial occupation probability of the sample state is given by $p_\lambda = e^{-\beta E_\lambda}/Z$ where $Z = \sum_\nu e^{-\beta E_\nu}$ is the partition function. The Dirac-delta function ensures the system energy conservation and $\hbar\omega$ is the neutron energy gain/loss after interacting with the system (sample). The index i is used to label all the magnetic lattice sites and unpaired electrons in the sample.

By using some vector-identities and the definition of the scattering vector, the matrix element of the magnetic interaction potential can be integrated over neutron coordinates [105] yielding

$$\begin{aligned} \frac{2\pi\hbar^2}{m_n} \left\langle \mathbf{k}_f \left| \hat{\boldsymbol{\sigma}} \cdot \nabla \times \frac{\hat{\mathbf{s}}_i \times \mathbf{R}}{|\mathbf{R}|^3} \right| \mathbf{k}_i \right\rangle &= 4\pi e^{i\mathbf{Q}\cdot\mathbf{r}_i} \hat{\boldsymbol{\sigma}} \cdot \left[\tilde{\mathbf{Q}} \times \left(\hat{\mathbf{s}}_i \times \tilde{\mathbf{Q}} \right) \right] \\ \frac{2\pi\hbar^2}{m_n} \left\langle \mathbf{k}_f \left| \hat{\mathbf{p}}_i \cdot \frac{\hat{\boldsymbol{\sigma}} \times \mathbf{R}}{|\mathbf{R}|^3} \right| \mathbf{k}_i \right\rangle &= -\frac{4\pi i}{|\mathbf{Q}|} e^{i\mathbf{Q}\cdot\mathbf{r}_i} \hat{\boldsymbol{\sigma}} \cdot \left(\tilde{\mathbf{Q}} \times \hat{\mathbf{p}}_i \right) \end{aligned} \tag{2.33}$$

where $\mathbf{r}_i$ denotes the position vector of the i^{th} electron, and $\mathbf{Q} = \mathbf{k}_i - \mathbf{k}_f$ and $\tilde{\mathbf{Q}} = \mathbf{Q}/|\mathbf{Q}|$. Defining the operator $\hat{\mathbf{Q}}_\perp$ as

$$\hat{\mathbf{Q}}_\perp = \sum_i e^{i\mathbf{Q}\cdot\mathbf{r}_i}\left[\tilde{\mathbf{Q}} \times \left(\hat{\mathbf{s}}_i \times \tilde{\mathbf{Q}}\right) - \frac{i}{\hbar|\mathbf{Q}|}\tilde{\mathbf{Q}} \times \hat{\mathbf{p}}_i\right] \tag{2.34}$$

Noting that the neutrons are sensitive only to the perpendicular component of the exchanged wave-vector. We can rewrite the differential cross section as

$$\begin{aligned}\frac{d^2\sigma}{d\Omega dE} &= \left(\frac{m_n}{2\pi\hbar^2}\right)^2 (8\pi\gamma_n\mu_n\mu_B)^2 \frac{k_f}{k_i}\sum_{\lambda\lambda'}\sum_{\sigma\sigma'}\Bigg[p_\lambda p_\sigma \\ &\times \langle\lambda\sigma|\left(\hat{\boldsymbol{\sigma}}\cdot\hat{\mathbf{Q}}_\perp\right)^\dagger|\lambda'\sigma'\rangle\langle\lambda'\sigma'|\hat{\mathbf{Q}}_\perp\cdot\hat{\boldsymbol{\sigma}}|\lambda\sigma\rangle\delta\left(\hbar\omega + E_\lambda - E_{\lambda'}\right)\Bigg].\end{aligned} \tag{2.35}$$

Since for the unpolarized neutrons, $\sum_\sigma p_\sigma\langle\sigma|\hat{\sigma}_\alpha\hat{\sigma}_\beta|\sigma\rangle = \delta_{\alpha\beta}$, and $r_0 = \frac{\gamma_n e^2}{m_e c^2}$, the differential cross-section becomes:

$$\frac{d^2\sigma}{d\Omega dE} = r_0^2\,\frac{k_f}{k_i}S(\mathbf{Q},\omega), \tag{2.36}$$

where the response function S($\mathbf{Q}$, ω) is

$$S(\mathbf{Q},\omega) = \sum_{\alpha\beta}\left(\delta_{\alpha\beta} - \tilde{Q}_\alpha\tilde{Q}_\beta\right)\sum_{\lambda\lambda'}p_\lambda\langle\lambda|\hat{Q}_\alpha^\dagger|\lambda'\rangle\langle\lambda'|\hat{Q}_\beta|\lambda\rangle\delta\left(\hbar\omega + E_\lambda - E_{\lambda'}\right), \tag{2.37}$$

and α, β run over x, y, z. In the second form, $\hat{\mathbf{Q}}$ is any operator related to the operator $\hat{\mathbf{Q}}_\perp$ through

$$\hat{\mathbf{Q}}_\perp = \tilde{\mathbf{Q}} \times (\hat{\mathbf{Q}} \times \tilde{\mathbf{Q}}),$$

and we have used the identity

$$\hat{\mathbf{Q}}_\perp^\dagger \cdot \hat{\mathbf{Q}}_\perp = \sum_{\alpha\beta}\left(\delta_{\alpha\beta} - \tilde{Q}_\alpha\tilde{Q}_\beta\right)\hat{Q}_\alpha^\dagger \cdot \hat{Q}_\beta.$$

The response function can be expressed both in terms of a correlation function formed with $\hat{\mathbf{Q}}_\perp$, or $\hat{\mathbf{Q}}$.

Scattering by ions with spin and orbital angular momentum In the MNMs containing rare earth ions both spin and orbital angular momentum contribution are present. Since all the systems studied in this thesis are Ln containing MNMs, we will discuss scattering theory for this case, though, limiting ourselves to the results and necessary changes to *form factor* and $\hat{\boldsymbol{Q}}$ calculations.

We need to make two fundamental assumptions before presenting the scattering cross section for the systems with both spin and orbital moment contributions.

The so-called *dipole approximation* states that the $\hat{\mathbf{Q}}_\perp^{-1}$ is much larger than the mean radius of the orbital wave functions of the unpaired electrons, $\hat{\boldsymbol{Q}}$. This is usually a reasonable approximation.

The second assumption states that all the magnetic ions are identical inside the system. The ions angular momentum state can be specified by the quantum numbers $\hat{\mathbf{L}}$, $\hat{\mathbf{S}}$, and $\hat{\mathbf{J}}$, where $\hat{\mathbf{L}}$ is the orbital angular momentum operator, $\hat{\mathbf{S}}$ is the spin angular momentum operator and $\hat{\mathbf{J}}$ is the total angular momentum operator. We have

$$\hat{\boldsymbol{Q}} \simeq \hat{\boldsymbol{Q}}^{(D)} = \sum_{l,d} e^{i\mathbf{Q}\cdot\mathbf{R}_{ld}} \left\{ \bar{J}_0 \hat{\mathbf{S}}_{ld} + \frac{1}{2}(\bar{J}_0 + \bar{J}_2)\hat{\mathbf{L}}_{ld} \right\} \tag{2.38}$$

where $\hat{\mathbf{L}}_{ld}$ is the angular momentum operator for the ion at the site $\mathbf{R}_{ld}$. The coefficient $\bar{J}_K(K)$ is called a radial integral:

$$\bar{J}_K(Q) = \int_0^\infty \bar{J}_K(Qr)|f(r)|^2 r^2 dr$$

with $\bar{J}_K$ is a spherical Bessel function of the order K and $f(r)$ is the radial part of the wave function which is same for all the unpaired electrons. In the limit $|\mathbf{Q}| \to 0$,

$$\bar{J}_0\hat{\mathbf{S}} + \frac{1}{2}(\bar{J}_0 + \bar{J}_2)\hat{\mathbf{L}} \to \frac{1}{2}(\hat{\mathbf{L}} + 2\hat{\mathbf{S}}),$$

so that the scattering amplitude is the forward direction is proportional to the total magnetic moment per ion.

In the rare-earth ions, the spin-orbit coupling results in combining the $\hat{\mathbf{S}}$ and $\hat{\mathbf{L}}$ to yield various $\hat{\mathbf{J}}$ values. Within the states of given $\mathbf{J}$ we write, $2\hat{\mathbf{S}} = g_s\ \hat{\mathbf{J}}$, $\hat{\mathbf{L}} = g_L\ \hat{\mathbf{J}}$ and $g\hat{\mathbf{J}} = \hat{\mathbf{L}}+2\ \hat{\mathbf{S}}$. From here one can calculate the values of g_s and g_L as [105]

$$g_s = \frac{J(J+1) - L(L+1) + S(S+1)}{J(J+1)},$$

and

$$g_L = \frac{J(J+1) + L(L+1) - S(S+1)}{2J(J+1)}.$$

Furthermore, g is called the Landé splitting factor for the ion, given as:

$$g = 1 + \frac{J(J+1) - L(L+1) + S(S+1)}{2J(J+1)}. \tag{2.39}$$

With all these definition, $\hat{\boldsymbol{Q}}^{(D)}$ is written as

$$\hat{\boldsymbol{Q}}^{(D)} = \frac{1}{2}F(\mathbf{Q}) \sum_{l,d} e^{i\mathbf{Q}\cdot\mathbf{R}_{ld}} \hat{\mathbf{J}}_{ld}, \tag{2.40}$$

where

$$F(\mathbf{Q}) = \bar{J}_0 \frac{g_s}{g} + (\bar{J}_0 + \bar{J}_2)\frac{g_L}{g}, \tag{2.41}$$

is the magnetic form factor of the ion. It must be stressed that $\hat{\boldsymbol{Q}}$ in equation (2.38) is only an approximation and for a detailed analysis of the effects of orbital angular momentum on the

cross-section for magnetic scattering is given in chapter 11 of the reference [105]. We can thus write differential cross-section within dipole-dipole approximation and identical magnetic ions as [105]:

$$\begin{aligned}\frac{d^2\sigma}{d\Omega dE} =& r_0^2 \frac{k_f}{k_i}\left(\frac{1}{2}gF(\mathbf{Q})\right)^2 \sum_{\alpha\beta}\left(\delta_{\alpha\beta}-\tilde{Q}_\alpha\tilde{Q}_\beta\right) \\ &\times \sum_{\lambda\lambda'} p_\lambda \sum_{d,d'} e^{i\mathbf{Q}\cdot(\mathbf{R}_{d'}-\mathbf{R}_d)} \times \langle\lambda|\hat{S}_{\alpha,d}|\lambda'\rangle\langle\lambda'|\hat{S}_{\beta,d'}|\lambda\rangle\delta\left(\hbar\omega+E_\lambda-E_{\lambda'}\right),\end{aligned} \tag{2.42}$$

where the spin operator $\hat{\mathbf{S}}$ would be regarded as actual spin or the total angular momentum $\hat{\mathbf{J}}$, or if the neutrons are scattered by an ion with partially quenched orbital angular momenta, as an effective spin operator. The Form factor in equation (2.42) is

$$F(\mathbf{Q}) = \bar{J}_0\frac{g_s}{g} + (\bar{J}_0+\bar{J}_2)\left(\frac{g-g_s}{g}\right) \tag{2.43}$$

where $\mu_B g_s\mathbf{S}$ is the spin contribution and $\mu_B(g-g_s)\mathbf{S}$ is the orbital moment contribution to the total magnetic moment of the ion $\mu_B g\mathbf{S}$.

2.2.2 The INS instruments

The inelastic neutron scattering experiments for this thesis were conducted at the ISIS neutron and muon facility of Rutherford Appleton Laboratory in the U.K., which is a *spallation source*; as opposed to the *reactor sources* like ILL (Grenoble) in France and HZB (Berlin) in Germany. In a spallation source, high-energy pulsed protons ($\sim$ 800 MeV at ISIS) produced from a synchrotron are fired onto a heavy metal (tungsten in case of ISIS) target resulting in the emission of a pulsed neutron beam. The so-produced neutrons are 'hot' neutrons i.e. are fast and the moderators are required to slow/cool them down to desired speeds/temperatures. We have used cold or thermal neutrons (T $\sim$ 25 K - 293 K) in our experiments. [3] There are a range of instruments available at different large-scale facilities (For instance over 20 at ISIS only), to perform different types of neutron scattering investigations. Here, we will present a brief overview of the instruments used for this thesis only, starting with an introduction to the time-of-flight technique. The specific sample details and experimental settings will be covered in the respective chapters.

Time of Flight Spectrometers

In *time-of-flight* (TOF) spectrometers, the scattered neutron beam flight-time over a known distance is measured to analyze the scattered energy. They can cover a large **Q-E** space in a single measurement, using wide position-sensitive detector arrays. Since the neutrons are detected through the nuclear reactions, their detection is possible only once. It is therefore necessary that their starting point is known by pulsing the incoming neutron beam using choppers or single-crystal monochromators. The neutrons coming out of the moderator have a wide distribution

[3] Neutron energy and temperature conversions are possible through the relation: $E_n = k_B T$; with k_B = 1.38065 $\times$ 10^{-23} J/K, is the Boltzmann constant.

of energies and velocities. With the aim of selecting a particular band of neutron energies, the *choppers* are placed at a distance D_0 from the moderator. Among various types of choppers being used in the instruments, the most common are the disk and Fermi choppers.

The *disk chopper*, as the name suggests, is a rotating disk made up of (or coated with) neutron absorber materials – with its axis of rotation parallel to the incoming neutron beam and having a small transmitting slit for neutron passage. The transmitted wavelength/energy band for disk choppers is triangular shaped centered at the desired incident energy E_i.

The *Fermi chopper*, is a rotating drum made up of alternating curved layers of neutron transparent or absorber materials, with its rotation axis perpendicular to the incident neutron beam. As the chopper rotates it allows only a section of the neutron pulse through, with neutrons of the desired energy value. With the chopper rotation frequency and phase, it is possible to control the width and energy range of the incident neutrons.

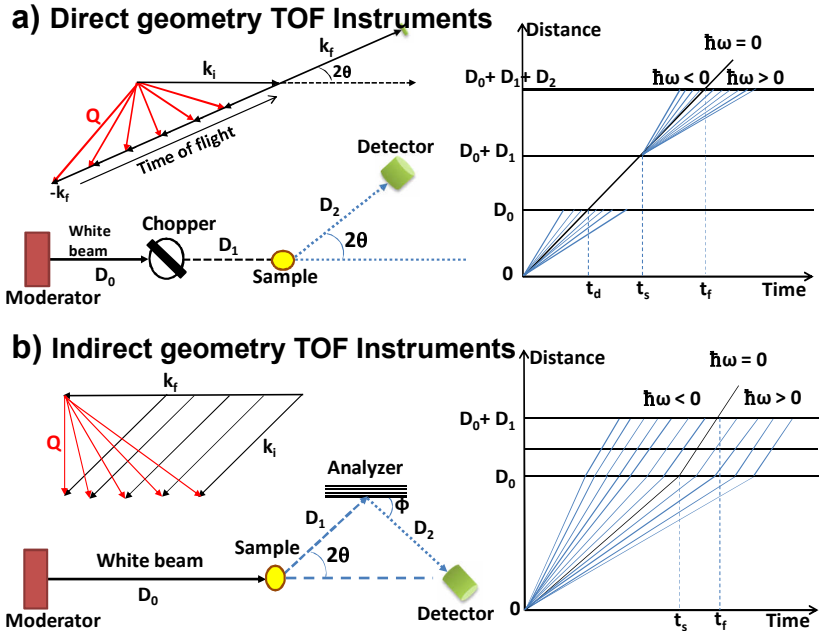

Figure 2.7: Schematic diagram of a) direct geometry TOF instrument, k_i is fixed using choppers and k_f is measured; b) inverted geometry TOF instrument, k_f is fixed using single crystal analyzers and k_i is measured. The respective scattering triangles and time−distance plots are also shown.

In the TOF technique either the incident wave vector (k_i) or the scattered wave vector (k_f) is measured, depending on this the spectrometer is termed the direct or inverted geometry TOF instrument, respectively. In direct geometry the neutrons incident energy (E_i)is fixed whereas the final energy (E_f), after scattering by the sample, is calculated by measuring neutron time of flight from sample to the detectors. Figure 2.7 shows the schematic diagram of direct and indirect geometry spectrometers with the corresponding scattering triangles and the time-distance plots.

Direct geometry TOF

The direct-geometry spectrometers are the 'workhorses' of pulsed neutron scattering for measuring the scattering law. Since the incident energy and wave-vector (E_i and k_i, respectively) are fixed, we need to find the relation for the final energy and wave-vector (E_f and k_f) from the available experimental information. The time neutrons leave the moderator is known, whereas the chopper slit opening time in relation with the source pulse time t_d centers the neutrons at a given velocity – so the desired incident energy and wave-vector are given as:

$$k_i = \frac{m_n}{\hbar}\frac{D_0}{t_d}; \qquad E_i = \frac{1}{2}m_n\left(\frac{D_0}{t_d}\right)^2, \tag{2.44}$$

where D_0 is the distance between the source (moderator) and the Fermi chopper. Each neutron pulse, after passing through the Fermi chopper, shares the same velocity and they arrive at the sample without much dispersion in time. The chopper frequency, irrespective of the chopper type, is always set at same or some multiple of the pulsed source frequency. The time that the neutron takes to travel from the chopper to the sample t_s is given as: $t_s = t_d\ (D_0 + D_1)\ /\ D_0$, with D_1 being the chopper-to-sample distance (figure 2.7−a). The final wave vector after the scattering event, can be determined by the time of flight t_f over the path D_1 from the sample to the detectors

$$k_f = \frac{m_n}{\hbar}\left(\frac{D_2}{t_f - t_s}\right) = \frac{m_n}{\hbar}\left(\frac{D_2}{t_f - t_d(D_0 + D_1)/D_0}\right), \tag{2.45}$$

similarly the neutron final energy (E_f) is

$$E_f = \frac{1}{2}m_n\left(\frac{D_2}{t_f - t_s}\right)^2 = \frac{1}{2}m_n\left(\frac{D_2}{t_f - t_d(D_0 + D_1)/D_0}\right)^2, \tag{2.46}$$

where D_2 is the sample to detector distance. The scattering vector Q can be directly determined from k_i and k_f and the scattering angle 2θ. Lets take an inelastic scattering process in which a neutron with incident wave-vector (=momentum) k_i imparts a momentum $\hbar\mathbf{Q}$ to the sample and scatters with a final wave-vector k_f. We already know the momentum transfer $\hbar\ \mathbf{Q} = \hbar\ (\mathbf{k}_i - \mathbf{k}_f)$ and the energy transfer $\hbar\omega = E_i - E_f$. Using

$$Q^2 = k_i^2 + k_f^2 - 2k_ik_fcos(2\theta), \tag{2.47}$$

we have

$$Q^2 = \frac{2m_n}{\hbar^2}[2E_i - \hbar\omega - 2cos(2\theta)\sqrt{E_i(E_i - \hbar\omega)}]. \tag{2.48}$$

For a fixed value of E_i, experimentally accessible values of Q and E_f are the only ones governed by equation (2.48), called the *dynamic range*. Clearly, with a larger incident energy neutrons it is possible to explore a wider range of Q-space and hence a greater number of magnetic excitations. However, the instrumental resolution is another fundamental limit which worsens as the energy of the incident neutrons increases. In other words, the full width at half maximum (FWHM) of the elastic peak (and therefore any other detectable peak) keeps increasing with the energy of incident neutrons, making it harder to energetically resolve close lying peaks.

Indirect geometry TOF

In an indirect/inverse geometry spectrometer, a white neutron beam directly hits the sample keeping the final (scattered) energy fixed, using a crystal analyzer (figure 2.7 - b), while scanning the incident energy E_i. The inverted geometry spectrometers boast an extended coverage of energy loss values, as compared to the direct geometry TOF instruments. The most versatile of all inverted geometry spectrometer are the crystal analyzer INS spectrometers. With a single custom-defined analyzer, they collect full S(**Q**, ω) scattering law information along a specific line in reciprocal space. The incident wave-vector and energy in the case of indirect geometry TOF is given as:

$$k_i = \frac{m_n D_0 \pi}{\pi \hbar t - m D_1 d_a sin\phi} \qquad E_i = \frac{1}{2} m \left(\frac{\pi \hbar D_0}{\pi \hbar t - m_n D_1 d_a sin\phi} \right)^2 \tag{2.49}$$

where D_0 is the neutron flight path from moderator to the sample, t is the total flight time $t = t_s + t_f$, D_1 is the distance from sample to detector, ϕ is the counter angle of the beam scattered from analyzer, and d_a is the analyzer spacing. See figure (2.7−b) for the schematic diagram of an inverted geometry spectrometer, the inverse scattering triangle and a time-distance illustration for indirect geometry. The analyzer crystal angle must be setup so that it satisfies the Bragg condition with equal incidence and reflection angles. D_1, the scattered flight path, must be kept as small as reasonably possible while taking instrument background and resolution into consideration. In inverted geometry TOF instruments, D_0 is always the longer flight path.

2.2.3 INS spectrometers

The powdered poly-crystalline MNM samples were measured on three different instruments at the ISIS facility, namely the MARI, the LET, and the IRIS spectrometers. MARI is used to study the crystal-field excitations, whereas the latter two are high-resolution instruments used to study low-energy transitions. In the following sections we will introduce different aspects and technical specifications of these instruments.

MARI

MARI is a TOF direct geometry chopper instrument, at ISIS Target Station 1, covering a vast (7-1000 meV) incident energy range. MARI takes the neutrons from a methane (CH_4) moderator at the temperature of 100 K, which is tilted so that the chopper sees the closest side of the moderator first. This allows the slower neutrons to go through the chopper first, resulting in a time focusing effect. Then it utilizes the Fermi chopper as a monochromator, filtering the neutron beam which emerges from the moderator. The sample-to-detector distance is 4.020m with the low and high angle adjacent detector banks covering a scattering angle that ranges from 3° to 135° in total, mapping a large **Q-E** plane in a single run.

MARI employs 919 ^{3}He-filled gas proportional counters of 30 cm length each, which are not position sensitive−making MARI more suitable to polycrystalline, liquid and powdered sample investigations. At the time of the experiments presented in this thesis, the incident neutron flux on MARI was rather low, due to the absence of neutron guides in the path of incoming neutrons.

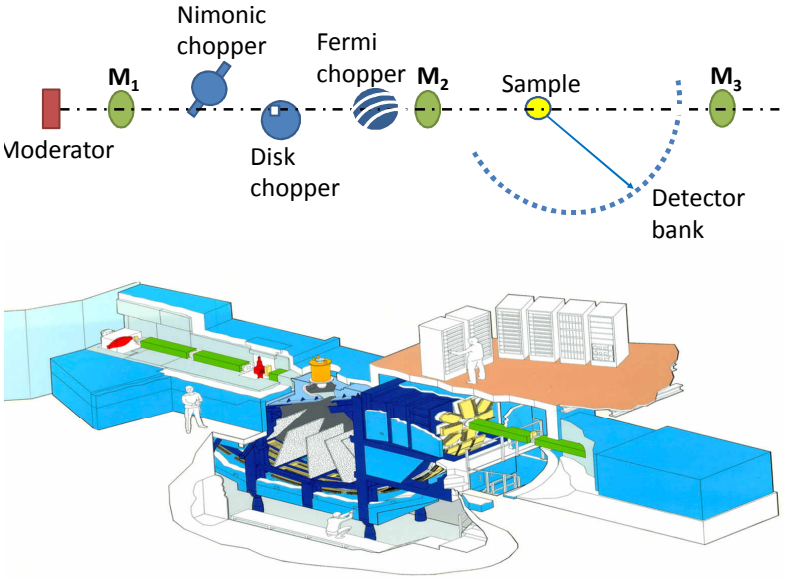

Figure 2.8: Illustrative diagram of MARI experimental setup showing the nemonic, disk, and Fermi choppers and a large underground detector bank. The lower part of figure shows 3D simulated sketch of actual MARI instrument, taken from the MARI web page [107].

The instrument is currently being upgraded to include neutron guides which will significantly enhance the neutron flux. The underground position of MARI detectors makes it an instrument with very low background noise with respect to all the other chopper spectrometers at ISIS, and it also compensates for the lower flux mentioned before. MARI uses a 10 - 100 Hz nimonic chopper and a 50 Hz Boronated resin single hole disk chopper for the background suppression which may include very high energy neutrons and gamma rays, produced as a result of neutron hitting the spallation target.

Three counter monitors at 7 m, 10.297 m, and 17.559 m distance from moderator are also included in the MARI setup for the time-of-flight analysis. A conceptual layout of MARI is shown in the upper part of figure 2.8, with the lower part showing the 3D graphical representation of the actual instrument. Depending on the setting of Fermi chopper, the energy resolution ($\Delta\hbar\omega$/E$_i$) varies from 1.5 to 8 %. There are 4 chopper setups available to achieve various energy ranges and resolutions, e.g. using G-Chopper we can get E$_i$ = 7 - 200 meV, and ΔE/E$_i$ = 2 - 5 %, whereas using high resolution A-Chopper gives us the incident energy E$_i$ = 100 - 1000 meV, and resolution ΔE/E$_i$ = 1.5 - 3 %.

Spectrometer: LET

LET is a direct multi-chopper spectrometer, at ISIS Target Station 2, which can measure multiple incident energies in a single run. LET uses cold neutrons with incident energies between 0.5 - 20 meV, especially suited to study low-energy excitations. Neutrons coming from the target are cooled down by high efficiency solid methane moderators which emit neutrons of a wide range of wavelengths. These moderators consist of a pre-moderator (thin water layer) surrounding the

half liquid Hydrogen/half solid methane inner moderators at T = 18 K. Along the moderator-to-sample distance of 25 m (D_0 + D_1), neutrons are directly transported by the super-mirror guides avoiding the loss of neutron flux. The guides start at 1.7 m from the moderator with 94 mm × 40 mm wide opening, whereas they start gradual vertical diminution after chopper 4, affording a beam of 50 mm × 40 mm at the sample position [108].

There are five disk choppers employed at LET following the moderator, allowing for pulse shaping, background/contaminant removal, and energy selection of the incident neutrons. All

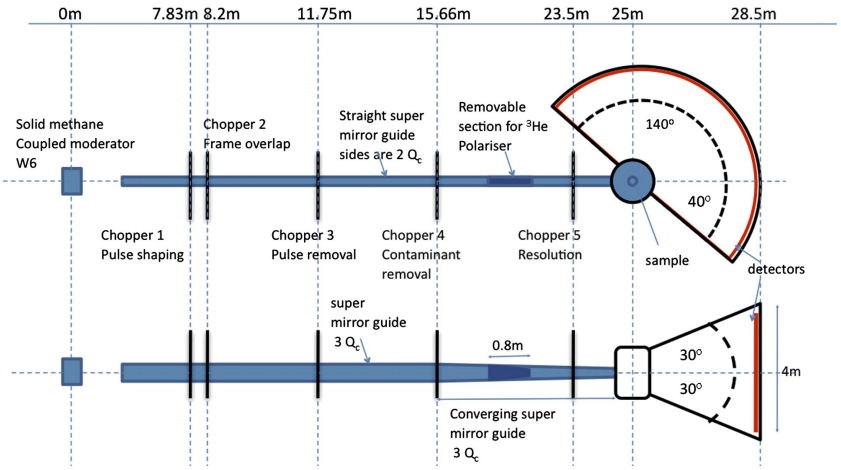

Figure 2.9: Schematic diagram of LET instrumental setup, indicating the multi-chopper configuration, wide detector bank and super-mirror guides installed at LET (both top and side view are depicted); taken with permission from [108].

the choppers are made of composite carbon fiber coated with Boron (^{10}B) as neutron absorbing material. Chopper 1 at 7.83 meters distance from the moderator, effectively controls the moderator pulse width as seen by the detectors, while chopper 5 calibrates the energy resolution. Apart from these two high-speed choppers, other three choppers installed on LET are slower. Chopper 2 and 4 function as the background removers, whilst chopper 3 ensures the appropriate spacing between the pulses to avoid time-of-flight overlap. A schematic diagram of the LET instrument is shown in figure 2.10, depicting a side and top view configurations.

A sample can/holder is placed inside a 110 m^3 vacuum box without any windows between the sample and the detectors positioned at a distance of 3.5 meters. The position sensitive detectors filled with ^{3}He at 10 atm pressure use nuclear reactions to detect neutrons. The detectors, 1 inch diameter each, form a 4 m high cylindrical curtain around the sample. The detectors cover 180° plane horizontally and ±30° vertically with a smallest angle of 3° [108]. As already pointed out, one distinctive feature of LET is that thanks to its multi-chopper configuration, it can measure multiple (up to five) incident energies (E_i) in a single experiment, saving a lot of beam time in the process.

In view of all the aforementioned features, LET can boast a high flux (5 × 10^4 n-counts m^{-2}s^{-1} at E_i = 2 meV), high energy resolution ($\Delta E_i/E_i \approx 2$ %), low flat background, and large **Q-E** space. Overall, LET is ideal for low energy excitations in magnetic materials, but

the resolution advantage quickly diminishes for relatively higher energy needs (i.e. crystal field excitations in MNMs).

Spectrometer: IRIS

IRIS is an indirect geometry, high resolution time of flight, quasi- and in-elastic neutron scattering spectrometer with a fixed final energy, situated at ISIS Target Station 1. At IRIS, after the neutrons are scattered from the sample, they are energy analyzed using Bragg's law from either one of the two large single crystal array analyzers made of pyrolytic graphite or muscovite/fluorinated mica – geometrically oriented close to the back-scattering profile. Primary

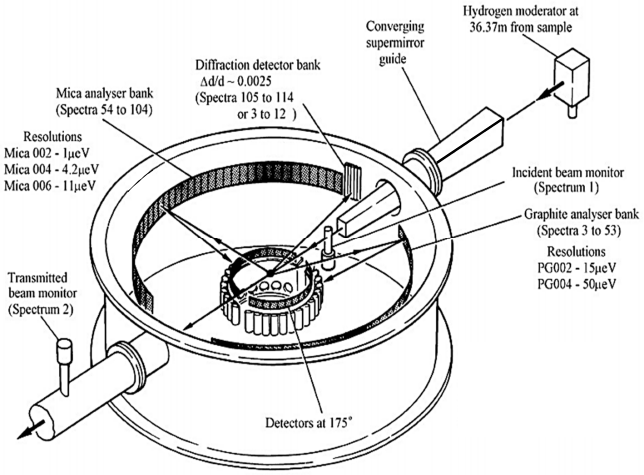

Figure 2.10: Schematic diagram of IRIS analyzer vacuum tank showcasing the neutron guides, graphite and mica analyzers, detector banks and the diffraction detectors; taken from [109]

spectrometer consists of the white neutron beam transport setup, from moderator to the sample. The liquid hydrogen based moderator is at 36.37 m from the sample, and uses converging supermirror neutron guides (starting at 1.7 m from the moderator) to focus the beam onto the sample while preserving the maximum flux along the path. Two disk choppers are also part of the primary setup at IRIS, serving the purpose of defining the neutron wavelength range impinging on the sample while avoiding the frame overlap.

The secondary spectrometer consists of a 2 m diameter stainless-steel vacuum vessel containing both of the crystal analyzers, two ZnS based 51-element scintillator detector arrays spanning 25 to 155 degree angular range, and ^{3}He gas based detector bank for diffraction at $2\theta = 170^\circ$ which can also be used as a diagnostic tool for the samples (see figure 2.10). The graphite analyzer accessible energy range is extendable up to $\sim$10 meV using a beryllium filter at 25 K; moreover the analyzer is cooled down to 10 K for reducing the background contributions coming from the diffuse scattering events. Two neutron beam monitors are present before and after the sample. With indirect geometry spectrometers like IRIS, energy loss studies enable to access a larger dynamic range than direct ones, while preserving higher energy resolutions, thanks

to the partial decoupling between energy transfer and energy resolution. Another advantage of the IRIS spectrometer is that it is possible to simultaneously record the diffraction pattern and inelastic spectra of a sample.

2.2.4 Data analysis tools

INS experiment raw data must be processed in order to be manipulated, visualized and further analyzed. In the following subsection all the software applied to the data analysis of the INS data presented in this work will be briefly introduced.

Mantid

Mantid is a versatile, open-source, software package written in Python programming language for neutron scattering and muon spectroscopy data analysis and manipulation [110]. The aim of the Mantid framework is to provide a single platform for the data reduction and analysis of the neutron scattering and muon relaxation/resonance data, across the instruments and facilities around the world. Mantid takes raw TOF data from the instrument detectors as an input and transform them into *.nxspe* and *.sqω* format i.e. files ready to be plotted as **Q**-E transfer data. It already contains all the instrumental parameter information for various spectrometers to perform these conversions. In the following paragraphs we outline the data operations performed inside the Mantid in order to obtain the scattering function S($\mathbf{Q}$, ω) starting from the raw experimental data.

Detector calibration Since different detectors do not have the same efficiency and they do not subtend the same solid angle with respect to the sample, a calibration measurement must be carried out at the beginning of each experimental cycle run using white beam on a vanadium sample. Vanadium has an incoherent cross section of 5.08 barn but a coherent cross section of just 0.02 barn so the experiment results in the uniform neutron diffusion in all directions with a known energy. The number of neutrons counted by a detector with the vanadium sample is proportional to the solid angle subtended by the particular detector and its intrinsic efficiency. The number of neutrons counted at each detector during the actual experiment is divided with the ones from the vanadium measurement to get correct relative intensity. The detector calibration data of every instrument is stored in Mantid repository after the measurements at the start of each run. These data are utilized during the data reduction step, vide infra.

Data reduction The experimentally collected data are normalized for the incident neutron flux which may vary during the measurement. In the absence of availability of the absolute value of the neutron flux, one can use a proportional quantity like the proton current in the spallation source. The data reduction is then performed using pre-written routines in the Mantid project by inputting relevant information e.g. the experimental run numbers, incident energies, white beam vanadium run data, and the sample mass. For a powdered sample measurements, like those performed at MARI, the software automatically assigns an angle 2θ to each pixel of the detectors. All pixels within a certain Debye-Sherrer cone would be identified by the same angle,

as each 2θ is associated with a value of $|\mathbf{Q}|$ vector. This yields the energy transfer in terms of $|\mathbf{Q}|$, which is taken as equivalent to the aforementioned angle. It is also possible to mask specific detectors after performing the experiment, during the data reduction step in Mantid, so that if any detector is malfunctioning/out-or-order, its pixel will be removed from the experimental data. There are special 'masking files' present in the repository path for this purpose.

Mantid also performs simple algebraic operations on the S($\mathbf{Q}$, ω) data (like addition, subtraction, multiplication, fitting etc). Among the numerous functionalities and modules available inside Mantid project, we will just comment on one, the Crystal-field (CF) python interface, as we will be using this in the later part of this thesis. With this module it is possible to calculate CF Hamiltonian by inserting the CF parameters, rare-earth ion name and the symmetry of molecule from a list of allowed entries available Mantid project website [111]. It is also possible to specify which CF parameters to consider, together with the sample temperature, peak-shape and FWHM for the calculation of the INS spectrum. The Mantid CF module can calculate energy eigenvalues, eigenvectors, and the Hamiltonian matrix while plotting the simulated INS spectrum.

Background subtraction The magnetic contribution to S($\mathbf{Q}$, ω) can be determined by the subtraction of the phonon contribution, which can be achieved by measuring the non-magnetic analogue of the magnetic sample in similar experimental conditions. The non-magnetic analogue should ideally be isostructural to the magnetic sample and should have similar atomic weight of the substituting atoms. Once the non-magnetic compound measurement is done, the magnetic scattering function ($S_{mag}(\mathbf{Q}, \omega)$ for the magnetic sample can be obtained using

$$S_{mag}(\mathbf{Q},\omega) = S(\mathbf{Q},\omega) - \rho S_{ph}(\mathbf{Q},\omega) \tag{2.50}$$

where S_{ph} is the phonon contribution (scattering law for non-magnetic sample analogue), and ρ is an appropriate scaling factor which ensures that there are no negative intensities after performing the background subtraction.

The relation (2.50) is a standard method for phonon background subtraction. However, in some situations due to disparities between the phonon energies of the compounds, the subtraction is not adequate to remove phonon background contribution. The discrepancy in the phonon energies could arise from various factors, e.g. the difference in the exact amount of samples, the difference in the neutron absorption cross section for magnetic and non-magnetic samples, or any difference in the experimental conditions. Therefore, an alternative way to perform background subtraction is then to take an integration cut of S($\mathbf{Q}$, ω) and $S_{ph}(\mathbf{Q}, \omega)$ over both low $|\mathbf{Q}|$ region (S_{lowQ}) and high $|\mathbf{Q}|$ region (S_{highQ}), for both the magnetic sample and non-magnetic analogue, respectively. Further assumption is made for both the compounds, that the phonon contribution has the same $|\mathbf{Q}|$-dependence whereas the magnetic contribution to S_{highQ} is negligible. This is reasonable as the phonon background contribution increases with $|\mathbf{Q}|$ and the magnetic scattering falls due to *form factor* $F^2(\mathbf{Q})$ dependence. Finally the magnetic contribution can be calculated as

$$S_{mag} = S_{lowQ} - \frac{S^{ph}_{lowQ}}{S^{ph}_{highQ}} S_{highQ} \tag{2.51}$$

here $S^{p}_{lowQ}h$ and $S^{p}_{highQ}h$ are the low $|\mathbf{Q}|$ and high $|\mathbf{Q}|$ region integrations for the phonon contributions.

The background subtraction in all of our experimental data analysis was carried out using Mantid or Mslice programs, by employing the background subtraction method described before.

Mslice

Mslice is a program written in MATLAB environment for displaying the single crystal and powder time of flight experimental data [112]. It has a simple graphical user interface (GUI) for visualization of a single data-set at a time, but a more powerful use is possible through Matlab command prompt. It accepts .nxspe files as an input and shows 2D graphs of the respective S($\mathbf{Q}$, ω). Mslice further provides the option of taking 1D-cuts from the 2D ($|\mathbf{Q}|$, E) dataset, by integrating along a chosen interval in $|\mathbf{Q}|$ or E, and plotting the results as I(E) or I($\mathbf{Q}$). One can also perform basic analysis functions like subtracting background, plotting multiple graphs in the same window for comparison, and saving the results as text files.

Chapter 3

Yb(trensal) Molecular Magnet

3.0 Introduction

Building a quantum computer, a machine based on quantum mechanical phenomena like superposition and entanglement, is one of the hottest topics of current research, attracting huge investments from many important companies and focusing efforts of researchers from very different areas. The basic units of such devices are the quantum two-level systems (the qubits), which can be realized using a variety of physical systems, including trapped ions and neutral atoms, infrared photons, nuclear spins in liquid molecules, electron spins in quantum dots, nitrogen vacancy centers in diamond, and so on [113, 114]. After the first proposal of exploiting the distinct energy levels present in MNMs to implement Grover's database search algorithm by Leuenberger and Loss in 2001 [25], the molecular magnets based on transition metal spins emerged as truly promising systems for the QIP applications, with remarkably long coherence times, thus enabling their coherent manipulation using EPR [28–35] and the demonstration of single-qubit gates [36–39].

Ln-based MNMs are a relatively new entry among MNM qubits, which has shown great promise in recent years [47–49]. An advantage of Ln-MNMs lies in their multilevel energy structure, which can be employed as the so-named *qudits*, where d is the number of levels, providing a larger Hilbert space for the quantum information and communication operations [115, 116]. Larger computational resources of qudits enable one to optimize the construction of quantum logic gates [117, 118], simplify quantum algorithms [119] and quantum simulations[120], implement quantum error correction [121, 122], enhance the security of quantum cryptography

[123] and realize bipartite entanglement [124]. Recently, a four-levels nuclear spin of a lanthanide ion (Tb) was employed to implement the Grover's quantum search algorithm for the first time in a molecular transistor [125].

Magnetic nuclei have recently emerged as a promising resource for the molecule-based QIP offering long coherence times [125–128], mostly because they are essentially isolated from the environmental sources of noise. This can however result in long manipulation times [129]. Still, this limitation can be surmounted by using the magnetic nucleus hosted by the magnetic ions, where the resulting electronic-nuclear hyperfine coupling results in a significant shortening of the quantum gate operation times [130–132].

Among various examples of Ln-MNMs, a very promising qubit system is the Yb(trensal) MNM of the Ln(trensal) series[133], in which coherent Rabi oscillations of the electronic spin were recently reported by Pedersen et al. [50]. Pedersen et al used the pulsed EPR technique to study selectively on the ions of the ^{173}Yb isotope, the electronic spin transitions, spin-lattice and spin-spin relaxation dynamics on the single crystals of Yb(trensal) [50]. We decided to unravel a new aspect of the Yb(trensal) MNM system , namely its multi-level patterns of nuclear spin transitions. Based on that , we propose an implementation of a coupled nuclear qudit − electronic qubit as error protected qubit.

The chapter is organized as follows. Starting with a brief description of the structure of the [Yb(trensal)] molecule, in section 3.1, we will systematically show that the ^{173}Yb isotope of [Yb(trensal)] provides the basis for the realization of a prototypical coupled electronic qubit-nuclear qudit system. For that, we will start by detailing the unconventional pulsed NMR experiments by spin-echo pulse sequences to measure ^{173}Yb spectra, and determine spin-lattice relaxation and spin-coherence times. A sizable enhancement of coherence times will be demonstrated by implementing Carr-Purcell-Meibum-Gill (CPMG) sequences. We will show that this six-level qudit that can be rapidly manipulated thanks to its strong hyperfine interaction with the effective electronic spin $S = 1/2$. Driving fast Rabi oscillations of the nuclear magnetization will explicitly demonstrate our capability to coherently manipulate the ^{173}Yb qudit. For the sake of completeness a possible encoding into a qudit, realized by the multi-level structure of [Yb(trensal)], of an error-protected logical qubit coupled to an electronic ancilla, will be presented in the last part of this chapter. In particular, we will show that a minimal code protecting against amplitude or phase shift errors can be implemented by the combined qudit-qubit available in this MNM system.

The author of this thesis performed all the NMR experiments and data analysis presented in this chapter, under the supervision of Prof. Giuseppe Allodi. The samples used were prepared and characterized by Prof. Stergios Piligkos's group in the Department of Chemistry, University of Copenhagen (Denmark). The Hamiltonian modeling and error-protected qubit implementation proposal were carried out by Prof. Stefano Carretta's group. Prof. Roberto De Renzi supervised the whole project.

3.1 Material Synthesis and Characterization

Single-crystals of Yb(trensal) doped into the isostructural Lu(trensal), were synthesized and grown using a mixture of $Yb(CF_3SO_3)_{3.9}H_2O$ (1 mol%) and $Lu(CF_3SO_3)_{3.9}H_2O$ (99 mol%).

The as-synthesized single crystals were pencil-shaped and yellowish in color. For the detailed synthesis, procedures and exact amounts of compounds/solutions, readers are referred to the references [134, 135].

The identity of the single-crystals was confirmed by single-crystal and powder (crushed single-crystals) X-ray diffraction experiments[50, 135]. The Inductively Coupled Plasma Mass

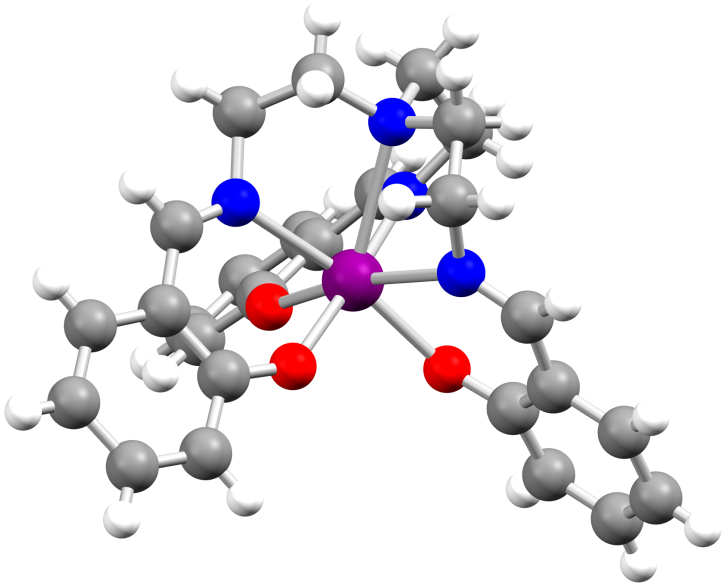

Figure 3.1: Molecular structure of [Yb(trensal)] molecule. Color code: purple, Yb; red, O; blue, N; gray, C; white, H.

Spectrometry (ICP-MS; Bruker Aurora Elite) was used to determine the actual doping concentration of Yb (in Lu). The analysis result revealed the mass percentages of 0.59% and 27.16% for Yb and Lu, respectively, giving a Yb/Lu ratio of 2.14%. For comparison, the theoretical mass percentages are calculated from $Yb_{0.02}Lu_{0.98}C_{27}H_{27}N_4O_3$, respectively to be 0.55% and 27.20% for Yb and Lu.
As shown in figure 3.1, Yb(trensal) crystallizes in the trigonal $P\bar{3}c1$ space group in which the Yb^{3+} ion and the apical tertiary amine nitrogen atom both lie on the crystallographic C_3 axis.

3.2 NMR Experimental Details

All the NMR measurements were performed at T = 1.4 K on a single-crystal of Yb(trensal), doped at 2% with Yb into the isostructural diamagnetic Lu(trensal) host as described above. The dilution is often used in MNMs to suppress the dipolar coupling between the electronic spins. Different orientations of the static field with respect to the crystallographic 3-fold rotation axis were explored, to probe the hyperfine coupling tensor anisotropy against the static magnetic field. For the purpose, a custom-designed sample holder was used to ensure the desired crystal orientation as well as keeping the single crystal fixed during the measurements.

The electronic ground Kramers doublet of the J = 7/2 multiplet of Yb^{III} is well isolated in energy from the excited crystal-field states (by about 464 cm^{-1}) [135], henceforth we treat Yb(trensal) MNM as an effective electronic spin S = 1/2 system coupled to a nuclear spin I. The natural composition of Yb includes several isotopes, however only the ^{171}Yb (with 14%

Table 3.1: NMR Properties of Yb Isotopes with non-zero nuclear spin I.

Isotope	**Natural Abundance**	**Nuclear Spin**	**Gyromagnetic ratio**
	%	I	MHz/T
^{171}Yb	14.31	$\frac{1}{2}$	7.526
^{173}Yb	16.13	$\frac{5}{2}$	2.073

abundance) and ^{173}Yb (16% abundance) have a non-zero nuclear spin. We will only focus on the ^{173}Yb isotope (with I = 5/2), that can encode a qudit with d=6. As presented in table 3.1, ^{171}Yb has much larger gyromagnetic ratio and therefore its nuclear-magnetic transitions occur at very different (higher) frequencies and do not influence our study.

The NMR measurements were carried-out using the home-built HyResSpect spectrometer [102], introduced in section 2.1.11. The NMR spectra were recorded point-by-point by exciting and detecting spin echoes by a sequence of two equal pulses of 500ns duration and power optimized for maximum signal. The rationale for using equal-pulse sequence is already narrated in last paragraph of section 2.1.11. Both frequency scans, i.e. varying the frequency while keeping the external magnetic field fixed, and field sweeps, i.e. measuring the spectra with small-step field variations at constant frequency, were performed. To measure the intrinsic T_2, which essentially is the coherence time of the nuclear spin system, the Hahn-echo sequence was applied repeatedly while gradually increasing the time τ between the first and the second pulse. The recorded integrated echo intensity plotted against τ gives the spin-spin decay profile of nuclear spin (T_2), which can be fitted with a single exponential decay. A CPMG pulse sequence, used to suppress extrinsic sources of decoherence (like e.g. spin diffusion) by repeatedly refocusing spins, will be detailed in the results section.

The spin-lattice relaxation was always measured using the saturation recovery method. An aperiodic pulse train was applied to saturate the system to achieve (almost) zero net polarization. The system was then allowed to evolve freely and re-polarize by the exchange of energy with the thermal bath. A usual spin-echo detection sequence was then used after a variable delay (D) to measure this re-polarization. Since ^{173}Yb is a multi-level system, the experimental curve for the saturation recovery law was observed to be multiexponential (more on this to follow in the appropriate section).

In order to observe Rabi oscillations in a spin-echo sequence, we fixed a properly calibrated detection pulse (180° or π), and changed the first pulse (t_{Rabi}) duration systematically while recording the echo amplitude. The Fourier transformed and phase corrected echo amplitude as a function of t_{Rabi} resulted in the Rabi oscillation cycles.

3.3 NMR Spectra and Hamiltonian Modeling

The NMR resonance spectra probe the static magnetic fields at the nucleus, either internal or externally applied. The former is proportional to the expectation value of the electronic moments (i.e. a static property of the electronic spin ensemble) through the hyperfine and dipolar coupling. Since the resonance spectra are rather broad in [Yb(trensal)] (the overall spectral width reaching up to few hundred MHz), as is typical of magnetic materials, it was not possible to excite the entire NMR spectrum by a single echo and the spectra was therefore constructed point-by-point at discrete frequency steps. Similarly the field-dependent spectra were constructed at discrete magnetic field steps while keeping the frequency fixed. Furthermore, as the ^{173}Yb is an I =

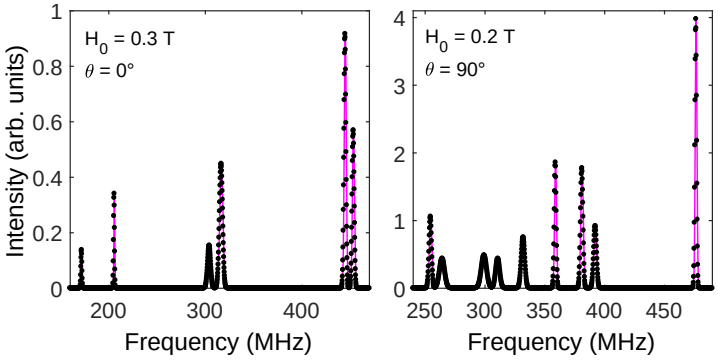

Figure 3.2: Representative examples of measured and fit-reconstructed NMR spectra of Yb(trensal) as a function of frequency, at T = 1.4 K for the θ = 0° and θ = 90° orientations w.r.t the static field at two applied magnetic fields H_0 = 0.3 T and 0.2 T, respectively.

5/2 nucleus and it is interacting with an effective electronic spin S= 1/2, we expect to see ten transitions at most, five for each of two electronic multiplets, in the presence of a large-enough external magnetic field, i.e. in the Paschen-Back limit where the ΔS_z = 0, I_z=$\pm$1 selection rule applied.

Two example of typical ^{173}Yb frequency sweep NMR spectra are presented in figure 3.2 for θ=0°, and θ=90° orientations at 0.2 T and 0.15 T applied fields. The effective spectral width observed by the individual spin echoes was limited by the Fourier transform of a pulse ($\pm$ 1 MHz wide), which is further filtered by the finite bandwidth of the tuned probehead. This was comparable or slightly smaller than the width of the individual resonance lines. Therefore, each resonance peak was reconstructed by a merger of the Fourier transforms of a few echoes (typically 5) recorded with a frequency offset of 200-300 kHz relative to each other. The peak position and width are determined by fitting a Gaussian component to each transitions. The Yb(trensal) MNM system is modeled by our colleagues in Parma using the following Hamiltonian:

$$\begin{aligned}\mathcal{H} =& \tilde{A}_{\parallel} S_z I_z + \tilde{A}_{\perp} \left(S_x I_x + S_y I_y\right) + p I_z^2 \\ &+ \mu_B \mathbf{S} \cdot \mathbf{g} \cdot \mathbf{H}_0 + \mu_N g_I \mathbf{I} \cdot \mathbf{H}_0\end{aligned} \tag{3.1}$$

where the first two terms describe the electron-nuclear hyperfine coupling, the third represents the nuclear quadrupolar interaction to a cylindrical EFG (in agreement with the molecular sym-

metry) and the last two terms are the electronic and nuclear Zeeman terms, respectively. The nuclear dipole interactions are conveniently ignored in the presence of a strong hyperfine coupling, whereas the electronic orbital moment contribution in the hyperfine term is quenched by the ligand field and does not participate in the magnetism to the first order perturbation approximation. The hyperfine coupling tensor $\tilde{A}$ is anisotropic and has different components along and perpendicular to the external field, denoted by $\tilde{A}_{\parallel}$ and $\tilde{A}_{\perp}$, respectively. In the electronic

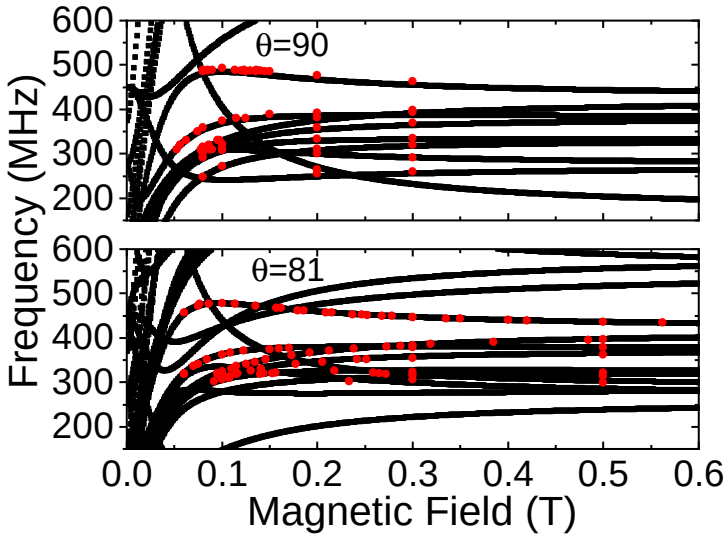

Figure 3.3: Red scatter (filled circles) represent the peak positions obtained from NMR spectra, measured at T = 1.4 K for θ = 81° and θ = 90° orientations of the applied static fields w.r.t main (C_3) crystal axis. Spectra at various magnetic field strengths in the accessible frequency range were recorded. Results from both the frequency-scan (fixed field) and field-scan (fixed frequency), measurements are reported in these figures. Black Scatter are the transition frequencies calculated from the Hamiltonian in equation 3.1. Only those transitions whose probability is higher than a given threshold are reported on the graph.

Zeeman term, the values for the axial **g** tensor components, g_x = g_y= 2.9 and g_z= 4.3, were taken as determined from the EPR measurements in reference [135].

The parameters of Hamiltonian (3.1) were obtained from a fit of peak positions (obtained by the single-Gaussian fit of the resonances lines mentioned above) as a function of the magnitude and orientation of the applied field. In figure 3.3, we present the sets of observed NMR peak frequencies for the orientations $\theta = 81°$ and 90°, while the peak frequencies for the $\theta = 0°$ orientation of the magnetic field $\mathbf{H}_0$ with respect to the main crystal (C_3) axis are reported in figure 3.4. Spectra were recorded at various magnetic field values (frequency scans) or the at various frequency values (magnetic field scans), in the accessible frequency/field range. From the calculations point of view, only the transitions whose probability is higher than a given threshold are reported in these plots. All the theoretical calculations also take into account a possible small error in the orientation of the crystal with respect to the applied magnetic field. We have labeled the detected NMR transitions (F1, F2, ..., F9) in the increasing order of frequency

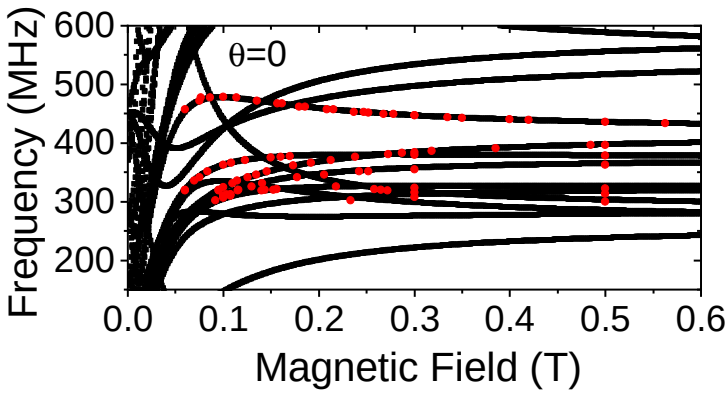

Figure 3.4: Red scatter (filled circles) represent the peak positions obtained from the NMR spectra, measured at T = 1.4 K for $\theta = 0°$ orientation of the applied static fields w.r.t main crystal axis. Spectra at various magnetic field strengths (frequency scan) or the at various frequency values (magnetic field scan) in the accessible frequency/field range are reported. Black Scatter are the transition frequencies calculated from the Hamiltonian in equation 3.1 with only the transitions whose probability is higher than a given threshold reported on the graph.

at the magnetic field 0.6 T. This labeling convention will be followed throughout this chapter.

Experimental frequencies (filled red circles) are very well reproduced by the model (black scatter plot), with hyperfine coupling coefficients values $A_{\parallel} = -0.02993$ cm^{-1} and $A_{\perp} = -0.0205$ cm^{-1} (sign determined from the Pedersen et al., see below) in good agreement with the EPR determination [135]. The nuclear g-factor value is known from the literature as $g_I = -0.2592$ [136] whereas the quadrupolar term is determined by our fit as $p = -0.0022$ cm^{-1}, in the range typical for ^{173}Yb [137]. The sign of the hyperfine coefficient $A_{\perp}$ (and thus of $A_{\parallel}$) cannot

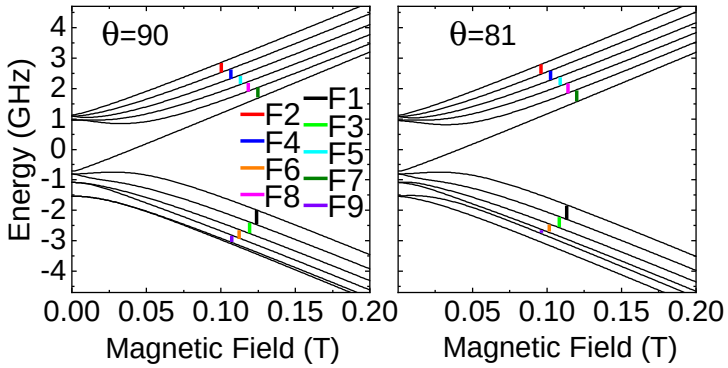

Figure 3.5: Energy level diagram as a function of the applied field for $\theta = 90°$ and $\theta = 81°$ orientations of the main crystal (C_3) axis. The colored lines indicate the experimentally detected transitions with our labeling convention is described in the text.

be determined from the NMR spectra modeling, as the transition frequencies are independent of the sign of $A_{\perp}$. For the sign estimation of the hyperfine coefficients, a detailed analysis of

the relative NMR peak intensities was required, which was not feasible due to the extremely broad spectrum and the difficulty of a reliable calibration of the instrumental sensitivity over a wide frequency span (due to the frequency response of the probehead, the receiver stage of the spectrometer, etc.). Despite this, here we have tried to optimize the signal intensity for each individual transition by fine tuning the transmitted pulse parameters, namely rf power and duration. Nonetheless the estimated uncertainty in the NMR signal intensity could be as high as 20% in some cases, rendering the intensity profile analysis in these spectra impractical.

We further note that the quadrupolar term p is essential to reproduce the NMR data and it is also allowed by the symmetry of molecule. This term could not be extracted from the EPR results and was not reported previously. Another confirmation of the presence of a quadrupolar term for ^{173}Yb comes from the fact that the shift of the transition frequencies is not uniform across the variation of angle θ w.r.t the static magnetic field, figures 3.3 and 3.4. Whereas, in the absence of a quadrupolar term, a variation of θ should only lead to rigid vertical shifts of all the transition frequencies (at a fixed, sufficiently intense magnetic field). The nuclear Zeeman

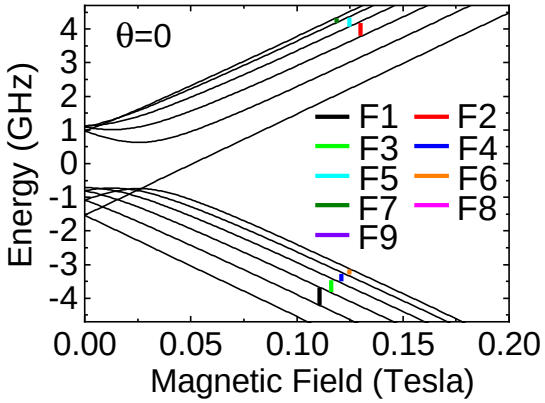

Figure 3.6: Level diagram as a function of the applied field for θ=0° orientations of the crystal C_3 axis. The colored lines indicate the experimentally detected transitions with our labeling convention is described in the text.

term in the Hamiltonian (3.1) was also included as the splitting of the nuclear Zeeman levels that it produces (approximately 2MHz/T), though much smaller than the hyperfine frequencies, is not completely negligible. Some of the calculated transitions were not experimentally visible either due the very short T_2 especially at low magnetic field values, or they were out of the experimentally accessible frequency band in a particular setup. In all the explored frequency ranges and crystal orientations, we were not able to detect any measurable NMR signal below 0.05 T (500 Gauss). Furthermore, we detected an intense, magnetic-field independent, signal in the 215-225 MHz frequency interval, upon further investigation it appeared to be spurious, and we ascribe it to the impurities (possibly Cu) inside the NMR probehead.

The field dependence of the Zeeman-hyperfine energy levels can be calculated from the diagonalization of (3.1). If we focus on parallel ($C_3 \parallel \mathbf{H}_0$) orientation, an analytical expression for the eigenstates can be obtained in the limit $g\mu_B H_0 >> |A_\perp|$ (here fulfilled for $H_0 \gtrsim 0.1$ T). Neglecting the nuclear quadrupolar and Zeeman interactions for simplicity, we can arrive at

an analytical expression for the systems' wave-function correct to the first order in $A_\perp$:

$$\begin{aligned}|\psi_{m_S m_I}\rangle &= |m_S, m_I\rangle \pm \frac{A_\perp \langle m_S \mp 1, m_I \pm 1|S_x I_y + S_y I_y|m_S, m_I\rangle |m_S \mp 1, m_I \pm 1}{g\mu_B H_0 + (m_I \pm 1/2)A_\parallel} \\ &= |m_S, m_I\rangle \pm \frac{\alpha A_\perp}{g\mu_B H_0 + (m_I \pm 1/2)A_\parallel}|m_S \mp 1, m_I \pm 1\rangle,\end{aligned} \tag{3.2}$$

where m_S and m_I are the eigenvalues of S_z and I_z, respectively. The $\pm$ signs depend on the value of m_S, while $\alpha A_\perp$ is the matrix element of the transverse hyperfine interaction. The coefficient α can be given as $\alpha = \langle m_I \pm 1|I_x|m_I = \frac{1}{2}\sqrt{\frac{35}{4} - m_I(m_I \pm 1)}$ (in the order of unit), and $|m_S, m_I\rangle$ is the unperturbed wave function.
The matrix element of the detected nuclear transitions is given as:

$$\begin{aligned}&|\psi_{m_S m_I}|g_I\mu_N I_x + g_x\mu_B S_x|\psi_{m_S m_{I\pm1}}\rangle \\ &\quad= g_I\mu_N\langle|I_x|m_I \pm 1\rangle \pm \frac{\alpha A_\perp}{g_z\mu_B H_0 + (m_I \pm 1/2)A_\parallel} g_x\mu_B\langle m_S \mp 1|S_x|m_S\rangle \\ &\quad= \alpha\left(g_I\mu_N \pm \frac{A_\perp g_x\mu_B}{2g_z\mu_B H_0 + (2m_I \pm 1)A_\parallel}\right) \approx \alpha\left(g_I\mu_N \pm \frac{A_\perp}{2H_0}\right),\end{aligned} \tag{3.3}$$

where the last equality only holds for large magnetic fields and $g_x \approx g_z$. The so-obtained NMR transitions for various nuclear energy levels $|\psi_{m_S,m_I}\rangle \rightarrow |\psi_{m_S,m_I\pm1}\rangle$, are indicated by colored vertical lines in the figures 3.5 ($\theta = 81°$, $\theta = 90°$) and 3.6 ($\theta = 0°$). The level diagrams evidence large anti-crossings at smaller magnetic field values resulting from the electronic and nuclear spin states entanglement, induced by the component of the hyperfine tensor perpendicular to $\mathbf{H}_0$.

As we have shown in equation (3.3), the matrix element of these transitions is approximately proportional to $g_I\mu_N \pm \frac{A_\perp}{2H_0}$, the first term there corresponds to a pure nuclear transition and the second one emerges from the electron-nuclear mixing. It is worth noting that even a small mixing (~ 0.02 at 0.15 T) of the wave-function will induce a huge enhancement in the matrix element when $A_\perp = 0$, since $\frac{A_\perp}{2H_0} \sim 10^3\, g_I\mu_N$. Consequently, a relatively fast manipulation of the nuclear Zeeman levels maybe attained by moderate rf power, vide infra.

3.4 Spin-spin Relaxation (T_2)

In order to investigate the coherence times of the Yb nuclear qudit, the spin-spin relaxation time T_2 was measured systematically for each measured frequency point (the red bullets) in the figures 3.3 and 3.4 by recording spin echoes as a function of a variable delay t between pulses.The relaxation times T_2 were determined by fits of the echo decay vs. delay t to an exponential law

$$A(t) = A(0)e^{-\frac{-2t}{T_2}}$$

which is obeyed by all the transitions. We stress that static inhomogeneities do not contribute to the echo decay, therefore the time constant T2 may me regarded in a first approximation as the (de)coherence time for the given nuclear transition.

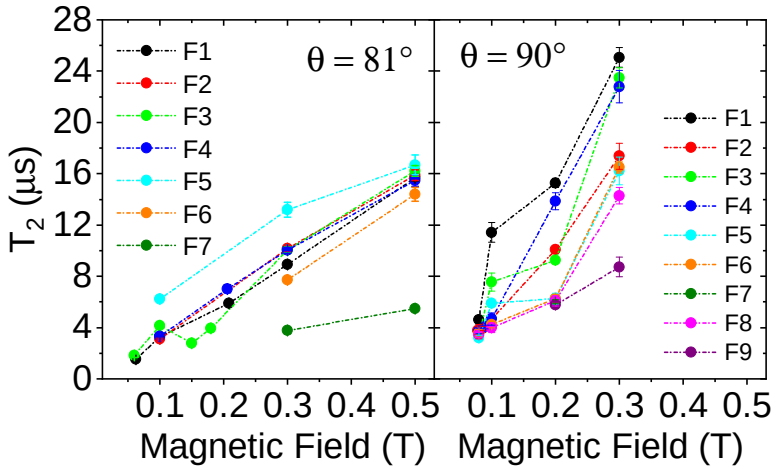

Figure 3.7: Phase memory time (T_2) measured by applying varying delay Hahn-echo sequence for the transitions indicated in figure 3.3 and the magnetic field orientations of θ = 81° and θ = 90° w.r.t crystal C_3 axis. The labeling scheme is same as in the energy level diagrams.

The resulting coherence times T_2 are reported in figure 3.7, as a function of the static magnetic field, for the θ = 81° (right) and 90° (left) orientations of H_0 w.r.t C_3 axis. Figure 3.8 on

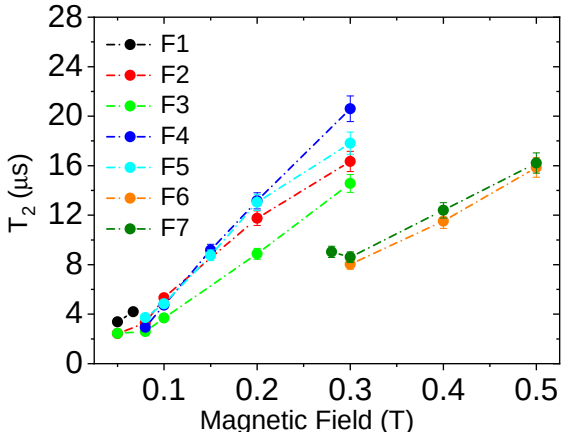

Figure 3.8: Phase memory time (T_2) measured with the decay-varied Hahn-echo sequence for the transitions indicated in figure 3.4. The magnetic field orientation was parallel to the crystal axis in this case i.e. θ=0° w.r.t C_3. The labeling scheme is same as in the energy level diagrams.

the other hand, presents the coherence times T_2 for field applied along the main crystal axis (θ = 0°), as a function of the static magnetic field.

It is clear that the observed values of T_2 increase with the increasing magnetic field. This can be easily understood, as in our diluted sample, inter-molecular dipole-dipole interactions with ligand nuclei are negligible, and the decay of the Yb nuclear spin coherence should be caused by the interactions internal to the ^{173}Yb nuclear spin bath. Therefore, this decay can be related

to the entanglement between the Yb nuclear spin and the nuclear spin bath, mediated by the electron-nuclear mixing (equation 3.2). The latter decreases linearly with H_0, thus explaining the observed field dependence of T_2. Moreover, the electronic polarization increases with H_0, thus reducing the probability of energy-allowed electronic spin flop events [138]. By comparing

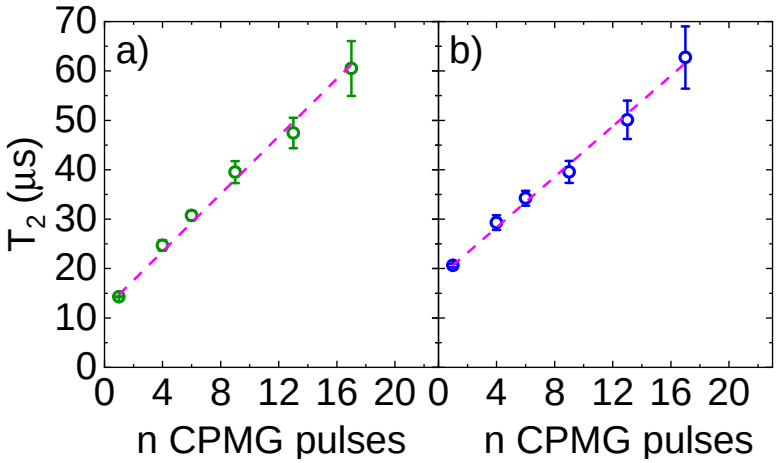

Figure 3.9: Phase memory time enhancement using the CPMG pulse sequence as a function of the number of applied pulses at $\theta = 0°$ orientation for transitions a) F3 and b) F4, following the same labeling scheme.

the T_2 values detected in transitions for the orientation angle 81°, against the ones for 90°, we can state that the coherence times are affected by the direction of applied magnetic field against the main crystal axis. Furthermore, we can qualitatively say that the T_2 decreases with the misalignment of C_3-axis w.r.t H_0 direction, although further experiments at different magnetic field orientations are required to test and quantify this hypothesis.

3.4.1 CPMG pulse sequence

The spin coherence times of the various transitions can be further enhanced by employing a Carr-Purcell-Meiboom-Gill (CPMG) pulse sequences [89]. The CPMG pulse profile is a concatenation of n refocusing pulses that dynamically decouple the system from the environment [139]. The sequence consists in an initial $\pi/2 - \tau - \pi$ echo sequence, followed by a train of N-1 π pulses at times 3τ, 5τ, ..., (2N - 1)τ from the initial $\pi/2$ pulse (times are indeed measured from pulse center to pulse center), as described in a detailed way in the section 2.1.7. This pulse scheme results in a clear linear enhancement of the observed coherence times with the number of applied pulses [140–142], as shown in figure 3.9 for the transitions F3 and F4 at the $\theta = 0°$ orientation.

Experimentally, we paid special attention to avoid any distortion of the decay profile due e.g. to uncalibrated π pulse. However, such a distortion may be compensated for by applying the $\pi/2$ pulse with a rf field H_1 along the x direction in the rotating frame, followed by either i) π pulses alternating along the $\pm$x direction, or ii) π pulses along the y direction [89]. We tried both the

$\pm x$ and the y sequences, and also checked the tolerance to pulse un-calibration by changing the rf output level by ± 1, ± 2 dB, obtaining the same CPMG echo profile in all cases.

The T_2 constant defined here in the case of CPMG, is conceptually the same that could be measured by varying the delay in a single spin echo sequence. In liquids, however, the echo decay may be affected by spin diffusion, leading to a faster non-exponential decay ($e^{-[at]^3}$), while a slower exponential decay, governed by true T_2 processes, is recovered by a CPMG sequence with an arbitrarily small echo delay t. The CPMG sequence therefore gives rise to an extended spin coherence time. Although spin diffusion cannot be at play in the present system, we observed a qualitatively similar coherence enhancement effect by applying multiple pulses in a CPMG sequence. The CPMG profile was modeled with a relatively faster exponential decay component (results reported in figure 3.9) up to 50μs, while a slower component with a much longer T_2 emerged at longer times, which has been often attributed to the presence of 'non-equivalent' nuclei with varying relaxation mechanisms (like rotational, diffusional, etc).

3.5 Spin-lattice Relaxations (T_1)

The spin-lattice relaxation time is the mean recovery time of the longitudinal nuclear magnetization (M_z). The T_1 relaxation process of ^{173}Yb arises, in principle due to a combination of magnetic and the EFG fluctuations, whereby the magnetic part of the fluctuations is contributed for by fluctuations in the electron spin and conduction electron interactions. While the EFG fluctuations depend upon the charge fluctuations and dynamics lattice distortions (e.g. phonons). Thereupon, an experimental measure of T_1 will provide useful insight on all of these dynamics in the Yb(trensal) MNM. The spin-lattice relaxations were measured using the saturation recovery method. Therein, a series of pulses were used to saturate the spin system to achieve virtually zero net polarization (i.e. an infinite spin temperature). The spins were then allowed to freely evolve and re-polarize before applying a usual spin echo detection sequence systematically, with varying delays between the last saturating pulse and the beginning of detection sequence. This gave us the experimental curve for the saturation recovery law. Since ^{173}Yb has I = 5/2 and non-degenerate Zeeman levels, a multiexponential recovery was expected and observed experimentally in the spin-lattice relaxation profile.

The spin lattice relaxation time T_1 in this case is defined more generally as $1/T_1 = 2W$, where W is the transition rate between two adjacent nuclear levels m_I and m_{I+1}. The quantity accessed here experimentally, is the population difference of the level pairs involved in the observed nuclear resonance, rather than the entire nuclear magnetization. Such a behavior can be accounted for in detail by rate equations for the nuclear populations in the framework of the Redfield theory, as it was commented earlier in the last part of section 2.1.4. Further, the rate equations for the nuclear populations then lead to multi-exponential decay/recovery laws for each resonance even in the case of a single transition probability W [89, 98], with up to 2I exponential components exhibiting enhanced rates $2W$, $6W$, $12W$, $20W$, $30W$, ... and weights depending on the preparation (i.e. saturation) method for the nuclear ensemble, namely, whether just the populations of the observed transition are altered, or the preparation pulse sequence is long enough to allow for a recovery to the thermal equilibrium for the other nuclear levels, or any intermediate case between these two. Clearly, a precise control of the initial conditions and

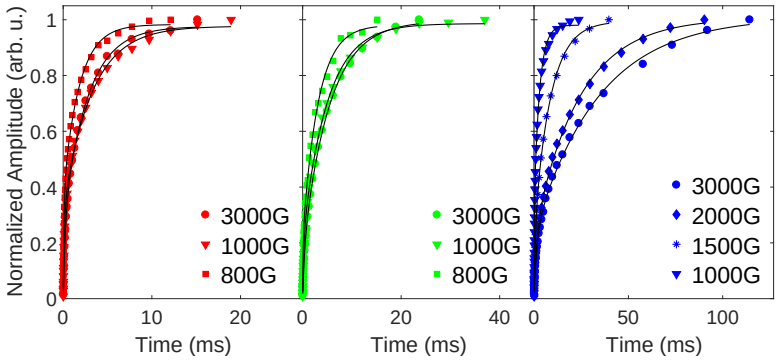

Figure 3.10: Few examples of saturation recovery curves (T_1), measured as described in the text, for the $\theta = 0°$ field orientation at various values of H_0 as labeled. Black lines are the bi-exponential law fits to the experimental points and a guide to the eye.

a detailed theoretical modeling in the framework of the Redfield theory, would be required for a quantitative determination of the spin lattice relaxation rate $1/T_1$.

At the time of this writing, we can just provide an estimate for its order of magnitude as well as its relative dependence on the applied field. Figures 3.10 shows few recovery curves for the polarization of a selected transitions after a fast saturation of the resonance line, performed by a short pulse train of overall duration $\sim$12 μs followed by a usual spin echo measurement sequence. Notoriously, the relative weight of the faster relaxing exponential components is enhanced by the fast saturation method [98]. Nonetheless, we can conclude from the figure 3.10 that i) the slowest exponential components recover to their asymptotic values with characteristic times $t \leq T_1$ in the order of several milliseconds, and ii) relaxation rates decrease with increasing magnetic field, as a consequence of field-induced decoupling of the nuclear and electronic spins. Furthermore, from this analysis, we can assert that the spin-lattice relaxation takes place on a relatively long time scale in the [Yb(trensal)] MNM, and it is not of concern for spin decoherence and the quantum computation operations which we are going to propose later in this chapter.

3.6 Rabi Oscillations

The periodic nutation of the net nuclear magnetization driven by a resonant field, whence the periodic absorption and release of the Zeeman energy by the nuclear spin, is called *Rabi oscillation* and the frequency of this oscillation is called the Rabi frequency. Driving several Rabi oscillation cycles demonstrates the ability to coherently manipulate the spins over a sufficiently long time scales, a basic requirements in the QIP. The Rabi oscillations were observed using a $\phi - \pi$ spin-echo sequence by systematically changing the first pulse (ϕ) duration (t_{Rabi}), while recording the echo amplitude at each step. The 180° (or π) detection pulse was properly calibrated and kept fixed during this process. The so-obtained echo amplitude was Fourier transformed, phase corrected, and plotted as a function of t_{Rabi}, yielding the Rabi oscillations.

Our analysis procedure compensated for the fact that at large ϕ values, corresponding to relatively small spectral widths irradiated by the first pulse, a fraction of nuclei of the inhomoge-

neously broadened resonance line (namely, those with a shift larger than the spectral width of the pulse) were not being effectively excited and did not participate in the echo. Figure 3.11−(a-c)

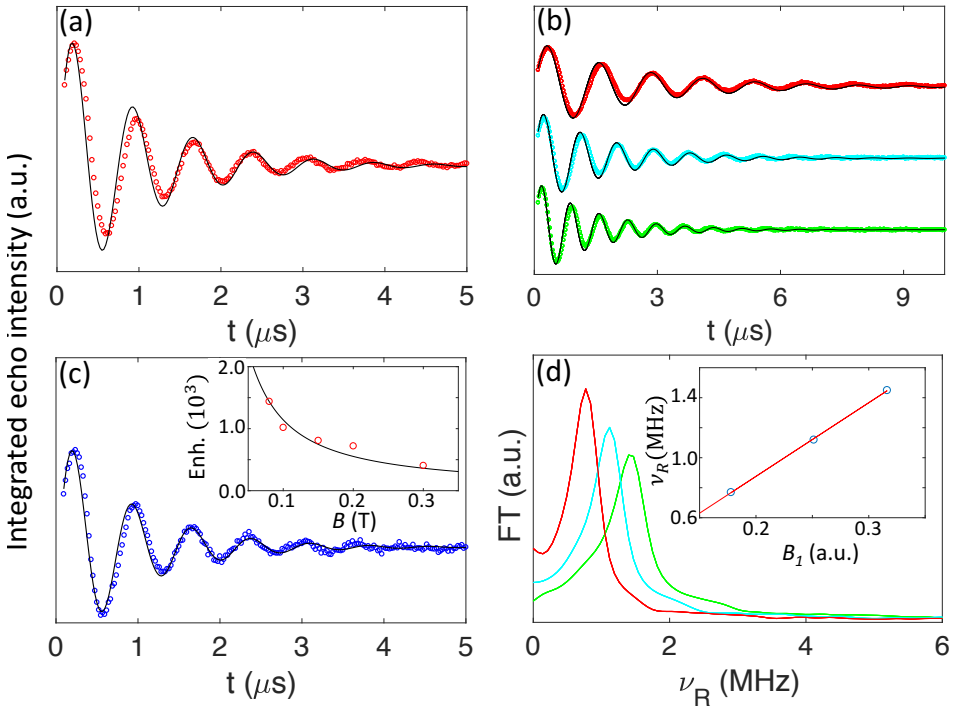

Figure 3.11: (a-c) Rabi oscillations for the three transitions (F1, F3, F4), at parallel C_3 vs. field orientation, necessary to operate the error-protected qubit (see text below). NMR pulses of different duration are used to induce Rabi oscillations, detected by a final π-pulse for refocusing. Continuous lines are a fit with the damped function $\propto e^{-t/\tau}\sin[2\pi\nu_R(t-t_0)]$. Different rf powers are reported for F3 (b). Inset of (c): measured (dots) and calculated (line) enhancement of the Rabi frequency ν_R (with respect to the case $A_\perp = 0$) as a function of magnetic field. (d) Fourier transform, evidencing the monochromatic character of the oscillations reported in panel (b). The inset shows the linear scaling of ν_R (indicated by the position of the peak) with the oscillating field H_1.

reports the measured coherent Rabi oscillations for the three transitions F1, F3, F4 respectively, at a parallel C_3 vs. field orientation.

As discussed before, even a small mixing of the wave-function (~ 0.02 at 0.15 T), induces a large enhancement of the matrix element, since $\frac{A_\perp}{2H_0} \sim 10^3\, g_I\mu_N$. Therefore, manipulations of the nuclear qudit are actually very fast in [Yb(trensal)]. In particular, we have found an enhancement of nearly 10^3 in the observed Rabi frequencies compared to the $A_\perp = 0$ case, shown in the inset of figure 3.11-c, in an excellent agreement with the calculations based on (3.1). The empty circles are experimental points while the blue line represents the calculated enhancement at various magnetic field values.

Rabi oscillations are damped by T_2 relaxations or the inhomogeneities of the driving rf field

H_1, whichever of the two is stronger. For sufficiently large powers, however, this damping/decay

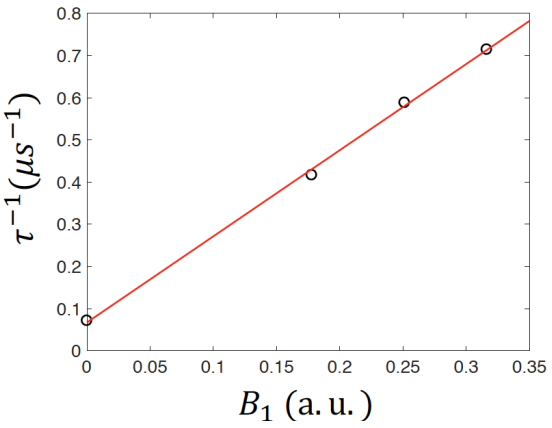

Figure 3.12: The damping rate of the Rabi oscillations for transition F3 (at $\theta = 0$ field orientation) as a function of the oscillating field H_1. The experimental points are overlaid to the modeling described in the text.

is dominated by the inhomogeneities of the oscillating H_1 field. This Rabi damping rate can be modeled as

$$\tau^{-1} = \frac{1}{T_2} + mH_1, \tag{3.4}$$

where the first term is the measured T_2 of the particular transition whereas the second one accounts for the inhomogeneities in the rf-field and is therefore proportional to H_1. The experimentally observed damping rate, overlaid to the modeling, is presented in figure 3.12 for transition F3 at the $C_3 \parallel H_0$ orientation. The increase in the damping rate with the applied

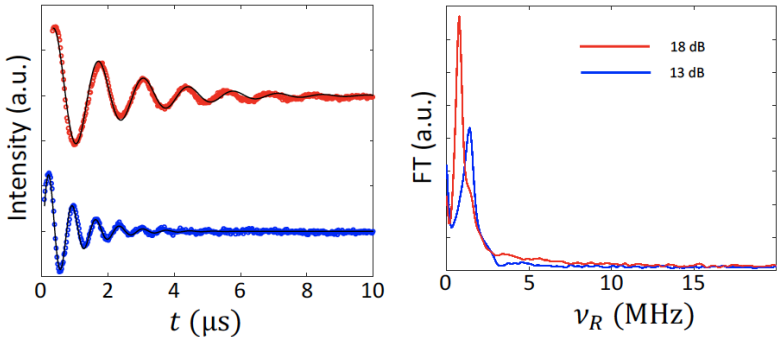

Figure 3.13: Left: Rabi oscillations for transition F4, for two different attenuations (13 and 18 dB). Right: corresponding Fourier transforms of the signal, evidencing the monochromatic character of the oscillations.

power, points towards the dominance of the inhomogeneities of the applied rf field H_1.

In order to ascertain that the amplitude wiggles that we have driven are indeed Rabi oscillations, we undertook a standard procedure to see if such oscillations show a linear dependence of

their frequency ν_R on the applied rf field strength. Indeed we observe a linear scaling of ν_R with the oscillating field amplitude H_1, for both the F3 and F4 transitions at parallel field orientation (figures 3.11-(d) and 3.13). This check unambiguously confirms that in our experiments we are manipulating the populations of the nuclear spin states. The detected echo intensity shows that we are able to perform many coherent oscillations before the signal is lost. This is vital for the potential implementation of QIP in this system.

3.7 Error-protected Qubit Proposal

Quantum error correction techniques are based on the redundant encoding of information. This implies embedding a quantum information unit (a qubit), belonging to a two-dimensional Hilbert space into a larger one. Standard quantum information algorithms are based on *block-encoding* of the logical qubit into a set of several physical qubits (three at least) in order to extract the error syndrome by majority voting. Here we pursue a different approach, i.e. we exploit the extra space available in the d = 2I+1 dimensional Hilbert space of ^{173}Yb nucleus to obtain a qudit-encoding of the logical qubit. The observed values of T_2, the important enhancement in the Rabi frequencies and the fact that transitions are well resolved (figures 3.3, 3.4, 3.5 and 3.6) make [Yb(trensal)] a promising coupled electronic qubit-nuclear qudit system.

In the following we show that the multi-level structure ($d = 6$) of the ^{173}Yb nucleus can be used to encode a qubit protected against amplitude or phase shift errors [122], whereas the electronic qubit provides a fast ancilla to detect errors and help efficient qugate implementation. The possible errors acting upon a single qudit can be expanded in terms of a unitary operator

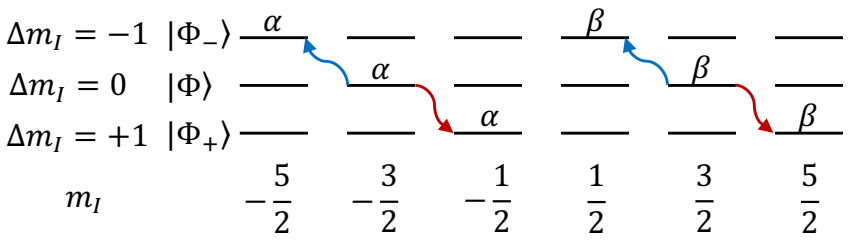

Figure 3.14: Encoding of a qubit protected from amplitude shift errors in the nuclear levels of [Yb(trensal)], corresponding to the m_S = -1/2 manifold. Possible amplitude shift errors are indicated by arrows.

basis with d^2 elements the "generalized Pauli operators": $X^a Z^b$, with a, b = 0, 1, ..., d − 1, where $X|j\rangle = |j + 1 \; mod \; d\rangle$ and $Z|j\rangle = e^{i\frac{2\pi}{d}}|j\rangle$. These operators represent the basic quantum errors which a quantum correcting code must correct [122]. They can be distinguished into amplitude shifts X^a (which we will briefly discus in this section) and complementary phase shifts Z^b. It can be shown [122] that the smallest qudit which protects against a single amplitude (X) or phase (Z) shift is characterized by d = 6. In general, we need $d = 2(2k + 1)$ to correct k shifts. This should be compared with the corresponding exponential scaling of the Hilbert space dimension required by block-encoding $d = 2^{2k+1}$. Hence, block-encoding algorithms are exponentially

more demanding that shift-resistant codes based on qudit-encoding. In our Yb(trensal) based physical system $|j\rangle$ are the nuclear levels.

Considering the experimental scope of this thesis, we will focus only on the amplitude shift errors, i.e. unwanted $\Delta m_I = \pm 1$ transitions, further details on the error-protected qubit implementation can be found in reference 143.

Following reference [122], the qudit states can be relabeled according to $|m_S = -1/2, m_I\rangle \rightarrow \overline{|m_I + 5/2\rangle} = |0\rangle, |1\rangle, |2\rangle, |3\rangle, |4\rangle, |5\rangle$. By encoding the logical qubit in the generic state $\alpha|0\rangle + \beta|1\rangle$ in $|\Phi\rangle = \alpha|\psi_{m_S=-1/2,m_I=-3/2}\rangle + \beta|\psi_{m_S=-1/2,m_I=3/2}\rangle$ (with $\mathbf{H}_0$ along z-axis), the effect of an amplitude shift is to induce a transition to a state outside the computational basis. In the relabeled scheme this means to encode the generic state into $\alpha\overline{|1\rangle} + \beta\overline{|4\rangle}$, which protects from an amplitude shift X. Therefore, the error can be detected using microwave pulses in ancilla and then corrected [122]. In the case of a $\Delta m_I = 1$ shift $|\Phi\rangle \rightarrow |\Phi_+\rangle = \alpha|\psi_{-1/2,-1/2}\rangle + \beta|\psi_{-1/2,5/2}\rangle$. This state conserves the superposition and has no overlap with $|\Phi\rangle$ (see figure 3.14). Thus, by two simultaneous and fast microwave π pulses resonant with the $|\psi_{-1/2,-1/2}\rangle \rightarrow |\psi_{1/2,-1/2}\rangle$ and $|\psi_{-1/2,5/2}\rangle \rightarrow |\psi_{1/2,5/2}\rangle$ gaps, (echo detected in reference 50), it is possible to rotate the electronic spin only if the molecule is in $|\Phi_+\rangle$. Therefore, a measure of the electronic spin after the pulses detects and identifies the error, without affecting the qubit state (i.e., without collapsing the nuclear wavefunction). After restoring the ancilla in $m_S = -1/2$ (by repeating the microwave pulses), the error can be corrected by radiofrequency pulses. An analogous procedure detects and corrects $\Delta m_I = -1$ errors leading to $|\Phi_-\rangle = \alpha|\psi_{-1/2,-5/2}\rangle + \beta|\psi_{-1/2,1/2}\rangle$. It is important to note that the minimal number of qudit levels to implement this code is exactly 6 as in the present case ($I = 5/2$), because it enables $|\Phi\rangle$, $|\Phi_+\rangle$ and $|\Phi_-\rangle$ not to overlap. Remarkably, this quantum error correction code requires less levels than the textbook 3-qubit repetition code [55].

An important point is to implement a universal set of single-qubit gates with the present error-protected encoding. In particular, rotations around x and y of $|\Phi\rangle = \alpha|\psi_{-1/2,-3/2}\rangle + \beta|\psi_{-1/2,3/2}\rangle$ can be implemented by a sequence of radiofrequency pulses resonant with the $-3/2 \rightarrow -1/2$, $-1/2 \rightarrow 1/2$ and $1/2 \rightarrow 3/2$ gaps, i.e. F1, F3 and F4 in figure 3.6. Figure 3.11-(a-c) reports the corresponding measured coherent Rabi oscillations, showing that few hundreds of ns are sufficient to implement π rotations, whereas the echo intensity shows that we are able to perform many coherent oscillations before the signal is lost. Rotations around z of the encoded qubit state can be easily implemented by a single microwave 2π pulse semi-resonant with the $|\psi_{-1/2,3/2}\rangle \rightarrow |\psi_{1/2,3/2}\rangle$ gap. We finally note that the complementary phase-shift code could be implemented in the same way by encoding in the conjugate basis [122].

3.8 Conclusions

In this chapter, [Yb(trensal)] molecular nanomagnet was studied using the pulsed nuclear magnetic resonance spectroscopy. The lowest transition of the hyperfine coupled ^{173}Yb-Yb^{3+} I = 5/2, S = 1/2 spin system, essentially nuclear in nature, were probed by exciting them and observing their coherent evolution by means of a pulsed NMR apparatus. These nuclear transitions were distinctly resolved using both the frequency and field sweep measurements. A spin Hamiltonian approach was then used to model this system and the energy level diagrams were

obtained. The spin-spin relaxation time (T_2) was measured to exhibit long enough coherence times for potential applications of [Yb(trensal)] in quantum computation. Using the CPMG pulse sequence it was demonstrated that the coherence times can be further enhanced by applying short refocusing pulses at frequent intervals to decouple the system from the environment. The spin-lattice relaxation was measured and shown not to be a limitation for quantum computation operations. Several Rabi oscillation cycles were driven for some of the detected transitions to demonstrate our ability to coherently manipulate the nuclear spins over a sufficient long time scale. The observation of Rabi oscillations was made possible by a huge enhancement, of the order of few thousand, from the electron-nuclei wave-function mixing.

The observed relatively long values of T_2, the important enhancement in the Rabi frequencies and the fact that transitions are well resolved enabled us to show that the [Yb(trensal)] MNM behaves as a nuclear qudit coupled to an electronic qubit. Using these unique experimental evidences we showed that the [Yb(trensal)] MNM can be exploited to define a quantum error protected qubit system, where any error can be detected and corrected inside the proposed algorithm using the electronic qubit as an ancilla. The encoded algorithm protects against both amplitude and phase shift quantum errors. These results open new perspectives in the relatively new field of f-electron molecular qubits, by exploiting a multi-level structure from both the nuclear and electronic degrees of freedom in a coupled system.

Chapter 4

Lanthanide (4f) Dimers

Reproduced, in part, with permission from "Measurement of Magnetic Exchange in Asymmetric Lanthanide Dimetallics: Toward a Transferable Theoretical Framework" Marcus J. Giansiracusa, Eufemio Moreno-Pineda, **Riaz Hussain**, Raphael Marx, María Martínez Prada, Petr Neugebauer, Susan Al-Badran, David Collison, Floriana Tuna, Joris van Slageren, Stefano Carretta, Tatiana Guidi, Eric J. L. McInnes, Richard E. P. Winpenny, and Nicholas F. Chilton:
Journal of the American Chemical Society 2018 140 (7), 2504-2513 DOI: 10.1021/jacs.7b10714

4.0 Introduction

The unique magnetic properties of Ln-MNMs arise from their large magnetic anisotropy, which originates from the strong spin-orbit coupling and the crystal field (CF) effects, whereas role of inter- and intra- molecular dipolar interactions and magnetic exchange is also important [19, 144]. Intra-molecular magnetic interactions, although they are usually much weaker than CF splitting in lanthanides, can still significantly affect the magnetic properties of a MNM by providing alternative relaxation pathways via the intermediate states, mixing of the low lying states, and increasing the quantum tunneling of the magnetization (QTM). Alternatively, they can lift the ground state degeneracy in Ln-MNMs by exchange interactions, resulting in a shift of resonant QTM relaxation steps away from zero-field, known as the exchange bias, thus increasing zero-field magnetic remanence [145, 146].

Barring some examples of magnetic exchange interaction mediated via radial species[147–149], the super-exchange interactions are usually very weak for Ln-ions due to the contracted nature of 4f orbitals, rendering the thermodynamic techniques entirely insensitive to their presence [150]. Therefore the spectroscopic techniques, such as inelastic neutron scattering (INS) and electron paramagnetic resonance (EPR), become much more significant to probe these interactions. Recently, INS spectroscopy has quite often been employed to investigate the CF excitations in Ln ions [151–155]. The INS spectroscopy is a powerful probe with neutron energies ranging from below 1 meV to over 1 eV (8 - 8000 cm^{-1}), elucidating interaction from

smaller energy exchange to larger CF energy splittings in MNM systems. The technique was extensively used to study simple Ln dimers by Güdel and coworkers, during 80's and 90's, for the direct probing of the exchange manifold [156–161]. Moreover, the INS does not rely on the application of an external magnetic field and thus yields zero-field information unlike field dependent techniques such as EPR.

The magnetic moments of Ln ions are large and usually accompanied by the significant magnetic dipole interactions, many times comparable in magnitude to the superexchange interactions, while both being highly anisotropic. Furthermore, even if the exchange states can be probed directly using spectroscopic techniques, there is no transferable microscopic Hamiltonian available at present for modeling the magnetic interactions between Ln ions, with recent results suggesting a case-specific formalism for the modeling of the exchange coupling between J multiplets might be required [162–164]. Information on the magnetic exchange between Ln ions, both from experimental and theoretical point of view, is seldom available in the literature due to aforementioned reasons. In the current chapter, we employ the INS, EPR and far-IR (FIR) spectroscopies, magnetometry and complete active space self-consistent field spin-orbit (CASSCF-SO) calculations, in order to obtain a comprehensive picture of the CF states for each of the molecular sites in the Ln-dimers and subsequently arrive at an accurate quantification of the magnetic exchange interactions between the Ln ions.

The chapter will start by outlining the structural information of the all Ln-dimers. The next section outlines the INS experimental instrument settings and sample details. Following the first two sections, experimental results, calculations and interpretations are arranged in one section each for the Er, Yb, and Dy dimers. Each of these section starts with the magnetic characterization followed by the CF excitations INS results along with CASSCF-SO calculation modeling. Exchange interactions probed with low energy INS and EPR spectroscopy are presented later in all sections (the latter only for Er_2 and Yb_2).

All the samples used in this chapter were synthesized by Professor Richard Winpenny's group in the Department of Chemistry, University of Manchester (UK). Magnetic measurements, EPR, and CASSCF-SO calculations were also performed there. Far-infrared (FIR) spectroscopy was handled by Professor Joris van Slageren's group in Stuttgart (Germany). The author of this thesis and Dr. Tatiana Guidi (ISIS, STFC) performed all the INS experiments and data analysis. Prof. Stefano Carretta also helped and guided in INS data analysis. The effective point charge modeling for Dy_2 is being carried out in collaboration with Dr. Michael L. Baker in the Department of Chemistry, University of Manchester and the Diamond Light Source, Harwell Campus (UK).

4.1 Material Synthesis and Characterization

The pure dimers were prepared using proper amounts of 8-hydroxyquinoline and $LnNO_3 \cdot xH_2O$ salt (Ln = Y^{III}, Dy^{III}, Er^{III}, Yb^{III}, and Lu^{III}) and performing synthesis as detailed in references [165, 166]. The Ln-dimer family crystals are block-shaped and yellowish in color. The compounds are isostructural and crystallized in the in the monoclinic space group $P2_I/c$ and with the chemical formula $[hqH_2][Ln_2(hq)_4(NO_3)_3]$.MeOH (hq = 8-hydroxyquinoline). Samples were characterized by CHN microanalysis and powder XRD (PXRD) measurements to

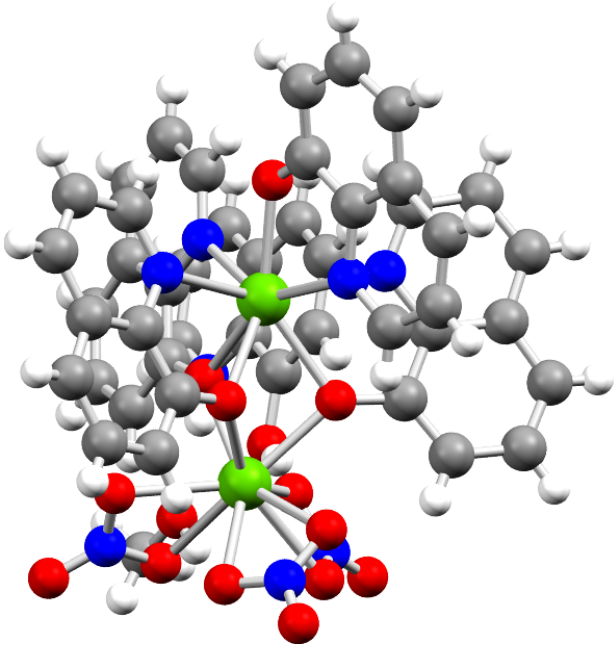

Figure 4.1: Crystal structure of $[Ln_2(hq)_4(NO_3)_3]^-$ (Ln = Er, Yb, Dy, Lu) showing two asymmetric coordination environments. Upper metal site is the *hq pocket*, lower metal site is the NO_3 *pocket*. Color scheme: green, Ln; red, O; blue, N; gray, C; white, H.

establish the consistency and phase purity of the bulk samples [165]. The choice of diamagnetic host (Y or Lu), enabled us to spatially isolate the paramagnetic Dy(III), Er(III) or Yb(III) dopant ions and while the probing of exchange-free properties of each site were possible within the molecule.

Site selectivity in these dilution experiments arises from the small differences in the ionic radii across the lanthanide 4f series. In the asymmetric molecule, the smaller Ln site coordinates four hq ligands (from now onwards, the hq pocket) making an N_4O_4 environment, whereas three of the oxygen donors also bridge to the second pocket, which is capped by three NO_3 anions (the NO_3 pocket), generating an O_9 coordination environment, figure 4.1. The spatial arrangement of the capping NO_3 ions is not rigidly fixed and thus they can host the larger Ln-ions than the hq pocket. Indeed, on average the volume of the NO_3 pocket's initial coordination polyhedron is $\sim$8% larger than the hq pocket. Therefore in the diluted samples (not used in the INS experiments), where the dopant ionic radius is smaller than the host, the dopant preferably occupies the hq pocket, and vice-versa. Diluted samples were prepared using 5% dopant during the synthesis, which will be referred to accordingly as Ln@Y or Ln@Lu depending upon the dopant used. Crystal structure of Ln_2 dimer series is shown in figure 4.1, with green spheres represent the lanthanide atoms, red are the oxygen, blue nitrogen, gray carbon, and the white are the hydrogen atoms.

Since there is no general model present and only the lowest-lying energy exchange states are known, the best strategy seems to model the system interactions in a limited basis. The ground

CF doublet state can be represented by pseudo-spin S = 1/2 for each individual lowest Kramers doublet, and the magnetic anisotropy of the state is represented by the principal g-values. The family of Ln-dimers studied in this thesis, is especially ideal because of the possibility of site selective doping thanks to the different sizes of the hosting sites, as mentioned before. This provided us with the possibility of studying each metal site individually, and then compare it with the pure dimer results.

4.2 INS Experimental Details

All the INS spectra were collected at the ISIS neutron and muon facility using the LET, IRIS, and MARI spectrometers. The IRIS and LET are the high-resolution instruments used for the detection of low-energy exchange interaction while the MARI was employed for the study of crystal field excitations. In the following paragraph, we outline the specific sample details and the experimental settings used in the INS experiments. The general introduction of the INS theory, instruments used, and the TOF technique was detailed in the section 2.2.

4.2.1 Sample description

The dimer samples used in the INS experiments have a chemical formula of $C_{46}H_{36}\mathbf{X}_2N_8O_{15}$, (**X**= Er, Yb, Dy, and Lu). The Lu with a ground state of $^4F_{14}$, have no unpaired electrons and is non-magnetic, therefore it was used as a measure of the INS background signal.

The samples were non-deuterated and in the form of lightly ground powders. The sample masses were 1.648 g, 1.788 g, 1.937 g, and 1.311 g for Er_2, Yb_2, Dy_2, and Lu_2, respectively. For the IRIS, sample powder was inserted inside an annular cross-section generated by a cylindrical aluminium (Al) can of 20 mm diameter and 1 mm thickness having another cylindrical insert of 18 mm diameter placed inside it. Sample height in this case was 26 mm. In case of LET, an Al can of 20 mm diameter was used to hold the sample packed in an Al sachet of 34 mm height placed inside the can making an inner cylinder. Similarly at MARI, a standard thin walled (0.1 mm wall thickness) Al cylindrical can with 40 mm diameter and 64 mm height was used as sample holder while the powder was packed in a cylindrical Al sachet of 34 mm height. Two Al foil supports having 15 mm height each, were placed above and below the sample sachet, inside the can, for making sure that sample's center coincides with the incoming neutron beam center.

4.2.2 Instrument settings

In this section we outline the experiment specific description of the instrument settings employed and the resolutions achieved, during the INS measurements.

MARI

All the MARI measurements were carried out at 5 K temperature using a closed cycle refrigerator. Four different incident energies (Ei) of 15 meV, 25 meV, 50 meV, and 100 meV with corresponding calculated resolutions of 0.4 meV, 0.6 meV, 2 meV, and 5 meV were measured for the Er_2 and Yb_2, while the Ei = 100 meV was not measured for Dy_2 sample. MARI data is

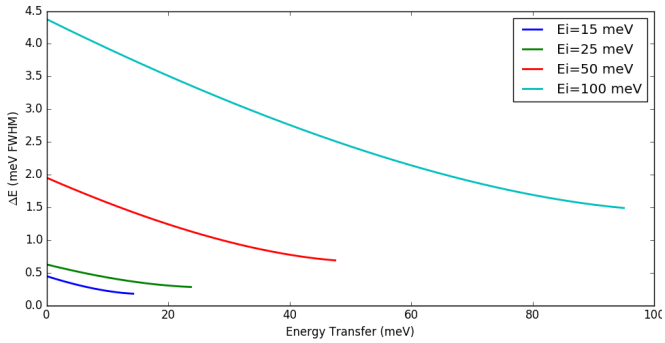

Figure 4.2: The setting used at the MARI instrument showing resolution plotted against transferred energy. The gain in the incident energy cost in the form of lower resolution.

integrated from $0 < |Q| < 3$ Å^{-1} for 15 and 25 meV ($0 < |Q| < 2.5$ Å^{-1} for Ei =15 meV Dy_2), and $0 < |Q| < 4$ Å^{-1} for 50 and $0 < |Q| < 5$ Å^{-1} 100 meV . The MARI resolution from the elastic line was found to be 0.65 meV, 0.95 meV, 2.75 meV, and 5.79 meV for incident energy of 15, 25, 50, and 100 meV, respectively. The Gd chopper setup was used with the frequency of the chopper set at 150, 250, 200, and 250 Hz for the incident energies of 15, 25, 50, and 100 meV, respectively. The figure 4.2 shows the calculated relation between the FWHM (ΔE) versus increasing energy transfer, for incident energies used at MARI.

LET

The temperature at LET was set at 5 K during all the measurements, using a closed cycle refrigerator. LET can access multiple energies in one go depending upon the selected chopper settings.

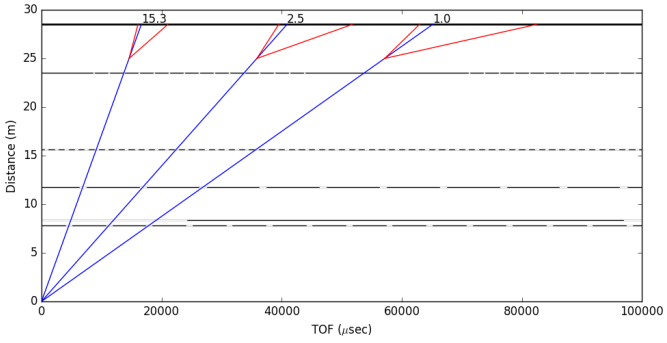

Figure 4.3: The LET chopper configuration used with corresponding accessible energies vs. neutron time of flight. Each of the five different dashed horizontal lines before the 25 m distance indicate a disk chopper.

Therefore, we measured the incident energies (Ei) of 1.00 meV, 2.54 meV, and 15.3 meV, with corresponding calculated instrument resolutions of 20 μeV, 70 μeV, and 0.9 meV. Low-energy (1 meV) LET data integration was $0 < |Q| < 2$ $^{-1}$. Chopper configuration for LET time-of-

flight vs. accessible energies are depicted in figure 4.3. The measured instrument resolutions from the elastic line is found to be 20 μeV, 70 μeV, and 1.02 meV, respectively. Since at the higher incident energies, the MARI resolution was better than the LET, we did not use the 15.3 meV data from the LET.

IRIS

IRIS being an indirect geometry quasi- and in- elastic neutron scattering spectrometer, have a fixed final energy of 1.845 meV, with the settings used in our experiments. Instrument analyzer reflection settings are named PG002−OFFSET6. In the PG002−OFFSET6 setup, calculated instrument resolution is 17.5 μeV, energy window is from − 1.0 to 2.0 meV, whereas the chopper frequency is set at 50 Hz. The IRIS data integration range was $0 < |Q| < 2$ Å^{-1}. Experiments were repeated at three different temperatures of 1.8 K, 20 K, and 50 K using a Helium flow cryostat. Measured IRIS resolution from elastic line was measured to be 20 μeV. Only the Er_2 and Yb_2 were measured at IRIS. Incident energies, (final energy in case of IRIS), and energy resolutions (both calculated and measured), for all three instruments used are summarized in table 4.1. The INS data reduction, analysis and curve fitting was done using the Mantid and

Table 4.1: Summary of the INS Instruments' Ei's and $FWHM$.

Instrument	$\mathbf{E}_i$	**FWHM Calc**	**FWHM** (elastic peak)
	meV	meV	meV
LET	1	0.02	0.02
LET	2.5	0.07	0.07
LET	15.3	0.9	1.0
MARI	15	0.4	0.65
MARI	25	0.6	0.95
MARI	50	2	2.75
MARI	100	5	5.79
IRIS ($\mathbf{E}_f$)	1.845	0.017	0.018

Mslice softwares, as introduced earlier in the experimental techniques, subsection 2.2.4, while the data plotting was carried out using the MATLAB (2017).

4.3 Er_2 Results

The Er^{3+} ion ground state is $^4I_{15/2}$, and being a Kramers ion its J = 15/2 states are doubly degenerate.

4.3.1 Magnetic measurements

Magnetometry was carried out in the temperature range of 1.8 K to 300 K using a Quantum Design MPMS-XL7 SQUID magnetometer, equipped with a 7 T superconducting magnet. The

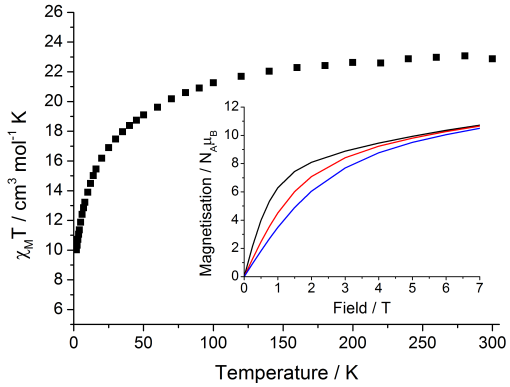

Figure 4.4: Experimental thermal dependence of the χ_MT data for Er_2 measured at a field of 1 kOe. Inset: Magnetization data field-dependence up to 7 T collected at the 2 (black), 4 (red) and 6 K (blue) temperatures.

Er_2 has a room temperature χ_MT product value of 22.9 cm^3 K mol^{-1}, in close agreement with the value for the two isolated $^4I_{15/2}$ Er(III) ions (23.0 cm^3 K mol^{-1}). The resulting curve shows minimal features, with the depopulation of excited CF states resulting in the usual decrease at lower temperatures, figure 4.4. The magnetization data measured up to 7 T at three different temperatures of 2, 4, and 6 K does not saturate, pointing towards the strong magnetic anisotropy, figure 4.4-inset. There is no direct evidence of the magnetic interactions visible from these data.

4.3.2 INS results

The exchange interactions are much smaller than the CF splitting in the Er_2 (as evidenced by the featureless χ_MT data), therefore we should expect to see the local CF transitions in the INS spectra for each magnetic site, possibly broadened by the weaker exchange interactions, when measured for the pure Er_2 species. The INS transitions for the diluted samples were not observed in the INS experiments. This could be explained as the neutrons interact weakly with the matter, so with diluted samples, signal from neutrons is not strong enough to be visible above phonon background. The INS data after the measurement were normalized and corrected with white beam vanadium sample measurements in order to account for the detector efficiency differences. The individual detectors were also checked and any detectors not functioning properly were masked using pre-written python routines in Mantid [110].

All the data we are going to present here have already been corrected for the detector efficiency and normalized with vanadium measurement. The **Q** vs. E maps are used to distinguish between magnetic and non magnetic (phonon) signals, as a first guess. The maps of the INS intensity for the 15 meV and 25 meV incident neutron energies are shown in figures 4.5 left and right panels, respectively. These 2D maps are plotted after the background subtraction, as

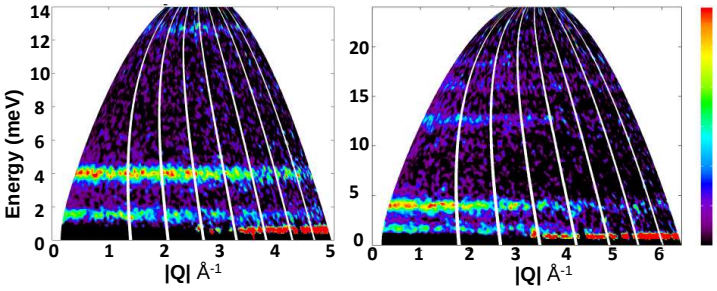

Figure 4.5: The INS **Q**−E plot for Ei = 15 meV (left) and 25 meV (right) after background subtraction. The magnetic signals are clearly visible around 1.5 meV and 4.0 meV (in both panels) while signals at 13 meV, 16 meV, and 18 meV are clearer in the right Ei=25 meV panel. All the magnetic signals fall off quickly with increasing Q, as expected from the magnetic form factor's intensity dependence.

explained in the next paragraph. Inelastic magnetic features are present around 1.5 meV and 4.0 meV energy transfer in both panels, whereas the signals at 13.5 meV,16 meV, and 18 meV are more clearly visible in the right panel of incident energy 25 meV. The scattering intensity is strongest at lower $|\mathbf{Q}|$ values and decays quickly with increasing $|\mathbf{Q}|$, as is expected from the magnetic form factor [F^2 (Q)] dependence of the magnetic scattering intensity. Figure 4.6

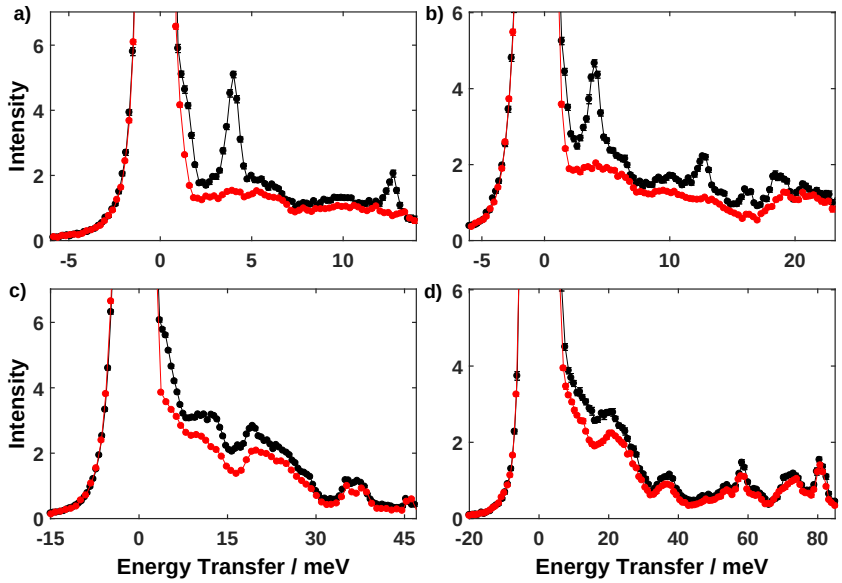

Figure 4.6: INS spectra for Er_2 collected on MARI using incident neutron energies of a) 15 meV, b) 25 meV, c) 50 meV, and d) 100 meV . The Er_2 magnetic signal in black dots is clearly visible when plotted over the red dots of phonon (Lu_2) background.

shows the INS spectra of the incident energies of 15 meV, 25 meV, 50 meV, and 100 meV for the Er_2, filled black circles, and Lu_2 in filled red circles. The data is integrated from $0 < |Q| < 3$

Å^{-1} for both 15 and 25 meV, while for 50 and 100 meV integration is $0 < |Q| < 4$ Å^{-1} and $0 < |Q| < 5$ Å^{-1}, respectively. Since the Lu^{3+} ion has a completely filled f-orbital, it bears no spin or orbital moment, and hence its nonmagnetic. Replacing the Er ion with Lu in the same molecule and measuring it under exactly similar experimental conditions means that we will only get the pure phonon background signal without any magnetic contribution. Therefore, the Lu dimer molecule has been used as a phonon background measure and any signal above this background (black dots and line) should be magnetic in nature (red dots and line). We can see a shoulder at lower energy around energy transfer of 1.5 meV, both in the 15 and 25 meV data. The peaks around 4 meV and 13.5 meV Ei are more pronounced on top of the non magnetic background data. Indeed, we loose the resolution by moving higher in Ei, but there are some magnetic peaks visible around 18 meV and 37 meV .

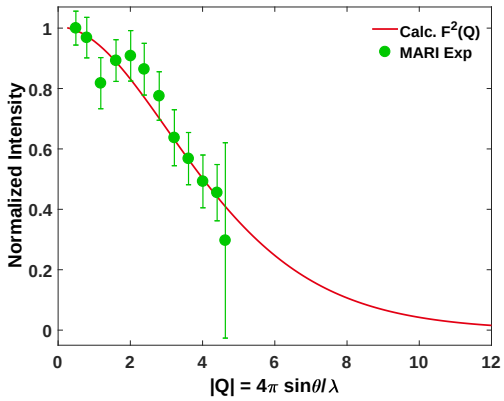

Figure 4.7: An example of the magnetic form factor comparison of Er calculated (red line) and experimental data (green dots). The experimental data is from Ei = 15 meV spectrum, taking a cut in E for the peak around 4 meV .

As anticipated above, another way to ascertain the magnetic nature of a particular peak is via the magnetic form factor. The magnetic form factor F^2(Q) governs the single ion Q-dependence of the magnetic scattering amplitude. In the dipole approximation, where only the lowest spherical harmonics is considered, form factor is independent of the scattering direction. The dipole approximation is reasonable for the smaller momentum transfers. The magnetic form factor is then defined in the formula for dσ/dΩ, as the matrix element is normalized to unity at Q = 0. If the ground state of the ion is precisely known, the magnetic form factor can be calculated using:

$$F^2(Q) = \langle j_0 \rangle + \langle j_2 \rangle \frac{J(J+1) - S(S+1) + L(L+1)}{3J(J+1) + S(S+1) - L(L+1)}, \tag{4.1}$$

where the $\langle j_0 \rangle$ and $\langle j_2 \rangle$ are the functions of the momentum transfer describing the spin and current densities' radial distribution. They usually vary significantly from one magnetic ion to another and have been tabulated [167]. An example of magnetic form factor for Er, both calculated with equation (4.1) by using tabulated values and from the 15 meV INS experimental spectrum (peak around 4 meV) by taking a cut in E, is shown in figure 4.7. The green dots

(experimental data) are clearly in very good agreement with the red line (calculated), and both decrease rapidly with increasing $|Q|$.

Multi-configurational ab initio CASSCF-SO calculations were used to evaluate the CF parameters (CFPs) B_k^q, which can be used in the CF Hamiltonian, as we mentioned in the Steven's formalism section in chapter 1. However, we rewrite it here for clarity

$$\mathcal{H}_{CF} = \sum_{k,q} B_k^q \hat{O}_k^q$$

B_k^q are the Stevens′ crystal field parameters and the $\hat{O}_k^q$ are the Stevens′ operator equivalent of CF potential. The Stevens′ CF parameters B_k^q are always real. Both the metal pockets have low symmetry in this molecule, so the reduction in the number of allowed crystal field parameters (CFPs) using symmetry arguments, is not possible and we are left with no less than 27 free (Stevens) parameters to describe each pocket.

Using these CFPs as an input, we simulated the INS spectra with Mantid CF python interface [111]. Mantid can calculate the energy eigenvalues, eigenvectors, and the Hamiltonian matrix while plotting the CF spectrum at the same time. We further re-scaled and subtracted

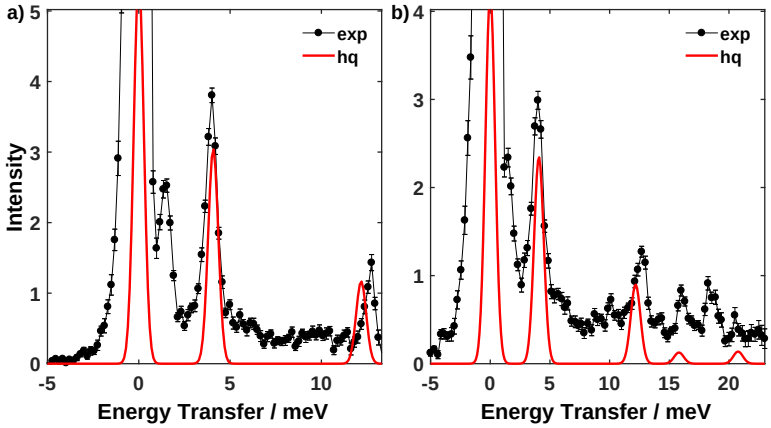

Figure 4.8: INS spectra for Er_2 after phonon background (Lu_2) subtraction plotted with simulated INS spectra for hq pocket based on CASSCF-SO CFPs. a) 15 meV and b) 25meV.

the background from magnetic data, while ensuring that there is no negative data value after the subtraction, using following relation as mentioned before in the experimental procedures:

$$S_{mag}(\mathbf{Q},\omega) = S(\mathbf{Q},\omega) - \rho S_{ph}(\mathbf{Q},\omega)$$

where S_{ph} is the phonon contribution (scattering function for non-magnetic sample analogue), and ρ is the appropriate scaling factor which is chosen to keep the intensity positive after background subtraction. Plotting the subtracted data over the simulated INS spectra for hq pocket based on CASSCF-SO CFPs gives an excellent agreement for both 15 meV and 25 meV data, as shown in the figure 4.8. Comparison with the calculations reveal that the experimental peaks at 32.0 and 102 cm^{-1} (3.97 and 12.6 meV) arise from the hq pocket. These features are well-reproduced both in position and relative intensity and correspond to the transitions to the first

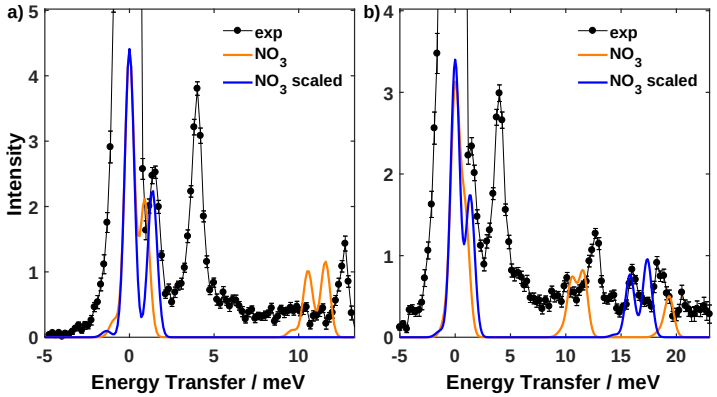

Figure 4.9: INS spectra for Er_2 after phonon background (Lu_2) subtraction plotted with simulated INS spectrum for NO_3 pocket based on CASSCF-SO CFPs. The original unscaled spectra (yellow) is not in good agreement with the experiment while a CFPs scaling factor of 1.5 brings the agreement to an excellent level. a) 15 meV and b) 25meV.

and second CF excited states, respectively. However, it must be noted that there might a slight error in the calculated intensity values among different peaks as we have not accounted for the form factor effect while simulating, and different INS peaks have been measured in different Q ranges. With the peaks at 32.0 and 102 cm^{-1} (3.97 and 12.6 meV) ascribed to the hq pocket, we can directly assign the features at 12.1, 130 and 148 cm^{-1} (1.5, 16.1 and 18.3 meV, respectively) to the NO_3 pocket. However, a measurement at high resolution IRIS spectrometer

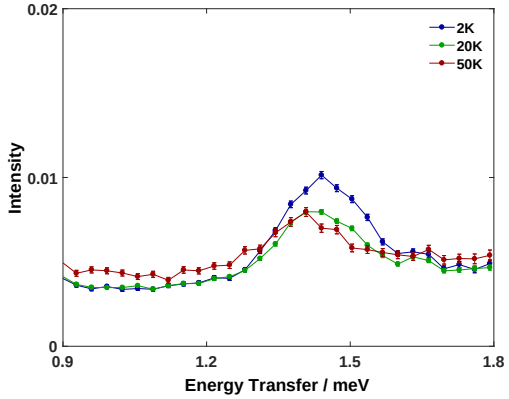

Figure 4.10: INS spectra for Er_2 collected on the IRIS beamline at 2 (black), 20 (red) and 50 K (green), integrated over $0 < |Q| < 2$ $Å^{-1}$ using the neutrons with final energy of 1.845 meV .

places the peak at 11.7 cm^{-1} (1.45 meV) instead of 1.5 meV, when measured at three different temperatures, figure 4.10.

The experimental energies do not agree perfectly with the simulated spectra of the CASSCF-SO calculations for the NO_3 pocket, as indicated by the orange line in figure 4.9. Nonetheless, using a simple scaling factor of 1.5 on the CASSCF-SO CFPs dramatically brings the calcu-

lated energies into agreement with the experimental peak positions, figure 4.9 blue line, where the intensity ratios of the three transitions are also correctly predicted by the simulation. The

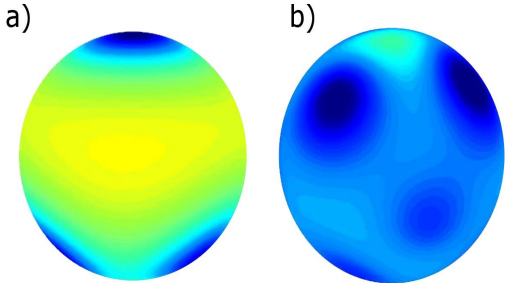

Figure 4.11: Electrostatic potential energy calculated on a sphere of 1.5 Åradius centered at the Er ion considering only the coordinating atoms with formal charges. The color scale between the two pockets is the same and clearly indicates more uniform electrostatic surface for the NO_3 pocket (b), as compared to the hq pocket (a). The vertical direction is aligned along the capping oxide direction (single hq-O bond on top).

scaling factors are often required to improve the matching between ab-initio calculations and the experimental data in lanthanide systems[152, 157, 166]. However, in order to understand the reasons behind the need for the scaling factor only for the NO_3 pocket, we performed the electrostatic potential calculations around the Er ions for both pockets individually. The NO_3 pocket appears to present a near-spherical electrostatic potential, as shown in figure 4.11, thus making the electronic structure particularly sensitive to the local environment. Therefore, the original CASSCF-SO calculations considering the isolated gas-phase molecule may not have described the electrostatic potential with sufficient accuracy. Compounding this sensitivity are the small quadrupole moments of the Er(III) free-ion m_J states, that are likely the origin of generally poor agreement between CASSCF-SO calculations and experimental data for Er compounds. Inclu-

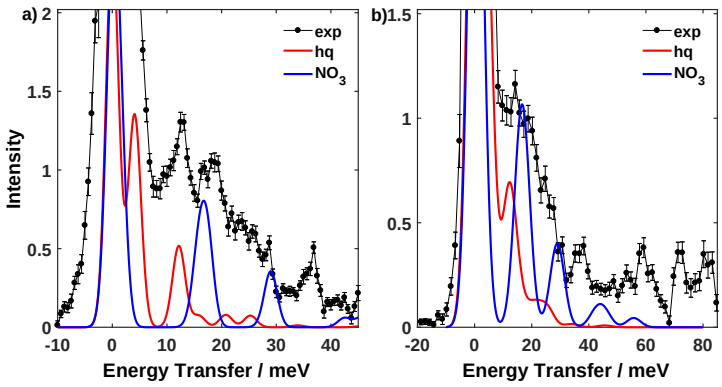

Figure 4.12: INS spectra for Er_2 after phonon background (Lu_2) subtraction plotted with simulated INS spectrum for both pockets based on CASSCF-SO CFPs, with a scaling factor of 1.5 for the NO_3 pocket. a) 50 meV and b) 100 meV .

sion of the two nearest counter-cations into the CASSCF-SO calculations shows a slight increase in the energies of the CF states, and further inclusion of formal point charges within a sphere of 25 Åradius from the active Er(III) site continues to raise their energies. These changes are consistent with the experimental observations, that place three CF excitations at higher energy than originally predicted. We can therefore safely assume that the three INS transitions at 11.7, 130 and 148 cm^{-1} (1.45, 16.1 and 18.3 meV) owe to the first three CF excitations of the NO_3 pocket, and suggest that the discrepancy with theory is due to the subtle electrostatic potential at this site.

We further note that the transition at 1.45 meV is much broader (FWHM= 200 μeV) than the IRIS experimental resolution (18 μeV), which is likely the result of the exchange interactions, vide infra. As we move higher in incident neutron energy, we lose the resolution advantage. Nevertheless, CASSCF-SO calculations also reproduce experimental data at 50 meV and 100 meV incident energies quite remarkably, as shown in figure 4.12. The NO_3 pocket calculation data in

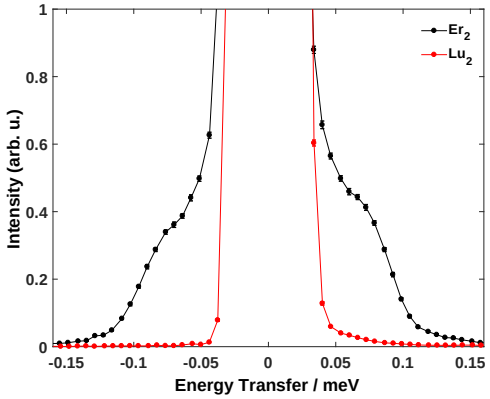

Figure 4.13: INS spectra for Er_2 (black) with Lu_2 spectra (red) collected on LET using incident neutrons of 1.0 meV . Q cuts are integrated as $0 < |Q| < 2$ $Å^{-1}$.

figure 4.12 is also rescaled by a factor of 1.5, as before. The third excited state is now placed at an energy of $\sim$ 234 cm^{-1} ($\sim$ 29 meV), which seems in agreement with one of the weak features observed at higher energy, figure 4.12.

We now turn to the exchange interaction between lanthanide centers to obtain an order-of-magnitude estimate for the magnetic exchange interaction in the pure Er_2 species. We used the power of high resolution LET spectrometer to directly probe the low-lying exchange manifold with INS. Measurements with the LET used 1.0 meV incident energy neutrons and elucidated a broad, cold transition centered at 0.56 cm^{-1} (0.07 meV), as clearly depicted in figure 4.13, that we can assign to the transitions within the low-lying exchange manifold of Er dimer. Hence the exchange interactions are expected to be of the order of 0.6 cm^{-1} from INS and should be visible clearly in the EPR spectra of the pure Er_2 species.
In the next paragraph, we will concisely present the EPR measurements and discuss the results for Er dimers.

4.3.3 EPR spectra and discussion

The X- (∼9.5 GHz) and Q-band (∼34 GHz) EPR spectra were collected, in Manchester, using a Bruker EMX300 spectrometer while the S-band (∼3.8 GHz) spectra was measured with a Bruker Elexsys580 spectrometer. The experiments were carried out on the lightly ground polycrystalline samples, at a temperature of 5 K. To determine the magnetic exchange, we aim to find a model Hamiltonian in the basis of the ground Kramers doublets of the two ions that is able to reproduce these EPR spectra. The anisotropic exchange Hamiltonian, and the Zeeman contribution from the presence of external magnetic field, in the case of pure dimers can be written using equation (1.8), and (1.5), with the underlying assumption that the EPR transitions are induced in the ground multiplet, which can be represented by an effective Hamiltonian given as

$$\mathcal{H}_{ex} = -2\mathbf{J}_{hq} \cdot \overline{\mathcal{J}} \cdot \mathbf{J}_{NO_3} + \mu_B(\mathbf{S}_{hq} \cdot \overline{\boldsymbol{g}}_{hq} + \mathbf{S}_{NO_3} \cdot \overline{\boldsymbol{g}}_{NO_3}) \cdot \mathbf{H}_0, \tag{4.2}$$

where the $\overline{\mathcal{J}}$ are the generalized exchange tensor and J are the total angular momenta encompassing both the spin and orbit momenta part. The $\overline{\mathbf{g}}$ in equation (4.2), is the *effective spectroscopic splitting tensor* given by the g-matrices for each dimer site. From the dilute EPR experiments

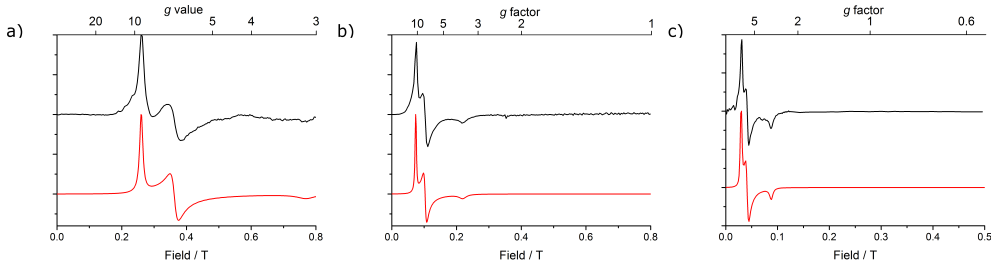

Figure 4.14: Er_2 in Lu_2 EPR spectra (black) and simulations (red) for measured at the 5 K temperature and (a) Q-band 34.055 GHz, (b) X-band 9.543 GHz and (c) S-band 3.875 GHz frequencies. The simulations are performed with EasySpin using the parameters values reported in the text.

we can define the three principal g-values of the Ln pockets. EPR spectra for Er@Lu2 show the three distinct features in all three frequencies, figure 4.14, which were modeled simultaneously using the PHI [168] or EasySpin [169] softwares with a pseudo-spin S = 1/2 model, equation (4.2), with g-values as g_1 = 9.5, g_2 = 6.8 and g_3 = 3.2.

From the calculations with CASSCF-SO the Kramers ground doublets are expected to be markedly different in the two Ln sites. The ground doublet for the hq-pocket is isolated by 32.4 cm^{-1} from the first excited state with the ground state g-values of 13.3, 4.3 and 0.6, whereas a low-lying excited state at 7.3 cm^{-1} for NO_3 pocket could be mixed with the ground state having g-values 11.8, 3.8 and 2.2. The electronic structure of Er(III) appears to be extremely sensitive to even the minute variations in the molecule/site geometry, from the electronic structure calculations. As we stated before that the exchange interactions are expected to be in the order of 0.6 cm^{-1} from the INS experiments, and should be visible in the EPR spectra. Indeed the pure Er specie EPR spectra collected from S-, X-, and Q-bands, exhibit features that are not there in the dilute spectra, indicating the presence of the magnetic interactions clearly, figure 4.15.

Table 4.2: Various parameters optimized for the Er_2 EPR spectra simulation

Parameter	**Value(s)**		
	$\mathbf{J}_x(cm^{-1})$	$\mathbf{J}_y(cm^{-1})$	$\mathbf{J}_z(cm^{-1})$
J	− 0.057	0.45	0.72
	$\boldsymbol{g}_1$	$\boldsymbol{g}_2$	$\boldsymbol{g}_3$
$\boldsymbol{g}_{hq}$	13.3	4.3	0.6
$\boldsymbol{g}_{NO_3}$	9.5	6.8	3.2
	$\alpha(^\circ)$	$\beta(^\circ)$	$\gamma(^\circ)$
$\mathbf{R}(g_{hq})$	−54.9	−80.0	−110
$\mathbf{R}(g_{NO_3})$	3.69	169	45.0
R(J)	54.5 (fixed)	81.3 (fixed)	8.85
	$\mathbf{Iw}_x$(GHz)	$\mathbf{Iw}_y$(GHz)	$\mathbf{Iw}_z$(GHz)
Q-band	4.3	5.1	7.9
X-band	5.0	5.0	3.0
S-band	2.5	4.0	5.5

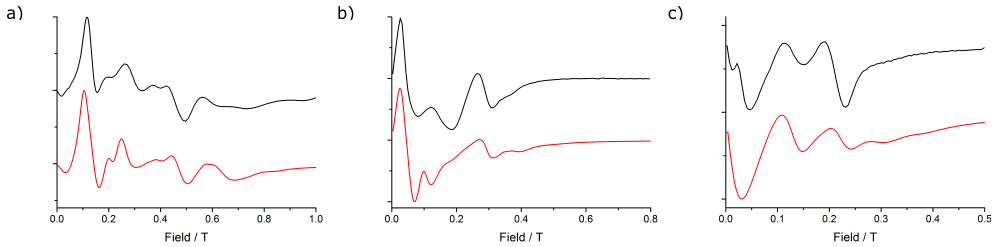

Figure 4.15: Er_2 EPR spectra (black) and simulations (red) measured at 5 K temperature and (a) Q-band 33.980 GHz, (b) X-band 9.5426 GHz and (c) S-band 3.8744 GHz frequencies. The Simulations performed with PHI using the parameters values reported in table 4.2.

For modeling the exchange interaction, we used alternative parameters for the x-, y-, and z-components of $\mathcal{J}$ in the range of -1 to 1 cm^{-1}, which encompass the INS measured exchange. Further allowing the flexibility in the local rotations of the principal g-values yielded the best-fit showing an excellent agreement with the experimental EPR spectra for all three frequencies, figure 4.15 and table 4.2, as well as reasonably good agreement with the magnetization data at low temperatures. The simulations are not sensitive enough to determine the absolute sign and a

simulation of equivalent quality yielded by the inversion of the exchange matrix. The exchange manifold for the Er_2 has an overall energy span of 1.1 cm^{-1} encompassing four singlet states which are mixed to result in non-zero magnetic moment transition matrix element between each pair. The relative intensity profile is generally in good agreement with the lowest energy INS transition detected at ~0.56 cm^{-1}, further supporting the proposed exchange model.

The expected dipolar interaction between the two Er(III) ions within Er_2 can be calculated from the experimental g-values and the orientations. The exchange matrix resulting from these fitted values is given as:

$$\mathcal{J}_{Er_2}^{dip} = \begin{pmatrix} -0.159 & 0.108 & 0.011 \\ 0.376 & 0.269 & 0.186 \\ 0.098 & 0.130 & 0.047 \end{pmatrix} \tag{4.3}$$

In the dipolar exchange matrix $\mathcal{J}_{Er_2}^{dip}$ equation (4.3), the J_{xy} and J_{yy} have the largest values; and are of the same order of magnitude as the fit-determined exchange parameters. Therefore, the dipolar exchange mechanism in Er_2 must be a significant component of the overall exchange interaction.

$$\mathcal{J}_{Er_2} = \begin{pmatrix} -0.057 & 0 & 0 \\ 0 & 0.45 & 0 \\ 0 & 0 & 0.72 \end{pmatrix} \tag{4.4}$$

In this frame of reference, the experimental exchange matrix which accounts for both dipolar and superexchange interactions is diagonal and J_{zz} is its dominant component, equation (4.4). The marked differences between $\mathcal{J}_{Er_2}^{dip}$ and $\mathcal{J}_{Er_2}$ matrices also indicate that the dipolar interactions alone are not enough to fully account for the interaction and the superexchange component is also important.

4.4 Yb_2 Results

The Yb^{3+} ion possesses a ground state of $^4F_{7/2}$, and being a Kramers ion its J = 7/2 states are doubly degenerate.

4.4.1 Magnetic measurements

The Yb magnetometry was also carried out in the same experimental conditions/parameters as described for the Er_2 in the previous section. The Yb_2 has a room temperature χ_MT product value of 5.01 cm^3 K mol^{-1}, in reasonable agreement with the value for the two $^4F_{7/2}$ Yb(III) ions (5.14 cm^3 K mol^{-1}). The resulting curve gradually decreases with the temperature resulting from the excited CF levels depopulation,as depicted in figure 4.16. The magnetization data measured up to 7 T, at temperature of 2 K almost saturates to the values of 3.54 $N_A\mu_B$, figure 4.16-inset, without any evidence of the magnetic exchange in magnetization or χ_MT data.

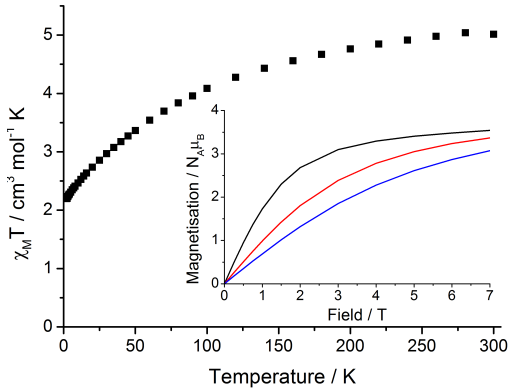

Figure 4.16: Experimental thermal dependence of the χ_MT data for Yb_2 measured at an external field of 1 kOe. Inset: Magnetization data field-dependence up to 7 T collected at the 2 (black), 4 (red) and 6 K (blue) temperatures.

4.4.2 INS results

The Yb dimer INS data after the measurements was corrected and normalized with white beam vanadium measurements to account for the detector efficiency differences, as detailed for Er dimer in previous section. The individual detectors were also checked and any detectors not functioning properly were masked using python routines in Mantid [110]. All the data we are going to present here have already been corrected and normalized with vanadium measurements. Figure 4.17 shows the INS spectra of the incident energies of 15 meV, 25 meV, 50 meV, and 100 meV for the Yb_2, filled black dots, and Lu_2 in filled red dots. The data is integrated from $0 < |Q| < 3$ Å^{-1} for both 15 and 25 meV, while for 50 and 100 meV integration is $0 < |Q| < 4$ Å^{-1} and $0 < |Q| < 5$ Å^{-1}, respectively. Since the measurements with Yb_2 result in very weak magnetic signals over the Lu_2 background, figure 4.17, therefore its not easy to judge the presence of any magnetic peaks this way. Indeed, the simulations of INS spectra using Mantid, based on the CASSCF-SO CFPs predicted much weaker Yb_2 dimers absolute intensity by about 70% as compared to the Er_2 species, as shown in figure 4.18, explaining the results obtained in these experiments.

Using the CFPs from CASSCF-SO calculations as an input, we simulated the Yb_2 INS spectra with Mantid CF python interface [111]. We re-scaled and subtracted the Lu-dimer background from magnetic data, similar to Er_2 case, while ensuring that there is no negative intensity values after the subtraction. We used the same relation as mentioned before:

$$S_{mag}(\mathbf{Q},\omega) = S(\mathbf{Q},\omega) - \rho S_{ph}(\mathbf{Q},\omega),$$

with S_{ph} being the phonon contribution i.e. scattering function for the non-magnetic sample analogue, and ρ is the appropriate scaling factor used during the subtraction. Plotting the subtracted data over the simulated INS spectra for both the hq and rescaled NO_3 pockets based on CASSCF-SO CFPs for both 15 meV and 25 meV data is shown in the figure 4.17, (rescaling is explained in next paragraph). Unlike Er_2 in previous section, the experimental noise and less

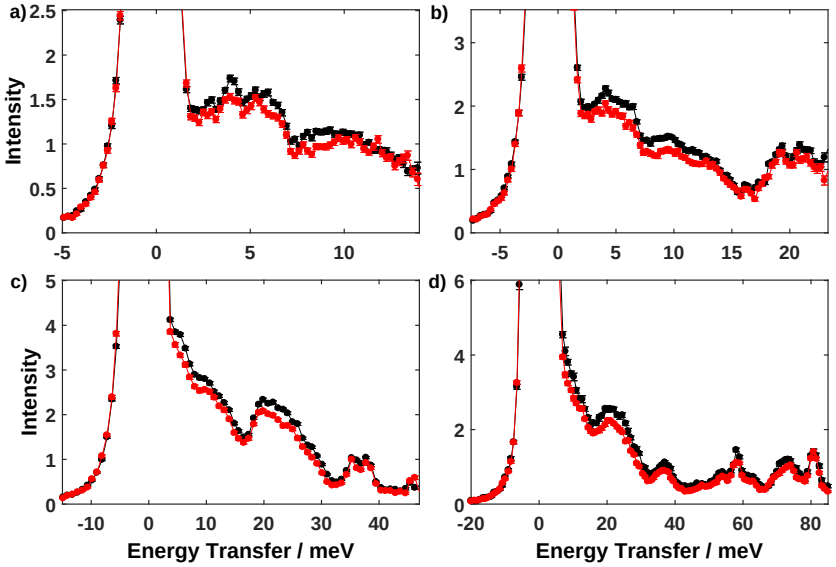

Figure 4.17: INS spectra for Yb_2 collected on MARI using incident neutrons of a) 15 meV, b) 25 meV, c) 50 meV, and d) 100 meV . The Yb_2 magnetic signal in black dots are not very distinctly visible when plotted over the red dots phonon background (Lu_2).

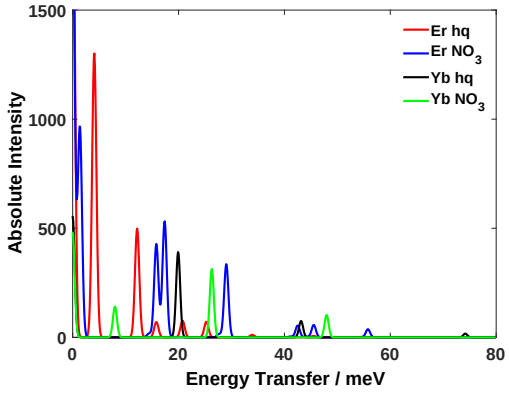

Figure 4.18: Simulations of the INS spectra using mantid, calculated from CASSCF-SO CFPs. Er_2 hq pocket (red) and NO_3 pocket (blue) are clearly much stronger in absolute intensity as compared to the Yb_2 hq pocket (black) and NO_3 pocket (green).

intense magnetic signal from Yb_2 MNM makes it rather difficult to assign distinct magnetic peaks, nonetheless a broad signals is present between $24 - 80$ cm^{-1} (3 - 10 meV).

We employed magnetic field dependent far-infrared (FIR) measurements on the Yb_2 species for the possibility of getting information about the magnetic signal not resolved by the INS. The FIR spectroscopy in the presence of a magnetic field yields a distinct separation between the vibrational and magnetic excitations in a sample. FIR spectra showed a clear magnetic peak at 64 cm^{-1} (8 meV), figure 4.20, which is in agreement with the broad signal from the INS.

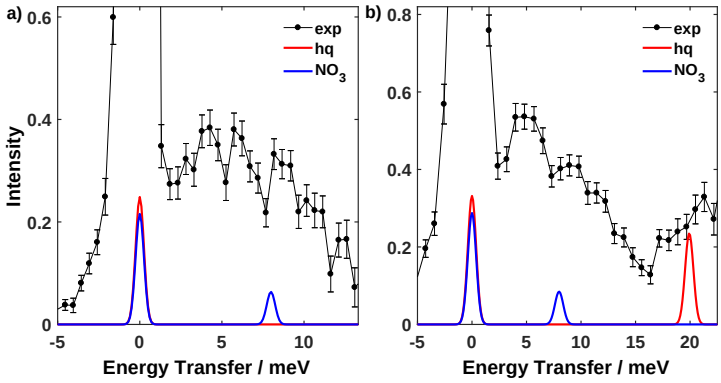

Figure 4.19: INS spectra for Yb_2 after phonon background (Lu_2) subtraction plotted with simulated INS spectra for both pockets based on CASSCF-SO CFPs , with a scaling factor of 1.6 for the NO_3 pocket. a) 15 meV and b) 25meV.

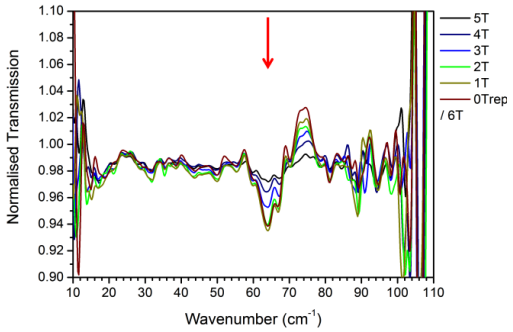

Figure 4.20: Far-IR transmission spectra of the Yb_2 normalized to the 6 T data at 9 K. The red arrow indicates the position of magnetic peak.

The CASSCF-SO had predicted a transition around 40 cm^{-1} emanating from the NO_3 pocket. However, in line with what we observed for the Er_2 specie, the calculated and experimentally observed CF states for the NO_3 pocket are not in excellent agreement. Once again using the exact argument as for the Er_2 NO_3 pocket, we use a scaling factor of 1.6, giving a very good agreement with the experiment. This scaling factor is nearly identical to the one for Er_2. Therefore, we once more speculate that the reason for the need of scaling factor stems from first principle calculations poor description of the electrostatic potential in the gas-phase molecule.

The high energy INS data shows slightly better signal-to-noise ratio for Yb_2, figure 4.21. The weaker magnetic signal might be present around the $160 - 240$ cm^{-1} (20 - 30 meV) and a potential peak in the vicinity of 290 $^{-1}$ (36 meV). CASSCF-SO CFPs simulations after rescaling predict three peaks in the similar energy ranges, originating from the NO_3 pocket. A single magnetic peak at 160 cm^{-1} (19.8 meV) from the hq pocket is expected in the measured energy range; which is consistent with the limited INS experimental data.

To get the order of magnitude estimate for the magnetic exchange interaction between lanthanide centers in the pure Yb_2 species, we used the high resolution IRIS spectrometer and

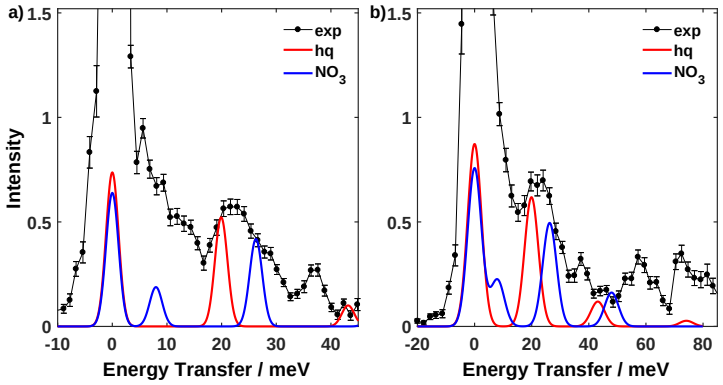

Figure 4.21: INS spectra for Yb_2 after phonon background (Lu_2) subtraction plotted with simulated INS spectrum for both pockets based on CASSCF-SO CFPs, with a scaling factor of 1.6 for the NO_3 pocket. a) 50 meV and b) 100 meV .

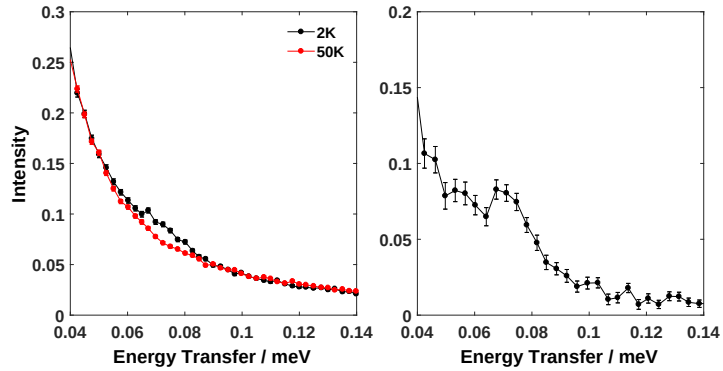

Figure 4.22: The measured INS spectrum for the Yb_2 from the IRIS with final energy of 1.845 meV . The overlay of 5 K and 50 K data is plotted in left panel while their subtraction is shown in the right. Data integration is over the full energy range $0 < |Q| < 2$ Å^{-1}.

measured it at two different temperatures of 2 K and 50 K. As the temperature rises, phonon background rise while the magnetic signal goes down. Consequently, temperature dependent INS measurements have been used to ascertain magnetic nature of a peak/signal. The IRIS Yb dimer spectrum shows a marked shoulder near the elastic line which disappears at higher temperature, as expected from the magnetic peak, figure 4.22. The magnetic peak position after background subtraction seems broadly comparable to the observed Er_2 exchange magnitude, therefore we assumed that the Yb_2 exchange interactions are similar in the order of magnitude to the Er_2 ones. From these arguments, the exchange interactions of the pure Yb_2 species should also be visible unambiguously in the EPR spectra .

4.4.3 EPR spectra and discussion

The X- (∼9.5 GHz) and Q-band (∼34 GHz) EPR spectra for Yb_2 were collected on the lightly ground polycrystalline samples. The experimental conditions and parameters were similar to what described for the Er_2. Once again the aim is to find a model Hamiltonian in the basis of the ground Kramers doublets of the two Yb ions which reproduces the measured EPR spectra and yields the exchange interactions. The anisotropic exchange Hamiltonian and the Zeeman

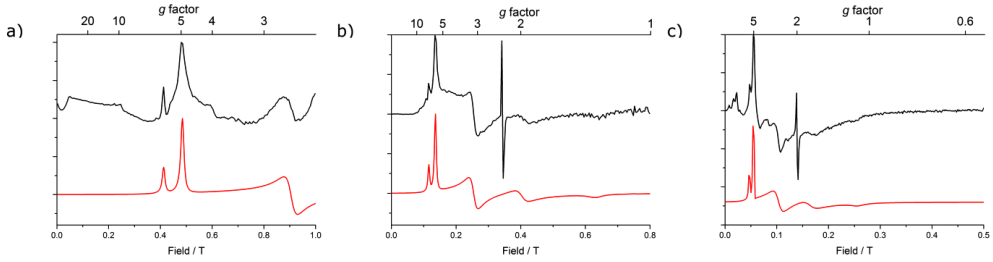

Figure 4.23: Yb_2 in Lu_2 EPR spectra (black) and simulations (red) for measured at the 5 K temperature and (a) Q-band 33.98 GHz, (b) X-band 9.543 GHz and (c) S-band 3.874 GHz frequencies. The simulations are performed with EasySpin using the parameters values reported in the text. The spike at $g \approx 2$ comes from the impurities in the EPR tube while the spurious signals are observed at Q- and S-band near the zero field.

contribution from the presence of external magnetic field, in the case of pure dimers is given by equation (4.2), with the assumption that the EPR transitions are induced in the ground multiplet. From the diluted EPR experiments we can define three principal g-values for the individual pockets. The EPR spectra of Yb@Lu_2 clearly resolve two g_1 features, two g_2 features and a weak, broad g_3 feature, while the hyperfine interactions for ^{171,173}Yb nuclei were not resolved. Modeling these spectra as two non-interacting effective spin S = 1/2 states, with g-values of g_1 = 5.0, g_2 = 2.7 and g_3 = 1.1 for NO_3 pocket doublet, and g_1 = 5.9 and g_2 = 1.7 for hq pocket doublet, the results are in an excellent agreement with the experimental data, figure 4.23. Although we have not observed g_3 from the hq pocket in EPR measurements.

From the calculations with CASSCF-SO, the Kramers ground doublets are expected to be markedly different in the two Ln sites as the ground doublet for the hq-pocket is well isolated by 140 cm^{-1} from the first excited state with the experimental ground state g-values of 5.9, 1.8 and third not observed. While the low-lying excited state at 30 cm^{-1} from the ground state, for NO_3 pocket is also well separated with experimental g-values of ground state as 5.8, 2.4 and 1.0. The electronic structure of Yb(III) NO_3 pocket is appears extremely sensitive to even minute variations in the molecule/site geometry, whereas the hq pocket seems relatively less affected by these variations, from the electronic structure calculations. As we have noted before, the exchange interactions are expected to be similar in order of magnitude as for Er_2 from the INS experiments and should in principle be visible in the EPR spectra. Indeed the pure Yb specie EPR spectra collected from S-, X- and Q-band at 5 K is highly structured, figure 4.15. Like before, the parameters for the x-, y-, and z-components of $\mathcal{J}$ were alternated in the range -1 to 1 cm^{-1} encompassing the INS estimated exchange. Moreover, allowing flexibility in the

Table 4.3: Various parameters optimized for the Yb_2 EPR spectra simulation.

Parameter	**Value(s)**		
	$\mathbf{J}_x(cm^{-1})$	$\mathbf{J}_y(cm^{-1})$	$\mathbf{J}_z(cm^{-1})$
J	− 0.25	0.25	0.72
	g_1	g_2	g_3
g_{hq}	5.9	1.8	0.5
g_{NO_3}	5.0	2.7	1.1
	$\alpha(^\circ)$	$\beta(^\circ)$	$\gamma(^\circ)$
$\mathbf{R}(g_{hq})$	−36.9	−78.1	86.8
$\mathbf{R}(g_{NO_3})$	16.6	− 60.0	85.0
R(J)	54.5 (fixed)	81.3 (fixed)	8.5
	$\mathbf{Iw}_x$(GHz)	$\mathbf{Iw}_y$(GHz)	$\mathbf{Iw}_z$(GHz)
Q-band	2.9	1.6	3.5
X-band	1.2	0.8	3.6
S-band	0.4	1.2	2.2

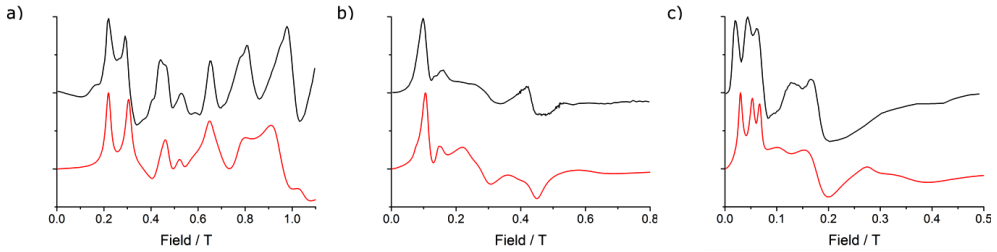

Figure 4.24: Yb_2 EPR spectra (black) and simulations (red) measured at 5 K temperature and (a) Q-band 34.074 GHz, (b) X-band 9.564 GHz and (c) S-band 3.875 GHz frequencies. The simulations are performed with PHI using the parameters values reported in table 4.3.

local rotations of the principal g-values yielded the best-fit showing an excellent agreement with the experimental EPR spectra for all three frequencies, figure 4.24 and table 4.3, as well as reasonably good agreement with the magnetization data at low temperatures. The simulations were not sensitive to the absolute sign and an equivalent quality simulation was obtained by the inversion of exchange matrix. The exchange manifold for the Yb_2 has an overall energy span of 0.54 cm^{-1} including two singlet states and one doublet state. The largest transition probability

of magnetic moment is from second to the third excited state with calculated transition energy in good qualitative agreement with the INS exchange shoulder for the Yb_2 measurement at IRIS spectrometer.

The dipolar interaction between the two Yb(III) ions within Yb dimer can be calculated from the experimental g-values and the orientations, similar to what we did for the Er_2. The exchange matrix resulting from these fitted values is given as

$$\mathcal{J}^{dip}_{Yb_2} = \begin{pmatrix} -0.034 & 0.014 & -0.011 \\ 0.034 & -0.091 & 0.061 \\ 0.007 & -0.014 & 0.019 \end{pmatrix} \tag{4.5}$$

The elements of the calculated dipolar interaction matrix for Yb_2, in the diagonal frame of reference are much smaller than their Er_2 counterparts, due to the lower value of Yb_2 magnetic moment.

$$\mathcal{J}_{Yb_2} = \begin{pmatrix} -0.25 & 0 & 0 \\ 0 & 0.25 & 0 \\ 0 & 0 & -0.29 \end{pmatrix} \tag{4.6}$$

Thus the dipolar exchange interaction in the Yb_2 is significantly weaker than the total exchange coupling from the fit, equation (4.6). Hence the magnetic interaction within Yb_2 are dominated by the superexchange interactions.

4.5 Dy_2 Results

The Dy^{3+} ion ground state is ${}^6H_{15/2}$, and being a Kramers ion its J = 15/2 states are at least doubly degenerate.

4.5.1 INS Results

While measuring INS spectra of the Dy dimer, a huge problem often encountered is the large neutron absorption cross-section of Dy ion at the natural abundance. Indeed, from the table 4.4,

Table 4.4: Examples of some neutron absorption cross sections (in barns) for natural abundance.

H	**Cr**	**Mn**	**Fe**	**Y**	**La**	**Nd**
0.33	3.05	13.3	2.56	1.28	8.97	50.5
Tb	**Dy**	**Ho**	**Er**	**Yb**	**Lu**	
23.4	994	64.7	159	34.8	74	

it is clear that the neutron scattering experiments with compounds of Dy are even more difficult than the other Ln ions due to its large neutron absorption cross section [170]. However, we were able to measure INS spectra for the Dy-dimer MNM with reasonable magnetic signal strength. As before, the Dy_2 INS data after the measurements was also normalized and corrected with white beam vanadium sample measurements for the detector efficiency differences, while the individual detectors were also checked and masked when needed using the python scripts in Mantid. All the data presented here onwards have already been corrected for the detector

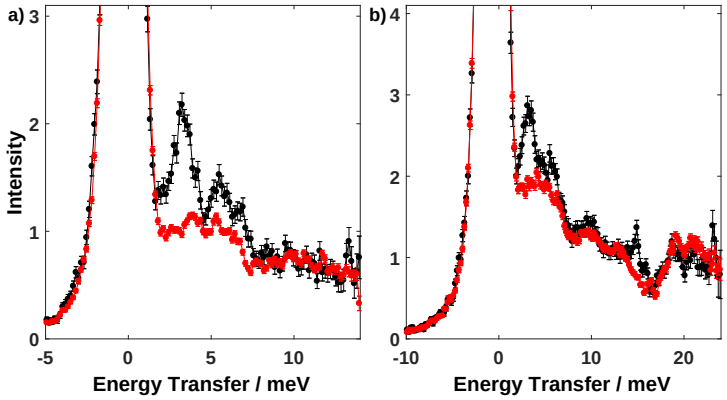

Figure 4.25: INS spectra for Dy_2 and Lu_2 collected on MARI using incident neutrons of a) 15 meV and b) 25 meV . The Dy_2 magnetic signal in black dots is visible over the red dots phonon background (Lu_2).

behavior and the vanadium measurement normalization.

Figure 4.25 presents the INS spectra of the incident energies of 15 meV and 25 meV for the Dy_2, filled black circles, and Lu_2 in filled red circles. The data is integrated from $0 < |Q| < 2.5$ Å^{-1} and $0 < |Q| < 3$ Å^{-1} for 15 and 25 meV, respectively. The magnetic peak around 3 meV is clearer on top of the non magnetic background data, while the peaks around 5 meV and 7 meV, though weak, are also present. In the 25 meV spectrum there seems to be a magnetic signal around 15 meV as well. We loose in the resolution by moving higher in the incident energy of neutrons and the magnetic peaks are not distinctly resolved in 50 meV data, figure 4.26. Nevertheless, there are weak magnetic signals around 20 meV and 37 meV energy transfer. In order to better illustrate the magnetic signal, we re-scaled and subtracted the background from the magnetic data, while ensuring to avoid the negative intensity data post subtraction, using the same relation as mentioned before

$$S_{mag}(\mathbf{Q},\omega) = S(\mathbf{Q},\omega) - \rho S_{ph}(\mathbf{Q},\omega),$$

with S_{ph} is the phonon contribution, the scattering function for non-magnetic sample analogue, and ρ is the appropriate scaling factor employed, as previously for Er_2 and Yb_2 data. Furthermore, we use the CFPs from CASSCF-SO calculations as an input to simulate the Dy_2 INS spectra with Mantid CF python interface. Plotting the subtracted data over the simulated INS spectra for both hq and rescaled NO_3 pockets based on CASSCF-SO CFPs for both 15 meV and 25 meV data, as shown in the figure 4.27, shows distinct broad peaks at 3.2 meV and 15 meV .

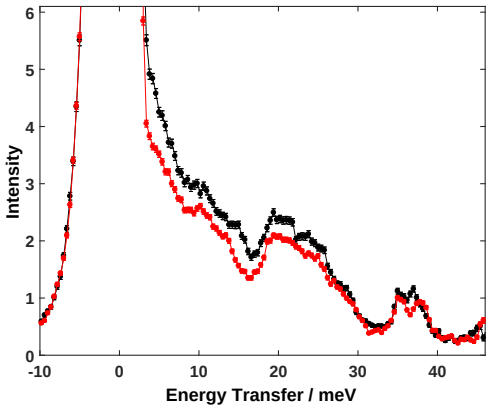

Figure 4.26: INS spectrum of Dy_2 collected on MARI using incident neutrons of 50 meV plotted over the Lu_2 as background. The Dy_2 magnetic signal is in black dots while the red dots are the phonon background (Lu_2).

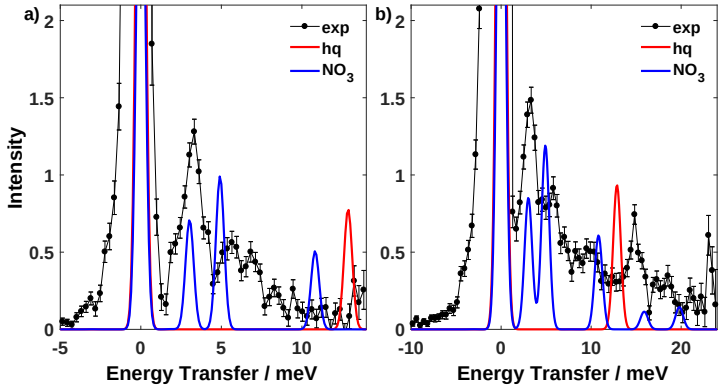

Figure 4.27: INS spectra for Dy_2 after the phonon background (Lu_2) subtraction plotted with simulated INS spectra for both pockets (hq as red and NO_3 as the blue line) based on CASSCF-SO CFPs, using a scaling factor of 1.6 for the NO_3 pocket. a) 15 meV and b) 25meV.

While the peaks are 5.5 meV, 7 meV, and 10 meV are relatively weak. The scaling factor of 1.6 was used for the NO_3 pocket from [166], using the same arguments as for the Er_2 and Yb_2. The speculation is that the need for the scaling factor arises from the poor description of the spherical electrostatic potential at the NO_3 pocket.

Clearly, the CASSCF-SO calculations are still not as helpful to simulate the Dy dimer CF spectra as they were in the Er dimer case, as presented in section 4.3. The calculations could not reproduce a good match in both the peak positions and intensity with the experimental INS data. It is worth mentioning that the first-principle generated CF parameters used here were further optimized and they are different than what our colleagues in Manchester used earlier [166], although we checked with the published values and did not find a good match using those parameters as well. Since the CASSCF-SO calculations are ab-initio, and though powerful, they don't take any initial parameters as an input, therefore if the simulations fail to produce a good

agreement with the experiment, one is practically left helpless to improve the fit/match. Same is the case for Dy dimer here, as due to the low symmetry of the molecule, we have to deal with no less than 27 free (Stevens) parameters, and in practice we cannot do much to further optimize the fit. In order to overcome the overparameterization problem and to understand the reasons

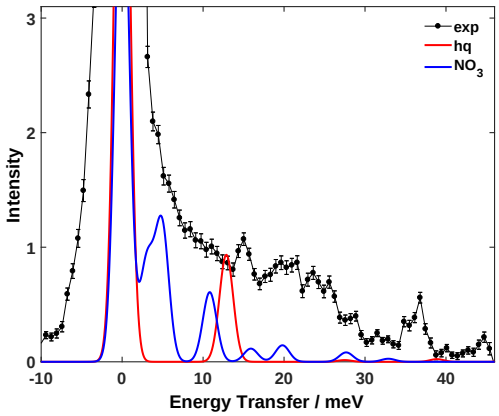

Figure 4.28: INS spectrum for Dy_2 at E_i = 50 meV after the phonon background (Lu_2) subtraction plotted with simulated INS spectrum for both pockets based on CASSCF-SO CFPs, with a scaling factor of 1.6 for the NO_3 pocket.

behind this discrepancy, a very simple but effective strategy we are using is the point charge modeling approach, see below.

From the background subtracted 50 meV data in addition to a peak at ∼15 meV energy transfer, a magnetic peak around 37 meV is clearly resolved whereas a broad signal between $18 - 27$ meV is also present, figure 4.28. Once again, CASSCF-SO generated CFPs when

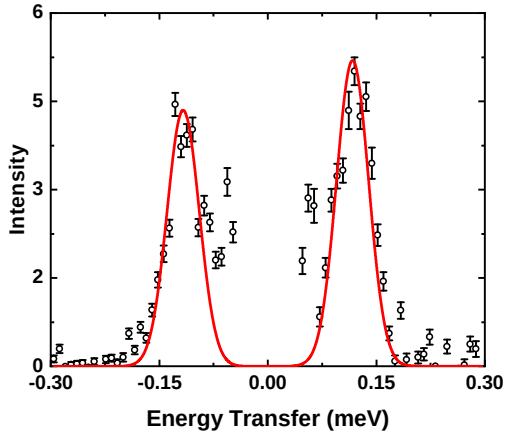

Figure 4.29: The measured INS spectrum for the Dy_2 from the LET with incident energy of 1 meV, after the background (Lu_2) subtraction. Data integration is $0 < |Q| < 2$ Å^{-1}. The red line is the gaussian fit and a guide to the eye.

simulation does not reproduce both of larger magnetic signals.

To get the order of magnitude estimate for the magnetic exchange interaction between lanthanide centers in the pure Dy_2 species we used the high resolution LET spectrometer at low energy (1 meV) incident neutrons. Figure 4.29 shows the Dy_2 exchange splitting after background subtraction, with a clear magnetic peak both on the neutron energy gain and loss sides. From the gaussian fit, the peak position is placed at 0.97 cm^{-1} (0.12 meV) and the peak width

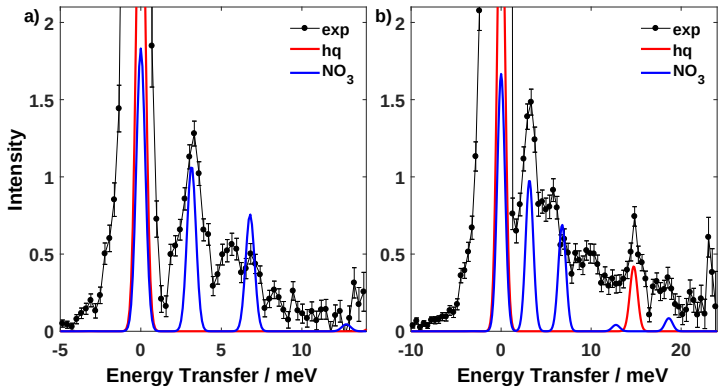

Figure 4.30: INS spectra of the Dy_2 after the phonon background (Lu_2) subtraction plotted alongside the effective point charge modeling calculated spectra for both pockets, hq red and NO_3 as the blue line, with a) 15 meV and b) 25meV.

is larger than the elastic line width. As mentioned before, our colleagues in Manchester have previously studied Dy_2 MNM using the CASSCF calculations, EPR and FIR spectroscopies, as reported in [166]. INS determined exchange splitting is quite close to the value of what they estimated from EPR experiments and simulations. INS Crystal field data, however does not seem to be in good agreement with the calculations, with or without rescaling.

4.5.2 Effective point charge modeling

We are employing a simpler approach than the first-principle calculations discussed above, for the modeling of Dy_2 MNM. It is a semi-empirical approach to combine the spectroscopic data with a simple point-charge electrostatic model (PCM) improved by semi-empirical models, for the interpretation of the CF splittings [171]. As compared with the first principle based approach, this method enables intuitive comparisons among various derivatives of same molecular families, allowing for the extrapolation of CF effects of each specific type of ligand. Furthermore, the effective PCM allows a better control at the computational parameters.

The PCM approach starts with taking into account the CF experienced by a lanthanide ion due to the coordinated ligand atoms at a positions R. The effect of covalency is taken into account empirically by tuning just a couple of parameters, namely the effective metal-ligand distance D which in turn is controlled by changing R, and the effective phenomenological electric charge q of the ligand. The goodness of the model then is judged by fitting it to the experimental INS, χ_MT and/or magnetization data. This model has been successfully applied to describe the magnetic behavior of several lanthanide SMMs where the metal-ligand distance parameter D

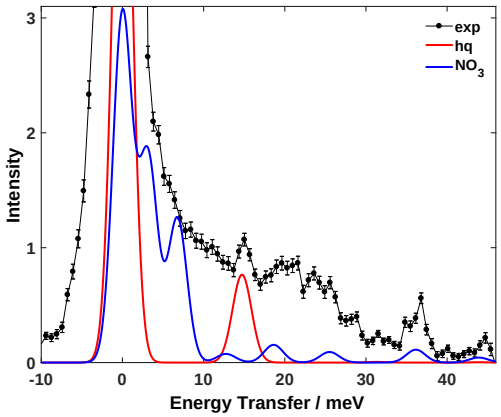

Figure 4.31: INS spectra of the Dy_2 at E_i = 50 meV after the phonon background (Lu_2) subtraction, plotted alongside the effective point charge modeling calculated spectra for both pockets, hq as red and NO_3 as the blue line.

and the effective charge q were found to be transferable between various lanthanide complexes that share equivalent ligation [172]. In this model, we are employing a multi-step optimization strategy for which several Matlab programs are written to help in running, fitting and visualizing the calculations with *SIMPRE* software package [173].

Looking again at the structural diagram 4.1, there are three NO_3 ligands exclusively attached to the Dy in the lower (NO_3) pocket, while three hq−O ions are shared between two Dy-ions in both pockets. The upper Dy has four N ions coordinated to it in the equatorial plane while

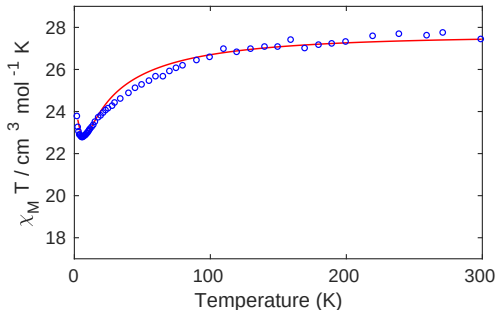

Figure 4.32: Experimental (black circles) and calculated (red line) χ_MT data is plotted as a function of temperature. The calculations are performed from the effective point charge modeling, as described in the text.

a single hq−O atom is axially sitting on top of this Dy. From this description, we can separate these ligands into several groups, and to model the PCM we must establish D and q for all of them. This modeling strategy is still ongoing at the time of this writing, nevertheless, we present a brief overview of the optimization procedures we have adopted. The displacement value of the NO_3 ligand is already known from the literature and used as reported in [174], while hq-O was

calculated using the relation [175]:

$$D = \left(\frac{CN}{V_M}\right) \frac{1}{E_M(E_L - E_M)}, \tag{4.7}$$

where CN is the coordination number, V_M the metallic valence, while E_M and E_L are the Pauling electronegativities for the metal and ligand, respectively. Next we systematically varied the effective charge on the hq and NO_3 ligands for achieving a minimal deviation between the calculated single ion energy levels of Dy at NO_3 pocket and the experimental (INS) data. Following the first step, a step-by-step variation of the exchange parameter (J) and the effective charge on N ions (hq pocket), resulted in the minimum deviation between the calculated and the experimental INS and the low temperature χ_MT data. Finally, taking into account the optimized (Dy-Dy) exchange interaction, the effective charge on both the sites sequentially fine-tuned, to get a best fit between the experimental and calculated INS and χ_MT data.

The preliminary results from this effective PCM are presented in figures 4.30 (for E_i = 15 and 25 meV) and 4.31 (for E_i = 50 meV). The CF parameters calculated by SIMPRE are used in Mantid to simulate the INS CF spectra. Clearly, with a minimal computational cost as compared to the ab-initio calculations, we have already achieved a reasonable agreement between two significant INS peaks at ∼4 meV and 13.5 meV emanating from NO_3 and hq pockets respectively. Furthermore, our model also places a peak from NO_3 pocket at ∼37 meV, observed in the INS 50 meV incident energy spectrum. The weak features between 18-27 meV from INS are also well reproduced by our modeling, figure 4.31. Using the same PCM parameters to simulate the χ_MT data reproduces the observed experimental features quite nicely, as shown in figure 4.32.

Nonetheless, there are still features missing from INS data e.g. around 5 meV, and the fit is to be performed on the χ_MT data as well, although we suspect that we are not very far from the correct model. The optimization of fit and improving the CF modeling are still underway at the time of this writing.

4.6 Conclusions

In this chapter, a direct measurement and the modeling of the magnetic interactions between highly anisotropic Ln-ions in the asymmetric dimer molecular nanomagnet, was presented. Three different INS spectrometers were utilized to fully harness the power of inelastic neutron scattering enabling us to elucidate the crystal field structure and the exchange interactions of few Kramers analogues of this dimer family. INS results were aided by magnetization measurements and FIR spectroscopy, the latter only in some cases.

For the Er_2 and Yb_2, the CASSCF-SO calculations were used to compute the crystal field parameters and simulate the initial estimates of the local magnetic properties of individual sites. The high resolution INS provided the energy span of the exchange splitting while the experiments and simulations of the multi-frequency EPR spectra of the pure and diluted species enabled g-values determination as well as provided the direct measurement of the exchange interactions. Our results reveal that the dipolar interactions are a significant component of the magnetic interactions in Er_2, although they do not account for all the experimental features.

On the other hand, superexchange interactions are dominant in the Yb dimer and the dipolar interactions are much weaker.

The Dy_2 crystal field and exchange interaction were also elucidated by the INS spectroscopy. These results, along with χ_MT data, are being analyzed and modeled using an effective point charge modeling approach. Preliminary results have been presented here, while this effort is still going on at the time of this writing.

Chapter 5

Dysprosocenium SIM

5.0 Introduction

The progress towards the SMMs with high blocking temperatures, for storing information in single molecules, has been rather slow since the advent of first SMM $Mn_{12}Ac$ [4]. The discovery that Ln-based single-ion systems can display an SMM behavior opened a new research direction, with the synthesis of systems displaying magnetic hysteresis up to 14 K in a Tb-based SMM (or SIM), at a stable magnetic field sweep rate of about 20 Oersted per second (Oe s^{-1}) [147]. The situation changed abruptly in 2017 with the dysprosocenium SIM compound, for which Goodwin at al demonstrated the record blocking temperature of 60 K [23]. They observed the slow relaxation dynamics of the SIM up to 60 K for highly-diluted samples, demonstrating that the hysteresis is indeed of molecular origin. Their investigations were supported by first principle calculations and they tentatively ascribed the origin of hysteresis to intra-molecular vibrational modes localized between the Ln-ion and the ligand. However, a detailed study of relaxation dynamics and spin-phonon interaction was still missing.

Guo et al. independently reported the synthesis and magnetic properties of same dysprosium metallocene, around the same time [24]. They recorded an anisotropy barrier reaching up to 1277cm^{-1} (1837 K) in zero applied field at a magnetic field sweep rate of 39 Oe s^{-1}. These discoveries brought the state-of-the-art in the information storage at a molecular level based on SMMs very close to liquid nitrogen temperature operation (77 K), which is considered the initial target for the real-case applications. In a paper published in October 2018 Layfield group have in fact reported the synthesis of a dysprosium metallocene complex displaying magnetic hysteresis up to 80 K [22].

In the present chapter we outline the preliminary results of the ^{1}H-NMR experiments carried out on dysprosocenium SIM single crystals, mostly aimed at studying its relaxation dynamics. The author of this thesis and Prof. Giuseppe Allodi performed all the NMR experiments and data analysis outlined in this chapter.Since the analysis is still on-going, the modeling and interpretations presented here are preliminary.

5.1 Material Synthesis and Characterization

Synthesis and structural characterization of samples was performed by the Prof. D. Mills and Dr. N. Chilton's groups in Department of Chemistry, University of Manchester (UK). The dysprosocenium (Dy-cene) SIMs molecular formula is $[Dy(Cp^{ttt})_2][B(C_6F_5)_4]$, where the Cp^{ttt} is $\{ C_5H_2^tBu_3-1,2,4 \}$ and the $^tBu = C(CH_3)_3$ [23]. The Dy-cene crystals were bright yellow, they are air sensitive and must be stored below $-30°C$. Lanthanides with an oblate distribution of the electronic clouds, which can be induced by placing organic ligands at axial positions, have been considered particularly favorable for the generation of large magnetic anisotropy [147]. These Ln-ions include the terbium, dysprosium, and holmium. However, often-encountered presence of spherically distributed coordinating ligand atoms around the Ln-ions strongly reduces the magnetic anisotropy of the Ln-SIMs. The uniqueness of Dy-cene molecular structure is the absence of these ligands in the immediate surrounding of the Ln-ion, thus providing robust magnetic bistability up to temperature of 60 K. Structure diagram of Dy-cene is shown in figure 5.1.

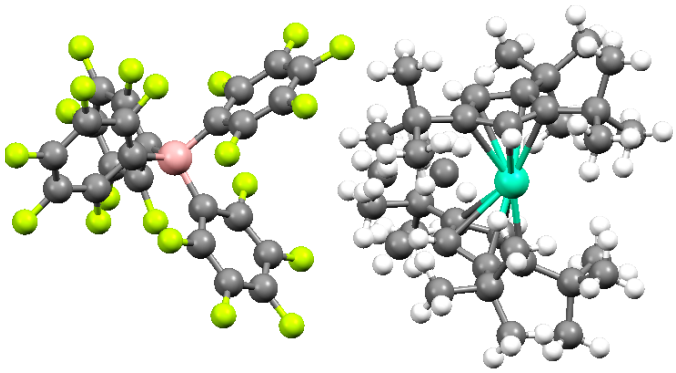

Figure 5.1: Molecular structure of dysprosocenium SIM molecule with counterion shown on the left. Color code: Cyan, Dy; yellow, F; salmon pink, B; gray, C; and white, H.

On left hand side in the figure, is the counterion used to maintain the net electrical neutrality against the metallocenium cation. The counterion contains boron ion at the center surrounded by fluorine and carbon atoms.

Using first principle calculations Goodwin and coworkers proposed that the unique coupling of the atomic vibrations (phonons) with the molecular magnetic moment of the Dy-ion inside the crystal lattice, could be a possible explanation for the remarkable properties of the Dy-cene. Clearly, further studies to understand the phonon-induced relaxation dynamics are required. NMR is an ideal probe to study the evolution of magnetization relaxation in MNMs, as previously proposed [176], and successfully demonstrated by several studies e.g. the theses [92, 93].

5.2 NMR Experimental Details

Conventional echo-detected NMR experiments were carried out on single crystals of dysprosocenium SIMs employing the HyReSpect spectrometer applying a field of 4 T. The NMR spectra

were recorded using the standard Hahn echo sequence with pulses, as detailed in section 2.1, measuring the echo amplitude point-by-point at discrete frequency steps at a temperature of 4 K. As mentioned before, the samples are air-sensitive and must always be kept below $-30°$C, each single crystals was suspended inside the eicosane ($C_{20}H_{42}$) gel and sealed inside a glass tube of about 1 cm length. However, because of the large presence of ^{1}H in the eicosane, a high unwanted NMR signal at the proton resonance (I = 1/2, gyromagnetic ratio 42.557 MHz/T) was recorded in the first set of experiments. Therefore, in the second set of experiments deuterated cyclohexane (C_6D_{12}) gel was used instead, which significantly reduced the unwanted ^{1}H echo signal. The samples were sealed inside a 3 mm quartz tube of length around 1-1.5 cm. Due to the coupling of nuclear spins with the dipolar field of magnetic Dy ions, a broad proton spectra was recorded. Moreover, a nearly as broad ^{19}F spectrum from ^{19}F nuclei (I=1/2, gyromagnetic ratio 40.05 MHz/T) was detected, centered on the ^{19}F reference frequency and partly overlapped to the ^{1}H spectrum. This was expected due to the presence of a large number of F atoms in the molecule formula from the cation, as shown in the structural diagram 5.1.

For both sets of experiments, we recorded the ^{1}H relaxation rates, 2 MHz away from the ^{1}H central resonance frequency i.e. we sampled a fraction of nuclei experiencing a longitudinal dipolar field of approx. 500 G, hence close enough to the magnetic ion (vide infra). The relaxation rates were measured by using the saturation-recovery method, by applying a comb of pulses to excite and saturate the system and recording the magnetization recovery with the same standard echo pulse sequence as for the NMR spectra, against a variable delay time between the exciting pulse train and the measurement sequence. The longitudinal relaxation rate measurements were carried out by varying both the magnetic field and temperatures. Spin-spin relaxation rates ($1/T_2$) were also measured above the temperature where the hysteresis disappears. The T_2 time was obtained by fitting the amplitude of the spin echo, produced by the same sequence employed for the NMR spectra, to a single exponential decay law as a function of the varying delay between the two pulses, equation (2.11).

5.3 NMR Results

The nuclear species in dysprosocenium SIM which can be in-principle measured with NMR include dysprosium, hydrogen (protons), fluorine (on the counter-ion), carbon and boron. However, in practice not all of these nuclei are 'good' candidates. dysprosium has two NMR active nuclei, ^{161}Dy and ^{163}Dy, both with a nuclear spin I = 5/2. At first, we attempted to measure the Dy NMR signal up to our instrument limit of 800 MHz frequency but the absence of signal indicated that Dy transition frequencies fall outside of the accessible frequency range for our spectrometer. We then reverted to measuring the resonances of the other two available good nuclei, ^{1}H and ^{19}F. These nuclei are coupled to the Dy electronic spin by the dipolar interaction. The dipolar field intensities are in the other of 1 kG and several hundred G for ^{1}H and ^{19}F, respectively. Their exact values and directions depend on the positions of the nuclear probes relative to the magnetic ions. The presence of a large number of inequivalent H and F sites in the crystal then gives rise to a broad field distributions. Such internal fields are too weak and inhomogeneous to allow zero-field NMR (e.g. in MnFePSi compounds, chapter 6 of this thesis) or NMR in the spontaneous field perturbed by a moderate external field (e.g. in Yb(trensal)

chapter 3 of this thesis), and much stronger external fields must be applied. In this experimental condition, broad ^{1}H and ^{19}F spectra centered around their reference frequencies in the given external field are detected, with line shapes arising from the distributions of the secular (i.e. longitudinal) components of the dipolar fields.

The sample was cooled down in an applied magnetic field of 4 T and measured at 4 K keeping the field fixed. The resulting spectra is shown in figure 5.2. The large signal visible

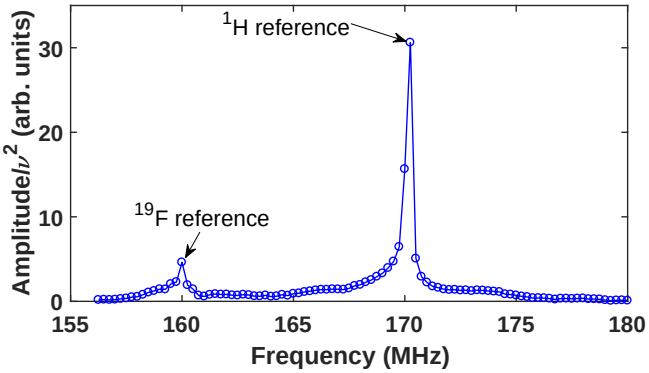

Figure 5.2: Spectrum targeted at ^{1}H and ^{19}F inside the Dy-cene SIM at 4 K temperature collected using a standard Hahn sequence in an applied field of 4 T, with the sample vial in the first rotation in the xy-plane. The strong peaks labeled in the figure are zero-shift ^{1}H and ^{19}F resonances, as explained in the text.

at the ^{1}H zero-shift resonance frequency in 4 T i.e. $\sim$170.2 MHz, is due to protons that are not affected by the dipolar field, whereas the signal from the protons coupled to Dy ions, is highly broadened around this frequency (the spectral tails extend up to $\pm$ 10 MHz). The high

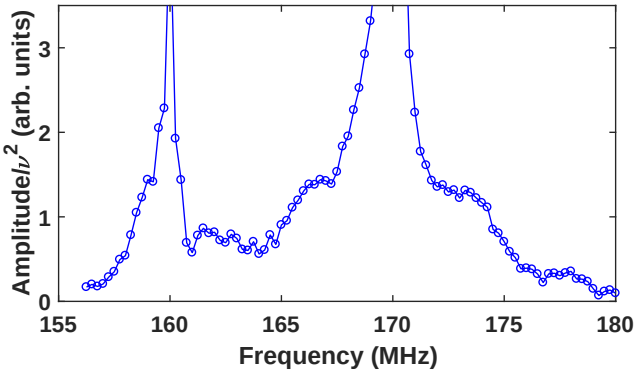

Figure 5.3: Vertical zooming of figure 5.2, showing the spectral components with shift, i.e. a large dipolar coupling to the Dy ion.

number of protons in the eicosane gel (with chemical formula $C_{20}H_{42}$), are responsible for this non-broadened signal in the spectrum. Furthermore, another intense signal is detected close

to the ^{19}F reference frequency, equal to 160.2 MHz in 4 T applied field. The ^{19}F signal was verified to be due to the sample itself by performing the measurements with an empty probe. Nonetheless, vertical magnification of figure 5.2 reveals a broad and featured spectra of ^{1}H and ^{19}F overlapped to each other, spanning altogether the 155-180 MHz range, figure 5.3. The features in this spectrum originate from protons or fluorine nuclei at specific sites in the crystal, experiencing well-defined dipolar fields. In order to explore the easy-axis alignment of the Dy-

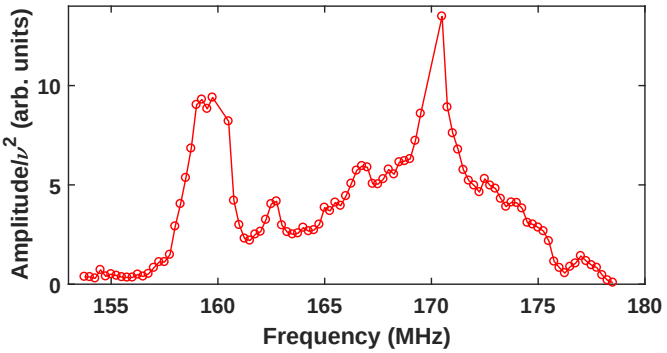

Figure 5.4: Spectrum targeted at ^{1}H and ^{19}F inside the Dy-cene SIM at 4 K temperature collected using a standard Hahn sequence in an applied field of 4 T, with the sample vial in the second rotation in the xy-plane, as explained in the text.

cene, we rotated the sample by about 90° inside the measurement coil. The so-measured spectra is shown in figure 5.4, skipping the central ^{1}H resonance in the frequency step.

We chose a spectral point away from the unshifted ^{1}H resonance by 2 MHz and measured the spin lattice relaxations for this spectral component, corresponding to the population of ligand protons experiencing a longitudinal dipolar field of ~ -500G, i.e. close enough to the magnetic ion. Spin lattice relaxations are presented in next subsection. Due to the coupling of protons to the electronic spins, we can probe phonon-induced electronic relaxations in the Dy-cene SIM using the ^{1}H relaxation rate ($1/T_1$) as a probe.

5.3.1 ^{1}H relaxations

The longitudinal relaxation rates $1/T_1$, were measured at the target temperature and applied magnetic field at a constant offset from the ^{1}H reference frequency (-2MHz, as detailed above), following various field and temperature cycles. The first cycle of measurements was started by warming up the sample up to 120 K, a temperature safely above the blocking temperature for this SIM, then the sample was cooled down to 4 K in an applied magnetic field of 4 T (pink filled circles in figure 5.5), or 1.8 T (orange filled squares). Then we started the relaxation measurement vs. temperature on warming from 10 K (4 T) or 4 K (1.8 T). After measuring up to 67.5 K in the first cycle, the second cycle (dark drown filled circles) started by cooling down to 32.5 K in the 4 T field and measuring once again from such a temperature. The T_1 relaxation rates measured in these cycles are shown figure 5.5. It is evident from the ^{1}H relaxation rate plot, that ^{1}H relaxations do not (or only weakly) depend on the magnetic field. Furthermore, the

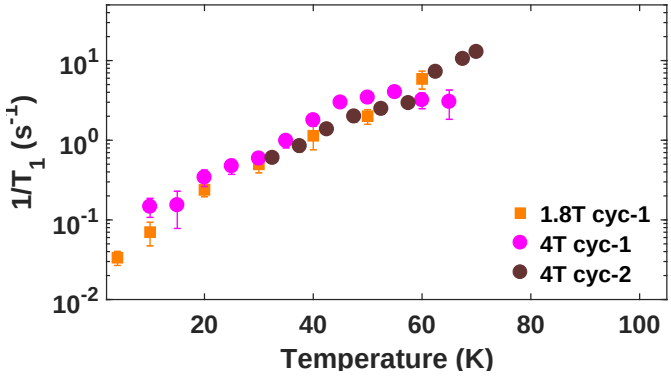

Figure 5.5: Comparison of the Dy-cene ^{1}H spin-lattice relaxation rates measured vs. temperature in 4 T (dark brown and pink filled circles) or 1.8 T (filled orange squares), as detailed in the text.

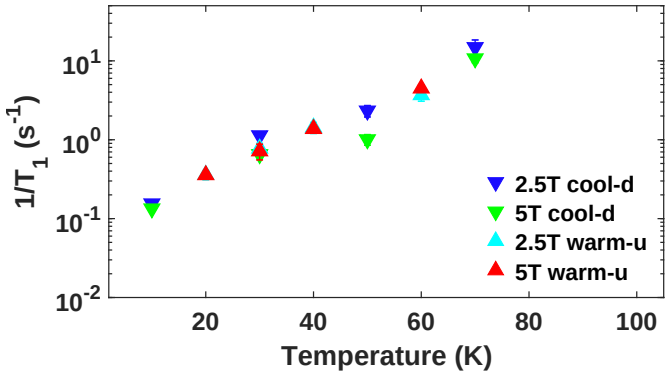

Figure 5.6: A comparison of the Dy-cene ^{1}H spin-lattice relaxation rates measured in 2.5 T or 5 T on cooling down (blue and and light green downward pointing triangles, respectively), and 2.5 T or 5 T while warming up (cyan and red upwards pointing triangles respectively), as detailed in the text.

relaxation rate peak is not visible in the measured temperature range.

In another set of experiments, measurements were performed while cooling down in an applied field of 2.5 T or 5 T, to 10 K (respectively, blue and and light green downward pointing triangles). The relaxation rate measurements have been then performed while warming up from 20 K, cyan and and red upward pointing triangles respectively as presented in figure 5.6. Once again we do not see a strong field dependence in the ^{1}H relaxation rates. A measurement at a field of $\sim$8 T (dark green filled circles in figure 5.7), plotted alongside all the measurements described before, clearly shows only a weak field dependence of relaxation rates $1/T_1$. Furthermore, these 8 T measurements seem to display a shallow peak in ^{1}H relaxation rates $1/T_1$ around 80 K, as shown in figure 5.7. However, the slight downturn of $1/T_1$ above 80 K is probably an artifact due to a corresponding decrease in the number of ^{1}H nuclei probed by this NMR signal (see below). The signal loss (wipeout) is due to very fast and inhomogeneous spin-spin relaxations, whereby only the signal components with longer spin-spin relaxation times T_2 are detected.

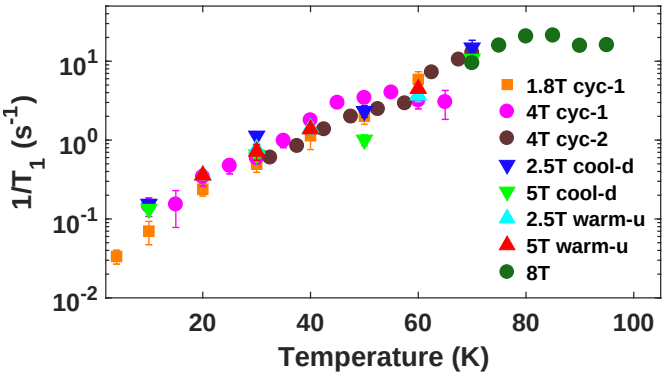

Figure 5.7: A comparison of the Dy-cene ^{1}H spin-lattice relaxation rates measured in various magnetic fields and temperatures in different cycles of experiments. Dark green filled circles are the measurements in ∼8 T applied field.

It is therefore plausible that this residual fraction of nuclei also exhibit longer T_1 times. The signal was completely lost above ∼95 K. The asymptotic amplitudes A of the recovery curves

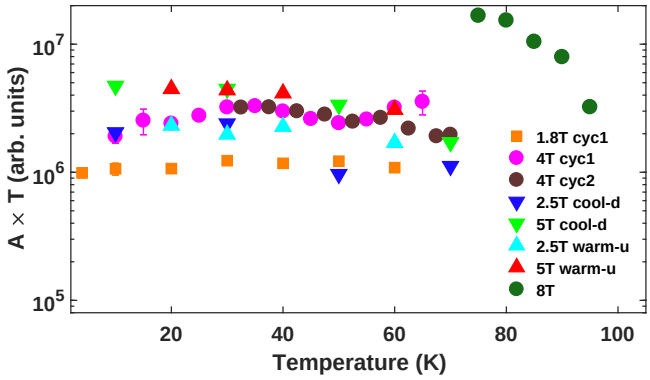

Figure 5.8: Temperature times asymptotic amplitudes of the recovery curves following saturation, plotted as a function of temperature. The color code is same as described previously.

following saturation (whence T_1 was determined), multiplied by temperature T, are plotted as a function of temperature in figure 5.8 for all the different applied fields. The same color code is followed here as well. For a given temperature scan in a constant applied field, such normalized amplitudes are proportional to the number of resonating nuclei. The figure clearly shows that the product A×T is constant within error in each temperature scan up to 80 K, which demonstrates that the various T_1^{-1}(T) curves in figures 5.5 to 5.7, probe a constant fraction of nuclei up to such a temperature. Data at higher temperature (only available in ∼8 T) show however a marked decrease with temperature.

The explanation for the progressive disappearance of the NMR signal (a phenomenon often referred to as “wipeout”) above 80K is provided by the temperature dependence of spin-spin relaxation rates. The transverse relaxation rate $1/T_2$ rises sharply after 80 K, figure 5.9, and

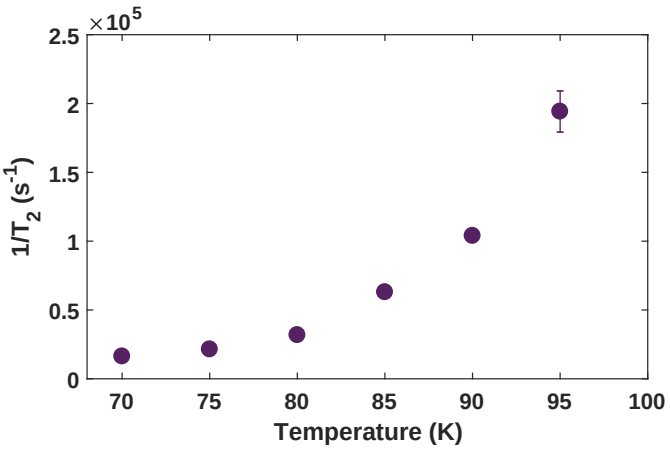

Figure 5.9: A measurement of the Dy-cene ^{1}H spin-spin relaxation rates measured in ≈8 T external magnetic field as a function of temperature.

correspondingly the relaxation time T_2 drops to values smaller than the experimental lower limit of our setup (mostly determined by the dead time of the spectrometer receiver), in the order of 4-5 μs at 8 T. Echo signals with a shorter T_2 than such a limit are almost completely decayed when they are recorded, and hence they are not detected. However, due to the inherent inhomogeneities in this system, with a number of inequivalent protons participating in the NMR signal, the T_2 values of the various proton species are subject to a certain statistical distribution. Therefore the drop of T_2 below the minimum measurable value is not sharp, and the missing signal fraction increases smoothly with temperature in qualitative agreement with $1/T_2$ (figures 5.8 and 5.9). For this reason, the spin lattice relaxation values at the highest temperatures are likely correlated with the signal wipeout, in that they were measured out of an ensemble of nuclei which is progressively depleted of its faster-relaxing components, namely protons which are more strongly coupled to dysprosium spins.

Until now, we have only presented the experimental NMR results, with both the static and dynamic probing of the nuclear magnetization provided by spectra and nuclear relaxations, respectively. In the next section we will hint upon the way NMR can be used in theoretical formalism, for the modeling and detailed explanation of these nuclear magnetization dynamics, which our colleagues in Parma are going to use. This theoretical framework also allows to reproduce the wipeout effect, by identifying the protons probed by the NMR.

5.4 Theoretical Formalism

In order to understand the relaxation dynamics in the Dy-cene SIM the *rate master equation formalism* is going to be used. The molecular observables are affected by the electronic spin interactions with the lattice vibrations (i.e. phonons) behaving like a heat bath. These interactions result in the decoherence of the spins time-evolution leading to irreversible relaxation dynamics towards the thermal equilibrium. The thermal fluctuations of the electronic spins are

responsible for the fluctuations in the hyperfine dipolar field and thus for the nuclear spin-lattice relaxation. The nuclear spin lattice relaxation rate $1/T_1$, measured experimentally and presented in the previous section, is therefore a powerful probe of the electronic relaxation times.

This relaxation rate $1/T_1$ can be computed by perturbation theory treatment of the hyperfine interactions between electronic and nuclear spins [177]. Within this framework, $1/T_1$ is proportional to a linear combination of the Fourier transforms of electronic spin correlation functions $S_{P,Q}(\omega, T, H_0)$, evaluated at the Larmor frequency $\omega_L(H_0)$. We have [176]:

$$\frac{1}{T_1} \propto \sum_{i=1}^{n} A(\lambda_i, T, H_0) \frac{\lambda_i(T, H_0)}{\lambda_i^2(T, H_0) + \omega_L^2} \tag{5.1}$$

with $\lambda_i(T, H_0)$ are the eigenvalues of the rate matrix **W** [176], and correspond to the characteristic electronic relaxation rates, n being the molecules' spin Hilbert-space dimensions, while $A(\lambda_i, T, H_0)$ are the frequency weights of each rate λ_i. Hence, NMR can be exploited to probe electronic relaxation. In many MNMs, for a substantially wide range of T and H_0 values, a single frequency $\lambda_0(T, H_0)$ i.e. a single Lorentzian dominates the spectrum. In these systems, the calculated dynamical structure factor in equation (5.1) can be expressed by a single contribution as

$$\frac{1}{T_1} \approx A(\lambda_0, T, H_0) \frac{\lambda_0(T, H_0)}{\lambda_0^2(T, H_0) + \omega_L^2} \tag{5.2}$$

The product of the magnetic susceptibility and the temperature (χT) is proportional to the sum of these weights i.e. $\sum_i^n A(\lambda_i, T, H_0) \propto \chi T$, from the linear-response theory. In the regime, when $\omega_L(H_0) \gg \lambda_L(T, H_0)$, which is the case in our measurements, we can write equation (5.2) as

$$\frac{1}{T_1} = A(\lambda_0, T, H_0) \frac{\lambda_i(T, H_0)}{\omega_L^2} \tag{5.3}$$

Since we observe weak (or no) magnetic field dependence from the ω_L, it points towards the $(H_0)^2$ dependence of the λ(T, H_0).

5.5 Perspective

We have presented preliminary NMR experimental results, carried out on the Dy-cene single ion magnet. Both the nuclear spin NMR spectra and the relaxation rates are measured. The initial results reveal a weak dependence of the proton relaxation rates on the strength of externally applied magnetic field. From the theoretical relaxation rate picture, it seems that this should be due to the electronic relaxation rate increasing approximately as the square of the applied field.

Further analysis of the NMR results, magnetization experiments and the theoretical modeling is still ongoing.

Chapter 6

MnFePSi Alloys for Magnetocalorics

6.0 Introduction

Magnetic materials showing a fist order magnetic transition (FOMT) have been attracting sustained research interest because of their inherent giant magnetocaloric effect (GME), originating from the large entropy change taking place at the transition. The GME is the key to the employment of these compounds for the magnetic refrigeration applications, whereby the vapor based thermodynamic cycles of traditional refrigerators are replaced by magnetization-demagnetization cycles, which are environment-safer and potentially more efficient. To this end, Fe_2P-based $Mn_xFe_{1.95-x}Si_yP_{1-y}$ alloys ($1 \leq x < 1.95$) are among the most promising materials. Their paramagnetic (PM) to ferromagnetic (FM) FOMT is governed by a magneto-elastic transition taking place at the Curie point, characterized by a sizable variation of the crystal cell parameters without a symmetry change. By varying the composition, T_C can be tuned over a wide temperature interval including room temperature, which makes these systems eligible for real case applications. Like their parent Fe_2P compound, the Mn-Fe-Si-P systems crystallize in the hexagonal space group $P6\bar{2}m$, with a crystal structure characterized by the stacking of $3g$, $1b$ sites and $3f$, $2c$ sites on alternate layers. The magnetic Fe, Mn ions occupy the $3f$ and $3g$ sites, with a marked preference of Mn for $3g$ site [78, 178], while the $1b$ and $2c$ sites are occupied by the non metallic P and Si ions, with a partial preference of Si for $2c$ sites at $y > 1/3$ [179]. The magnetism of the $3f$ ions exhibits an itinerant character witnessed by a fractional magnetic moment $\leq 1.5\ \mu_B$ at low temperature, as compared to $\geq 2.5\ \mu_B$ on Mn at the $3g$ sites, which behave as nearly localized spins. The moment at the $3f$ sites exhibits a steep drop at T_C, in coincidence with a marked in-plane lattice contraction, partly compensated by an expansion along c. The accompanying magneto-elastic transition at T_C fits into the scenario of an enhanced chemical bonding of the $3f$ atoms, and increased spin itineracy above the FOMT.

The coexistence of large $3g$ Mn moments with weaker and possibly vanishing $3f$ moments is referred to as the mixed magnetism. However, the exact nature of the electronic state of the $3f$ ions in the PM state is still controversial. X-ray magnetic circular dichroism (XMCD) experiments indicated in fact that the moment quenching above T_C is incomplete, [180], in contrast with earlier predictions for a total $3f$ moment extinction by band structure calculations [181].

The critical temperature and the character of the magneto-elastic transition are strongly affected by the Mn/Fe and Si/Pi substitutions. An increasing substitution of P with the larger Si ions at the $2c$ sites gives rise to an in-plane expansion, accompanied by increased $3f$-$3f$ and decreased $3f$-$3g$ minimum distances. In agreement with the tendency observed on crossing the FOMT, this leads to a relative localization of the $3f$ moments and an enhanced inter-layer exchange coupling whence a more robust ferromagnetism and an increased T_C are observed. Silicon-poor compositions, on the other hand, yield lower T_C, an unsaturated magnetic moment and strong magnetization hysteresis vs. both temperature and applied field. The latter are manifestations of a *kinetically arrested* magnetic transition, i.e. a frozen-in metastable state separated from thermodynamic equilibrium by a large free-energy barrier. The kinetic arrest can be however mitigated and eventually suppressed by doping a few percent boron into the $1b$ sites, producing a qualitatively similar, though more dramatic effect as the Si/P substitution. The progressive substitution of Fe by Mn at the $3f$ sites at Mn concentrations $x > 1$, on the other hand, depresses T_C and drives a decrease of the order moment [178]. However, the magnetoelastic transition coupled to the FOMT is depressed as well, as witnessed by a smaller step in the lattice parameters. As a consequence, the first order character of the magnetic transition becomes less pronounced.

In this chapter, we present the ^{55}Mn nuclear magnetic resonance (NMR) study of a representative set of Mn-Fe-Si-P compounds to address the nature of the magnetic transitions and mixed magnetism. The first order nature of the magnetic transitions in Mn-Fe-Si-P compounds is established by ^{55}Mn NMR even at Mn-rich compositions where a nearly second order magnetic transition (SOMT) was inferred from magnetization and magneto-caloric effect measurements. The mixed magnetism of these systems is unambiguously ascribed to the vanishing of the spin polarization at the $3f$ sites in the PM phase, with a very stringent limit for the fluctuating $3f$ moment set by the comparison of NMR and magnetization data. Moreover, a sizable fraction of diamagnetic manganese, independent of temperature, was found at the $3f$-site at $x > 1$ compositions. Such a diamagnetic fraction, never reported earlier, seemingly plays a role in the decreasing average $3f$ moment at increasing x reported by neutron scattering and the lower T_C of the Mn-rich compounds.
The author of this thesis, Samuele Baldini and Prof. Giuseppe Allodi carried out all the NMR experiments and analyzed the data. Synthesis and structural characterization of samples was performed by the Prof. E Brück's group in Delft (NL), while the magnetization measurements were handled by Prof. M. Solzi's group in Parma. Prof. Roberto De Renzi supervised all the project.

6.1 Magnetic Measurements

There are four representative compositions used in magnetization and NMR experiments, including two higher than unit Mn samples, $Mn_{1.27}Fe_{0.68}Si_{0.52}P_{0.48}$ and $Mn_{1.7}Fe_{0.25}Si_{0.5}P_{0.5}$, as well as two other with Mn = 1 in the formula, $Mn_1Fe_{0.95}Si_{0.29}P_{0.71}$ and $Mn_1Fe_{0.95}Si_{0.33}P_{0.67}B_{0.03}$, referred to hereafter as S1-S4, respectively. The magnetic characterization of the samples was carried out by a superconducting quantum interference device (SQUID) magnetometer (Quantum Design MPMS-XL) in the 2-330 K temperature range and by a magnetic balance (Manics DSM8) magnetometer equipped with an oven in the 300-800 K range. The magnetization curves

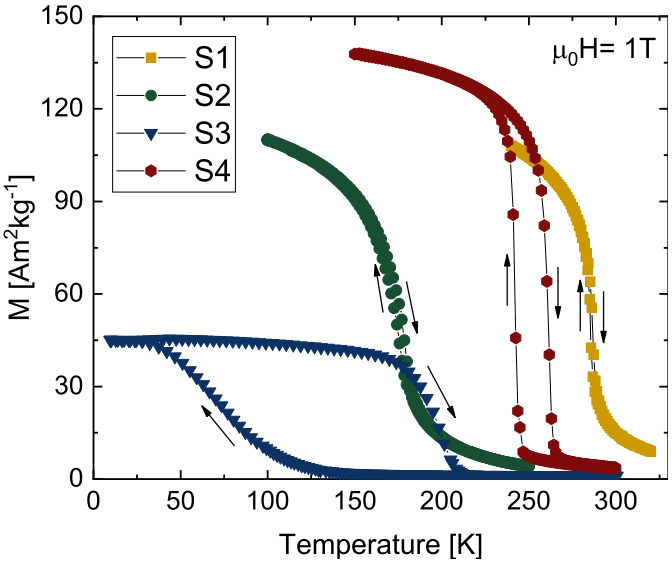

Figure 6.1: Magnetization curves vs temperature of the four (S1-S4) samples, measured in an applied field of 1 T on both cooling and warming.

of the four samples, recorded as a function of temperature in an applied field of 1 T, are shown in figure 6.1. Sample S1 shows a sharp transition close to room temperature with negligible hysteresis, making this compound of interest for applications. The Mn-richer S2 shows a reduced T_C and a smoother $M(T)$ curve suggesting a SOMT. The Si-poor S3 exhibits a strong temperature hysteresis and an unsaturated magnetic moment characteristic of a kinetically arrested magnetic state. The full magnetization is recovered and thermal hysteresis is nearly suppressed in S4, similar to S3 but for a slight B doping. The transition temperatures of the various

Table 6.1: Composition and critical temperatures of the investigated samples.

Sample	Composition	$T_C^{\uparrow}$ (K)[1]	$T_C^{\downarrow}$ (K)[2]
S1	$Mn_{1.27}Fe_{0.68}Si_{0.52}P_{0.48}$	286.6(2)	285.2(2)
S2	$Mn_{1.7}Fe_{0.25}Si_{0.5}P_{0.5}$	178.5(3)	175.5(3)
S3	$MnFe_{0.95}Si_{0.29}P_{0.71}$	199(1)	73(3)
S4	$MnFe_{0.95}Si_{0.33}P_{0.67}B_{0.03}$	261.7(3)	242(1)

samples, determined as the inflection points of $M(T)$, are summarized in Tab. 6.1.

[1]From $M(T)$ on warming (figure 6.1) .
[2]From $M(T)$ on cooling (figure 6.1).

6.2 NMR Measurements

The NMR experiments were carried out by means of a home-built phase-coherent spectrometer [102] and a helium-flow (in the 5-80 K range) or a nitrogen-flow cryostat (70-360 K) on finely powdered samples, in order to maximize the penetration of the radiofrequency (rf) magnetic field. Whenever an intense signal with a large rf enhancement was present, namely in ZF or in a moderate external field applied as a perturbation of the much larger spontaneous hyperfine field, measurements were performed by using a small coil ($\leq$ 50 nH) wound around the sample and terminated onto a 50 Ω resistor as a probe. The sensitivity penalty of a non-resonant circuit was in fact compensated by the enhancement of the NMR arising from the hyperfine coupling of nuclear and electronic magnetization, characteristic of ferromagnets, [182, 183] while the untuned probehead allowed automated frequency scans. A conventional LC resonator was however employed for the weaker $3f$ resonance lines very close to T_C, in order to improve sensitivity, as well as in all the other cases.

In zero applied field (ZF), ^{55}Mn nuclei resonate in a hyperfine field essentially proportional to the ordered component of the on-site Mn electronic spin, thus probing locally the magnetic order parameter and the electronic configuration of the Mn ions. To this end, ^{55}Mn NMR provides complementary information to ^{57}Fe Mössbauer spectroscopy, [184] with a benefit for NMR due to its simpler spectra, yielding a precise determination of the order parameter even in the presence of a broad distribution of hyperfine fields. As seen by a local probe of magnetism, a FOMT appears as a *truncated* transition, [185] i.e. a non-vanishing local moment probed by the hyperfine field and, rather, a phase-separated magnetic state with a vanishing volume of the ordered phase at the transition temperature.

The NMR spectra were recorded by means of a standard $P - \tau - P$ spin echoes pulse sequence, with equal rf pulses P of intensity and duration optimized for maximum signal, and delay τ limited by the dead time of apparatus. Each spin echo, representing one frequency point in the spectrum, was analyzed by taking the maximum magnitude of the Fourier-transformed signal, as detailed elsewhere [185].

6.3 ^{55}Mn NMR Results

The ^{55}Mn spectra detected at low-temperature in zero and in a perturbing field, their evolution with temperature, the distinct behavior of the spontaneous field at the two Mn sites on approaching T_C, and the detection of non-magnetic Mn fractions from ^{55}Mn NMR in applied fields, are presented for clarity in separate subsections. Each one addresses specific issues: the assignment of the spontanteous ^{55}Mn NMR peaks to corresponding crystal sites and the local moment probed therein; the order of the magnetic transition and the kinetic arrest phenomenon in silicon-poor compounds; the nature of mixed magnetism; and the electronic state at the $3f$ site above T_C, respectively.

6.3.1 Mn moment and site occupancy

Very intense spontaneous ^{55}Mn NMR signals were detected below T_C by very low rf excitation power, thanks to a sizable enhancement $\eta \approx 400$ [182], a value compatible with nuclei in domain walls. The ZF spin echo amplitudes at low temperature (5 K), divided by the frequency-dependent sensitivity $\propto \nu^2$, are plotted vs frequency in figure 6.2 for all of measured samples. After such a correction, the plotted quantities correspond to the distributions of hyperfine fields at the ^{55}Mn nuclei. The spectra exhibit two broad peaks with composition-dependent positions and relative weights. The more intense resonance is found in the 260-320 MHz frequency interval (24-30 T in field units), whereas the minority peak, increasing in intensity with increasing Mn concentration, is located in the 150-220 MHz range (14-21 T). Assuming an isotropic hyperfine coupling term in the order of -11 T/μ_B as in manganites [185] and in other magnetic compounds [186], and neglecting transferred contributions to the contact hyperfine field by neighboring ions, which are known to be very small in these systems, we estimate electronic spin moments of approximately 2.2-2.7 μ_B and 1.3-1.9 μ_B at the corresponding Mn sites. These values and the relative amplitudes of the two peaks are in qualitative agreement with the determination of the magnetic moment and the Mn occupancy at the two sites by neutron scattering [178]. The low- and high-frequency ^{55}Mn resonance peaks are therefore unambiguously assigned to Mn nuclei at the $3f$ and $3g$ sites, respectively.

The best-fit mean frequencies of the two resonance peaks and the ratios of their integrated amplitudes, corresponding to the relative occupancy of the $3f$ and $3g$ sites by Mn, are listed for each sample in table 6.2. The amplitude ratios are compared with the values expected for a

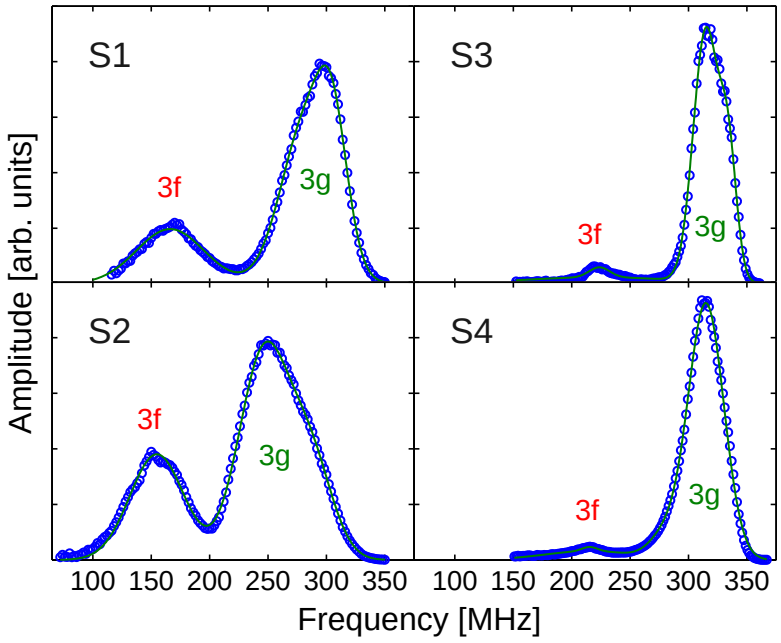

Figure 6.2: ZF ^{55}Mn NMR spectra of the S1-S4 samples at $T = 5\ K$. Spectral amplitudes are corrected for the frequency dependent sensitivity $\propto \nu^2$.

total preference of Mn for the $3g$ site, whereby only Mn atoms in excess of 1 per formula unit (FU) occupy $3f$ sites. It is apparent from samples S3 and S4 ($x = 1$), showing however a small but finite $3f$-Mn fraction, that the preferential occupation of $3g$ sites by Mn is not perfect, and some spillage of Mn and Fe to the disfavored sites occur. The Mn-rich sample S2 ($x = 1.7$), on the other hand, exhibits a low-moment $3f$-Mn fraction significantly smaller than the expected 0.7 value. The missing $3f$-Mn ordered fraction in this sample will be commented again in section 6.4, along with the detection of a sizable amount of non-magnetic Mn ions.

The mean spontaneous NMR frequencies of the $3f$ and $3g$ peaks are plotted vs. Mn concentration x in figure 6.3, overlaid to the $3f$, $3g$ and overall moment per FU determined by neutron scattering, and to the macroscopic saturation moment per FU reported in the literature for similar compounds [178]. In the figure, NMR frequencies are scaled to moments by assuming a mean

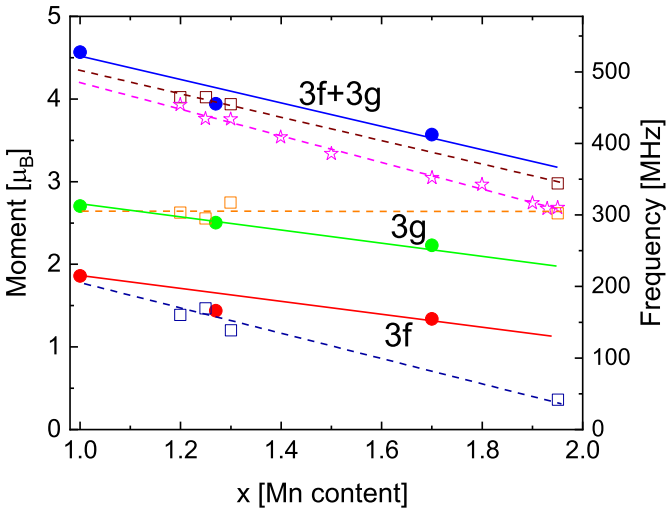

Figure 6.3: Low-temperature $3f$, $3g$ and overall ordered moment per FU vs Mn concentration x, determined by neutron scattering (squares) and macroscopic magnetization (stars) in various Mn-Fe-Si-P compounds from the literature, [178] compared to the $3f$ and $3g$ ^{55}Mn ZF NMR frequencies and their sum in the present samples (bullets). NMR frequencies are scaled to moments by assuming a 11 T/μ_B hyperfine coupling constant.

hyperfine field of 11 T/μ_B, as stated above. The total moment $\mu_{3g} + \mu_{3f}$ assessed by ^{55}Mn ZF-NMR is in good agreement with its determinations by the other techniques. The agreement of the $\bar{\nu}_{3g}$ and $\bar{\nu}_{3f}$ NMR frequencies with the individual $3g$ and $3f$ moment values refined by neutrons is however poorer. In particular, NMR shows a similar relative decrease with increasing x for the $\bar{\nu}_{3g}$ and $\bar{\nu}_{3f}$ resonance frequencies, while a constant μ_{3g} and a more rapidly decreasing μ_{3f} moment were estimated from neutron data.

The attribution of both the resonance peaks to ^{55}Mn nuclei (rather than ^{31}P, which also experience a large transferred hyperfine field in the parent Fe_2P compound) [187] is further demonstrated by the application of moderate external fields acting as a perturbation of the much larger internal field. Typical spectra in external fields up to a few Tesla (T) are shown in figure 6.4 for a representative sample (S1). Both the $3g$ and $3f$ mean resonance frequencies shift to lower

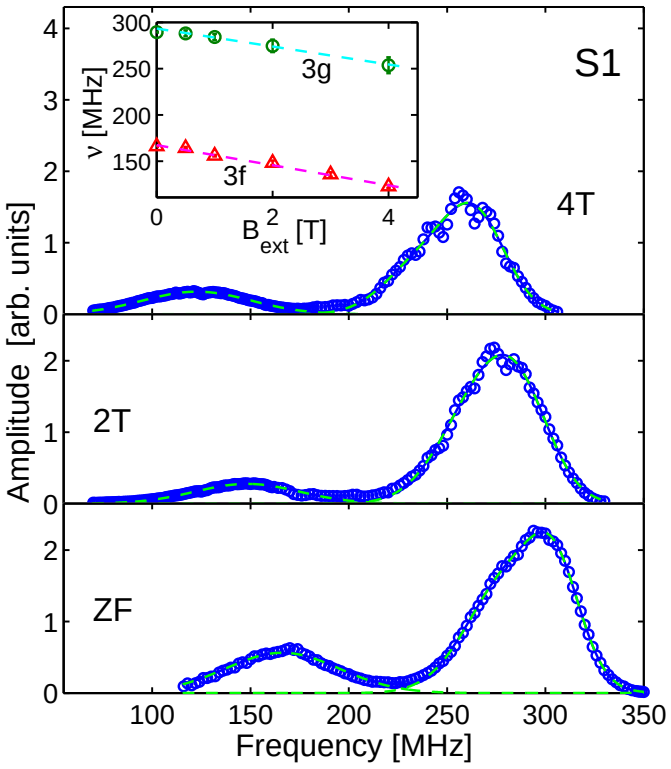

Figure 6.4: ^{55}Mn NMR spectra of sample S1 at $T = 5$ K, in zero and in perturbing applied fields. Inset: mean positions of the $3f$ and $3g$ lines as a function of the external field. The dashed lines are fits to equation (6.1).

frequency following a linear dependence on the applied field (α = 3g, 3f), where $B_{hf}^{(\alpha)}$ is the isotropic component of the hyperfine field and $\gamma/2\pi = 10.5$ MHz/T is the gyromagnetic ratio of ^{55}Mn (figure inset).

$$\bar{\nu}_\alpha(H) = \frac{\gamma}{2\pi}|B_{hf}^{(\alpha)} + \mu_0 H| = \frac{\gamma}{2\pi}\left(|B_{hf}^{(\alpha)}| - \mu_0 H\right), \tag{6.1}$$

The shifts with H without line splitting or appreciable broadening, along with their absolute rate $\mu_0^{-1}|d\bar{\nu}_\alpha/dH|$ equal to the full ^{55}Mn gyromagnetic ratio $\gamma/2\pi$, prove the collinear composition of the isotropic hyperfine field, which is collinear in turn to the on-site electronic moment, and the external field, namely the full FM order. Notably, the latter also warrants that two resonances at ν_{3g} and ν_{3g} are both from ^{55}Mn nuclei rather than ^{31}P, which also experiences a large transferred hyperfine field in the parent Fe_2P compound.[187] The sign of $d\nu_\alpha/dH$ indicates that the hyperfine field is negative (i.e. antiparallel to the electronic spin), in agreement with the core-polarization mechanism dominant in the contact hyperfine coupling of transition metal ions. [188]

Similar field-dependent spectra were recorded in all samples. In particular, they were detected also in the kinetically arrested S3, which shows a $M(H)$ curve saturating in two steps (figure 2b of Miao et al. [189]), with the full saturation taking place in a field H_s as high as

$\mu_0 H_s \approx 5$ T, and a large hysteresis in $M(H)$ below H_s [189]. The field dependence of the mean frequency $\bar{\nu}_{3g}$ of the majority peak is plotted vs field in the inset of figure 6.5, overlaid to a plot of the $\nu(H)$ law of equation 6.1 (with slope $\gamma/2\pi$ set equal to the 10.5 MHz/T value of ^{55}Mn). It is apparent from the figure that, above an external field of 2 T corresponding to the saturation of the magnetically ordered domains, the colliner composition of the internal with the external field as of Eq. 6.1 is obeyed by $\bar{\nu}_{3g}(H)$. The local magnetic order probed by NMR is therefore fully FM in sample S3 as well. In the main panel of figure 6.5 two low temperature

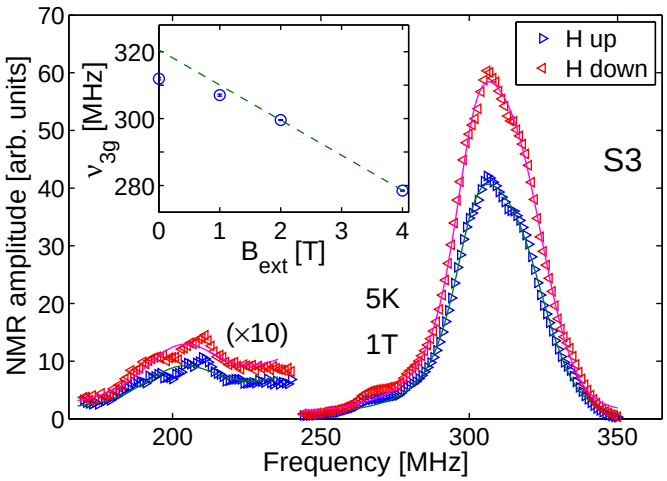

Figure 6.5: ^{55}Mn NMR spectra of sample S3 at $T = 5$ K in an applied field $B_{ext} = 1$ T, applied after ZFC to the working temperature (blue right triangles) and after ZFC to 5 K, followed by a isothermal field cycle $0 \rightarrow 5$ T $\rightarrow 1$ T (red left triangles). Inset: mean position $\bar{\nu}_{3g}$ of the $3g$ line vs B_{ext}. The dashed line a fit of the two highest-field points $\bar{\nu}_{3g}(B_{ext})$ to equation 6.1, with γ constrained to the ^{55}Mn value.

spectra are compared, recorded in the same field $\mu_0 H = 1$ T $< \mu_0 H_s$ applied after zero-field cooling (ZFC) and after a isothermal field ramp up to H_s followed by a ramp down to the measuring field, respectively. Clearly, only the signal amplitude is hysteretic vs field cycles, while the spectra are identical but for a vertical scaling relative to each other. This indicates that the microscopic properties of the magnetically ordered phase are unaffected by the applied fields, and only its volume is increased.

Therefore these results provide evidence that the unsaturated magnetization of this sample is due to the coexistence of spatially segregated FM and non-FM domains, and that the full moment saturation develops as a field-induced nucleation of FM domains from the competing phase.

6.3.2 First order transitions and kinetic arrest

The temperature evolution of the ZF ^{55}Mn NMR spectra could be recorded up to T_C in all samples. The temperature dependence of the centers of gravity $\bar{\nu}_{3g}$ and $\bar{\nu}_{3f}$ of the two resonance peaks, proportional to the mean local moments at the two Mn sites, is plotted in figure 6.6 and

figure 6.7 for samples S1-S2 and S3-S4, respectively. In the figures, the warming-up higher transition temperatures $T_C^{\uparrow}$ of table 6.1 are marked by vertical dashed lines for reference. It is

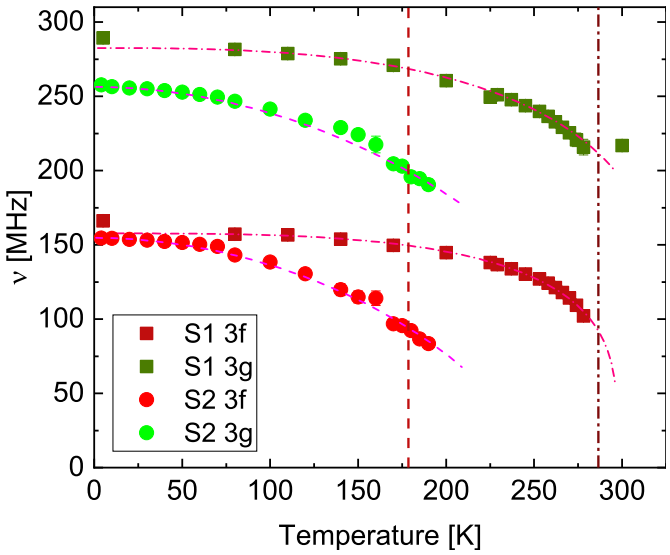

Figure 6.6: ZF $3g$ and $3f$ mean ^{55}Mn resonance frequencies vs temperature in samples S1 (squares) and S2 (bullets). The lines overlaid to symbols are guides to the eye. Vertical dashed lines mark the upper transition temperatures $T_C^{\uparrow}$ of the two samples.

apparent from the figures that the $\bar{\nu}_{3g}(T)$ order parameter curves do not vanish at T_C in any sample. The reduced order parameter at the $3g$ site $\bar{\nu}_{3g}(T)/\bar{\nu}_{3g}(0)$ is approximately 0.8 at T_C and extrapolates to zero at a significantly higher temperature. This holds true also for samples S2, showing a comparatively small thermal hysteresis and a magnetization vs temperature dependence resembling that of a SOMT (figure 6.1). These *truncated* order parameter curves (i.e. not vanishing at T_C), as seen by a local probe in direct space like NMR, indicate that the magnetically ordered phase does not collapse on warming due to critical spin fluctuations but, rather, to an independent mechanism which abruptly breaks down exchange coupling. The truncation effect is therefore a clear indication of a FOMT.

In Fe_2P-based alloys, the driving mechanism for the magnetic transition is known to reside in the concomitant magneto-elastic transition at T_C. Similar truncated transitions have been observed e.g. in manganites [185, 190], where they have been ascribed to the breakdown of half-metallicity and the onset of a polaron phase [191]. In order to reconcile the seeming SOMT from magnetization data in sample S2 with the marked first order character apparent from ^{55}Mn NMR, it is worth noting that spontaneous ^{55}Mn resonances are detected in this sample several kelvin above T_C without noticeable anomalies in $\bar{\nu}_{3g}(T)$ and $\bar{\nu}_{3f}(T)$ (figure 6.6). This behavior indicates the coexistence of a FM and a PM phase over a wide temperature interval across the transition, with the FM fraction surviving above T_C as a minority phase. Therefore, it is volume fraction of the ordered phase which tends continuously to zero on warming, as a consequence of broad distribution of critical temperatures for the driving magneto-elastic transition. This interpretation is actually corroborated by X-ray diffraction data, showing a smoother variation

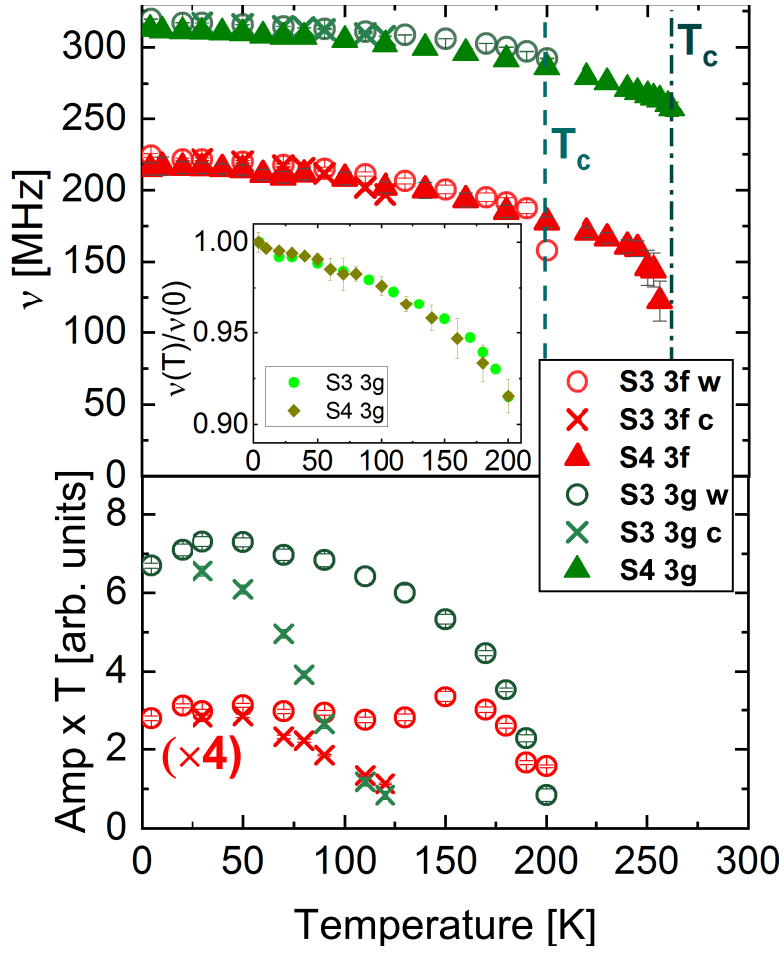

Figure 6.7: Top: ZF $3g$ and $3f$ mean ^{55}Mn resonance frequencies vs. temperature of samples S3 on cooling (crosses) and warming (empty symbols), and of S4 on warming (filled symbols). The upper transition temperatures $T_C^{\uparrow}$ of the two samples are marked by vertical dashed line. Inset: normalized $3g$ resonance frequencies $\bar{\nu}_{3g}(T)/\bar{\nu}_{3g}(0)$ vs. T of the two samples. Bottom: integrated $3f$ and $3g$ peak amplitudes times temperature T, as a function of T. For clarity, the $3f$ data are scaled by a vertical factor of 4.

of the lattice parameters in this sample, as compared to the step-like jump observed in the other ones [192].

The $3g$ and $3f$ order parameter curves of sample S3, showing a marked thermal hysteresis and the kinetic arrest phenomenon, are plotted vs temperature on both cooling and warming in figure 6.7. Very small and negligibly small differences in the values of $\bar{\nu}_{3f}$ and $\bar{\nu}_{3g}$, respectively, are detected between the cooling and warming scans, and only close to the lower transition $T_C^{\downarrow}$. In the figure, $\bar{\nu}_{3g}(T)$ and $\bar{\nu}_{3f}(T)$ of S3 are overlaid to the corresponding quantities of sample S4 containing the same nominal amount of Mn but showing in contrast higher T_C, a much narrower hysteresis and the full saturation moment. Notably, the spontaneous NMR frequencies of the

two samples follow the same relative dependence of temperature and can be made to overlap by a vertical scaling factor of ≈ 1.02 (figure inset). The near coincidence of the $\bar{\nu}$ absolute values in these macroscopically very different samples is in essential agreement with the reported finding that the local $3g$ and $3f$ moments depend to leading order only on Mn content [178, 179]. Their slight difference is probably related to the larger amount of misplaced Mn atoms at the $3f$ sites found in S4 (table 6.2).

The integrals of the NMR signal amplitude of S3 over the $3g$ and $3f$ peaks, normalized by the sensitivity proportional to ν^2 and the Boltzmann factor $1/T$, are plotted vs T in upper figure 6.7−inset. Here the signal loss due to the spin-spin nuclear relaxation is negligible, i.e. far enough from $T_C^{\uparrow}$, the plotted quantities are proportional to the number of resonating nuclei, hence to volume of the ordered phase. In contrast to $\bar{\nu}_{3f}(T)$ and $\bar{\nu}_{3g}(T)$, the normalized signal amplitude is strongly hysteretic vs T, and its temperature behavior closely reproduces that of $M(T)$. The thermal hysteresis of the magnetically ordered volume agrees with the onset of a FM moment by the nucleation of fully FM domains, as indicated by the similar hysteresis vs H reported above. Notably, a spin density wave (SDW) was detected in this sample by neutron scattering across T_C, and identified with the competing phase of the FM one [189]. However, no NMR signal component distinct from the two-peak spectrum of figure 6.2−c could be detected down to the lowest temperatures. Such a discrepancy may be understood in view of the different timescales of the two techniques. Either the SDW is dynamic in nature as probed by the slower NMR probe, making it indistinguishable from the PM phase, or ^{55}Mn nuclei therein are subject to exceedingly fast relaxations which wipe out their NMR signal.

6.3.3 Mixed magnetism

A careful examination of $\bar{\nu}_{3g}(T)$ and $\bar{\nu}_{3f}(T)$ in the various samples reveals that the two quantities, probing the ordered Mn moments at the $3g$ and the $3f$ sites, do not scale with each other as a function of temperature and seemingly behave as independent order parameters. In particular, $\bar{\nu}_{3f}(T)$ decreases faster than $\bar{\nu}_{3g}(T)$ on warming. This is apparent from figure 6.8, showing a continuous increase of the $\bar{\nu}_{3g}(T)/\bar{\nu}_{3f}(T)$ ratio with temperature in all the four samples and a clear upturn at T_C in samples S1 to S3. The steeper temperature dependence of the $3f$ ordered moment on approaching T_C, in agreement with previous reports by other techniques [178, 180] and [181], is a clear manifestation of the weaker magnetism of the $3f$ ion, possibly evolving into a non-magnetic $3f$ state. Its coexistence with the larger and more localized $3g$ moment is referred to altogether as *mixed magnetism*, and it is believed to play an important role in the FOMTs of this class of materials. [189, 192–194]

Nevertheless, it is clear from figures 6.6 and 6.7 that also $\nu_{3f}(T)$, with the sole possible exception of sample S2, maintains a finite value at T_C, as in a truncated order parameter curve. This is particularly evident in the kinetically arrested S4 sample, showing just a moderate increase with temperature in $\bar{\nu}_{3g}(T)/\bar{\nu}_{3f}(T)$ (figure 6.8). Such a quantitatively different behavior may be understood in view of the more marked truncation effect in this sample, whose mean hyperfine frequencies $\bar{\nu}_{3g}(T)$, $\bar{\nu}_{3f}(T)$ closely follow those of S3, in spite of the large difference in the transition temperatures of the two compounds. It seems therefore that the FOMT and the drop of the $3f$ moment are decoupled to some extent, especially at compositions showing the

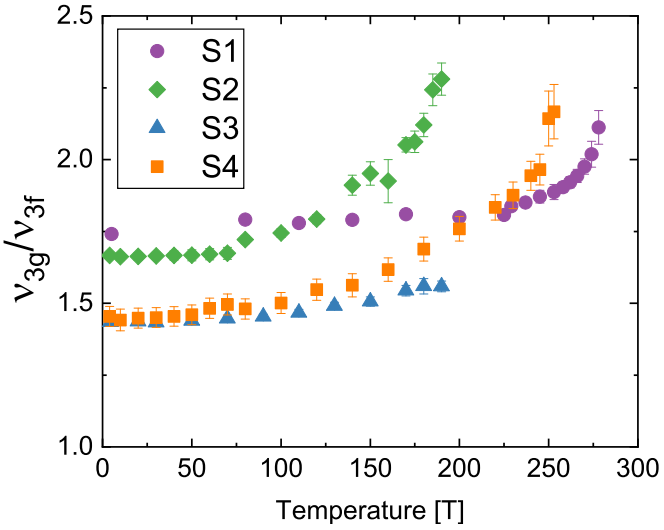

Figure 6.8: Mean frequency ratio $\bar{\nu}_{3g}/\bar{\nu}_{3f}$ of the $3g$ and $3f$ ZF ^{55}Mn NMR peaks in the four samples, as a function of temperature.

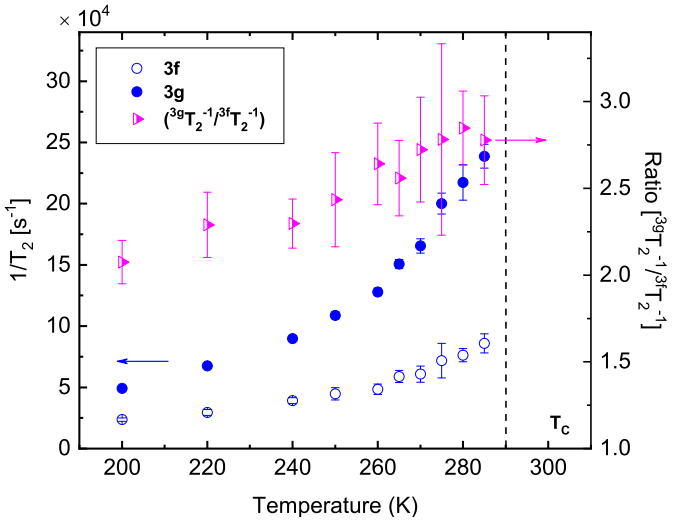

Figure 6.9: Spin-spin ^{55}Mn relaxation rates of sample S1, measured in ZF on the $3g$ (filled circles) and $3f$ peak (empty circles) as a function of temperature, and their ratios (triangles).

kinetic arrest like that of S4, and that a non magnetic state of the $3f$ ion (discussed below) is achieved at a higher temperature than T_C.

The nature of the observed drop of the $3f$ *ordered* moment on approaching T_C is demonstrated by nuclear relaxations. Spin-spin relaxation rates T_2^{-1}, measured in ZF on the two resonance peaks, are plotted against temperature in figure 6.9 for a representative sample (S1). Far enough from T_C, T_2^{-1} is smaller at the $3f$ site by a factor of 2, in qualitative agreement with the smaller ν_{3f}. This experimental ratio is smaller than the $(\bar{\nu}_{3g}/\bar{\nu}_{3f})^2 \approx 3$ value expected from the

isotropic hyperfine couplings of the two sites. Such a discrepancy is probably accounted for by anisotropic couplings, which also produce nuclear relaxations without a net effect on the mean resonance frequencies, and which are comparable for the two peaks as indicated by their similar absolute linewidths. Nevertheless, the ratio of T_2^{-1} at the $3g$ over the $3f$ site increases on warming. This rules out enhanced spin fluctuations (due e.g. to weakened exchange interactions) as the origin for the loss of the $3f$ ordered moment, as the latter would lead to relatively stronger nuclear relaxations on the $3f$ peak, contrary to evidence. The $3f$ moment drop is therefore due the vanishing of the spin polarization and the tendency to a non-magnetic state of the $3f$ ions, in agreement with ab initio band calculations [181].

6.3.4 Vanishing $3f$ moment and diamagnetic Mn

The PM phase at temperatures well above T_C was investigated by ^{55}Mn NMR in an applied field $B_{ext} = 7.96$ T mostly in sample S2, featuring both a large $3f$ fraction and relatively low T_C which matches the temperature range of our N_2-flow cryostat. A set of ^{55}Mn NMR spectra

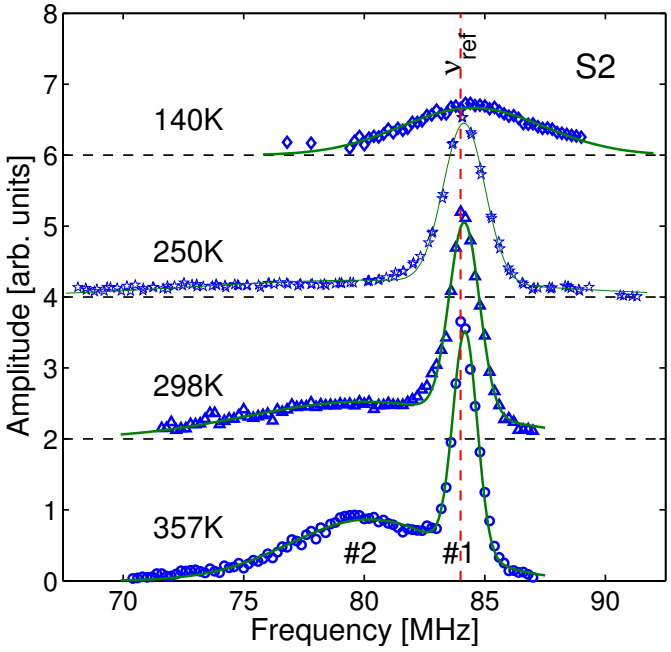

Figure 6.10: The ^{55}Mn NMR spectra of sample S2 in an applied field of 7.96 T (^{55}Mn reference frequency $\nu_{\rm ref} = 83.998$ MHz) at several temperatures.

recorded at several temperatures above T_C is shown in figure 6.10. The highest temperature spectrum (357 K) consists of two well resolved resonance peaks: a sharper line with a small positive shift with respect to the ^{55}Mn reference (83.998 MHz), referred to hereafter as line 1, and a much broader resonance with a negative shift $K \approx -4.5\%$ (-4 MHz in absolute units), referred to as peak 2. The two peaks exhibit comparable integrated amplitudes from the raw data of the plot. However, line 2 is strongly relaxed, and its measured transverse relaxation time

$T_2 = 12(1)$ μs is shorter than the dead-time-limited duration of the spin-echo pulse sequence employed to excite the resonance. The signal loss due to relaxation, on the contrary, is negligible for line 1 ($T_2 = 85(1)$ μs). When the T_2 relaxation is accounted for, the corrected amplitude of peak 2 is estimated 4 times larger than that of line 1, which is therefore a minority signal.

The evolution of the ^{55}Mn NMR spectrum on cooling down to 250 K, a temperature still well above T_C, is summarized by figure 6.11, showing the shifts $K(T)$ (panel a) and widths $\sigma(T)$ (b) of the two lines as a function of temperature. The spin lattice relaxation rates $T_1^{-1}(T)$

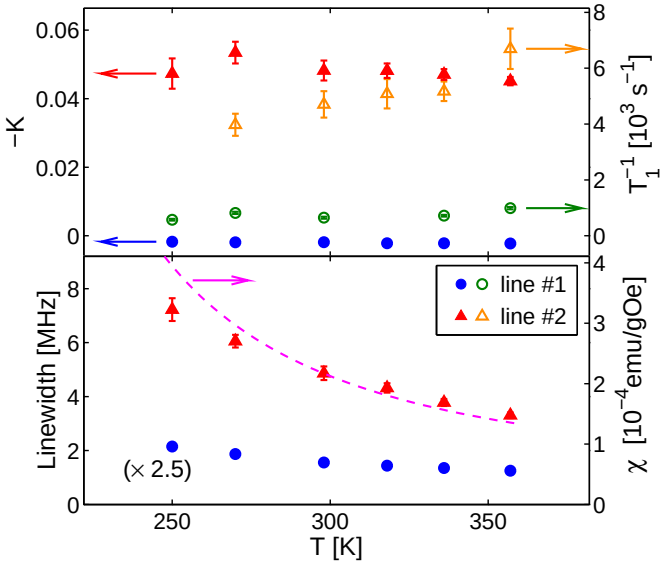

Figure 6.11: Top: line shifts, plotted with reversed in sign (filled symbols) and spin-lattice relations T_1^{-1} (open symbols) as a function of temperature, for the two resonance lines in the ^{55}Mn NMR spectra of sample S2 in the PM phase (figure 6.10). Bottom: Gaussian NMR linewidths σ vs. T of the two ^{55}Mn resonance lines (symbols) and dc susceptibility measured in $H = 10$ kOe (line). For clarity, the $\sigma(T)$ data of the narrower line 1 are magnified by a constant factor 2.5 in the plot.

are also plotted in figure 6.11-a, overlaid to the $K(T)$ data. The larger linewidth of peak 2 and T_1^{-1} relaxation rates higher thereon than on peak 1 by nearly an order of magnitude, in agreement with a similar ratio observed in T_2^{-1} (see above), indicate stronger interactions with electronic spins for the ^{55}Mn nuclei of peak 2. The magnitude of its Gaussian linewidth $\sigma_{\#2}(T)$ is much larger than the dipolar contribution, for which a limiting value of approximately 2 MHz is calculated in the FM phase, while its temperature dependence mimics that of the of the magnetic susceptibility $\chi(T)$ (overlaid to the $\sigma(T)$ data of figure 6.11-b for reference). These two features of $\sigma_{\#2}(T)$ demonstrate therefore a sizable *anisotropic* hyperfine coupling term for the corresponding nuclei.

The isotropic hyperfine contact term proportional to the on-site spin density, on the other hand, is probed by the line shift $K(T)$ after the subtraction of possible temperature-independent chemical shift terms. Figure 6.11a clearly shows that the sizable shift $K_{\#2}(T)$ of line 2 is nearly

independent of temperature, and it is therefore dominated by a chemical shift in the order of -4%. Such a large value demonstrates its origin from low-lying excited crystal field states via the van Vleck mechanism,[195] and is comparable to the values found in the non-magnetic ground state of transition metal ions, like e.g. low-spin cobalt [196]. The isotropic hyperfine coupling of these

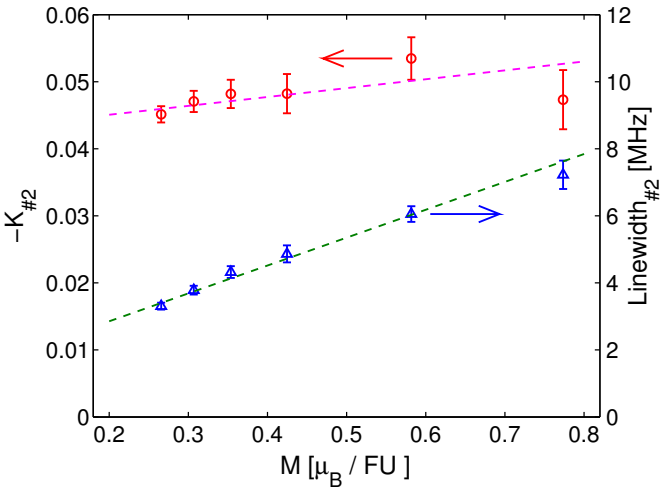

Figure 6.12: Opposite lineshift $-K_{\#2}$ and linewidth $\sigma_{\#2}$ of line 2 in the ^{55}Mn NMR spectra of sample S2 of figure 6.10, plotted as a function of the macroscopic magnetic moment calculated from the $\chi(T)$ data of figure 6.11.

^{55}Mn nuclei, probed by the residual temperature-dependent component of $K_{\#2}(T)$, can be better estimated by comparison with magnetometry data in the K vs M plot of figure 6.12, where temperature is the implicit parameter. The linear fit in the figure extrapolates to a maximal spin-dependent component in $\Delta K_{\#2}^{(sat)} = (\partial K_{\#2}/\partial M)M_s = -0.04(2)$ for a saturation moment $M_s \approx 3\mu_B$, i.e. a hyperfine field $B_{hf}^{(iso)} = \Delta K_{\#2}^{(sat)} B_{ext} = -300 \pm 150$ mT in the virtual magnetically saturated state which would be attained either in much larger magnetic fields or at lower temperature while preserving however the high-temperature electronic and structural properties of the material. Assuming an on-site origin for the electronic polarization at the nucleus, the latter corresponds to a saturation Mn moment of just $\approx 0.03\ \mu_B$, according to the core-polarization coupling constant of circa $11\ \mathrm{T}/\mu_B$ demonstrated above by comparing NMR with neutron scattering data. For reference, the extrapolation from the analogous linear dependence of $\sigma_{\#2}$ on M (shown in figure 6.12 as well) yields an asymptotic linewidth $\sigma_{\#2}^{(sat)} = 25(2)$ MHz, whence a rms anisotropic hyperfine field $B_{hf}^{(anis)} = \sqrt{3}\,\sigma_{\#2}^{(sat)} 2\pi/\gamma = 4.1(3)$ T. Such a large value of $B_{hf}^{(anis)}$ cannot arise from the tiny on-site spin moment estimated above,[197] and must be therefore a transferred contribution from neighboring magnetic ions. Given the presence of a large, though anisotropic, transferred hyperfine field at the corresponding Mn site, a transferred origin cannot be ruled out for its much smaller $B_{hf}^{(iso)}$ as well. Therefore, this majority ^{55}Mn NMR signal is compatible with a strictly spinless Mn species.

In view of the mixed magnetism detected in these materials by several techniques, including

the ZF ^{55}Mn NMR experiments on this exact sample reported in this paper, this resonance is undoubtedly assigned to Mn ions at 3 site, and it proves that the drop of the $3f$ spontaneous resonance frequency observed below T_C evolves into a truly non magnetic in the PM phase. To this end, it is worth noting that the limiting linewidth $\sigma_{\#2}^{(sat)}$ of peak 2, defined above, coincides numerically with the experimental linewidth of the $3f$ peak in the low temperature ZF spectrum (figure 6.2). Such a coincidence suggests the same transferred origin for the inhomogeneous broadening of the spontaneous $3f$ resonance as well, in spite of the transition of the $3f$ ions to a magnetic state at low temperature.

We now focus on the sharper minority line 1. It is apparent from figure 6.11-a and 6.10) that its shift $K_{\#1}$, much smaller than $K_{\#2}$ and opposite in sign, is practically independent of temperature. Moreover the magnitude of its linewidth $\sigma_{\#1}(T)$, also much smaller than $\sigma_{\#2}(T)$, agrees with a dominant dipolar origin from classical electronic moments. These two facts indicate, respectively, vanishing isotropic and a small anisotropic hyperfine couplings, i.e. a *diamagnetic* behavior. Indeed, this Mn species does not develop a magnetic ground state on cooling, unlike the majority fraction probed by peak 2, as it is witnessed by the detection of the corresponding resonance safely below T_C, broadened ($\sigma_{\#1} \approx 3$ MHz at $T = 140$ K) but essentially unshifted (figure 6.10). Though a minority diamagnetic Mn fraction, however, its belonging to a non magnetic impurity phase can be safely ruled out. Its amount is estimated in fact as large as $0.12(2)$ atoms per FU from the amplitude of its ^{55}Mn NMR peak relative to peak 2 probing $3f$ Mn. A spurious phase in such an amount would have been detected by X ray diffraction, contrary to experimental evidence. Moreover its nuclear relaxations, though weaker than on peak 2, are however in the typical range of nuclei of non magnetic ions in magnetic materials, like e.g. ^{139}La in lanthanum manganites [198, 199] and cobaltates [196]. This proves that these nuclei experience electronic spin fluctuations and therefore belong to the proper MnFeSiP phase.

An indication on the origin of this so-called diamagnetic Mn fraction is provided by its systematic search in the other samples. Resonances perfectly similar to lines 1 and 2, except for a larger chemical shift of the former ($K_{\#1} \approx 1.3$) and overall broader spectra due the vicinity of T_C, were found in sample S1 as well above 290 K up to he highest available temperature (360 K). In such a temperature range, the very large linewidth of peak 2 makes a reliable assessment of its position and amplitude, hence a cross-calibration of the amplitudes of the two peaks, impossible. Qualitatively, the intensity of peak 1 in S1 appears comparable or just slightly smaller than in S2. Its origin from diamagnetic Mn atoms which retain their non-magnetic character down to the lowest temperature is confirmed by the ^{55}Mn resonance peaks detected at $T = 5$ K in the frequency scans of figure 6.13 in moderate applied fields (so that the corresponding frequency intervals safely do not overlap to field-shifted $3f$ spontaneous resonance). The common origin of these peaks with the high-temperature line 1 is proven by their shift with field by the ^{55}Mn gyromagnetic ratio γ (times a small correction for the chemical shift $K_{\#1}$) and a small positive internal field $B_{hf} = 0.7$ T, according to the relation

$$\bar{\nu}(H) = \frac{\gamma}{2\pi}\left[B_{hf} + \mu_0(1 + K_{\#1})H\right] \tag{6.2}$$

As illustrated in the figure 6.13 inset. The positive sign of B_{hf}, in contrast with the negative spin hyperfine coupling of transition metal ions arising from the core polarization mechanism, warrants in fact its transferred origin, compatibly with a spinless Mn state. The search for

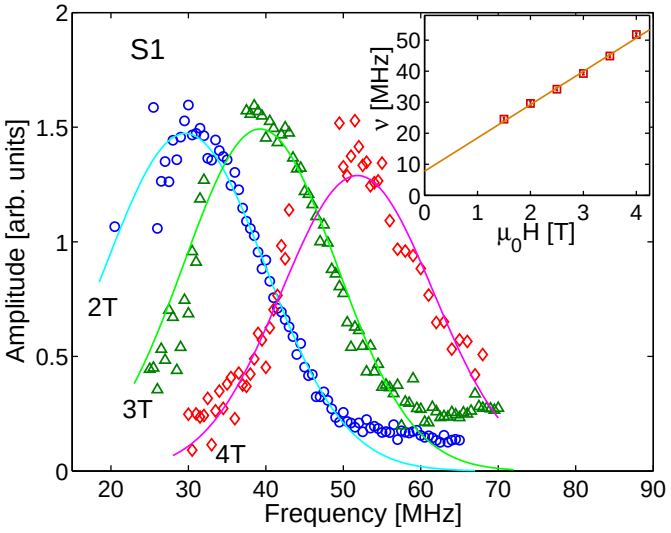

Figure 6.13: ^{55}Mn NMR resonance lines from the diamagnetic Mn fraction of sample S1 at $T = 5$ K, in various applied fields. Inset: mean resonance frequency $\bar{\nu}$ vs. applied field.

Table 6.2: Low-temperature mean ^{55}Mn ZFNMR frequencies and relative amplitudes of the main peaks in spectra of the various samples.

Sample	$\bar{\nu}_{3g}$	$\bar{\nu}_{3f}$	A_{3f}/A_{3g}	A_{3f}/A_{3g}[1]
	(MHz)	(MHz)	(measured)	(expected)
S1	289.4(2)	166.2(2)	0.32(3)	0.27
S2	258.0(2)	154.2(2)	0.50(4)	0.7
S3	320.0(1)	224(1)	0.04 (1)	0
S4	312.6(2)	216.2(5)	0.10 (2)	0

signals from non-magnetic Mn at both room and low temperature, on the contrary, was unsuccessful in samples S3 and S4. Based on the estimated sensitivity of our NMR measurements, the missed detection of such signals poses an upper limit to a possible diamagnetic Mn fraction not exceeding 1% per FU. Its practical absence in these two samples, incidentally with the same $x = 1$ Mn content and hence with a small, if not vanishing, concentration of Mn atoms at the $3f$ sites (Tabs. 6.1, 6.2), as opposed to its sizable amount found in the Mn-richer S1 and S2 samples, suggests that diamagnetic Mn atoms are located at $3f$ sites.

[1] Assumed equal to $x - 1$ (see text).

6.4 Discussion and Conclusions

ZF ^{55}Mn NMR proves that the magnetic transition of Fe_2P based Mn-Fe-Si-P alloys is strongly first order even at a Mn concentration as high as $x = 1.7$ (sample S2), where a SOMT was inferred from a smoother $M(T)$ magnetization curve and a shallower magnetic entropy peak at T_C[78]. At this composition, however, the truncation effect on the magnetic order parameter, probed locally by the spontaneous ^{55}Mn resonance frequency $\bar{\nu}_{3g}(T)$, is as severe as at other compositions. As already discussed above, the magnetic transition in this compound is actually characterized by a PM-FM phase coexistence over a wide temperature interval, indicative of broad distribution of T_C driven by a blurred magnetoelastic transition. Although the overall effect of such inhomogeneities on the macroscopic magnetism accidentally mimics a SOMT, it is clear that here the continuous parameter at T_C is the ordered volume instead of the local moment, and that this magnetic transition is not driven by critical fluctuations. Based on this finding for this compound, whose macroscopic response shows the closest resemblance to that of a SOMT, we conclude that no real SOMT can be found in the composition phase diagram of Mn-Fe-Si-P alloys, and therefore FOMTs are a general property of these materials.

Similarly, a phase-separated state, rather than a weak FM structure, is responsible for the kinetically-arrested magnetic order of the Si-poor S4 compound, apparent from its unsaturated and strongly hysteretic magnetization. ^{55}Mn NMR demonstrates that the macroscopic magnetic moment develops by the nucleation of fully FM domains, while only the magnetically ordered volume is hysteretic vs. both temperature and applied field. The missed detection of any other magnetic phase, including the SDW reported by neutron scattering, indicates that the competing phase to the FM fraction, as seen by a comparatively slow probe like NMR, cannot be distinguished from the PM phase.

The mixed magnetism of the Mn-Fe-Si-P systems is detected by NMR through the independent temperature dependence of the ordered moments at the $3f$ and $3g$ sites. The drop of the spin polarization at the $3f$ site on warming up to T_C, and not just its ordered component, is demonstrated by the steeper decrease of the $\bar{\nu}_{3g}$ NMR order parameter not accompanied by excess spin fluctuations, as it is witnessed by relatively weaker nuclear relaxations on the $3f$ resonance peak. The extinction of the $3f$ moment develops as a progressive reduction over a wide temperature range on warming and it is still incomplete at T_C, as it is apparent by the non-zero $\bar{\nu}_{3g}(T_C)$ value (sample S2, featuring the highest T_C, is a possible exception to the latter behavior). This suggests that the FOMT of these materials, though related to the weakening of the $3f$ magnetism observed with increasing temperature, is not simply triggered by it. This is particularly evident in the kinetically arrested S4 compound, showing only a moderate reduction of the $3f$ moment at its upper transition temperature $T_C^{\uparrow}$. As already pointed out in Sec. 6.3.3, the stronger truncation effect on its order parameter curve might be the clue to the decoupling of the $3f$ moment quenching from the magneto-elastic transition of this sample. Nevertheless, the drop of the $3f$ moment proceeds up to a spinless state of the $3f$ ions at temperatures high enough. This could be verified directly by ^{55}Mn NMR well above T_C in a strong applied field whenever it was applicable, namely in the Mn-richer sample S2 (and, with much lower accuracy, S1) showing a significant fraction of $3f$ sites occupied by Mn ions. The direct detection of a non-magnetic $3f$ Mn state confirms the prediction of a vanishing spin density at the $3f$ sites

by band structure calculations, [181] later challenged, however, by XMCD, [180] thus solving a long-standing controversy.

Besides the majority fraction of "normal" $3f$ Mn atoms that develop itinerant magnetism below T_C, a Mn species with even weaker interactions with the surrounding magnetic ions and preserving its character down to the lowest temperatures, is revealed by the same NMR experiments at the same Mn-rich compositions. Though minority, such a so-called diamagnetic fraction, which is reported in this work for the first time, is sizable ($\approx 12\%$ per FU in S2) and ^{55}Mn nuclei therein experience spin fluctuations. This rules out its belonging to a non magnetic manganese-based impurity phase, whose possible nature is however unclear. Unlike e.g. cobalt, whose Co^{3+} ion exhibits a low-spin (i.e. spinless) ground state in a octahedral crystal field, [196, 200] we are not aware, indeed, of any non-magnetic ionic state of manganese. The disproportionation of Mn into high-spin and low-spin species at distinct sites, on the other hand, is possible in intermetallic compounds, including metallic manganese itself (α-Mn), [201] whose Mn-IV atoms exhibit a nearly spinless state. [202] We argue therefore that the diamagnetic Mn state found in these compounds may be driven by a similar spontaneous electronic segregation within the proper Mn-Fe-Si-P phase. To this end, the lack of a significant diamagnetic Mn signal in the Mn-poorer S3 and S4 compounds where no Mn occupancy of $3f$ sites by Mn is expected (and a small one is detected by ZF NMR) indicates that diamagnetic Mn as well occupy $3f$ sites. In this view the electronic segregation, still to be identified, should involve two slightly different states of the $3f$ ion, weakly magnetic and strictly non magnetic, respectively.

The relevance of a diamagnetic Mn fraction at the $3f$ sites for the magnetic and magnetocaloric properties of the materials where it is present in a significant amount is unclear so far. However, it accounts qualitatively for some discrepancies found from the ZF ^{55}Mn NMR spectra of the Mn-richer S2 compound ($x = 1.7$), namely, a $3f$ to $3g$ peak intensity ratio smaller than expected (Tab. 6.2) and, on the contrary, a larger estimate for $3f$ moment than neutron scattering (figure 6.3). Notably, the estimated diamagnetic fraction of sample S2 nearly equals within experimental errors its missing fraction of $3f$ ordered moments. In sample S1 ($x = 1.27$), also showing a significant diamagnetic Mn fraction, the $3f$ ZF NMR peak amplitude in fair agreement with its expected value may the results of a compensation by off-site Mn atoms spilled over from their preferential $3g$ site, as in sample S4. In the presence of a disproportionation between a magnetic and non-magnetic species at the same crystallographic site, on the other hand, a probe in reciprocal space (neutron scattering) yields an averaged moment between the two sites, while a probe in direct space (NMR) probes only the moment of the magnetic species. This observation qualitatively explains the steeper decrease vs the Mn concentration of the $3f$ ordered moment determined by neutrons than by NMR. We have however no explanation for the opposite relative dependence observed by the two techniques at the $3g$ site, where a moment decrease is detected by NMR only.

Chapter 7

Summary and Outlook

In conclusion, we characterized several classes of materials by applying two powerful spin spectroscopy techniques, nuclear magnetic resonance (NMR) and inelastic neutron scattering (INS). There have been several key results from this thesis, which we summarize in the following paragraphs, while also commenting on the future outlook for each.

The lowest-energy spin excitations of a lanthanide-based molecular nanomagnet, namely the Yb^{3+} ions with a ^{173}Yb-nucleus of [Yb(trensal)], were thoroughly characterized by the NMR spectroscopy, as illustrated in chapter 3. The spin transitions in this system exhibit a mixed electronic-nuclear character, due to the hyperfine coupling, although electronic and nuclear degrees of freedom are progressively decoupled by an increasing external field. The lower-frequency resonances which, in a large enough applied field, may be regarded to many respects as the NMR of a I = 5/2 nuclear spin in a hyperfine field, were distinctly resolved using both the frequency and field sweep measurements. The system was successfully modeled using the spin Hamiltonian approach, yielding the energy level structure. The phase memory times (T_2) were measured to show that the coherence times of the [Yb(trensal)] are long enough for its potential applications in quantum computation as a nuclear qudit (d = 6). Furthermore, the application of CPMG pulse sequences demonstrated that the coherence times can be further enhanced by applying intense refocusing pulses at continuous intervals to decouple the system from the environment. The spin-lattice relaxation times were also found to be long enough for the quantum operations. In addition, driving several Rabi oscillation cycles for selected transitions established our capability to coherently manipulate the nuclear spins over a sufficiently long time scales. These observations were only made possible by the huge enhancement, of the order of few thousand, from the mixing of electron-nuclei matrix-element. Finally, these unique experimental results enabled us to show that the [Yb(trensal)] MNM can be exploited to define a quantum error protected qubit, where any error can be detected and corrected inside the proposed algorithm using electronic qubit as an ancilla. The encoded algorithm protects against amplitude or phase shift quantum errors. These results open a new perspective in the field of f-electron molecular qubits, where the multi-level hyperfine coupled structure of the Ln-MNMs can be exploited as a powerful tool for quantum information processing. In particular, the next step would be to investigate a dimer of interacting and inequivalent Ln-molecular units enabling

an error-resilient two-qudit gate.

In chapter 4, a direct measurement and the modeling of the magnetic interactions between highly anisotropic lanthanide ions in a family of Kramers asymmetric, dimetallic molecular nanomagnet was carried out using three different INS spectrometers. INS results on 4f dimer MNMs (Ln= Er, Yb, Dy) elucidated the crystal field structure, enabling the distinct assignment of crystal field transitions from each inequivalent lanthanide site. Furthermore, high resolution INS experiments provided the magnitude of the exchange interactions in the dimer family. Combining our results with other experimental techniques and ab initio calculations, we showed that the dipolar interactions were a significant component of the magnetic interactions in Er_2, although they do not account for all the experimental features. On the other hand, the superexchange interactions are dominant in the Yb dimer and the dipolar interactions are much weaker. The Dy_2 crystal field and exchange interaction are being analyzed and modeled using an effective point charge approach. Preliminary results were presented in this chapter. These results are also important for the progress towards obtaining a transferable Hamiltonian for the exchange interactions in Ln-MNMs.

Chapter 5 presented the NMR experiments carried out on the dysprosocenium single ion magnet. This single ion magnet belongs to the family of molecules which holds the record for the highest blocking temperatures, but their slow magnetic relaxation is still not understood. The NMR spectra measurements targeted the ^{1}H and ^{19}F resonances, broadened by dipolar interactions between the ligand and the magnetic ion electronic spins. The ^{1}H relaxation rates were measured to probe the fluctuations in the hyperfine field induced by the dipolar interactions between molecular electronic spins. Modeling of these results will provide valuable information on the latter's relaxation mechanisms. At this moment, our results have revealed a weak dependence of the proton relaxation rates on the strength of external magnetic field pointing to the approximate increase of the electronic relaxation rate as the square of the applied field. Further analysis of the NMR results and the theoretical modeling is ongoing. These results will be useful for tailoring single ions magnets with higher blocking temperatures.

Finally, several compositions of the Fe_2P based Mn-Fe-Si-P alloys were studied in chapter 6 with zero- and applied-field ^{55}Mn NMR. There are two metal sites in their crystal structure, $3g$ and $3f$, where Mn prefers to occupy the former. Our results proved the strong first order nature of the magnetic transition in all these compounds, even where a second order magnetic transition was inferred from a smoother M(T) magnetization curve and a shallower magnetic entropy peak at T_C. Our experiments revealed that the first order magnetic transition in these materials is not simply triggered by the weakening of the $3f$ magnetism, observed with increasing temperature, though they both are related. Besides the majority fraction of normal 3f Mn atoms that develop itinerant magnetism below T_C, a Mn species with even weaker interactions with the surrounding magnetic ions and preserving its character down to the lowest temperatures, is revealed by the NMR experiments at the Mn-rich compositions. These results have settled some long standing questions about this family of magnetocaloric compounds. Indeed the deeper understanding of the magneto-structural transitions in the MnFePSi alloys will be helpful in tailoring even better compounds for the magnetic energy conversion applications.

Chapter 8

Bibliography

[1] O. Kahn. *Molecular Magnetism*. VCH Publishers, Inc, 1993. 2

[2] Dante Gatteschi, Roberta Sessoli, and Jacques Villain. *Molecular Nanomagnets*. Mesoscopic Physics and Nanotechnology. Oxford University Press, Oxford, 2006. 2

[3] Andrea Caneschi, Dante Gatteschi, Roberta Sessoli, Anne Laure Barra, Louis Claude Brunel, and Maurice Guillot. Alternating current susceptibility, high field magnetization, and millimeter band epr evidence for a ground S = 10 state in $[Mn_{12}O_{12}(Ch3COO)_{16}(H_2O)_4].2CH_3COOH.4H_2O$. *Journal of the American Chemical Society*, 113(15):5873–5874, 1991. 2

[4] Roberta Sessoli, Dante Gatteschi, Andrea Caneschi, and M.A. Novak. Magnetic Bistability in a metal-ion cluster. *Nature*, 365:141–143, 1993. 2, 100

[5] L. Thomas, F. Linoti, R. Ballou, D. Gatteschi, R. Sessoli, and B. Barbara. Macroscopic Quantum Tunnelling of Magnetization in a single crystal of nanomagnets. *Nature*, 383:145–147, 1996. 2

[6] G. Christou, D. Gatteschi, D.N. Hendrickson, and R. Sessoli. Single-molecule magnets. *MRS Bull.*, 25:66–71, 2000. 2

[7] A.L. Barra, P. Debrunner, D. Gatteschi, C.E. Schulz, and R. Sessoli. Superparamagnetic-like Behavior in an Octanuclear Iron Cluster. *Europhys. Lett.*, 35:133–138, 1996. 2

[8] Roberto Caciuffo, Giuseppe Amoretti, Amir Murani, Roberta Sessoli, Andrea Caneschi, and Dante Gatteschi. Neutron spectroscopy for the magnetic anisotropy of molecular clusters. *Phys. Rev. Lett.*, 81:4744–4747, Nov 1998. 2

[9] S.L. Castro, Z. Sun, J.C. Bollinger, D.N. Hendrickson, and G. Christou. Tetranuclear Vanadium(III) Carboxylate Chemistry, and a new Example of a Metal Butterfly Complex exhibiting Spin Frustration: Structure and Properties of $[V_4O_2(O_2CEt)_7(bpy)_2](ClO_4)$. *J. Chem. Soc. Chem. Commun.*, 0:2517–2518, 1995. 2

[10] E.C. Yang and D.N. Hendrickson. Cobalt Single-Molecule Magnet. *J. Appl. Phys.*, 91:7382, 2002. 2

[11] A.J. Blake, C.M. Grant, S. Parsons, J.M. Rawson, and R.E.P. Winpenny. The Synthesis, Structure and Magnetic Properties of a Cyclic Dodecanuclear Nickel Complex. *J. Chem.*

Soc. Chem. Commun., 0:2363–2364, 1994. 2

[12] E.J. Schelter, A.V. Prosvirin, and K.R. Dunbar. Molecular cube of Re^{II} and Mn^{II} that exhibits Single-Molecule Magnetism. *J. Am. Chem. Soc.*, 126:15004–15005, 2004. 2

[13] Kun Qian, Xing-Cai Huang, Chun Zhou, Xiao-Zeng You, Xin-Yi Wang, and Kim R. Dunbar. A Single-Molecule Magnet Based on Heptacyanomolybdate with the Highest Energy Barrier for a Cyanide Compound. *Journal of the American Chemical Society*, 135(36):13302–13305, 2013.

[14] Naoto Ishikawa, Miki Sugita, Tadahiko Ishikawa, Shin-ya Koshihara, and Youkoh Kaizu. Lanthanide Double-Decker Complexes Functioning as Magnets at the Single-Molecular Level. *Journal of the American Chemical Society*, 125(29):8694–8695, 2003. 3

[15] Jeffrey D. Rinehart and Jeffrey R. Long. Slow Magnetic Relaxation in a Trigonal Prismatic Uranium(III) Complex. *Journal of the American Chemical Society*, 131(35):12558–12559, 2009. 2

[16] J.J. Sokol, A.G. Hee, and J.R. Long. A cyano-bridged single-molecule magnet: Slow magnetic relaxation in a trigonal prismatic $MnMo_6(CN)_{18}$ cluster. *J. Am. Chem. Soc.*, 124:7656–7657, 2002. 2

[17] Shutaro Osa, Takafumi Kido, Naohide Matsumoto, Nazzareno Re, Andrzej Pochaba, and Jerzy Mrozinski. A Tetranuclear 3d-4f Single Molecule Magnet: $[CuIILTbIII(hfac)_2]_2$. *Journal of the American Chemical Society*, 126(2):420–421, 2004. 2

[18] A.M. Ako, I.J. Hewitt, V. Mereacre, R. Clérac, W. Wernsdorfer, C.E. Anson, and A. K. Powell. A Ferromagnetically Coupled Mn_{19} Aggregate with a Record S=83/2 Ground Spin State. *Angew. Chem. Int. Ed.*, 45:4926–4929, 2006. 3

[19] Daniel N. Woodruff, Richard E. P. Winpenny, and Richard A. Layfield. Lanthanide single-molecule magnets. *Chemical Reviews*, 113(7):5110–5148, 2013. 3, 70

[20] O. Waldmann. A Criterion for the Anisotropy Barrier in Single-molecule Magnets. *Inorg. Chem.*, 46:10035–10037, 2007. 3

[21] C.R. Ganivet, B. Ballesteros, G. de la Torre, J.M. Clemente Juan, E. Coronado, and T. Torres. Influence of peripheral substitution on the magnetic behaviour of single-ion magnets based on homo- and heteroleptic Tb III Bis(phthalocyaninate). *Chem. Eur. J.*, 19:1457–1465, 2012. 3

[22] Fu-Sheng Guo, Benjamin M. Day, Yan-Cong Chen, Ming-Liang Tong, Akseli Mansikkamäki, and Richard A. Layfield. Magnetic hysteresis up to 80 Kelvin in a dysprosium metallocene single-molecule magnet. *Science*, xx:xxxx, 2018. 3, 100

[23] Conrad A.P. Goodwin, Fabrizio Ortu, Daniel Reta, Nicholas F. Chilton, and David P. Mills. Molecular magnetic Hysteresis at 60 Kelvin in dysprosocenium. *Nature*, 548(7668):439–442, 2017. 3, 100, 101

[24] Guo Fu-Sheng, Day Benjamin M., Chen Yan-Cong, Tong Ming-Liang, Mansikkamäki Akseli, and Layfield Richard A. A dysprosium metallocene single-molecule magnet functioning at the axial limit. *Angewandte Chemie International Edition*, 56(38):11445–11449, 2017. 3, 100

[25] M. N. Leuenberger and D. Loss. Quantum computing in molecular magnets. *Nature*, 410:789–793, 2001. 4, 52

[26] Filippo Troiani, Marco Affronte, Stefano Carretta, Paolo Santini, and Giuseppe Amoretti. Proposal for Quantum Gates in Permanently Coupled Antiferromagnetic Spin Rings without Need of Local Fields. *Phys. Rev. Lett.*, 94:190501, May 2005. 4

[27] A. Ardavan, O. Rival, J. J. L. Morton, S. J. Blundell, A. M. Tyryshkin, Timco G. A., and R. E. P. Winpenny. Will spin-relaxation times in molecular magnets permit quantum information processing? *Phys. Rev. Lett.*, 77:054428, 2007. 4

[28] C. J. Wedge, G. A. Timco, E. T. Spielberg, R. E. George, F. Tuna, S. Rigby, E. J. L. McInnes, R. E. P.Winpenny, S. J. Blundell, and A. Ardavan. Chemical engineering of molecular qubits. *Phys. Rev. Lett.*, 108:107204, 2012. 4, 52

[29] Michael J. Graham, Joseph M. Zadrozny, Muhandis Shiddiq, John S. Anderson, Majed S. Fataftah, Stephen Hill, and Danna E. Freedman. Influence of electronic spin and spin–orbit coupling on decoherence in mononuclear transition metal complexes. *J. Am. Chem. Soc.*, 136:7623–7626, 2014.

[30] K. Bader, D. Dengler, S. Lenz, B. Endeward, S.-D. Jiang, P. Neugebauer, and J. van Slageren. Room temperature quantum coherence in a potential molecular qubit. *Nature Commun.*, 5:5304, 2014.

[31] Joseph M. Zadrozny, Jens Niklas, Oleg G. Poluektov, and Danna E. Freedman. Millisecond coherence time in a tunable molecular electronic spin qubit. *ACS Cent. Sci.*, 1:488–492, 2015.

[32] Matteo Atzori, Elena Morra, Lorenzo Tesi, Andrea Albino, Mario Chiesa, Lorenzo Sorace, and Roberta Sessoli. Quantum Coherence Times Enhancement in Vanadium(IV)-based Potential Molecular Qubits: the Key Role of the Vanadyl Moiety. *J. Am. Chem. Soc.*, 138:11234–11244, 2016.

[33] Chung-Jui Yu, Michael J. Graham, Joseph M. Zadrozny, Jens Niklas, Matthew D. Krzyaniak, Michael R. Wasielewski, Oleg G. Poluektov, and Danna E. Freedman. Long coherence times in nuclear spin-free Vanadyl qubits. *J. Am. Chem. Soc.*, 138:14678–14685, 2016.

[34] Matteo Atzori, Lorenzo Tesi, Stefano Benci, Alessandro Lunghi, Roberto Righini, Andrea Taschin, Renato Torre, Lorenzo Sorace, and Roberta Sessoli. Spin Dynamics and Low Energy Vibrations: Insights from Vanadyl-Based Potential Molecular Qubits. *J. Am. Chem. Soc.*, 139:4338–4341, 2017.

[35] Lorenzo Tesi, Eva Lucaccini, Irene Cimatti, Mauro Perfetti, Matteo Mannini, Matteo Atzori, Elena Morra, Mario Chiesa, Andrea Caneschi, Lorenzo Sorace, and Roberta Sessoli. Quantum coherence in a processable Vanadyl complex: new tools for the search of molecular spin qubits. *Chem. Sci.*, 7:2074–2083, 2016. 4, 52

[36] S. Bertaina, S. Gambarelli, T. Mitra, B. Tsukerblat, A. Müller, and B. Barbara. Quantum oscillations in a molecular magnet. *Nature*, 453:203–207, 2008. 4, 52

[37] Joseph M. Zadrozny, Jens Niklas, Oleg G. Poluektov, and Danna E. Freedman. Multiple quantum coherences from hyperfine transitions in a Vanadium(IV) complex. *J. Am. Chem. Soc.*, 136:15841–15844, 2014.

[38] Majed S. Fataftah, Joseph M. Zadrozny, Scott C. Coste, Michael J. Graham, Dylan M. Rogers, and Danna E. Freedman. Employing Forbidden Transitions as Qubits in a Nuclear

Spin-Free Chromium Complex. *J. Am. Chem. Soc.*, 138:1344–1348, 2016.

[39] Matteo Atzori, Lorenzo Tesi, Elena Morra, Mario Chiesa, Lorenzo Sorace, and Roberta Sessoli. Room-Temperature Quantum Coherence and Rabi Oscillations in Vanadyl Phthalocyanine: Toward Multifunctional Molecular Spin Qubits. *J. Am. Chem. Soc.*, 138:2154–2157, 2016. 4, 52

[40] G. A. Timco, S. Carretta, F. Troiani, F. Tuna, R. J. Pritchard, C. A. Muryn, E. J. L. McInnes, A. Ghirri, A. Candini, P. Santini, G. Amoretti, M. Affronte, and R. E. P. Winpenny. Engineering the coupling between molecular spin qubits by coordination chemistry. *Nature Nanotech.*, 4:173, 2009. 4

[41] E. Garlatti, T. Guidi, S. Ansbro, P. Santini, G. Amoretti, J. Ollivier, H. Mutka, G. Timco, I.J. Vitorica-Yrezabal, G.F.S. Whitehead, R.E.P. Winpenny, and S. Carretta. Portraying entanglement between molecular qubits with four-dimensional inelastic neutron scattering. *Nature Commun.*, 8:14543, 2017. 4

[42] Alessandro Chiesa, George F. S. Whitehead, Stefano Carretta, Laura Carthy, Grigore A. Timco, Simon J. Teat, Giuseppe Amoretti, Eva Pavarini, Richard E. P. Winpenny, and Paolo Santini. Molecular nanomagnets with switchable coupling for quantum simulation. *Sci. Rep.*, 4:7423, 2014. 4

[43] Jesus Ferrando-Soria, Eufemio Moreno Pineda, Alessandro Chiesa, Antonio Fernandez, Samantha A. Magee, Stefano Carretta, Paolo Santini, Inigo J. Vitorica-Yrezabal, Floriana Tuna, Grigore A. Timco, Eric J.L. McInnes, and Richard E.P. Winpenny. A modular design of molecular qubits to implement universal quantum gates. *Nature Nanotech.*, 7:11377, 2016.

[44] Jesus Ferrando-Soria, Samantha A. Magee, Alessandro Chiesa, Stefano Carretta, Paolo Santini, Inigo J. Vitorica-Yrezabal, Floriana Tuna George F.S. Whitehead, Stephen Sproules, Kyle M. Lancaster, Anne-Laure Barra, Grigore A. Timco, Eric J.L. McInnes, and Richard E.P. Winpenny. Switchable interaction in molecular double qubits. *Chem*, 1:727–757, 2016. 4

[45] S. Nakazawa, S. Nishida, T. Ise, T. Yoshino, N. Mori, R. Rahimi, K. Sato, Y. Morita, K. Toyota, D. Shiomi, M. Kitagawa, H. Hara, P. Carl, P. Höfer, and T. Takui. Universal control of nuclear spins via anisotropic hyperfine interactions. *Angew. Chem. Int. Ed.*, 51:9860, 2012. 4

[46] Arzhang Ardavan, Alice M Bowen, Antonio Fernandez, Alistair J Fielding, Danielle Kaminski, Fabrizio Moro, Christopher A Muryn, Matthew D Wise, Albert Ruggi, Eric JL McInnes, Kay Severin, Grigore A Timco, Christiane R Timmel, Floriana Tuna, George FS Whitehead, and Richard EP Winpenny. Engineering coherent interactions in molecular nanomagnet dimers. *npj Quantum Information*, 1:15012, 2015. 4

[47] Muhandis Shiddiq, Dorsa Komijani, Yan Duan, Alejandro Gaita-Ariño, Eugenio Coronado, and Stephen Hill. Enhancing coherence in molecular spin qubits via atomic clock transitions. *Nature*, 531(7594):348–351, 2016. 4, 52

[48] F. Luis, A. Repollés, M. J. Martínez-Pérez, D. Aguilá, O. Roubeau, D. Zueco, P. J. Alonso, M. Evangelisti, A. Camón, J. Sesé, L. A. Barrios, and G. Aromí. Molecular Prototypes for Spin-Based CNOT and SWAP Quantum Gates. *Phys. Rev. Lett.*, 107:117203, 2011.

[49] J David Aguilá, Leoní A. Barrios, Verónica Velasco, Olivier Roubeau, Ana Repollés, Pablo J. Alonso, Javier Sesé, Simon J. Teat, Fernando Luis, and Guillem Aromí. Heterodimetallic [LnLn'] Lanthanide Complexes: Toward a Chemical Design of Two-Qubit Molecular Spin Quantum Gates. *J. Am. Chem. Soc.*, 136:14215–14222, 2014. 52

[50] Kasper S. Pedersen, Ana Maria Ariciu, Simon McAdams, Høgni Weihe, Jesper Bendix, Floriana Tuna, and Stergios Piligkos. Toward molecular 4f single-ion magnet qubits. *Journal of the American Chemical Society*, 138(18):5801–5804, 2016. 4, 53, 54, 68

[51] P. Siyushev, K. Xia, R. Reuter, M. Jamali, N. Zhao, N. Yang, C. Duan, N. Kukharchyk, A. D. Wieck, R. Kolesov, and J. Wrachtrup. Coherent properties of single rare-earth spin qubits. *Nature Commun.*, 5:3895, 2014. 4

[52] S. Takahashi, I. S. Tupitsyn, J. van Tol, C. C. Beedle, D. N. Hendrickson, and P. C. E. Stamp. Decoherence in crystals of quantum molecular magnets. *Nature*, 476:76, 2011. 4

[53] P. C. E. Stamp. Environmental decoherence versus Intrinsic decoherence. *Philosophical Transactions of the Royal Society of London A: Mathematical, Physical and Engineering Sciences*, 370(1975):4429–4453, 2012. 4

[54] P. C. E. Stamp and I. S. Tupitsyn. Coherence window in the dynamics of quantum nanomagnets. *Phys. Rev. B*, 69:014401, Jan 2004. 4

[55] M. A. Nielsen and I. L. Chuang. *Quantum Computation and Quantum Information*. Cambridge University Press, Cambridge (UK), 2000. 6, 68

[56] Simon J Devitt, William J Munro, and Kae Nemoto. Quantum error correction for beginners. *Reports on Progress in Physics*, 76(7):076001, 2013. 6

[57] Julia Kempe. *Approaches to Quantum Error Correction*, pages 85–123. Birkhäuser Basel, Basel, 2007. 6

[58] Brück E. Developments in magnetocaloric refrigeration. *J Phys D Appl Phys*, 38:381, 2005. 7

[59] O. Gutfleisch, M. A. Willard, E. Brück, C. H. Chen, S. G. Sankar, and J. P. Liu. Magnetic materials and devices for the 21st century: stronger, lighter, and more energy efficient. *Adv Mater*, 23:821, 2011. 7

[60] E. Warburg. Magnetische untersuchungen. *Ann. Phys.*, 249:141–164, 1881. 7

[61] P. Debye. Some observations on magnetisation at a low temperature. *Ann. Physik.*, 81:1154–1160, 1926. 7

[62] W. F. Giauque. A thermodynamic treatment of certain magnetic effects. a proposed method of producing temperatures considerably below 1° absolute. *J. Am. Chem. Soc.*, 49:1864–1870, 1927. 7

[63] W. F. Giauque and D. P. MacDougall. Attainment of temperatures below 1° absolute by demagnetization of $Gd_2\ (SO_4)_3 \cdot 8H_2O$. *Phys. Rev.*, 43:768–768, 1933. 7

[64] G. V. Brown. Magnetic heat pumping near room temperature. *Journal of Applied Physics*, 47(8):3673–3680, 1976. 7

[65] V. K. Pecharsky and K. A. Gschneidner, Jr. Giant magnetocaloric effect in $Gd_5(Si_2\ Ge_2)$. *Phys. Rev. Lett.*, 78:4494–4497, Jun 1997. 7

[66] S.A. Nikitin, G. Myalikgulyev, A.M. Tishin, M.P. Annaorazov, K.A. Asatryan, and A.L. Tyurin. The magnetocaloric effect in $Fe_{49}Rh_{51}$ compound. *Physics Letters A*, 148(6):363

– 366, 1990. 7

[67] Feng-xia Hu, Bao-gen Shen, Ji-rong Sun, Zhao-hua Cheng, Guang-hui Rao, and Xi-xiang Zhang. Influence of negative lattice expansion and metamagnetic transition on magnetic entropy change in the compound $LaFe_{11.4}Si_{1.6}$. *Applied Physics Letters*, 78(23):3675–3677, 2001. 7

[68] A. Fujita, S. Fujieda, Y. Hasegawa, and K. Fukamichi. Itinerant-electron metamagnetic transition and large magnetocaloric effects in $La(Fe_x\ Si_{1-x})_{13}$ compounds and their hydrides. *Phys. Rev. B*, 67:104416, Mar 2003. 7

[69] N. T. Trung, L. Zhang, L. Caron, K. H. J. Buschow, and E. Brück. Giant magnetocaloric effects by tailoring the phase transitions. *Applied Physics Letters*, 96(17):172504, 2010. 7

[70] F. C. Nascimento, A. O. dos Santos, A. de Campos, S. Gama, and L. P. Cardoso. Structural and magnetic study of the MnAs magnetocaloric compound. *Materials Research*, 9:111 – 114, 2006. 7

[71] H. Wada and Y. Tanabe. Giant magnetocaloric effect of $MnAs_{1-x}Sb_x$. *Applied Physics Letters*, 79(20):3302–3304, 2001. 7

[72] Thorsten Krenke, Eyüp Duman, Mehmet Acet, Eberhard F. Wassermann, Xavier Moya, Lluis Mañosa, and Antoni Planes. Inverse magnetocaloric effect in ferromagnetic Ni–Mn–Sn alloys. *Nature Materials*, 4:450–454, 2005. 7

[73] Feng-xia Hu, Bao-gen Shen, and Ji-rong Sun. Magnetic entropy change in $Ni_{51.5}Mn_{22.7}Ga_{25.8}$ alloy. *Applied Physics Letters*, 76(23):3460–3462, 2000. 7

[74] Feng-xia Hu, Bao-gen Shen, Ji-rong Sun, and Guang-heng Wu. Large magnetic entropy change in a heusler alloy $Ni_{52.6}Mn_{23.1}Ga_{24.3}$ single crystal. *Phys. Rev. B*, 64:132412, 2001.

[75] R. Kainuma, Y. Imano, W. Ito, Y. Sutou, H. Morito, S. Okamoto, O. Kitakami, K. Oikawa, A. Fujita, T. Kanomata, and K. Ishida. Magnetic-field-induced shape recovery by reverse phase transformation. *Nature*, 439:957–960, 2006. 7

[76] O. Tegus, E. Brück, K. H. J. Buschow, and F. R. de Boer. Transition-metal-based magnetic refrigerants for room-temperature applications. *Nature*, 415:150–152, 2002. 7

[77] N. T. Trung, Z. Q. Ou, T. J. Gortenmulder, O. Tegus, K. H. J. Buschow, and E. Brück. Tunable thermal hysteresis in MnFe(P,Ge) compounds. *Applied Physics Letters*, 94(10):102513, 2009.

[78] N. H. Dung, L. Zhang, Z. Q. Ou, and E. Brück. From first-order magneto-elastic to magneto-structural transition in $(Mn,Fe)_{1.95}P_{0.50}Si_{0.50}$ compounds. *Applied Physics Letters*, 99(9):092511, 2011. 109, 126

[79] F. Guillou, G. Porcari, H. Yibole, N. van Dijk, and E. Brück. Taming the first-order transition in giant magnetocaloric materials. *Advanced Materials*, 26(17):2671–2675, 2014.

[80] F. Guillou, H. Yibole, G. Porcari, L. Zhang, N. H. van Dijk, and E. Brück. Magnetocaloric effect, cyclability and coefficient of refrigerant performance in the MnFe(P, Si, B) system. *Journal of Applied Physics*, 116(6):063903, 2014. 7

[81] K A GschneidnerJr, V K Pecharsky, and A O Tsokol. Recent developments in magne-

tocaloric materials. *Reports on Progress in Physics*, 68(6):1479, 2005. 7

[82] V. Franco, J.S. Blázquez, J.J. Ipus, J.Y. Law, L.M. Moreno-Ramírez, and A. Conde. Magnetocaloric effect: From materials research to refrigeration devices. *Progress in Materials Science*, 93:112 – 232, 2018.

[83] Anders Smith, Christian R.H. Bahl, Rasmus Bjørk, Kurt Engelbrecht, Kaspar K. Nielsen, and Nini Pryds. Materials challenges for high performance magnetocaloric refrigeration devices. *Advanced Energy Materials*, 2(11):1288–1318, 2012. 7

[84] G. Amoretti. Chapter 1 - Crystal field and exchange interaction for magnetic ions in solids. Magnetic Properties of Matter. World Scientific Publishing Co. Singapore, 1988. 10, 13, 14

[85] Hans A. Bethe. Splitting of terms in crystals. *Annalen der Physik*, 3:133–206, 1929. 12

[86] K.W.H. Stevens. Matrix elements and operator equivalents connected with the magnetic properties of rare earth ions. *Proc. Phys. Soc. A*, 65:209–215, 1952. 13

[87] Elena Bartolomé, Ana Arauzo, Javier Luzón, Juan Bartolomé, and Fernando Bartolomé. Chapter 1 - Magnetic relaxation of lanthanide-based molecular magnets. volume 26 of *Handbook of Magnetic Materials*, pages 1 – 289. Elsevier, 2017. 14

[88] J. Jensen and A. R. Mackintosh. *Rare Earth Magnetism: Structures and Excitations*. International Series of Monographs on Physics 81. Clarendon Press, Oxford, 1991. 14

[89] C. P. Slichter. *Principles of Magnetic Resonance*. Springer Verlag, Berlin (Germany), 1996. 18, 26, 62, 63

[90] A. Abragam. *Principles of Nuclear Magnetism*. Oxford Science Publications, Oxford (UK), 1989. 22, 23, 25

[91] Eiichi Fukushima and Stephen B.W. Roeder. *Experimental Pulse NMR: A Nuts and Bolts Approach*. Addison-Wesley Publishing Company, Inc., Reading, Massachusetts (USA), 1981. 18, 34

[92] Elena Garlatti. Quantum effects in Molecular Nanomagnets: from Theory to Applications. *PhD Thesis*, 2013. 18, 36, 101

[93] Sara Bordignon. Magnetic properties and Spin dynamics in magnetic Molecular Rings. *PhD Thesis*, 2015. 18, 101

[94] F. Bloch. Nuclear Induction. *Phys. Rev.*, 70:460, 1946. 20, 21

[95] A.G. Redfield. Nuclear magnetic resonance saturation and rotary saturation in solids. *Phys. Rev.*, 98:1787, 1955. 25

[96] R. Wangsness and F Bloch. The dynamical theory of nuclear induction. *Phys. Rev.*, 89:728, 1953. 25

[97] F Bloch. Dynamical theory of nuclear induction. II. *Phys. Rev.*, 102:104, 1956. 25

[98] Albert Narath. Nuclear spin-lattice relaxation in hexagonal transition metals: Titanium. *Phys. Rev.*, 162:320, 1967. 26, 63, 64

[99] E. L. Hahn. Spin echoes. *Phys. Rev.*, 80:580, 1950. 27

[100] W. M. Witzel and S. Das Sarma. Multiple-pulse coherence enhancement of solid state spin qubits. *Phys. Rev. Lett.*, 98:077601, Feb 2007. 28

[101] R. Zaripov, E. Vavilova, V. Miluykov, I. Bezkishko, O. Sinyashin, K. Salikhov, V. Kataev, and B. Büchner. Boosting the electron spin coherence in binuclear Mn complexes by

multiple microwave pulses. *Phys. Rev. B*, 88:094418, Sep 2013. 28

[102] G. Allodi, A. Banderini, R. De Renzi, and C. Vignali. Hyrespect: A broadband fast-averaging spectrometer for nuclear magnetic resonance of magnetic materials. *Rev. Sci. Instrum.*, 76(8):083911, 2005. 30, 55, 112

[103] Albert Furrer, Joël Mesot, and Thierry Strässle. *Neutron Scattering in Condensed Matter Physics*. WORLD SCIENTIFIC, 2009. 36, 38

[104] G. L. Squires. *Introduction to the Theory of Thermal Neutron Scattering*. Cambridge University Press, 3 edition, 1978. 36

[105] S.W. Lovesey. *Theory of Neutron Scattering from Condensed Matter*. Number Volume I and II: Polarization Effects and Magnetic Scattering in International Series of Monographs on Physics 72. Clarendon Press, Oxford, 1986. 36, 38, 39, 41, 42

[106] Tatiana Guidi. Spin Excitations and Magnetic Properties of Molecular Nanomagnets. *PhD Thesis*, 2004. 36

[107] ISIS STFC. MARI website. https://www.isis.stfc.ac.uk/Pages/MARI.aspx. Accessed: 2018-08-30. 46

[108] R.I. Bewley, J.W. Taylor, and S.M. Bennington. LET, a cold neutron multi-disk chopper spectrometer at ISIS. *Nuclear Instruments and Methods in Physics Research Section A: Accelerators, Spectrometers, Detectors and Associated Equipment*, 637(1):128 – 134, 2011. 47

[109] M. A. Adams, W. S. Howells, and M. T. F. Telling. *The IRIS User Guide*. ISIS Facility Rutherford Appleton Laboratory, Oxforshire Didcot (UK), 2 edition, 2001. 48

[110] O. Arnold, J.C. Bilheux, J.M. Borreguero, A. Buts, S.I. Campbell, L. Chapon, M. Doucet, N. Draper, R. Ferraz Leal, M.A. Gigg, V.E. Lynch, A. Markvardsen, D.J. Mikkelson, R.L. Mikkelson, R. Miller, K. Palmen, P. Parker, G. Passos, T.G. Perring, P.F. Peterson, S. Ren, M.A. Reuter, A.T. Savici, J.W. Taylor, R.J. Taylor, R. Tolchenov, W. Zhou, and J. Zikovsky. Mantid – Data analysis and visualization package for neutron scattering and μSR Experiments. *Nuclear Instruments and Methods in Physics Research Section A: Accelerators, Spectrometers, Detectors and Associated Equipment*, 764:156 – 166, 2014. 49, 76, 86

[111] ISIS STFC. Mantid Project crystal field interface website. http://docs.mantidproject.org/v3.9.0/interfaces/CrystalFieldPythonInterface.html. Accessed: 2018-09-11. 50, 79, 86

[112] ISIS STFC. Mslice website. http://mslice.isis.rl.ac.uk/Main_Page. Accessed: 2018-08-30. 51

[113] T. D. Ladd, F. Jelezko, R. Laflamme, Y. Nakamura, C. Monroe, and J. L. O'Brien. Quantum computers. *Nature*, 464:46–53, 2010. 52

[114] I. M. Georgescu, S. Ashab, and F. Nori. Quantum Simulation. *Rev. Mod. Phys.*, 86:153, 2014. 52

[115] Tong Liu, Qi-Ping Su, Jin-Hu Yang, Yu Zhang, Shao-Jie Xiong, Jin-Ming Liu, and Chui-Ping Yang. Transferring arbitrary d-dimensional quantum states of a superconducting transmon qudit in circuit QED. *Sci. Rep.*, 7:7039, 2017. 52

[116] Stephen S. Bullock, Dianne P. O'Leary, and Gavin K. Brennen. Asymptotically optimal quantum circuits for d-level systems. *Phys. Rev. Lett.*, 94:230502, 2005. 52

[117] Benjamin P. Lanyon, Marco Barbieri, Marcelo P. Almeida, Thomas Jennewein, Timothy C. Ralph, Kevin J. Resch, Geoff J. Pryde, Jeremy L. O'Brien, Alexei Gilchrist, and Andrew G. White. Simplifying quantum logic using higher-dimensional Hilbert spaces. *Nature Phys.*, 5:134–140, 2008. 52

[118] M. D. Jenkins, Y. Duan, B. Diosdado, J. J. García-Ripoll, A. Gaita-Arino, C. Giménez-Saiz, P. J. Alonso, E. Coronado, and F. Luis. Coherent manipulation of three-qubit states in a molecular single-ion magnet. *Phys. Rev. B*, 95:064423, 2017. 52

[119] E.O. Kiktenko, A.K. Fedorov, A.A. Strakhov, and V.I. Man'ko. Single qudit realization of the Deutsch algorithm using superconducting many-level quantum circuits. *Phys. Lett. A*, 379:1409, 2015. 52

[120] Matthew Neeley, Markus Ansmann, Radoslaw C. Bialczak, Max Hofheinz, Erik Lucero, Aaron D. O'Connell, Daniel Sank, Haohua Wang, James Wenner, Andrew N. Cleland, Michael R. Geller, and John M. Martinis. Emulation of a quantum spin with a superconducting phase qudit. *Science*, 325:722–725, 2009. 52

[121] H. F. Chau. Correcting quantum errors in higher spin systems. *Phys. Rev. A*, 55:R839, 1997. 52

[122] Stefano Pirandola, Stefano Mancini, Samuel L. Braunstein, and David Vitali. Minimal qudit code for a qubit in the phase-damping channel. *Phys. Rev. A*, 77:032309, 2008. 52, 67, 68

[123] D. Bruss and C. Macchiavello. Optimal eavesdropping in cryptography with three-dimensional quantum states. *Phys. Rev. Lett.*, 88:127901, 2002. 53

[124] Adetunmise C. Dada, Jonathan Leach, Gerald S. Buller, Miles J. Padgett, and Erika Andersson. Experimental high-dimensional two-photon entanglement and violations of generalized bell inequalities. *Nature Phys.*, 7:677–680, 2011. 53

[125] C. Godfrin, A. Ferhat, R. Ballou, S. Klyatskaya, M. Ruben, W. Wernsdorfer, and F. Balestro. Operating Quantum States in Single Magnetic Molecules: Implementation of Grover's Quantum Algorithm. *Physical Review Letters*, 119(18):1–5, 2017. 53

[126] Kazunobu Sato, Shigeaki Nakazawa, Robabeh Rahimi, Tomoaki Ise, Shinsuke Nishida, Tomohiro Yoshino, Nobuyuki Mori, Kazuo Toyota, Daisuke Shiomi, Yumi Yakiyama, Yasushi Morita, Masahiro Kitagawa, Kazuhiro Nakasuji, Mikio Nakahara, Hideyuki Hara, Patrick Carl, Peter Höfer, and Takeji Takui. Molecular electron-spin quantum computers and quantum information processing: pulse-based electron magnetic resonance spin technology applied to matter spin-qubits. *J. Mat. Chem.*, 19:3739–3754, 2009.

[127] Stefan Thiele, Franck Balestro, Rafik Ballou, Svetlana Klyatskaya, Mario Ruben, and Wolfgang Wernsdorfer. Electrically driven nuclear spin resonance in single-molecule magnets. *Science*, 344:1135, 2014.

[128] Satoru Yamamoto, Shigeaki Nakazawa, Kenji Sugisaki, Kazunobu Sato, Kazuo Toyota, Daisuke Shiomi, and Takeji Takui. Adiabatic quantum computing with spin qubits hosted by molecules. *Phys. Chem. Chem. Phys.*, 17:2742, 2015. 53

[129] J. A. Jones. Quantum computing with nmr. *Progress in Nuclear Magnetic Resonance*

Spectroscopy, 59:91–120, 2011. 53

[130] Michael Mehring and Jens Mende. Spin-bus concept of spin quantum computing. *Phys. Rev. A*, 73:052303, 2006. 53

[131] J. S. Hodges, J. C. Yang, C. Ramanathan, and D. G. Cory. Universal control of nuclear spins via anisotropic hyperfine interactions. *Phys. Rev. A*, 78:010303(R), 2008.

[132] Yingjie Zhang, Colm A. Ryan, Raymond Laflamme, and Jonathan Baugh. Coherent control of two nuclear spins using the anisotropic hyperfine interaction. *Phys. Rev. Lett.*, 107:170503, 2011. 53

[133] Eva Lucaccini, Lorenzo Sorace, Mauro Perfetti, Jean-Pierre Costes, and Roberta Sessoli. Beyond the anisotropy barrier: slow relaxation of the magnetization in both easy-axis and easy-plane Ln(trensal) complexes. *Chem. Commun.*, 50:1648–1651, 2014. 53

[134] Kasper S. Pedersen, Liviu Ungur, Marc Sigrist, Alexander Sundt, Magnus Schau-Magnussen, Veacheslav Vieru, Hannu Mutka, Stephane Rols, Hø gni Weihe, Oliver Waldmann, Liviu F. Chibotaru, Jesper Bendix, and Jan Dreiser. Modifying the properties of 4f single-ion magnets by peripheral ligand functionalisation. *Chem. Sci.*, 5:1650–1660, 2014. 54

[135] Kasper S. Pedersen, Jan Dreiser, Høgni Weihe, Romain Sibille, Heini V. Johannesen, Mikkel A. Sorensen, Bjarne E. Nielsen, Marc Sigrist, Hannu Mutka, Stephane Rols, Jesper Bendix, and Stergios Piligkos. Design of single-molecule magnets: Insufficiency of the anisotropy barrier as the sole criterion. *Inorg. Chem.*, 54:7600, 2015. 54, 55, 57, 58

[136] N. Stone. *Table of Nuclear Magnetic Dipole and Electric Quadrupole Moments*. International Atomic Energy Agency, INDC(NDS)-0658, 2014. 58

[137] A. Abragam and B. Bleaney. *Electron Paramagnetic Resonance of Transition Ions*. International Series of Monographs on Physics. Clarendon Press, Oxford, 1970. 58

[138] A. Ghirri, A. Chiesa, S. Carretta, F. Troiani, J. van Tol, S. Hill, I. Vitorica-Yrezabal, G. A. Timco, R. E. P. Winpenny, and M. Affronte. Coherent spin dynamics in molecular Cr_8Zn wheels. *J. Phys. Chem. Lett.*, 6:5062, 2015. 62

[139] G. de Lange, Z. H. Wang, D. Ristè, V. V. Dobrovitski, and R. Hanson. Universal dynamical decoupling of a single solid-state spin from a spin bath. *Science*, 330:60, 2010. 62

[140] Lorenza Viola and Seth Lloyd. Dynamical suppression of decoherence in two-state quantum systems. *Phys. Rev. A*, 58:2733, 1998. 62

[141] G. S. Uhrig. Keeping a quantum bit alive by optimized π-pulse sequences. *Phys. Rev. Lett.*, 98:100504, 2007.

[142] J. Medford, L. Cywinski, C. Barthel, C. M. Marcus, M. P. Hanson, and A. C. Gossard. Scaling of dynamical decoupling for spin qubits. *Phys. Rev. Lett.*, 108:086802, 2012. 62

[143] Riaz Hussain, Giuseppe Allodi, Alessandro Chiesa, Elena Garlatti, Dmitri Mitcov, Andreas Konstantatos, Kasper S. Pedersen, Roberto De Renzi, Stergios Piligkos, and Stefano Carretta. Coherent Manipulation of a Molecular Ln-Based Nuclear Qudit Coupled to an Electron Qubit. *Journal of the American Chemical Society*, 140(31):9814–9818, 2018. PMID: 30040890. 68

[144] Lorenzo Sorace, Cristiano Benelli, and Dante Gatteschi. Lanthanides in molecular mag-

netism: old tools in a new field. *Chem. Soc. Rev.*, 40:3092–3104, 2011. 70

[145] W. Wernsdorfer, N. Aliaga-Alcalde, D. N. Hendrickson, and G. Christou. Exchange-biased quantum tunnelling in a supramolecular dimer of single-molecule magnets. *Nature*, 416:406, 2002. 70

[146] E. Moreno-Pineda, Y. Lan, O. Fuhr, W. Wernsdorfer, and M. Ruben. Exchange-bias quantum tunnelling in a CO_2-based Dy_4-single molecule magnet. *Chem. Sci.*, 8:1178, 2017. 70

[147] J. D. Rinehart, M. Fang, W. J. Evans, and J. R. Long. A N_2^{3-} radical-bridged terbium complex exhibiting magnetic hysteresis at 14 K. *J. Am. Chem. Soc.*, 133:14236, 2011. 70, 100, 101

[148] K. R. Meihaus, J. F. Corbey, M. Fang, J. W. Ziller, J. R. Long, and W. J. Evans. Influence of an inner-sphere K^+ ion on the magnetic behavior of N_2^{3-}-radical-bridged dilanthanide complexes isolated using an external magnetic field. *Inorg. Chem.*, 53:3099, 2014.

[149] J. D. Rinehart, M. Fang, W. J. Evans, and J. R. Long. Strong exchange and magnetic blocking in N_2^{3-}-radical-bridged lanthanide complexes. *Nat. Chem.*, 3:538, 2011. 70

[150] G. Brunet, F. Habib, I. Korobkov, and M. Murugesu. Significant enhancement of energy barriers in dinuclear dysprosium single-molecule magnets through electron-withdrawing effects. *Inorg. Chem.*, 54:6195, 2015. 70

[151] M. Kofu, O. Yamamuro, T. Kajiwara, Y. Yoshimura, M. Nakano, K. Nakajima, S. Ohira-Kawamura, T. Kikuchi, and Y. Inamura. Hyperfine structure of magnetic excitations in a Tb-based single-molecule magnet studied by high-resolution neutron spectroscopy. *Phys. Rev. B: Condens. Matter Mater. Phys.*, 88:64405, 2013. 70

[152] R. Marx, F. Moro, M. D´orfel, L. Ungur, M. Waters, S. D. Jiang, M. Orlita, J. Taylor, W. Frey, L. F. Chibotaru, and J. van Slageren. Spectroscopic determination of crystal field splittings in lanthanide double deckers. *Chem. Sci.*, 5:3287, 2014. 81

[153] M. Vonci, M. J. Giansiracusa, R. W. Gable, W. Van den Heuvel, K. Latham, B. Moubaraki, K. S. Murray, D. Yu, R. A. Mole, A. Soncini, and C. Boskovic. Ab initio calculations as a quantitative tool in the inelastic neutron scattering study of a single-molecule magnet analogue. *Chem. Commun.*, 52:2091, 2016.

[154] M. J. Giansiracusa, M. Vonci, W. Van Den Heuvel, R. W. Gable, B. Moubaraki, K. S. Murray, D. Yu, R. A. Mole, A. Soncini, and C. Boskovic. Carbonate-bridged lanthanoid triangles: Single-molecule magnet behavior, inelastic neutron scattering, and ab initio studies. *Inorg. Chem.*, 55:5201, 2016.

[155] M. Vonci, M. J. Giansiracusa, W. Van Den Heuvel, R. W. Gable, B. Moubaraki, K. S. Murray, D. Yu, R. A. Mole, A. Soncini, and C. Boskovic. Magnetic excitations in Polyoxotungstate-supported lanthanoid single-molecule magnets: An inelastic neutron scattering and ab initio study. *Inorg. Chem.*, 56:378, 2017. 70

[156] A. Furrer, H. U. Güdel, H. Blank, and A. Heidemann. Direct observation of exchange splittings in $Cs_3Tb_2Br_9$ by neutron spectroscopy. *Phys. Rev. Lett.*, 62:210, 1989. 71

[157] H. U. Güdel, A. Furrer, and H. Blank. Exchange interactions in rare-earth-metal dimers. neutron spectroscopy of $Cs_3Yb_2Cl_9$ and $Cs_3Yb_2Br_9$. *Inorg. Chem.*, 29:4081, 1990. 81

[158] A. Donni, A. Furrer, H. Blank, and A. Heidemann. Structure and magnetic excitations in

$Cs_3Ho_2Br_9$ studied by neutron scattering. *Phys. B*, 156-157:370, 1989.

[159] J. Glerup and H. Weihe. Magnetic susceptibility and EPR spectra of (μ-Hydroxo)bis[pentaamminechromium(III)] chloride monohydrate. *Inorg. Chem.*, 36:2816, 1997.

[160] M. A. Aebersold, H. U. Güdel, A. Furrer, and H. Blank. Inelastic neutron scattering and optical spectroscopy of Dy^{3+} single ions and dimers in $Cs_3Y_2Br_9$:10% Dy^{3+} and $Cs_3Dy_2Br_9$. *Inorg. Chem.*, 33:1133, 1994.

[161] A. Furrer, H. U. Güdel, E. Krausz, and H. Blank. Neutron spectroscopic study of anisotropic exchange in the dimer compound $Cs_3Ho_2Br_9$. *Phys. Rev. Lett.*, 64:68, 1990. 71

[162] N. Iwahara and L. F. Chibotaru. Exchange interaction between J multiplets. *Phys. Rev. B: Condens. Matter Mater. Phys.*, 91:174438, 2015. 71

[163] W. W. Lukens, N. Magnani, and C. H. Booth. Application of the hubbard model to $Cp^*_2Yb(bipy)$, a model system for strong exchange coupling in lanthanide systems. *Inorg. Chem.*, 51:10105, 2012.

[164] A. Palii, B. Tsukerblat, J. M. Clemente-Juan, and E. Coronado. Magnetic exchange between metal ions with unquenched orbital angular momenta: basic concepts and relevance to molecular magnetism. *Int. Rev. Phys. Chem.*, 29:135, 2010. 71

[165] Marcus J. Giansiracusa, Eufemio Moreno-Pineda, Riaz Hussain, Raphael Marx, María Martínez Prada, Petr Neugebauer, Susan Al-Badran, David Collison, Floriana Tuna, Joris van Slageren, Stefano Carretta, Tatiana Guidi, Eric J. L. McInnes, Richard E. P. Winpenny, and Nicholas F. Chilton. Measurement of magnetic exchange in asymmetric lanthanide dimetallics: Toward a transferable theoretical framework. *Journal of the American Chemical Society*, 140(7):2504–2513, 2018. PMID: 29373020. 71, 72

[166] E. Moreno-Pineda, N. F. Chilton, R. Marx, M. Dörfel, D. O. Sells, P. Neugebauer, S.-D. Jiang, D. Collison, J. van Slageren, E. J. L. McInnes, and R. E. P. Winpenny. Direct measurement of dysprosium(iii)$\cdots$dysprosium(iii) interactions in a single-molecule magnet. *Nat. Commun.*, 5:5243, 2014. 71, 81, 94, 96

[167] P.J. Brown. ILL Grenoble website. `https://www.ill.eu/sites/ccsl/ffacts/ffachtml.html`. Accessed: 2018-09-26. 78

[168] N. F. Chilton, R. P. Anderson, L. D. Turner, A. Soncini, and K. S. Murray. PHI: a powerful new program for the analysis of anisotropic monomeric and exchange-coupled polynuclear d- and f-block complexes. *J. Comput. Chem.*, 34:1164, 2013. 83

[169] S. Stoll and A. Schweiger. Easyspin, a comprehensive software package for spectral simulation and analysis in EPR. *J. Magn. Reson.*, 178:42, 2006. 83

[170] Varley F. Sears. Neutron scattering lengths and cross sections. *Neutron News*, 3(3):26–37, 1992. 93

[171] J. J. Baldovi, J. J. Borras-Almenar, J. M. Clemente-Juan, E. Coronado, and A. Gaita-Arino. Modeling the properties of lanthanoid single-ion magnets using an effective point-charge approach. *Dalton Trans.*, 41:13705–13710, 2012. 96

[172] J. J. Baldovi, J. M. Clemente-Juan, E. Coronado, Y. Duan, A. Gaita-Arino, and C. Giménez-Saiz. Rational design of single-ion magnets and spin qubits based on

mononuclear lanthanoid complexes. *Inorganic Chemistry*, 53:9976–9980, 2014. 97

[173] José J. Baldoví, Salvador Cardona-Serra, Juan M. Clemente-Juan, Eugenio Coronado, Alejandro Gaita-Ariño, and Andrew Palii. SIMPRE: A software package to calculate crystal field parameters, energy levels, and magnetic properties on mononuclear lanthanoid complexes based on charge distributions. *Journal of Computational Chemistry*, 34(22):1961–1967, 2013. 97

[174] Kwang Soo Lim, José J. Baldoví, Woo Ram Lee, Jeong Hwa Song, Sung Won Yoon, Byoung Jin Suh, Eugenio Coronado, Alejandro Gaita-Ariño, and Chang Seop Hong. Switching of slow magnetic relaxation dynamics in mononuclear Dysprosium(III) compounds with charge density. *Inorganic Chemistry*, 55(11):5398–5404, 2016. 97

[175] J. J. Baldovi, A. Gaita-Arino, and E. Coronado. Modeling the magnetic properties of lanthanide complexes: relationship of the REC parameters with Pauling electronegativity and coordination number. *Dalton Trans.*, 44:12535–12538, 2015. 98

[176] P. Santini, S. Carretta, E. Liviotti, G. Amoretti, P. Carretta, M. Filibian, A. Lascialfari, and E. Micotti. NMR as a probe of the relaxation of the magnetization in magnetic molecules. *Phys. Rev. Lett.*, 94:077203, 2005. 101, 108

[177] T. Moriya. Nuclear magnetic relaxation in antiferromagnetics. *Progress of Theoretical Physics*, 16(1):23–44, 1956. 108

[178] N. H. Dung, L. Zhang, Z. Q. Ou, L. Zhao, L. van Eijck, A. M. Mulders, M. Avdeev, E. Suard, N. H. van Dijk, and Ekkes Brück. High/low-moment phase transition in hexagonal Mn-Fe-P-Si compounds. *Phys. Rev. B*, 86:045134, Jul 2012. 109, 110, 113, 114, 119

[179] X. F. Miao, L. Caron, P. Roy, N. H. Dung, L. Zhang, W. A. Kockelmann, R. A. de Groot, N. H. van Dijk, and E. Brück. Tuning the phase transition in transition-metal-based magnetocaloric compounds. *Phys. Rev. B*, 89:174429, May 2014. 109, 119

[180] H. Yibole, F. Guillou, L. Caron, E. Jiménez, F. M. F. de Groot, P. Roy, R. de Groot, N. H. van Dijk, and E. Brück. Moment evolution across the ferromagnetic phase transition of giant magnetocaloric (Mn Fe)$_2$(P, Si B), compounds. *Phys. Rev. B*, 91:014429, Jan 2015. 109, 119, 127

[181] Nguyen H. Dung, Zhi Qiang Ou, Luana Caron, Lian Zhang, Dinh T.Cam Thanh, Gilles A. De Wijs, Rob A. De Groot, K. H.Jürgen Buschow, and Ekkes Brück. Mixed magnetism for refrigeration and energy conversion. *Advanced Energy Materials*, 1(6):1215–1219, 2011. 109, 119, 121, 127

[182] P. C. Riedi. Magnetic studies with zero field NMR. *Hyperfine Interact.*, 49:335–356, 1989. 112, 113

[183] M. A. Turov and M. P. Petrov. *Nuclear Magnetic Resonance in Ferro- and Antiferromagnets*. Halsted, New York, 1972. 112

[184] Per Jernberg, A.A. Yousif, Lennart Häggström, and Yvonne Andersson. A Mössbauer study of $Fe_2P_{1-x}Si_x$ (x $\leq$ 0.35). *Journal of Solid State Chemistry*, 53(3):313 – 322, 1984. 112

[185] G Allodi, R De Renzi, K Zheng, S Sanna, A Sidorenko, C Baumann, L Righi, F Orlandi, and G Calestani. Band filling effect on polaron localization in $La_{1-x}(Ca_ySr_{1-y})_x$ MnO_3

manganites. *Journal of Physics: Condensed Matter*, 26(26):266004, 2014. 112, 113, 117

[186] AM Portis and RH Lindquist. Magnetism ed. GT Rado and H. Suhl, 1965. 113

[187] E. Koster and B. G. Turrell. Nmr studies of fe2p and fe3p. *Journal of Applied Physics*, 42(4):1314–1315, 1971. 114, 115

[188] A. J. Freeman and R. E. Watson. Hyperfine interactions in magnetic materials. In G. T. Rado, editor, *Magnetism*, volume IIA. Academic Press, New York, 1965. 115

[189] X. F. Miao, Y. Mitsui, A. Iulian Dugulan, L. Caron, N. V. Thang, P. Manuel, K. Koyama, K. Takahashi, N. H. van Dijk, and E. Brück. Kinetic-arrest-induced phase coexistence and metastability in (Mn ,Fe)$_2$(P, Si). *Phys. Rev. B*, 94:094426, Sep 2016. 115, 116, 119

[190] G. Allodi, M. Bimbi, R. De Renzi, C. Baumann, M. Apostu, R. Suryanarayanan, and A. Revcolevschi. Magnetic order in the double-layer manganites $(La_{1-z}Pr_z)_{1.2}Sr_{1.8}Mn_2O_7$: Intrinsic properties and role of intergrowth. *Phys. Rev. B*, 78(6):064420, Aug 2008. 117

[191] C. P. Adams, J. W. Lynn, V. N. Smolyaninova, A. Biswas, R. L. Greene, W. Ratcliff, S-W. Cheong, Y. M. Mukovskii, and D. A. Shulyatev. First-order nature of the ferromagnetic phase transition in (La-Ca)MnO_3 near optimal doping. *Phys. Rev. B*, 70(13):134414, Oct 2004. 117

[192] X. F. Miao, L. Caron, J. Cedervall, P. C. M. Gubbens, P. Dalmas de Réotier, A. Yaouanc, F. Qian, A. R. Wildes, H. Luetkens, A. Amato, N. H. van Dijk, and E. Brück. Short-range magnetic correlations and spin dynamics in the paramagnetic regime of (Mn,Fe)$_2$(P,Si). *Phys. Rev. B*, 94:014426, Jul 2016. 118, 119

[193] X.F. Miao and N.V. Thang and L. Caron and H. Yibole and R.I. Smith and N.H. van Dijk and E. Brück. Tuning the magnetoelastic transition in (Mn,Fe)$_2$(P,Si) by B, C, and N doping. *Scripta Materialia*, 124:129 – 132, 2016.

[194] X.F. Miao and L. Caron and P.C.M. Gubbens and A. Yaouanc and P. Dalmas de Réotier and H. Luetkens and A. Amato and N.H. van Dijk and E. Brück. Spin correlations in (Mn,Fe)$_2$(P,Si) magnetocaloric compounds above Curie temperature. *Journal of Science: Advanced Materials and Devices*, 1(2):147 – 151, 2016. Special Issue in Memory of Dr. P.E. BROMMER. 119

[195] K. Nehrke and M. W. Pieper. Local Magnetism and Crystal Fields of Pr in $PrBa_2Cu_3O_7$ Studied by ^{141}Pr NMR. *Phys. Rev. Lett.*, 76:1936–1939, Mar 1996. 123

[196] T. Lancaster, S. R. Giblin, G. Allodi, S. Bordignon, M. Mazzani, R. De Renzi, P. G. Freeman, P. J. Baker, F. L. Pratt, P. Babkevich, S. J. Blundell, A. T. Boothroyd, J. S. Möller, and D. Prabhakaran. Stripe disorder and dynamics in the hole-doped antiferromagnetic insulator $la_{5/3}sr_{1/3}coo_4$. *Phys. Rev. B*, 89:020405, Jan 2014. 123, 124, 127

[197] Takeji Kubo, Akira Hirai, and Hisashi Abe. Mn55 nuclear magnetic resonance of the Mn3+ ion located at the B-site in manganese ferrite single crystal–anisotropic hyperfine field due to the local Jahn-Teller distortion. *Journal of the Physical Society of Japan*, 26(5):1094–1109, 1969. 123

[198] G. Allodi, R. De Renzi, F. Licci, and M. W. Pieper. First order nucleation of charge ordered domains in $La_{0.5}Ca_{0.5}MnO_3$ detected by ^{139}La and ^{55}Mn NMR. *Phys. Rev. Lett.*, 81(21):4736–4739, Nov 1998. 124

[199] G. Allodi, M. Cestelli Guidi, R. De Renzi, A. Caneiro, and L. Pinsard. Ultraslow polaron dynamics in low-doped manganites from ^{139}La NMR-NQR and muon spin rotation. *Phys. Rev. Lett.*, 87:127206, Aug 2001. 124

[200] G. Allodi, R. De Renzi, S. Agrestini, C. Mazzoli, and M. R. Lees. Nmr study of magnetic order, metamagnetic transitions, and low-temperature spin freezing in $Ca_3Co_2O_6$. *Phys. Rev. B*, 83:104408, Mar 2011. 127

[201] D. Hobbs, J. Hafner, and D. Spisák. Understanding the complex metallic element Mn. I. crystalline and noncollinear magnetic structure of α-Mn. *Phys. Rev. B*, 68:014407, Jul 2003. 127

[202] Hideki Yamagata and Kunisuke Asayama. NMR study of antiferromagnetic α-Mn metal. *Journal of the Physical Society of Japan*, 33(2):400–408, 1972. 127

List of Publications

Refereed publications

1. Riaz Hussain, Giuseppe Allodi, Alessandro Chiesa, Elena Garlatti, Dmitri Mitcov, Andreas Konstantatos, Kasper S. Pedersen, Roberto De Renzi, Stergios Piligkos and Stefano Carretta, *Coherent Manipulation of a Molecular Ln-Based Nuclear Qudit Coupled to an Electron Qubit*, DOI: 10.1021/jacs.8b05934 Journal of American Chemical Society 140 (31), (2018), 9814-9818.

2. Marcus J. Giansiracusa, Eufemio Moreno-Pineda, Riaz Hussain, Raphael Marx, María Dörfel, Andreas Döring, Susan Al-Badran, David Collison, Floriana Tuna, Joris van Slageren, Stefano Carretta, Tatiana Guidi, Eric J. L. McInnes, Richard E. P. Winpenny and Nicholas F. Chilton, *Measurement of Magnetic exchange in asymmetric Lanthanide Dimetallics: Towards a Transferable theoretical framework*, DOI: 10.1021/jacs.7b10714) Journal of American Chemical Society 140 (7) (2018), 2504-2513.

Publications in preparation

1. Riaz Hussain et al., ^{55}*Mn NMR evidence for mixed magnetism, nanoscale electronic segregation and ubiquitous first order transitions in Fe2P-based MnFeSiP alloys*

2. *Effective Point Charge Modeling for Dy dimer*

3. *Relaxation Dynamics of dysprosocenium single ion magnet*

Acknowledgements

These three years of my stay in Italy has been a truly fulfilling adventure, in which I have grown as a person, gained a new perspective on the life, and learned a lot in the process as well. I am so thankful for getting this opportunity, and my deepest gratitude goes to the MIUR (the Italian Ministry of Education, Universities and Research), and University of Parma, for the PhD position with scholarship. Now it's time to look back and remember all those people who have made this experience memorable and contributed in this journey both directly and indirectly. My sincere apologies if I miss someone because of my not-so-good memory.

I would like to start by thanking my supervisor, Prof. Giuseppe Allodi, for always being available to help and guide during these three years. I'm so thankful for the way he always responded to all the silly questions I asked and kept patience with my early-day blunders in the lab. Yet another big thanks to him, for carefully reading this thesis which indeed has greatly improved it. I have learned a lot from him, especially regarding his dedication to the subject and how meticulously he works to build instruments in the lab.

Huge thanks are also due to my co-supervisor Prof. Stefano Carretta, for the neutron scattering part of my research as well as obtaining all the molecular nanomagnet samples and handling the theory part. I'm also thankful to him for reading parts of this thesis, despite being super-busy. His scientific intuition and the way he organizes research is something I deeply wish to learn from.

My deepest gratitude and thanks to our group-head and the director of the department, Prof. Roberto De Renzi, about whom I can safely say that none of this was possible without him. From the day he responded to my first email, to each and every step along the way, his help was always there and I am so thankful for that. He was the one who kept me on-track, whenever I felt that I am lost in the wilderness of research. I have always turned to him for career advice and funding matters. His help even extended beyond the department/university to make sure that life was smooth for me outside, in particular, during the 'permesso di soggiorno' renewals and finding a place to stay during my early days in Italy. I am also grateful to him and his family, for the annual dinners at their house.

The coordinator of our doctoral program Prof. Cristiano Viappiani also deserves my deep gratitude and thanks for being patient and kind during all this time.

The exceptionally talented postdocs in Stefano's group, Dr. Elena Garlatti and Dr. Alessan-

dro Chiesa, were always open to help me in explaining various theoretical concepts whenever I needed it, for which I am very thankful. Also thank you both for reading some parts of this thesis.

I am thankful to all the referees and final exam committee for kindly agreeing to find time to evaluate my thesis. My heartfelt thanks go to all the collaborators, who prepared amazing samples and/or performed calculations and experiments, which helped me greatly in the completion of this thesis.

I am thankful to my friends in the 'gruppo del pranzo' for some memorable get-to-gathers and helping me learn some basics of the Italian language. Therein, Samuele Baldini who left soon after I arrived, but he made sure to guide me about life in the department early on. My next- door-lab neighbor (now Dr.) Francesco Cugini, was always available for my 'small chats' and also read the magnetocaloric theory part in this thesis. Thank you, Samuele and Francesco. I am also thankful to Prof. Giovanna Pelizza, my Italian language teacher due to which my life outside the university became easier although unfortunately I have not been able to become really fluent in the language.

My group fellow, Ifeanyi, was a constant source of motivation and my 'navigator-in-chief' through the corridors of all bureaucratic stuff here in Parma. I have come to know so many similarities between our countries, Nigeria and Pakistan, from him. My batch-mate Michele arranged an unforgettable trip to his house in 'Molise' and a short trip to Napoli in August'18. I was able to experience 'la famiglia' aspect of the south of Italy and I have become a profound supporter of 'il molise resiste' movement since then. These two guys, Anjali, and a few other members were part of our small 'English speaking group' in Parma. I have spent some of the most enjoyable moments with all of them. Thanks to all of you for making this last year so pleasant. I must note that the idea for this group emerged out of the 'English for research' course by Prof. Adrian Wallwork, and I am also grateful to him.

Starting with the much-needed help from Malik Tanvir on my first day in Parma to this day, a small Pakistani community was always there, to refuel my Punjabi language speaking and offering some free meals at the same time. Special thanks to Gulraiz and Irfan Bhai, who were my usual source of Pakistani meals. In addition, Gulraiz bhai was the exclusive source of information, advice and support outside of academic circles.

Instrument scientist at ISIS facility, Dr. Tatiana Guidi, from my first visit to U.K. in 2016 through the three months stay in 2017, was persistently a helpful mentor. She helped me in understanding the basics of neutron scattering and data analysis. I am tremendously thankful to her for extending support to me at any occasion I desired it, even beyond my stay there. During my last visit to the ISIS facility and Diamond light source in 2018, Dr. Mike Baker was very accommodating in explaining the point charge modeling background for which I am thankful.

A special mention is in order for Dr. Amina, who was a perpetual source of encouragement and motivation, especially in last few months. Also, I thank her so much for reading my thesis whenever I asked, at times without bothering about her tough job schedule.

I'm also thankful to all the excellent friends I have made in various schools and conferences I attended, in these three years.

I was a naïve, extremely shy and at times foolish 'village boy', when I started my bachelor's degree from the University of Gujrat. My friends there, all of whom are still dear friends, helped

me grow as a person. I am thankful to all the 'opposition alliance', especially Ch. Mohsan, Dr. Zubair, Rizwan, Isamil, Waqas and Samar, who are some of the best friends I have ever made. In particular, Dr. Zubair, 'the guru', has always been instrumental in helping me academically through all these years beyond graduation. My old friend from the town, Syed Hussan Raza, was/is always there for everything. I am grateful to have you as a friend 'murshad'.

Winning the scholarship for the master's degree from PIEAS was the very first moment when I realized that I can aim for, and achieve, bigger goals than what I had ever imagined as a child. My teachers at PIEAS were the first ones who instilled in me the courage and confidence to tackle scientific problems. Specifically, my thesis supervisors there, Prof. Sikander M. Mirza and Prof. Nasir M. Mirza, were/are always so helpful and kind for which I will always be thankful. Dr. Waqas Masood was not only a teacher, but still more of a friend and a source of inspiration to look through the dogmas and be a skeptic about the 'norms of society'. I wish to convey a special thanks to him for everything.

During my stay in the U.K., I feel lucky to have found friends like Alex and Erik, with whom I have enjoyed some of the best conversations ever, discussing everything from the philosophy of life and religion to the future of technology and the human race. Thank you, guys.

My brother-like cousin Liaqat Ali died a few months ago. He was one of the most precious people I met in my life, and I will always remember him. Rest in peace dear brother.

Last but not the least, my family has been, and is, the glue or the pillar, holding my life together. I have missed all of them so much during this time. I dedicate this thesis and any progress I have made in life, to my family and especially to my parents. My mother, who never went to school, and my father, who just had basic schooling, were always encouraging me to carry on with this endeavor. Although economically not so well-off, they made sure that their children did not miss any education related needs, to the best of their abilities (and at time even beyond). I will always be indebted to them. All my brothers, sisters-in-law, nephews and nieces have always been a source of motivation and love, and I am immensely grateful. I am so happy to have all of them in my life. Many thanks to my eldest brother Fiaz Hussain, who has always believed in me and has been always available for anything and everything. My brother Ijaz Hussain, who himself will earn a PhD in computer sciences soon, was always my guardian, confidant and more of a friend. He always helped and encouraged me to continue with this journey of knowledge. My life has been so much easier, at so many occasions, because of the presence of my brothers, Imran Ali and Farman Ali, for which I'm greatly thankful.

My family are all the colors in my 'rainbow of life', and I am immeasurably thankful to have their presence in this.